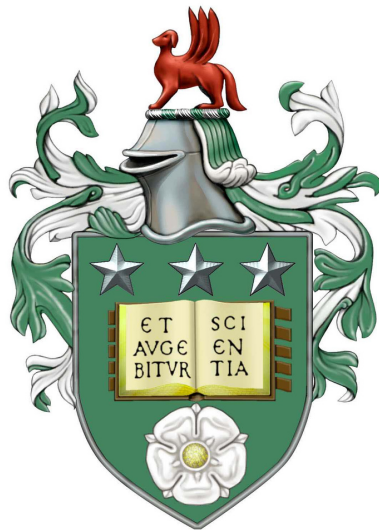


**A One-Field Fictitious Domain Method for
Fluid-Structure Interactions**

Yongxing Wang

Submitted in accordance with the requirements
for the degree of Doctor of Philosophy



The University of Leeds
School of Computing
August 2018

The candidate confirms that the work submitted is his/her own, except where work which has formed part of a jointly authored publication has been included. The contribution of the candidate and the other authors to this work has been explicitly indicated below. The candidate confirms that appropriate credit has been given within the thesis where reference has been made to the work of others.

Some parts of the work in this thesis have been published in the following articles:

Yongxing. Wang, P. K. Jimack, and M. A. Walkley, A one-field monolithic fictitious domain method for fluid-structure interactions, Computer Methods in Applied Mechanics and Engineering, 317 (2017), pp. 11461168, <https://doi.org/10.1016/j.cma.2017.01.023>.

The above publication is primarily the work of the candidate.

This copy has been supplied on the understanding that it is copyright material and that no quotation from the thesis maybe published without proper acknowledgement.

©2018 The University of Leeds and Yongxing Wang

Acknowledgements

I would like to thank my supervisors Prof. Peter Jimack and Dr. Mark Walkley for their support during my PhD life in the past three years. I thank Prof. Jimack for the financial support of this PhD and for my attendance at the relevant conferences; thanks also for his encouragement, suggestions and guidance, so that I can continuously pursue my initial goal, implement my ideas and finally form this PhD thesis; I thank Dr. Walkley for his suggestions, assistance and his patience – he is always there if you have any questions to ask; I appreciate their continuous support – we met almost every week to discuss my PhD project in the last three years. This thesis could not have been successfully finished without their specific help.

I would also want to thank my colleague and my friend Dr. Peter Bollada. Thanks for discussing every thing with me, including formulas, numerical simulations, life, politics and society, and playing table tennis with me, all of which made these three years in Leeds a wonderful and unforgettable experience.

Last but not the least person I would and should thank is my wife Minglei Tai, who gave up her own career and looked after our family during the past years. Without her support, there was no chance for me to start my PhD not to mention complete it. Thanks for her patience to take care of our children Taiqiao and Taiqi, and thanks for her encouragement so that I could finish this PhD.

Abstract

We present a one-field fictitious domain method (FDM) for simulation of general fluid-structure interactions (FSI). “One-field” means only one velocity field is solved in the whole (fluid and solid) domain based upon the finite element interpolation. The proposed method has the same generality and robustness as the FDM with a distributed Lagrange multiplier (DLM): both of them solve the fluid equations and solid equations as one system. However the one-field FDM only needs to solve for one velocity field while the FDM/DLM usually solves for fluid velocity, solid displacement and Lagrange multiplier. The proposed one-field FDM also has similar features with immersed finite element methods (IFEM): the explicit or implicit IFEM places all the solid information in a FSI force term which is arranged on the right-hand side of the fluid equations. The one-field FDM assembles the solid equations and implicitly includes them with the fluid equations. What we achieve is theoretically equivalent to an implicit IFEM but avoiding convergence problems, and a wide range of solid parameters can be considered in this scheme. In short, the one-field FDM combines the FDM/DLM advantage of robustness and the IFEM advantage of efficiency.

In this thesis, we present a thorough review, summary and categorization of the existing finite element methods for FSI problems. The finite element weak formulation of the one-field FDM and discretization in time and space are introduced, followed by a stability analysis by energy estimate. The proposed scheme is first implemented in implicit form, followed by numerical validation for the property of non-increasing energy under the conditions of $\rho^f \leq \rho^s$ (densities of the fluid and solid respectively) and $\nu^f \leq \nu^s$ (viscosities of the fluid and solid respectively), and numerical tests for stability under the conditions of $\rho^f > \rho^s$ and/or $\nu^f > \nu^s$. The proposed scheme is then implemented based upon three explicit splitting schemes: 2-step splitting, 3-step splitting and 4-step splitting scheme. The fully coupled implicit FSI system is decoupled into subproblems step by step, which can be effectively solved. The pros and cons of these splitting schemes are analysed followed by a selection of numerical tests in order to illustrate the capabilities and range of applicability of the proposed one-field FDM scheme. The thesis concludes with a presentation of some topics and open problems that may be worthy of further investigation.

Contents

1	Introduction	1
1.1	Applications of fluid-structure interactions	1
1.2	Numerical methods for fluid-structure interactions	2
1.3	Motivation for the one-field fictitious domain method	3
1.4	Structure of this thesis	4
2	Existing numerical methods	5
2.1	Governing partial differential equations	7
2.2	Saint Venant-Kirchhoff solid model	9
2.3	Incompressible neo-Hookean solid model	10
2.4	Methods using one mesh and interface fitting	12
2.4.1	Partitioned/Segregated methods	13
2.4.2	Monolithic/Fully-coupled methods	18
2.4.3	Monolithic Eulerian method	21
2.5	Methods using two meshes	24
2.5.1	Immersed finite element methods	25
2.5.2	Modified immersed finite element methods	26
2.5.3	Fictitious domain methods with distributed Lagrange multiplier	27
2.6	Methods using one mesh without interface fitting	30
2.6.1	A fully Eulerian formulation	31
2.7	Summary	32
3	A one-field fictitious domain method	33
3.1	The weak formulation of finite element method	33
3.2	Discretization in time	35
3.3	Discretization in space	36
3.4	Stability by energy estimate	38
3.4.1	Energy conservation in the continuous case	38
3.4.2	Stability analysis after discretization in time	41
3.4.3	Stability analysis after discretization in space	45

3.5	Summary	46
4	An implicit implementation	49
4.1	Treatment of convection	49
4.2	Iterative linear algebra solver	49
4.3	Solution algorithm	51
4.4	Numerical tests for energy conservation	51
4.4.1	Test1-2D (activated disc): Oscillating disc driven by an initial kinetic energy	52
4.4.2	Test2-2D (stretched disc): Oscillating disc driven by an initial potential energy	54
4.4.3	Test3-3D (activated ball): Oscillating ball driven by an initial kinetic energy	56
4.5	Limitation of the proposed method	56
4.5.1	Test4-2D (rotating disc): A rotating disc	58
4.5.2	Test5-2D (elastic wall): Cavity flow with an elastic solid wall	65
4.5.3	Test6-2D (rising bar): A rising bar	66
4.5.4	Test7-2D (cavity with disc): Cavity flow with a solid disc	67
4.5.5	Conclusion	69
4.6	Summary	71
5	Explicit splitting schemes	73
5.1	A 2-step splitting scheme	75
5.1.1	Treatment of the convection step	75
5.1.2	FEM discretization of the diffusion step	78
5.1.3	The 2-step splitting algorithm	78
5.2	Numerical tests for the 2-step splitting scheme	79
5.2.1	Test1-2D (activated disc): Oscillating disc driven by an initial kinetic energy	79
5.2.2	Test2-2D (stretched disc): Oscillating disc driven by an initial potential energy	80
5.2.3	Test3-3D (activated ball): Oscillating ball driven by an initial kinetic energy	81
5.2.4	Test7-2D (cavity with disc): Cavity flow with a solid disc (Parameter 1-3)	82
5.2.5	Test8-2D (leaflet): An oscillating leaflet	83
5.2.6	Test9-2D (thin flag): An oscillating thin flag	91
5.2.7	Test10-2D (channel with solids): Solids in a channel with gravity	94
5.3	A 3-step splitting scheme	99
5.3.1	“Degenerate” Stokes step	100
5.3.2	Diffusion step	101
5.4	Numerical tests for the 3-step splitting scheme	101

5.4.1	Test1-2D (activated disc): Oscillating disc driven by an initial kinetic energy	101
5.4.2	Test2-2D (stretched disc): Oscillating disc driven by an initial potential energy	102
5.4.3	Test3-3D (activated ball): Oscillating ball driven by an initial kinetic energy	104
5.4.4	Test7-2D (cavity with disc): Cavity flow with a solid disc (Parameter 1)	105
5.4.5	Test8-2D (leaflet): An oscillating leaflet (Parameter 1)	106
5.4.6	Test11-2D (thick flag): An oscillating thick flag	109
5.4.7	Test12-3D (cylinder): An oscillating cylinder	111
5.5	A 4-step splitting scheme	112
5.6	Numerical tests for the 4-step splitting scheme	114
5.6.1	Test1-2D (activated disc): Oscillating disc driven by an initial kinetic energy	115
5.6.2	Test2-2D (stretched disc): Oscillating disc driven by an initial potential energy	118
5.6.3	Test3-3D (activated ball): Oscillating ball driven by an initial kinetic energy	118
5.6.4	Test7-2D (cavity with disc): Cavity flow with a solid disc (Parameter 1)	119
5.6.5	Test8-2D (leaflet): An oscillating leaflet (Parameter 1)	119
5.7	Discussion of different splitting schemes	120
5.8	Energy analysis for the explicit splitting schemes	122
5.8.1	2-step splitting scheme	123
5.8.2	3-step splitting scheme	124
5.8.3	4-step splitting scheme	125
5.9	Summary	125
6	Further investigations	127
6.1	Discussion of the well-posedness	127
6.1.1	Well-posedness of Problem 6.1 (one step of Problem 3.2)	129
6.1.2	Well-posedness after discretization in space (one step of Problem 3.3)	131
6.2	Application to a non-Newtonian fluid	134
6.2.1	Test13-2D (one particle): A single freely suspended particle in Oldroyd-B shear-flow	135
6.2.2	Test14-2D (two particles): Particle-particle interaction	135
6.3	Problems with contact	137
6.3.1	Simulation without an explicit contact algorithm	137
6.3.2	A general contact model	140
6.4	The case of a truss structure	144
6.5	Extension to the case of a compressible solid	146

7 Conclusions	149
7.1 Achievements of this thesis	150
7.2 Further work based on the proposed method	150
Appendices	153
A Implementation by updating the solid stress	155
B Assembling the global matrix	157
C A method of computing the interpolation matrix	161
D An efficient approach for matrix multiplication	163
E A method to implement hanging nodes	165
F F-scheme and d-scheme	169

List of Figures

2.1	Schematic diagram of FSI, $\Omega = \Omega_t^f \cup \Omega_t^s$, $\Gamma = \Gamma_D \cup \Gamma_N$	7
2.2	Schematic diagram for an interface-fitted mesh, $\Omega = \Omega_t^f \cup \Omega_t^s$, $\Gamma = \Gamma_D \cup \Gamma_N$. Solve for fluid velocity \mathbf{u}^f in Ω_t^f and solid displacement \mathbf{d}^s in Ω_t^s	12
2.3	Schematic diagram for an interface-fitted mesh, $\Omega = \Omega_t^f \cup \Omega_t^s$, $\Gamma = \Gamma_D \cup \Gamma_N$. Solve for one velocity \mathbf{u} in Ω	22
2.4	Schematic diagram for a mesh without interface fitting, $\Omega = \Omega_t^f \cup \Omega_t^s$, $\Gamma = \Gamma_D \cup \Gamma_N$	31
4.1	Snapshot at $t = 0.25$ for Test1-2D (activated disc) in Section 4.4.1 using a time step of $\Delta t = 5.0 \times 10^{-3}$	52
4.2	Evolution of energy for Test1-2D (activated disc) in Section 4.4.1, $\Delta t = 5.0 \times 10^{-3}$. The peaks of the red curve (curve of $E_p(\Omega_X^s)$) indicate the time when the disc is maximally stretched. The first peak is horizontally stretched and the second peak is vertically stretched. The troughs of the red curve touch line $E_p(\Omega_X^s) = 0$, which are the stress-free stages.	53
4.3	Variation of mass and energy for Test1-2D (activated disc) in Section 4.4.1 using a time step of $\Delta t = 5.0 \times 10^{-3}$	53
4.4	Evolution of the energy ratio and residual R_n for Test1-2D (activated disc) in Section 4.4.1.	54
4.5	Computational domain and boundary conditions for Test2-2D (stretched disc) in Section 4.4.2.	54
4.6	A snapshot at $t = 1$ for Test2-2D (stretched disc) in Section 4.4.2 using a time step of $\Delta t = 5.0 \times 10^{-3}$	55
4.7	Evolution of energy for Test2-2D (stretched disc) in Section 4.4.2, $\Delta t = 5.0 \times 10^{-3}$. The peaks of the red curve (curve of $E_p(\Omega_X^s)$) indicate the time when the disc is maximally stretched. The first and third peaks are corresponding to the time when the disc is horizontally stretched and the second and fourth peaks are corresponding to the time when the disc is vertically stretched. The troughs of the red curve touch line $E_p(\Omega_X^s) = 0$ (numerical error could be observed from the first rough which does not touches line $E_p(\Omega_X^s) = 0$), which are the stress-free stages.	55
4.8	Evolution of the energy ratio and residual R_n for Test2-2D (stretched disc) in Section 4.4.2.	56
4.9	Velocity norm at $t = 0.2$ for Test3-3D (activated ball) in Section 4.4.3.	57
4.10	Evolution of the energy ratio (defined in (3.54)) for Test3-3D (activated ball) in Section 4.4.3.	57
4.11	Sketch of Test4-2D (rotating disc) in Section 4.5.1.	59
4.12	Revolution of the velocity norm for Test4-2D (rotating disc) in Section 4.5.1 (results of the 1D equation, using 200 linear elements and $\Delta t = 1.0 \times 10^{-3}$).	59

4.13 Comparison between the one-field FDM, the fitted mesh method in [67] and the semi-analytic solution at $t = 0.85$. Test4-2D (rotating disc) in Section 4.5.1.	60
4.14 Coarse meshes for Test4-2D (rotating disc) in Section 4.5.1.	60
4.15 Pressure and velocity on the fluid mesh at $t = 0.85$ for Test4-2D (rotating disc) in Section 4.5.1. . .	61
4.16 Velocity norm on the solid mesh at $t = 1$ using Parameter 1 in Table 4.2, the rotation angle of the disc is $\theta = 16.17^\circ$. Test4-2D (rotating disc) in Section 4.5.1.	61
4.17 Displacement on the solid mesh at $t = 2$ for Parameter 8 in Table 4.2, the rotation angle of the disc is $\theta = 25.97^\circ$. Test4-2D (rotating disc) in Section 4.5.1.	61
4.18 Deformatioin tensor \mathbf{F} at $t = 0.85$ for Test4-2D (rotating disc) in Section 4.5.1.	62
4.19 Evolustion of velocity for Parameters 2 in Table 4.2. 200 linear elements are used for the one dimensional equation with $\Delta t = 1.0 \times 10^{-4}$. Test4-2D (rotating disc) in Section 4.5.1.	62
4.20 Velocity norm at $t = 0.85$ for Parameter 4 in Table 4.2. Test4-2D (rotating disc) in Section 4.5.1. . .	63
4.21 Velocity norm and pressure at $t = 0.85$ for Parameter 4 in Table 4.2 using a coarse mesh. Test4-2D (rotating disc) in Section 4.5.1.	64
4.22 Pressure at $t = 0.85$ for Parameter 4 in Table 4.2. Test4-2D (rotating disc) in Section 4.5.1.	64
4.23 Mesh convergence for an unstructured fluid mesh. Test4-2D (rotating disc) in Section 4.5.1.	65
4.24 Computational domain for Test5-2D (elastic wall) in Section 4.5.2.	66
4.25 Distribution of pressure on the fluid mesh and velocity norm on the deformed solid mesh at $t = 2$. Test5-2D (elastic wall) in Section 4.5.2.	66
4.26 Velocity and mesh dispacement using an ALE mesh at $t = 2$ for Test5-2D (elastic wall) in Section 4.5.2. .	66
4.27 Comparison between the two-mesh method and the fitted-mesh method for Test5-2D (elastic wall) in Section 4.5.2, using a time step of $\Delta t = 5.0 \times 10^{-3}$	67
4.28 Sketch of Test6-2D (rising bar) in Section 4.5.3.	68
4.29 Vertical velocity on the background mesh at $t = 0.6$ for Test6-2D (rising bar) in Section 4.5.3. . . .	68
4.30 Evolution of the solid for Test6-2D (rising bar) in Section 4.5.3.	69
4.31 Sketch of the cavity with a solid disc for Test7-2D (cavity with disc) in Section 4.5.4.	69
4.32 Velocity norm on the fluid mesh at $t = 20$ for Test7-2D (cavity with disc) in Section 4.5.4.	69
4.33 Velocity norm on the solid mesh (Parameter 1) for Test7-2D (cavity with disc) in Section 4.5.4. . . .	70
5.1 Configuration of solid at $t = 0.7$ for Test1-2D (activated disc) in Section 5.2.1 (Least-squares method for convection).	80
5.2 Evolution of the energy ratio (defined in (3.54)) for Test1-2D (activated disc) in Section 5.2.1.	81
5.3 Configuration of solid at $t = 0.9$ for Test2-2D (stretched disc) in Section 5.2.2 (the solid is maximum stretched to the y direction).	82
5.4 Configuration of solid at $t = 2.0$ for Test2-2D (stretched disc) in Section 5.2.2.	83
5.5 Evolution of the energy ratio (defined in (3.54)) for Test2-2D (stretched disc) in Section 5.2.2. . . .	84
5.6 Evolution of energy ratio (defined in (3.54)) for Test3-3D (activated ball) in Section 5.2.3.	85
5.7 Velocity norm for a soft solid ($\mu^s = 0.1$) using the one-field FDM (left) and IFEM (right). Test7-2D (cavity with disc) in Section 5.2.4	85

5.8	Velocity norm for a soft solid ($\mu^s = 1.0$) using the one-field FDM (left) and IFEM (right). Test7-2D (cavity with disc) in Section 5.2.4.	86
5.9	Velocity norm for a hard solid ($\mu^s = 100$) using the one-field FDM. Test7-2D (cavity with disc) in Section 5.2.4.	86
5.10	Comparison of the solid deformation at $t = 20s$ for Test7-2D (cavity with disc) in Section 5.2.4, using the same mesh size and time step $\Delta t = 1.0 \times 10^{-3}$	87
5.11	Solid deformation for Parameter 1 in Test7-2D (cavity with disc) in Section 5.2.4.	88
5.12	Computational domain and boundary conditions for Test8-2D (leaflet) in Section 5.2.5.	88
5.13	Configuration of the leaflet and magnitude of velocity on the adaptive fluid mesh for Test8-2D (leaflet) in Section 5.2.5.	89
5.14	Evolution of horizontal and vertical displacement at top right corner of the leaflet ($r_m \approx 1$) for Test8-2D (leaflet) in Section 5.2.5.	90
5.15	Configuration of leaflet for different mesh ratio r_m , and contour plots of displacement magnitude at $t = 0.6$ for Test8-2D (leaflet) in Section 5.2.5.	90
5.16	Contour plots of the horizontal velocity at $t = 0.5s$ for Test8-2D (leaflet) in Section 5.2.5, using different sizes of mesh.	90
5.17	Contour plots of the horizontal velocity at $t = 0.5s$ for Test8-2D (leaflet) in Section 5.2.5, using different time steps and a medium size of mesh.	91
5.18	Parameters sets and results for Group (b)~(d) of Test8-2D (leaflet) in Section 5.2.5, using a time step of $\Delta t = 5.0 \times 10^{-4}s$	92
5.19	Computational domain and boundary condition for Test9-2D (thin flag) in Section 5.2.6.	92
5.20	Contour plots of leaflet displacement and fluid pressure at $t = 5.44s$ for Test9-2D (thin flag) in Section 5.2.6.	93
5.21	Distribution of pressure across the leaflet on the three lines in Figure 5.20 (b) for Test9-2D (thin flag) in Section 5.2.6.	93
5.22	Displacement of the leaflet tip as a function of time for Test9-2D (thin flag) in Section 5.2.6.	94
5.23	Computational domain for Test10-2D (channel with solids) in Section 5.2.7: a single falling disc.	95
5.24	Computational domain for different shapes of solids with different properties. Test10-2D (channel with solids) in Section 5.2.7.	95
5.25	Contour of vertical velocity at $t = 1s$ (fine mesh) for Test10-2D (channel with solids) in Section 5.2.7.	96
5.26	Evolution of velocity at the center of a falling disc for Test10-2D (channel with solids) in Section 5.2.7. (The blue solid line represents the empirical solution from formula (5.22).)	96
5.27	Contours of vertical velocity at different times for multi-solids falling in a channel. Test10-2D (channel with solids) in Section 5.2.7.	97
5.28	The energy ratio against time for Test1-2D (activated disc) in Section 5.4.1: comparison between implicit and explicit scheme.	102
5.29	Convergence of mass and energy for Test1-2D (activated disc) in Section 5.4.1 using $\Delta t = 5.0 \times 10^{-3}$: comparing with the divergence free 3-step splitting.	102

5.30 The solid deformation at $t = 0.74$ (the disc is maximally stretched in the vertical direction) for Test1-2D (activated disc) in Section 5.4.1. The curve of the divergence free splitting (solid red) overlaps with the curve of the implicit scheme (solid blue).	103
5.31 The energy ratio against time for Test2-2D (stretched disc) in Section 5.4.2: comparison between implicit and explicit scheme.	103
5.32 Convergence of mass and energy for Test2-2D (stretched disc) in Section 5.4.2 using $\Delta t = 5.0 \times 10^{-3}$: comparing with the divergence free 3-step splitting.	104
5.33 The solid deformation at $t = 1$ (the disc is maximally stretched in the vertical direction) for Test2-2D (stretched disc) in Section 5.4.2. The curve of the 3-step splitting (dashed green) overlaps with the curve of the implicit scheme (solid blue).	104
5.34 Evolution of the energy ratio for Test3-3D (activated ball) in Section 5.4.3: comparison between implicit and explicit scheme.	105
5.35 Comparison of the solid deformation at $t = 20$ for Test7-2D (cavity with disc) in Section 5.4.4, using a time step of $\Delta t = 1.0 \times 10^{-3}$	105
5.36 Convergence of mass for Test7-2D (cavity with disc) in Section 5.4.4, using the 3-step splitting scheme. .	106
5.37 The solid deformation at $t = 20$ for Test7-2D (cavity with disc) in Section 5.4.4 with $\Delta t = 1.0 \times 10^{-3}$. The curve of the divergence free 3-step splitting (solid red) overlaps with the curve of the 2-step splitting scheme (dashed blue).	106
5.38 Distribution of pressure on the fluid mesh and velocity norm on the solid mesh at $t = 1.0$ for Test8-2D (leaflet) in Section 5.4.5.	107
5.39 Distribution of pressure and velocity norm using an ALE mesh (same mesh as in Figure 5.38 (a)) for Test8-2D (leaflet) in Section 5.4.5.	107
5.40 Comparison of the leaflet deformation at $t = 0.1$ for Test8-2D (leaflet) in Section 5.4.5.	108
5.41 Comparison of the leaflet deformation at $t = 0.12$ for Test8-2D (leaflet) in Section 5.4.5.	108
5.42 Comparison of displacement at the leaflet tip (top-left corner) for Test8-2D (leaflet) in Section 5.4.5. The implicit ALE method uses a stable/converged time step of $\Delta t = 1.0 \times 10^{-4}$	109
5.43 Computational domain and boundary conditions for Test11-2D (thick flag) in Section 5.4.6.	110
5.44 A snap shot of the velocity norms in the fluid domain and on the solid mesh at $t=6$. Test11-2D (thick flag) in Section 5.4.6.	110
5.45 Vertical displacement at the tip of the leaflet versus time for Test11-2D (thick flag) in Section 5.4.6. The frequency and amplitude are around 5.3 and 0.03 respectively.	110
5.46 Sketch of the oscillating cylinder in a cuboid. Test12-3D (cylinder) in Section 5.4.7.	111
5.47 Computational domain of the corresponding 2D problem ($w = 2r$, corresponding to Figure 5.46) for Test12-3D (cylinder) in Section 5.4.7.	111
5.48 Velocity norm at $t = 2.0$ for Test12-3D (cylinder) in Section 5.4.7.	112
5.49 Solid deformation at three different stages for Test12-3D (cylinder) in Section 5.4.7.	112
5.50 Displacement at point (1.55, 0.8, 0.5) in the 3D case and point (1.55, 0.8) in the 2D case. Test12-3D (cylinder) in Section 5.4.7.	113
5.51 The energy ratio against time for Test1-2D (activated disc) in Section 5.6.1.	115

5.52	The solid deformation at $t = 0.74$ when the solid is maximally stretched along y direction, for Test1-2D (activated disc) in Section 5.6.1 using the mixed element (P_2/P_1)	116
5.53	The solid deformation at $t = 0.74$ when the solid is maximally stretched along y direction for Test1-2D (activated disc) in Section 5.6.1. The equal-order element (P_1) is used, and the mesh is twice finer (same number of nodes) than the mixed element (P_2/P_1)	116
5.54	Variation of mass as a function of time for Test1-2D (activated disc) in Section 5.6.1.	117
5.55	Evolution of all energy contributions, using equal-order element (P_1), for Test1-2D (activated disc) in Section 5.6.1.	117
5.56	Evolution of all energy contributions, using mixed element (P_1), for Test1-2D (activated disc) in Section 5.6.1.	118
5.57	The energy ratio against time for Test2-2D (stretched disc) in Section 5.6.2.	119
5.58	The solid deformation at $t = 1.0$ for Test2-2D (stretched disc) in Section 5.6.2. The equal-order element (P_1) is used, and the mesh is twice finer (same number of nodes) than the mixed element (P_2/P_1)	120
5.59	Evolution of the energy ratio for Test3-3D (activated ball) in Section 5.6.3.	121
5.60	The solid deformation at $t = 20$ for Test7-2D (cavity with disc) in Section 5.6.4 using $\Delta t = 1.0 \times 10^{-3}$	122
5.61	Comparison of displacement at the leaflet tip (top-left corner) for Test8-2D (leaflet) in Section 5.6.5. The ALE method is implicit and uses P_2/P_1 element. The 4-step splitting scheme uses the equal-order element (P_1), however whose mesh is twice finer than the ALE mesh (same number of nodes).	122
5.62	Comparison of displacement at the leaflet tip (top-left corner) for Test8-2D (leaflet) in Section 5.6.5. Both the ALE method and the 4-step splitting scheme use the mixed element (P_2/P_1).	123
6.1	Computational domain for Test13-2D (one particle) in Section 6.2.1.	135
6.2	Meshes used for the simulation of Test13-2D (one particle) in Section 6.2.1.	136
6.3	Angular velocity as a function of time for different Weissenberg numbers ($r = 0.05$). Test13-2D (one particle) in Section 6.2.1.	137
6.4	Angular velocity of a steady state as a function of Weissenberg number for two different particle sizes. Test13-2D (one particle) in Section 6.2.1.	137
6.5	Computational domain for Test14-2D (two particles) in Section 6.2.2.	137
6.6	Distribution of pressure on the adaptive background mesh in the case of $s = 0.075$ for Test14-2D (two particles) in Section 6.2.2.	138
6.7	Distribution of pressure on the solid mesh in the case of $s = 0.075$ for Test14-2D (two particles) in Section 6.2.2.	138
6.8	Trajectories of the two particles for the Test14-2D (two particles) in Section 6.2.2, using a radius 0.05 and a Weissenberg number of 0.8. Three different behaviours corresponding to three different initial separations.	139
6.9	Multiple discs in a cavity flow ($[0,1] \times [0,1]$).	140
6.10	Distribution of pressure and velocity norm on the deformed solid for multiple discs in a cavity flow.	141
6.11	An example of truss structure.	144

C.1	Quadrilateral element in the reference coordinate system.	161
D.1	An element of the solid mesh on the background meshes.	163

List of Tables

2.1	A categorization of the existing methods for FSI problems. DLM: Distributed Lagrange Multiplier, FEII: Finite Element Isoparametric Interpolation	6
4.1	Two groups of consistent units ($1\text{dyne} = 10^{-5}\text{N}$, $1\text{N} = 1\text{kg} \cdot \text{m/s}^2$)	52
4.2	Parameter sets for Test4-2D (rotating disc) in Section 4.5.1 with $\mu_c = \mu^s \Delta t + \nu^\delta$. “ \times ” means instability is observed (“ \checkmark ” means not) during $t = 0$ to 1, and “ $-$ ” means μ_c is not an indication for stability in the case $\nu^\delta \geq 0$	63
4.3	Parameter sets for Test5-2D (elastic wall) in Section 4.5.2 with $\mu_c = \mu^s \Delta t + \nu^\delta$. “ \times ” means instability is observed (“ \checkmark ” means not) during $t = 0$ to 2, and “ $-$ ” means μ_c is not an indicator for stability in the case $\nu^\delta \geq 0$	67
4.4	Parameter sets for Test6-2D (rising bar) in Section 4.5.3. “ \times ” means instability is observed (“ \checkmark ” means not) before the bar moves out of the cup, and “ $-$ ” means μ_c is not an indicator for stability in the case $\nu^\delta \geq 0$. $\mu_c = \mu^s \Delta t + \nu^\delta$ and gravity acceleration is 980.	68
4.5	Parameter sets for Test7-2D (cavity with disc) in Section 4.5.4 with $\mu_c = \mu^s \Delta t + \nu^\delta$. “ \times ” means instability is observed (“ \checkmark ” means not) up to $t = 20$, and “ $-$ ” means μ_c is not an indicator for stability in the case $\nu^\delta \geq 0$	70
5.1	The choice of element and mesh in all the numerical tests. LS: Least-squares method, TG: Taylor-Galerkin method. “ $-$ ”: low Reynolds number flow, the convection is either neglected or moved to the right-hand side of the equation as a force term.	74
5.2	Properties and domain size for Test8-2D (leaflet) in Section 5.2.5 with a leaflet oriented across the flow direction.	84
5.3	Comparison of maximum velocity for different meshes. Test8-2D (leaflet) in Section 5.2.5.	89
5.4	Comparison of maximum velocity for different time step size. Test8-2D (leaflet) in Section 5.2.5.	91
5.5	Fluid and material properties of a single falling disc for Test10-2D (channel with solids) in Section 5.2.7.	94

5.6	Properties for multi-solids falling in a channel as shown in Figure 5.24. Test10-2D (channel with solids) in Section 5.2.7.	96
6.1	Fluid properties and results of two different radii of the particle for Test13-2D (one particle) in Section 6.2.1. The Weissenberg number $Wi = \frac{\lambda \langle u \rangle}{H} = \frac{\lambda \cdot 1}{1} = \lambda$	136
6.2	Fluid and particle properties and domain size for Test14-2D (two particles) in Section 6.2.2.	136

List of Algorithms

1	Partitioned/Segregated methods	14
2	Immersed Finite Element Method	26
3	Modified Immersed Finite Element Method	27
4	The implicit algorithm for the one-field FDM	51
5	The explicit 2-step splitting algorithm for the one-field FDM	79
6	Modification of the element matrix related to velocity	167
7	Modification of the element matrix related to pressure	167

Chapter 1

Introduction

In order to understand the following material, we assume that the reader has a basic knowledge of the finite element method for fluid dynamics and structural mechanics. In this chapter, we start by introducing some typical problems involving fluid-structure interactions (FSI) and the existing numerical methods to solve them. We then discuss the motivation for designing a new approach to FSI problems. Finally the structure of this thesis is presented.

1.1 Applications of fluid-structure interactions

Problems involving FSI are common in many areas, such as wind-turbine aerodynamics [10, 11, 91], dynamics of spacecraft parachutes [14], biomedical science [1, 12, 14, 73], fixed or floating structures interacting with ocean waves [6, 26, 45, 52], and so on. For most FSI problems, analytical solutions of the controlling equations are impossible to obtain, whereas laboratory experiments are complex, expensive and limited in scope. Therefore, numerical simulations play an important role in order to understand the fundamental physics involved in the complex interaction between fluids and structures.

Aerodynamics is a major area in which FSI is widely applied. Applications range from modeling a full scale wind-turbine rotor with composite blades [10, 11] and simulation based on Isogeometric Analysis (IGA) [14] to large eddy simulation of flow passing airfoils [38]; from the simulation of flow around a high-speed train [125, 126] to simulation of a parachute interacting with the air around it [14, 80, 128] (space-time finite element methods in [14, 128] and parallel implementation in [80]). All these applications are about a solid body, from very large structures to small solid particles, interacting with its surrounding air flow.

There are also plenty of FSI applications in the area of biomechanics. These include modeling and simulation of blood flowing in the blood vessel and the interaction between them [9, 12–14, 20, 37, 93, 100]: applications to arterial blood flow [9, 37] and aneurysms [12, 13, 93], considering blood vessel tissue prestress [14, 20] and focusing on external tissue support [100];

the simulation of red blood cells interacting with blood vessels [103, 111, 120, 131, 155]: focusing on the red cell transitions in [103] and deformation in [111, 120] respectively, and the numerical methods for simulations [131, 155]; the heart valve simulation [28, 32, 141], etc.

Applications in ocean mechanics are very popular as well. For example, the ocean waves interacting with a fixed [6, 52] or floating [6, 26, 33, 45, 88, 144] structure; the interactions between waves and algae [85]; the modeling and simulation of underwater vehicles [36, 112]; simulation of seawater intrusion [27, 51]; interactions between internal waves with seamounts [71, 140], and so on.

Other FSI problems, such as particle dynamics of polymers [127, 148], sediment transport [39, 153] and lubricated motion [21, 130] can also be found in the literature.

All in all, fluid-structure interaction problems exist in a variety of areas. Numerical simulation for such kinds of problem plays an important role due to the limitation of analysis and laboratory experiments.

1.2 Numerical methods for fluid-structure interactions

Numerical simulation of fluid-structure interaction is often a computational challenge because of its strong nonlinearity, especially when large deformation is considered. Different kinds of numerical methods are used to solve FSI problems. Generally speaking, there are finite difference methods [48, 64, 92, 161], finite element methods [8, 14, 47, 69, 84, 137, 156, 157], finite volume methods [78, 81, 122], particle/meshless methods [76, 77, 113, 149], Lattice-Boltzmann methods [49, 82, 105, 129], and so on.

The finite difference methods directly discretize the partial differential equation, which is straightforward to implement. For FSI numerical schemes, such as the immersed boundary method (IBM), the finite difference method may be used to solve the fluid equation with a FSI force term on the right-hand side [48, 159]. However it is difficult to use finite difference scheme for problems with complex geometry.

The finite element method works with the weak form of a partial differential equation, which can adopt an unstructured mesh to treat complex geometry. In addition the Neumann boundary condition may be naturally treated in the framework of finite element methods. Coming to the FSI numerical algorithm, the finite element method may be adopted to solve both the fluid and solid equations sequentially [40, 84] or simultaneously [68, 69, 102].

The finite volume method only needs to evaluate fluxes on the boundaries of a cell, which makes it powerful for handling conservation laws. The finite volume method is convenient to deal with the non-linear convection term when solving large Reynolds number problems, which may be advantageous in a FSI numerical scheme to solve the fluid problem [81, 122].

The particle methods are naturally good at dealing with moving boundary, contact and fracture in the FSI problems. One could describe both the fluid and solid as particles [76, 77, 145], or just describe the solid as particles which are moving over a fixed Eulerian mesh [149].

Solving the Lattice-Boltzmann equation can be much faster than solving the Navier-Stokes equation, which makes the Lattice-Boltzmann Methods (LBM) popular in computational fluid dynamics. For FSI problems the LBM may be combined with schemes such as immersed boundary methods (IBM) [49, 129] or particle methods [82].

In this thesis, our discussion will be based upon the finite element method for both the fluid and solid part. The existing finite element schemes for FSI problems will be presented and a new numerical scheme will be introduced.

The FSI finite element methods discretize both the fluid and solid domain as a set of locally connected nodes, termed a mesh. A fitted mesh means that the fluid and solid meshes match each other at the interface, and the nodes on the interface are shared by both the fluid and the solid, which leads to the fact that each interface node has both a fluid velocity and a solid velocity (or displacement) defined on it. It is apparent that the two velocities on each interface node should be consistent. There are typically two methods to handle this: partitioned/segregated methods [40, 84] and monolithic/fully-coupled methods [68, 69, 102]. The former solve the fluid and solid equations sequentially and iterates until the velocities become consistent at the interface. The latter solve the fluid and solid equations simultaneously and often use a Lagrange Multiplier to weakly enforce the continuity of velocity on the interface [102]. The two-mesh methods represent the fluid and solid separately and these do not generally conform to each other on the interface. Popular approaches include the Immersed Finite Element Method (IFEM) [136–138, 156, 157] and the Fictitious Domain method (FDM) [5, 59, 70, 79, 150]. The classical IFEM does not solve solid equations at all. Instead, the solid equations are arranged on the right-hand side of the fluid equations as an FSI force, and these modified fluid equations are solved on the augmented domain (occupied by fluid and solid). The FDM approach usually uses a distributed Lagrange multiplier (DLM) to enforce the constraint and the FSI equations are either solved sequentially [59, 150] or simultaneously [18, 79].

1.3 Motivation for the one-field fictitious domain method

We aim to design a general FEM scheme for FSI problems that can

- cheaply and accurately simulate large solid deformation,
- simulate FSI problems with a wide range of physical parameters.

Considering efficiency for large deformations, we shall choose two meshes to describe the fluid and solid respectively, so that there is no need to remesh; considering simulation for a wide range of physical parameters in one scheme, we shall use a monolithic/fully-coupled method which is widely acknowledged to be more robust [25, 68, 69].

It can be seen from Section 1.2 that the major methods based on two meshes either avoid solving the solid equations (IFEM) or solve them with additional variables (two velocity fields and Lagrange multiplier) in the solid domain. However, physically, there is only one velocity

field in the solid domain. In this thesis, we follow the one-field spirit and only solve one velocity variable in the whole/augmented domain. We shall introduce a one-field FDM that (as we will demonstrate) combines the advantages of IFEM and FDM/DLM: efficiency of IFEM and robustness of FDM/DLM.

In the one-field spirit, [34, 67, 109, 110] introduces an monolithic Eulerian formulation by remeshing and [4] presents a 1D model using a one-field FDM formulation but does not discuss how to compute the integrals arising from the two different domains. There are other similar Eulerian formulations for FSI problems, such as the eXtended Finite Element Method (XFEM) [57], local modification of elements [54] and other fully Eulerian formulations [42, 43, 116, 142] that are coupled with either local adaptivity or ALE methods. However these formulations are not in the spirit of one-field, usually the velocity of the fluid (including fictitious fluid), the displacement of the solid and the Lagrange multiplier are solved monolithically, which are three-field formulations (four fields if the moving mesh is solved for as well).

The main features of the proposed one-field FDM are: (1) only one velocity field is solved in the whole domain, based upon the use of an appropriate L^2 projection; (2) the fluid and solid equations are solved monolithically; (3) The FSI interactions are decoupled until the final step of solving the final assembled algebraic equations. This means that the finite element procedures (weak formulation, discretization, computing element matrices and assembling global matrices) are carried out separately on the two different meshes for the fluid and solid respectively, and the final discrete linear system brings the fluid and solid parts together via an isoparametric interpolation matrix from the augmented fluid mesh to the solid mesh.

1.4 Structure of this thesis

In Chapter 2, existing numerical methods for the FSI problems are introduced in more detail following the definition of the basic governing partial differential equations. In Chapter 3, the principle of the one-field fictitious domain method is introduced with the weak formulations and time and space discretization with corresponding energy analysis. In Chapter 4, an implicit implementation based upon a neo-Hookean solid model is given, followed by several numerical tests for validation of stability and energy conservation. In Chapter 5, different explicit splitting methods are proposed to implement the proposed scheme, followed by a variety of numerical examples. We discuss some topics associated with the proposed scheme which may be worthy of further study in Chapter 6, and finally draw conclusions in Chapter 7.

Chapter 2

Existing numerical methods for fluid-structure interactions

Three major questions arise when considering a finite element method for the problem of Fluid-Structure Interactions (FSI): (1) what kind of meshes are used (interface fitted or unfitted); (2) how to couple the fluid-structure interactions (monolithic/fully-coupled or partitioned/segregated); (3) what variables are solved (velocity and/or displacement). Combinations of the answers to these questions lead to different types of numerical method. For example, [40, 83] solve for fluid velocity and solid displacement sequentially (partitioned/segregated) using an Arbitrary Lagrangian-Eulerian (ALE) fitted mesh, whereas [68, 69, 102] use an ALE fitted mesh to solve for fluid velocity and solid displacement simultaneously (monolithic/fully-coupled) with a Lagrange Multiplier to enforce the continuity of velocity/displacement on the interface. The Immersed Finite Element Method (IFEM) [17, 107, 136–138, 156, 157] and the Fictitious Domain Method (FDM) [5, 18, 59, 70, 79, 150] use two meshes to represent the fluid and solid separately. Although IFEM could be monolithic [17], the classical IFEM only solves for velocity, while the solid information is arranged on the right-hand side of the fluid equation as a prescribed force term. Although the FDM may be partitioned [150], usually the FDM approach solves for velocity in the whole domain (fluid plus solid) and displacement of the solid simultaneously via a distributed Lagrange multiplier (DLM) to enforce the consistency of velocity/displacement in the overlapped solid domain. There are also formulations using one Eulerian mesh (interface-unfitted), in which case the fluid-structure interface needs to be captured first, such as using the level-set method [90], or similar method based on an Initial Point Set [43, 54, 55, 116, 117, 142]. Then the interface may be smoothed by a phase parameter [43] or/and the shape functions may be modified locally in order to capture discontinuity across the interface [54, 134]. In the case of one-field and monolithic numerical methods for FSI problems, [4] introduces a 1D model using a one-field FDM formulation based on two meshes, and [67, 110] introduces an energy stable monolithic method (in 2D) based on one Eulerian

mesh and discrete remeshing.

Combinations of the answers to the three questions at the start of this chapter give the methods shown in Table 2.1. Although there are some types of approach in this table that have not been found by the author in the literature, it may be possible for them to exist as well. In theory at least, every method introduced here could be designed to be an implicit scheme or explicit scheme. However, we shall not distinguish between implicit or explicit forms when introducing the methods in the following sections.

	Solve for velocity and displacement		Only solve for velocity	
	Partitioned	Monolithic	Partitioned	Monolithic
One mesh (interface fitted)	1	2	3	4
Two meshes	5	6	7	DLM: 8 FEII: 9
One mesh (interface unfitted)	10		11	

Table 2.1: A categorization of the existing methods for FSI problems. DLM: Distributed Lagrange Multiplier, FEII: Finite Element Isoparametric Interpolation.

The following list provides examples of studies from the different categories introduced in Table 2.1 :

1. Partitioned/Segregated methods [29, 40, 41, 50, 53, 63, 83, 87, 98, 101, 135].
2. Monolithic/Fully-coupled methods [68, 69, 73, 74, 102].
3. *This combination has not been observed in literature by the author.*
4. Monolithic Eulerian methods [34, 67, 109, 110].
5. Modified immersed finite element methods [138].
6. Fictitious domain methods with distributed Lagrange multiplier (FDM/DLM) [5, 16–18, 58–60, 66, 70, 79, 106, 118, 121, 146, 150, 151].
7. Immersed finite element methods [17, 72, 96, 107, 136–138, 156, 157].
8. *This combination has not been observed in the literature by the author.*
9. **The proposed method in this thesis: a one-field fictitious domain method** [139].
10. A fully Eulerian formulation [42, 43, 54, 116, 117, 134, 142]. *For one mesh without interface fitting, the coupling strategy may always be monolithic/fully-coupled. It might not be reasonable to consider a partitioned algorithm based on one mesh without interface fitting.*
11. *This combination has not been observed in the literature by the author.*

In this chapter, we first present the governing equations for FSI problems with general

initial and boundary conditions in Section 2.1. Then a compressible Saint Venant-Kirchhoff solid model and an incompressible neo-Hookean solid model are given in Section 2.2 and 2.3 respectively. Finally, the existing methods for FSI problems are presented in more detail in the remaining sections. We first broadly categorize the existing methods into three wide groups based upon the meshes they use, i.e., one interface-fitted mesh, two meshes, and one mesh without interface fitting. The specific approaches are then discussed under these three wide categories.

2.1 Governing partial differential equations

In the following context, $\Omega_t^f \subset \mathbb{R}^d$ and $\Omega_t^s \subset \mathbb{R}^d$ with $d = 2, 3$ denote the fluid and solid domain respectively which are time dependent regions as shown in Figure 2.1. $\Omega = \Omega_t^f \cup \Omega_t^s$ is a fixed domain (with outer boundary Γ) and $\Gamma_t = \partial\Omega_t^f \cap \partial\Omega_t^s$ is the moving interface between fluid and solid. We denote by \mathbf{X} the reference (material) coordinates of the solid, by $\mathbf{x} = \mathbf{x}(\cdot, t)$ the current coordinates of the solid, and by \mathbf{x}_0 is the initial coordinates of the solid. We assume $\mathbf{x}(\cdot, t) : \Omega_{\mathbf{X}}^s \rightarrow \Omega_t^s$ is one-to-one and invertible.

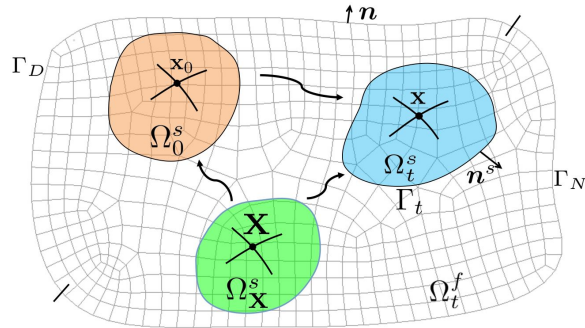


Figure 2.1: Schematic diagram of FSI, $\Omega = \Omega_t^f \cup \Omega_t^s$, $\Gamma = \Gamma_D \cup \Gamma_N$.

Let $\rho, \mathbf{u}, \boldsymbol{\sigma}, \mathbf{g}$ denote the density, velocity vector (column), Cauchy stress tensor and acceleration due to gravity respectively. We assume both an incompressible fluid and incompressible solid, then the conservation of momentum and conservation of mass take the same form as follows:

Momentum equation:

$$\rho \frac{d\mathbf{u}}{dt} = \nabla \cdot \boldsymbol{\sigma} + \rho \mathbf{g}. \quad (2.1)$$

Continuity equation:

$$\frac{d(J\rho)}{dt} = 0. \quad (2.2)$$

$J\rho = \rho_0$, where ρ_0 is the initial density. $J = \det \mathbf{F}$ is the determinant of \mathbf{F} , with $\mathbf{F} = \frac{\partial \mathbf{x}}{\partial \mathbf{X}} =$

$\frac{\partial \mathbf{x}}{\partial \mathbf{x}_0} \frac{\partial \mathbf{x}_0}{\partial \mathbf{X}} = \nabla_0 \mathbf{x} \nabla_{\mathbf{X}} \mathbf{x}_0$ being the deformation tensor. Using Jacobi's formula [97], we have

$$\frac{dJ}{dt} = J \text{tr} \left(\mathbf{F}^{-1} \frac{d\mathbf{F}}{dt} \right). \quad (2.3)$$

Since $\frac{d\mathbf{x}}{dt} = \mathbf{u}$, then

$$\frac{d\mathbf{F}}{dt} = \nabla_{\mathbf{X}} \mathbf{u} = \nabla \mathbf{u} \mathbf{F}. \quad (2.4)$$

Substituting (2.4) to (2.3), and using the trace property of cyclic permutations ($\text{tr}(\mathbf{ABC}) = \text{tr}(\mathbf{BCA}) = \text{tr}(\mathbf{CAB})$ for arbitrary square matrices \mathbf{A} , \mathbf{B} and \mathbf{C}), we get

$$\frac{dJ}{dt} = J \nabla \cdot \mathbf{u}. \quad (2.5)$$

Using (2.5), the continuity equation (2.2) then can also be expressed as:

$$\frac{d\rho}{dt} + \rho \nabla \cdot \mathbf{u} = 0. \quad (2.6)$$

For an incompressible material, the continuity condition (2.6) is equivalent to the following due to $\rho = \rho_0$:

$$\nabla \cdot \mathbf{u} = 0. \quad (2.7)$$

Let superscripts f and s refer to the fluid and solid respectively, and $D\mathbf{u} = \nabla \mathbf{u} + \nabla^T \mathbf{u}$, then the constitutive equations may be expressed as follows. For an incompressible Newtonian fluid in Ω_t^f ,

$$\boldsymbol{\sigma} = \boldsymbol{\sigma}^f = \boldsymbol{\tau}^f - p^f \mathbf{I} = \nu^f D\mathbf{u}^f - p^f \mathbf{I}, \quad (2.8)$$

where ν^f is the dynamic viscosity of the fluid, p^f is pressure in the fluid, and $\boldsymbol{\tau}^f = \nu^f D\mathbf{u}^f$ is the deviatoric part of stress $\boldsymbol{\sigma}^f$. For a general hyperelastic solid in Ω_t^s ,

$$\boldsymbol{\sigma} = \boldsymbol{\sigma}^s = J^{-1} \mathbf{P} \mathbf{F}^T, \quad (2.9)$$

where $\mathbf{P} = \frac{\partial \Psi(\mathbf{F})}{\partial \mathbf{F}}$ is the first Piola-Kirchhoff stress tensor, with $\Psi(\mathbf{F})$ being the energy function for the hyperelastic solid material.

The system is complemented with the following boundary and initial conditions.

Interface boundary conditions (see Figure 2.1):

$$\mathbf{u}^f = \mathbf{u}^s \quad \text{on} \quad \Gamma_t, \quad (2.10)$$

$$\boldsymbol{\sigma}^f \mathbf{n}^s = \boldsymbol{\sigma}^s \mathbf{n}^s \quad \text{on} \quad \Gamma_t. \quad (2.11)$$

Dirichlet and Neumann boundary conditions may be imposed for the fluid:

$$\mathbf{u}^f = \bar{\mathbf{u}} \quad \text{on} \quad \Gamma_D, \quad (2.12)$$

$$\boldsymbol{\sigma}^f \mathbf{n} = \bar{\mathbf{h}} \quad \text{on} \quad \Gamma_N. \quad (2.13)$$

Finally, initial conditions are set as:

$$\mathbf{u}^f|_{t=0} = \mathbf{u}_0^f \quad \text{in} \quad \Omega_0^f, \quad (2.14)$$

$$\mathbf{u}^s|_{t=0} = \mathbf{u}_0^s \quad \text{in} \quad \Omega_0^s. \quad (2.15)$$

Remark 2.1. In this thesis, all vectors are interpreted as column vectors. The gradient of a scalar ϕ is expressed as (two dimension case for example):

$$\nabla \phi = \frac{\partial \phi}{\partial x_i} = \begin{pmatrix} \frac{\partial \phi}{\partial x_1} \\ \frac{\partial \phi}{\partial x_2} \end{pmatrix}. \quad (2.16)$$

The gradient of a vector \mathbf{u} is expressed as (two dimension case for example):

$$\nabla \mathbf{u} = \nabla \begin{pmatrix} u_1 \\ u_2 \end{pmatrix} = \frac{\partial u_i}{\partial x_j} = \begin{bmatrix} \frac{\partial u_1}{\partial x_1} & \frac{\partial u_1}{\partial x_2} \\ \frac{\partial u_2}{\partial x_1} & \frac{\partial u_2}{\partial x_2} \end{bmatrix}. \quad (2.17)$$

2.2 Saint Venant-Kirchhoff solid model

The Energy function for the Venant-Kirchhoff solid model can be expressed as follows [12, 109]:

$$\Psi(\mathbf{F}) = \mu^s \text{tr}(\mathbf{E}^2) + \frac{\lambda^s}{2} \text{tr}^2(\mathbf{E}), \quad (2.18)$$

where

$$\mathbf{E} = \frac{1}{2} (\mathbf{F}^T \mathbf{F} - \mathbf{I}) \quad (2.19)$$

is the Lagrangian Green strain, μ^s and λ^s are the Lamé constants. It is straightforward to use the tensor form to take derivatives, for example in a 2D case, let matrix \mathbf{E} be denoted by the tensor form E_{ij} , then $\left[\frac{\partial \text{tr}(\mathbf{E})}{\partial \mathbf{E}} \right]_{mn} = \frac{\partial (\sum_{i=1}^2 E_{ii})}{\partial E_{mn}} = \frac{\partial (E_{11} + E_{22})}{\partial E_{mn}}$. Only the derivatives with respect to the components of $m = n$ are nonzero. If $m = n = 1$, then $\frac{\partial (E_{11} + E_{22})}{\partial E_{11}} = 1$. If $m = n = 2$, then $\frac{\partial (E_{11} + E_{22})}{\partial E_{22}} = 1$. Therefore $\frac{\partial \text{tr}(\mathbf{E})}{\partial \mathbf{E}} = \mathbf{I}$. Similarly, we have

$$\begin{aligned} \left[\frac{\partial \text{tr}(\mathbf{F}^T \mathbf{F})}{\partial \mathbf{F}} \right]_{mn} &= \frac{\partial \text{tr}(F_{ki} F_{kj})}{\partial F_{mn}} = \frac{\partial \sum_k^d \sum_i^d F_{ki}^2}{\partial F_{mn}} \\ &= \frac{\partial (F_{11}^2 + F_{12}^2 + \dots + F_{dd}^2)}{\partial F_{mn}} = 2\mathbf{F}_{mn}, \end{aligned} \quad (2.20)$$

hence

$$\frac{\partial \text{tr}(\mathbf{E})}{\partial \mathbf{F}} = \mathbf{F}. \quad (2.21)$$

Furthermore,

$$\begin{aligned}
\left[\frac{\partial \text{tr}(\mathbf{E}^2)}{\partial \mathbf{F}} \right]_{mn} &= \frac{1}{4} \left[\frac{\partial \text{tr}(\mathbf{F}^T \mathbf{F} \mathbf{F}^T \mathbf{F} - 2\mathbf{F}^T \mathbf{F} + \mathbf{I})}{\partial \mathbf{F}} \right]_{mn} \\
&= \frac{1}{4} \frac{\partial \text{tr}(F_{ki} F_{kl} F_{sl} F_{sj})}{\partial F_{mn}} - \frac{1}{2} \frac{\partial \sum_k^d \sum_i^d F_{ki}^2}{\partial F_{mn}} \\
&= \frac{1}{4} \frac{\partial (F_{ki} F_{kl} F_{sl} F_{si})}{\partial F_{mn}} - \mathbf{F}_{mn} \\
&= \frac{1}{4} \frac{\partial (F_{mn} F_{ml} F_{sl} F_{sn})}{\partial F_{mn}} + \frac{1}{4} \frac{\partial (F_{mi} F_{mn} F_{sn} F_{si})}{\partial F_{mn}} \\
&\quad + \frac{1}{4} \frac{\partial (F_{ki} F_{kn} F_{mn} F_{mi})}{\partial F_{mn}} + \frac{1}{4} \frac{\partial (F_{kn} F_{kl} F_{ml} F_{mn})}{\partial F_{mn}} - \mathbf{F}_{mn} \\
&= [\mathbf{FF}^T \mathbf{F} - \mathbf{F}]_{mn} = 2[\mathbf{FE}]_{mn}.
\end{aligned} \tag{2.22}$$

According to (2.9), (2.21) and (2.22), we get

$$\boldsymbol{\sigma}^s = J^{-1} \mathbf{P} \mathbf{F}^T = J^{-1} \frac{\partial \Psi}{\partial \mathbf{F}} \mathbf{F}^T = J^{-1} \mathbf{F} (2\mu^s \mathbf{E} + \lambda^s \text{tr}(\mathbf{E}) \mathbf{I}) \mathbf{F}^T. \tag{2.23}$$

Notice that

$$\mathbf{S} = 2\mu^s \mathbf{E} + \lambda^s \text{tr}(\mathbf{E}) \mathbf{I} \tag{2.24}$$

is the second Piola-Kirchhoff stress in the above equation. The relations between the first Piola-Kirchhoff stress \mathbf{P} , the second Piola-Kirchhoff stress \mathbf{S} and the Cauchy stress $\boldsymbol{\sigma}$ are as follows: $\mathbf{P} = \mathbf{FS}$, $\boldsymbol{\sigma} = J^{-1} \mathbf{FSF}^T$ [14].

2.3 Incompressible neo-Hookean solid model

For a general compressible neo-Hookean solid model, the energy function is given by [70]

$$\Psi(\mathbf{F}) = \frac{\mu^s}{2} (\text{tr} \mathbf{FF}^T - d) - \mu^s \ln(J) + \frac{\lambda^s}{2} \ln^2(J). \tag{2.25}$$

Using (2.3) (based on Jacobi's formula), we have

$$\left[\frac{\partial J}{\partial \mathbf{F}} \right]_{ij} = \frac{\partial J}{\partial F_{ij}} = J \text{tr} \left(\mathbf{F}^{-1} \frac{\partial \mathbf{F}}{\partial F_{ij}} \right) = J [\mathbf{F}^{-T}]_{ij}, \tag{2.26}$$

which is a special case of Jacobi's formula [97]. Using (2.20), we then have

$$\frac{\partial \Psi(\mathbf{F})}{\partial \mathbf{F}} = \mu^s (\mathbf{F} - \mathbf{F}^{-T}) + \lambda^s \ln(J) \mathbf{F}^{-T}. \tag{2.27}$$

According to (2.9) and (2.27), we get

$$\boldsymbol{\sigma}^s = \mu^s J^{-1} (\mathbf{FF}^T - \mathbf{I}) + J^{-1} \lambda^s \ln(J) \mathbf{I}. \quad (2.28)$$

For the incompressible case, one may replace $J^{-1} \lambda^s \ln(J)$ by a pressure term $-p^s$ and use $J = 1$ or $\nabla \cdot \mathbf{u}^s = 0$ to determine p^s [150]. Then the constitutive equation for an incompressible neo-Hookean model can be expressed as

$$\boldsymbol{\sigma}^s = \boldsymbol{\tau}^s - p^s \mathbf{I} = \mu^s J^{-1} (\mathbf{FF}^T - \mathbf{I}) - p^s \mathbf{I}, \quad (2.29)$$

where

$$\boldsymbol{\tau}^s = \mu^s J^{-1} (\mathbf{FF}^T - \mathbf{I}) \quad (2.30)$$

is the deviatoric part stress $\boldsymbol{\sigma}^s$.

Remark 2.2. It may be possible to arrange the term $-J^{-1} \mu^s$ into p^s as well [18]. In this case, the solid is not stress free, and one creates a jump of the pressure across the fluid-solid interface if the fluid is stress free. This does not matter if the discontinuity of pressure can be exactly captured, such as an interface-fitted method with discontinuous element for pressure. However, for the interface-unfitted methods (see Section 2.5 or 2.6) it is wiser to choose equation (2.29) as the constitutive equation.

Based upon the above remark, the corresponding energy function for the constitutive equation (2.29) may be expressed as:

$$\Psi(\mathbf{F}) = \frac{\mu^s}{2} (tr_{\mathbf{FF}^T} - d) - \mu^s \ln(J). \quad (2.31)$$

Remark 2.3. In the continuous case $J = 1$ exactly holds for an incompressible material, therefore the term $\ln(J)$ is zero in (2.31). However for the numerical methods using two meshes, $J = 1$ cannot be guaranteed. The reason is: we only solve $\nabla \cdot \mathbf{u} = 0$ in the whole domain Ω /background mesh, then the velocity in the solid domain Ω_t^s /mesh (say \mathbf{u}^s) is projected by \mathbf{u} , i.e., $\mathbf{u}^s = P(\mathbf{u})$, where P denotes the projection. Then $\nabla \cdot \mathbf{u}^s = 0$ only if P is linear, which however does not always hold. Therefore, we keep term $\ln(J)$ in the expression of the energy function. Another reason is that the energy function (2.31) is also consistent with the constitutive equation (2.29). Notice that the following energy function and constitutive equation are consistent with each other:

$$\Psi(\mathbf{F}) = \frac{\mu^s}{2} (tr_{\mathbf{FF}^T} - d), \quad (2.32)$$

and

$$\boldsymbol{\sigma}^s = \mu^s J^{-1} \mathbf{FF}^T - p^s \mathbf{I}. \quad (2.33)$$

2.4 Methods using one mesh and interface fitting

For the interface-fitted methods, the fluid and solid share an interface boundary, on which both the velocity variable from the fluid side and the displacement (or velocity) variable from the solid side are defined as shown in Figure 2.2. No matter whether the FSI problem is solved sequentially (as in Section 2.4.1) or simultaneously (as in sections 2.4.2 and 2.4.3), the major issue is that these two variables from both sides should be in accordance with each other.

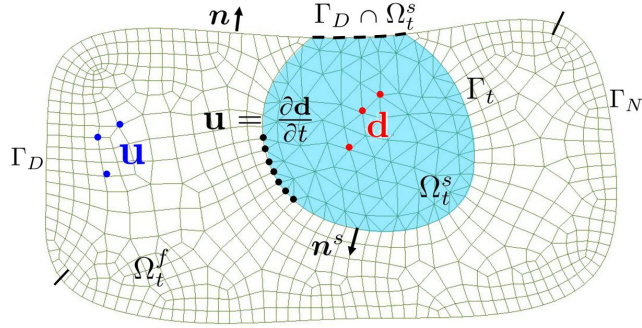


Figure 2.2: Schematic diagram for an interface-fitted mesh, $\Omega = \Omega_t^f \cup \Omega_t^s$, $\Gamma = \Gamma_D \cup \Gamma_N$. Solve for fluid velocity \mathbf{u}^f in Ω_t^f and solid displacement \mathbf{d}^s in Ω_t^s .

For a large deformation problem, as we consider in this thesis, one has to remesh and/or use a moving mesh strategy in order to guarantee the mesh is interface fitted at every time step. We shall use an ALE mesh to demonstrate the methodology in this section, in which case the fluid momentum equation (2.1) (in Ω_t^f) may be expressed as:

$$\rho^f \frac{\partial \mathbf{u}^f}{\partial t} + \rho^f ((\mathbf{u}^f - \mathbf{u}_m) \cdot \nabla) \mathbf{u}^f = \nabla \cdot \boldsymbol{\sigma}^f + \rho^f \mathbf{g}, \quad (2.34)$$

where $\frac{\partial}{\partial t}$ is the time-derivative with respect to a frame moving with the mesh velocity \mathbf{u}_m . Here we simply solve the following linear elastic equation in Ω_t^f at every time step in order to compute \mathbf{u}_m .

$$\nabla \cdot (\mu D \mathbf{u}_m - \lambda (\nabla \cdot \mathbf{u}_m) \mathbf{I}) = 0, \quad (2.35)$$

with μ and λ being the Lamé constants chosen according to the solid parameters (although other values could be chosen). The boundary conditions are set as follows.

$$\mathbf{u}_m \cdot \mathbf{n} = 0 \quad \text{on } \Gamma, \quad (2.36)$$

and

$$\mathbf{u}_m = \Delta \mathbf{d}^s / \Delta t \quad \text{on } \Gamma_t, \quad (2.37)$$

where Δt is the time step, and $\Delta \mathbf{d}^s$ is the solid displacement at the current step.

2.4.1 Partitioned/Segregated methods

In the literature of Partitioned/Segregated methods, the solid displacement (rather than solid velocity) is usually solved as the dependent variable, in which case it is convenient to express the solid momentum equation (2.1) in displacement form (in Ω_t^s):

$$\rho^s \frac{\partial^2 \mathbf{d}^s}{\partial t^2} = \nabla \cdot \boldsymbol{\sigma}^s + \rho^s \mathbf{g}. \quad (2.38)$$

The partitioned methods solve the fluid equation (2.34), mesh equation (2.35) and the solid equation (2.38) sequentially as described in Algorithm 1. There are two ways to consider the boundary conditions on Γ_t : one can solve the fluid equation (2.34) using Dirichlet boundary condition $\mathbf{u}^f = \mathbf{u}^s$, and compute a reaction force \mathbf{h}^f on Γ_t after solving (2.34). Then use the Neumann boundary condition $\boldsymbol{\sigma}^s \mathbf{n}^s = \mathbf{h}^f$ to solve the solid equation (2.38). One can also do this the other way around, i.e.: first solving the solid equation (2.38) using Dirichlet boundary condition $\mathbf{d}^s = \mathbf{u}^f \Delta t + \mathbf{d}_n$, and compute a reaction force \mathbf{h}^s on Γ_t after solving (2.38). Then use the Neumann boundary condition $\boldsymbol{\sigma}^f \mathbf{n}^s = \mathbf{h}^s$ to solve the fluid equation (2.34). In Algorithm 1 we adopt the former to illustrate the approach. Using the finite element method, the weak form of equation (2.34) could be expressed as follows for a given test function $\delta \mathbf{u}$:

$$\begin{aligned} & \int_{\Omega_t^f} \rho^f \frac{\partial \mathbf{u}^f}{\partial t} \cdot \delta \mathbf{u} d\mathbf{x} + \int_{\Omega_t^f} \rho^f ((\mathbf{u}^f - \mathbf{u}_m) \cdot \nabla) \mathbf{u}^f \cdot \delta \mathbf{u} d\mathbf{x} \\ &= \int_{\Gamma_D} (\boldsymbol{\sigma}^f \mathbf{n}) \cdot \delta \mathbf{u} d\Gamma + \int_{\Gamma_t} (-\boldsymbol{\sigma}^f \mathbf{n}^s) \cdot \delta \mathbf{u} d\Gamma + \int_{\Gamma_N} \bar{\mathbf{h}} \cdot \delta \mathbf{u} d\Gamma \\ & - \int_{\Omega_t^f} \boldsymbol{\sigma}^f : \nabla \delta \mathbf{u} d\mathbf{x} + \int_{\Omega_t^f} \rho^f \mathbf{g} \cdot \delta \mathbf{u} d\mathbf{x}. \end{aligned} \quad (2.39)$$

Solving the above equation with boundary conditions (2.12) and (2.13) to get \mathbf{u}^f , then the reaction force \mathbf{h}^f on $\Gamma_D \cup \Gamma_t$ could be computed as follows.

$$\begin{aligned} & \int_{\Gamma_D \cup \Gamma_t} \mathbf{h}^f \cdot \delta \mathbf{u} d\Gamma = \int_{\Gamma_D} (\boldsymbol{\sigma}^f \mathbf{n}) \cdot \delta \mathbf{u} d\Gamma + \int_{\Gamma_t} (-\boldsymbol{\sigma}^f \mathbf{n}^s) \cdot \delta \mathbf{u} d\Gamma \\ &= \int_{\Omega_t^f} \rho^f \frac{\partial \mathbf{u}^f}{\partial t} \cdot \delta \mathbf{u} d\mathbf{x} + \int_{\Omega_t^f} \rho^f ((\mathbf{u}^f - \mathbf{u}_m) \cdot \nabla) \mathbf{u}^f \cdot \delta \mathbf{u} d\mathbf{x} \\ & - \int_{\Gamma_N} \bar{\mathbf{h}} \cdot \delta \mathbf{u} d\Gamma + \int_{\Omega_t^f} \boldsymbol{\sigma}^f : \nabla \delta \mathbf{u} d\mathbf{x} - \int_{\Omega_t^f} \rho^f \mathbf{g} \cdot \delta \mathbf{u} d\mathbf{x}. \end{aligned} \quad (2.40)$$

Let us now skip introducing details of solving the fluid equations (step 3 in Algorithm 1), and focus on solving the solid equation (2.38) (step 5 in Algorithm 1). The reason for doing this is that the former can be found in standard literature (refer to the list after Table 2.1), and will also be presented in the following chapters, while the methods for solving the latter problem introduced below cannot be widely found. We refer to [14, 94, 114] and bring some components together in the following context. Let us take the Saint Venant-Kirchhoff solid model as an

Algorithm 1: Partitioned/Segregated methods

-
- 1 Given the solid displacement \mathbf{d}_n^s , fluid velocity \mathbf{u}_n^f at time t_n , the following iteration is to compute \mathbf{d}_{n+1}^s and \mathbf{u}_{n+1}^f at time t_{n+1} .
 - 2 Start with a reasonable guess of $\Delta\mathbf{d}^s$ on the interface Γ_t . Solve the mesh equation (2.35) with boundary conditions (2.36) and (2.37) to get the mesh velocity \mathbf{u}_m .
 - 3 Solve the fluid equation (2.34) and (2.7) with boundary conditions (2.10)
 $(\mathbf{u}^s|_{\Gamma_t} = \mathbf{u}_m|_{\Gamma_t})$, (2.12) and (2.13).
 - 4 Solve the interaction equation (2.40) to compute the reaction force \mathbf{h}^f on Γ_t .
 - 5 Solve the solid equation (2.38) or weak form (2.41), or linearized weak form (2.69)) with Neumann boundary condition $\boldsymbol{\sigma}\mathbf{n}^s = \mathbf{h}^f$ on Γ_t and Dirichlet boundary condition $\mathbf{d}^s = \bar{\mathbf{u}}\Delta t + \mathbf{d}_n^s$ on $\Gamma_D \cap \Omega_t^s$.
 - 6 Let $\Delta\mathbf{d}_t^s|_{\Gamma_t} = \mathbf{d}^s - \mathbf{d}_n^s|_{\Gamma_t}$. If $\|\Delta\mathbf{d}_t^s|_{\Gamma_t} - \Delta\mathbf{d}^s|_{\Gamma_t}\| \geq tol$, then let $\Delta\mathbf{d}^s|_{\Gamma_t} = (1 - \omega)\Delta\mathbf{d}_t^s|_{\Gamma_t} + \omega\Delta\mathbf{d}^s|_{\Gamma_t}$ and goto step 2 for the next cycle of iteration. tol is an error tolerance and ω is a factor of relaxation.
-

example, and consider a method of linearization in order to solve the solid equation (2.38). Given a test function $\delta\mathbf{d}$, the weak form of the solid equation (2.38) can be expressed as

$$\int_{\Omega_{\mathbf{x}}^s} \rho_0^s \frac{\partial^2 \mathbf{d}^s}{\partial t^2} \cdot \delta\mathbf{d} d\mathbf{X} + \int_{\Omega_t^s} \boldsymbol{\sigma}^s : \nabla \delta\mathbf{d} d\mathbf{x} = \int_{\Gamma_t} (\boldsymbol{\sigma}^s \mathbf{n}^s) \cdot \delta\mathbf{d} d\Gamma + \int_{\Omega_{\mathbf{x}}^s} \rho_0^s \mathbf{g} \cdot \delta\mathbf{d} d\mathbf{X}. \quad (2.41)$$

According to the constitutive equation (2.23), we have

$$\int_{\Omega_t^s} \boldsymbol{\sigma}^s : \nabla \delta\mathbf{d} d\mathbf{x} = \int_{\Omega_t^s} J^{-1} \mathbf{F} \mathbf{S} \mathbf{F}^T : \nabla \delta\mathbf{d} d\mathbf{x}. \quad (2.42)$$

Using the trace property $\mathbf{A} : \mathbf{B} = \text{tr}(\mathbf{AB}^T)$ for arbitrary square matrices \mathbf{A} and \mathbf{B} , we then have

$$\begin{aligned} & \int_{\Omega_t^s} J^{-1} \mathbf{F} \mathbf{S} \mathbf{F}^T : \nabla \delta\mathbf{d} d\mathbf{x} \\ &= \int_{\Omega_t^s} J^{-1} \text{tr}(\mathbf{F} \mathbf{S} \mathbf{F}^T \nabla^T \delta\mathbf{d}) d\mathbf{x} \\ &= \int_{\Omega_t^s} J^{-1} \text{tr}(\mathbf{F} \mathbf{S} (\nabla \delta\mathbf{d} \mathbf{F})^T) d\mathbf{x} \\ &= \int_{\Omega_t^s} J^{-1} \mathbf{F} \mathbf{S} : (\nabla \delta\mathbf{d}) \mathbf{F} d\mathbf{x} \\ &= \int_{\Omega_{\mathbf{x}}^s} \mathbf{F} \mathbf{S} : \nabla_{\mathbf{x}} \delta\mathbf{d} d\mathbf{X}. \end{aligned} \quad (2.43)$$

Further using the cyclic permutation property $\text{tr}(\mathbf{ABC}) = \text{tr}(\mathbf{BCA}) = \text{tr}(\mathbf{CAB})$ for arbitrary

square matrices \mathbf{A} , \mathbf{B} and \mathbf{C} , we have

$$\int_{\Omega_{\mathbf{X}}^s} \mathbf{F} \mathbf{S} : \nabla_{\mathbf{X}} \delta \mathbf{d} d\mathbf{X} = \int_{\Omega_{\mathbf{X}}^s} \mathbf{S} : \mathbf{F}^T (\nabla_{\mathbf{X}} \delta \mathbf{d}) d\mathbf{X}. \quad (2.44)$$

Because the second Piola-Kirchhoff stress \mathbf{S} is a symmetric tensor, i.e.:

$$\mathbf{S} : \mathbf{F}^T (\nabla_{\mathbf{X}} \delta \mathbf{d}) = \mathbf{S}^T : \mathbf{F}^T (\nabla_{\mathbf{X}} \delta \mathbf{d}) = \text{tr} (\mathbf{S}^T (\nabla_{\mathbf{X}}^T \delta \mathbf{d}) \mathbf{F}) = \mathbf{S} : (\nabla_{\mathbf{X}}^T \delta \mathbf{d}) \mathbf{F}, \quad (2.45)$$

we further have

$$\int_{\Omega_{\mathbf{X}}^s} \mathbf{S} : \mathbf{F}^T (\nabla_{\mathbf{X}} \delta \mathbf{d}) d\mathbf{X} = \frac{1}{2} \int_{\Omega_{\mathbf{X}}^s} \mathbf{S} : [\mathbf{F}^T (\nabla_{\mathbf{X}} \delta \mathbf{d}) + (\nabla_{\mathbf{X}}^T \delta \mathbf{d}) \mathbf{F}] d\mathbf{X} = \int_{\Omega_{\mathbf{X}}^s} \mathbf{S} : \delta \mathbf{E} d\mathbf{X}, \quad (2.46)$$

where

$$\delta \mathbf{E} = \frac{1}{2} [\mathbf{F}^T (\nabla_{\mathbf{X}} \delta \mathbf{d}) + (\nabla_{\mathbf{X}}^T \delta \mathbf{d}) \mathbf{F}]. \quad (2.47)$$

Finally we get the following by combining equations (2.42) to (2.47).

$$\int_{\Omega_t^s} \boldsymbol{\sigma}^s : \nabla \delta \mathbf{d} d\mathbf{x} = \int_{\Omega_{\mathbf{X}}^s} \mathbf{S} : \delta \mathbf{E} d\mathbf{X}. \quad (2.48)$$

Notice that $\delta \mathbf{E}$ can also be interpreted as a virtual strain, $\int_{\Omega_{\mathbf{X}}^s} \mathbf{S} : \delta \mathbf{E}$ is then the work done by the second Piola-Kirchhoff stress \mathbf{S} on virtual strain $\delta \mathbf{E}$, and equation (2.41) can then be interpreted as a work balance.

Let us also interpret $\delta \mathbf{E}$ as the variation of the Lagrangian Green strain \mathbf{E} based on the following Gâteaux variation.

Definition 2.1. The 1st order Gâteaux variation of a functional $\mathcal{F}(\mathbf{d})$ in the direction $\Delta \mathbf{d}$ is defined by [14, 114]

$$\delta \mathcal{F}(\mathbf{d}; \Delta \mathbf{d}) = \left. \frac{d}{d\epsilon} \mathcal{F}(\mathbf{d} + \epsilon \Delta \mathbf{d}) \right|_{\epsilon=0}, \quad (2.49)$$

and the 2nd order Gâteaux variation of a functional $\mathcal{F}(\mathbf{d})$ in the direction $\Delta \mathbf{d}_1$ and $\Delta \mathbf{d}_2$ is defined by [114, Page 157]

$$\delta^2 \mathcal{F}(\mathbf{d}; \Delta \mathbf{d}_1, \Delta \mathbf{d}_2) = \left. \frac{\partial^2}{\partial \epsilon_1 \partial \epsilon_2} \mathcal{F}(\mathbf{d} + \epsilon_1 \Delta \mathbf{d}_1 + \epsilon_2 \Delta \mathbf{d}_2) \right|_{\epsilon_1=\epsilon_2=0}. \quad (2.50)$$

If $\mathcal{F}(\mathbf{d})$ is a vector or matrix the above derivative $\frac{d}{d\epsilon}$ or $\frac{\partial^2}{\partial \epsilon_1 \partial \epsilon_2}$ is taken based on components.

Let us digress to state the following properties of Gâteaux variation, which are straightforward to obtain from the above definition.

1. For two arbitrary functionals $\mathcal{F}(\cdot)$ and $\mathcal{G}(\cdot)$:

$$\delta (\mathcal{F}\mathcal{G}) = (\delta \mathcal{F}) \mathcal{G} + \mathcal{F} (\delta \mathcal{G}). \quad (2.51)$$

2. For a linear functional $\mathcal{L}(\cdot)$ and an arbitrary functional $\mathcal{F}(\cdot)$:

$$\delta(\mathcal{L} \circ \mathcal{F}) = \mathcal{L} \circ \delta\mathcal{F}. \quad (2.52)$$

3. For the linear functional $\mathcal{L}(\mathbf{d}) = \mathbf{d}$, taking the 1st variation in direction $\Delta\mathbf{d}$ and taking the 2nd variation in any two directions:

$$\delta\mathcal{L} = \delta\mathbf{d} = \Delta\mathbf{d}, \quad \delta^2\mathcal{L} = \delta^2\mathbf{d} = 0. \quad (2.53)$$

4. For a constant functional $\mathcal{F}(\mathbf{d}) = \mathbf{c}$:

$$\delta\mathcal{F} = \mathbf{0}. \quad (2.54)$$

5. For a functional $\mathcal{F}(\cdot)$ and two directions $\Delta\mathbf{d}_1$ and $\Delta\mathbf{d}_2$:

$$\delta^2\mathcal{F}(\mathbf{d}; \Delta\mathbf{d}_1, \Delta\mathbf{d}_2) = \frac{d}{d\epsilon}\delta\mathcal{F}(\mathbf{d} + \epsilon\Delta\mathbf{d}_1; \Delta\mathbf{d}_2)\Big|_{\epsilon=0}. \quad (2.55)$$

Remark 2.4. In the following context, we omit the direction of a variation which refers to an arbitrary direction $\delta\mathbf{d}$, i.e.: $\delta\mathcal{F}(\mathbf{d}) = \delta\mathcal{F}(\mathbf{d}; \delta\mathbf{d})$, or $\delta^2\mathcal{F}(\mathbf{d}) = \delta^2\mathcal{F}(\mathbf{d}; \delta\mathbf{d}, \delta\mathbf{d})$. We may further omit the independent variable \mathbf{d} if it is not a specified point (such as \mathbf{d}^0 , $\bar{\mathbf{d}}$ or $\tilde{\mathbf{d}}$). This is consistent with the differentiation of a scalar function $f(x)$: $df = f'dx$ or $d^2f = f''dx^2$. The terminology arbitrary $\delta\mathbf{d}$ is also consistent with the finite element arbitrary test function.

Having introduced the definition and properties of the Gâteaux variation, let us now deduce the variation of the Lagrangian Green strain \mathbf{E} and linearize expression (2.48). According to the definition of \mathbf{E} (2.19), $\mathbf{F} = \mathbf{I} + \nabla_{\mathbf{X}}\mathbf{d}$ and the above properties (except the last one) of Gâteaux variation, taking the variation of \mathbf{E} gives

$$\delta\mathbf{E} = \frac{1}{2} (\mathbf{F}^T \delta\mathbf{F} + \delta\mathbf{F}^T \mathbf{F}) = \frac{1}{2} (\mathbf{F}^T (\nabla_{\mathbf{X}}\delta\mathbf{d}) + (\nabla_{\mathbf{X}}^T \delta\mathbf{d}) \mathbf{F}). \quad (2.56)$$

Further, we have

$$\begin{aligned} \delta\mathbf{E} &= \frac{1}{2} [(\nabla_{\mathbf{X}}^T \mathbf{d} + \mathbf{I})(\nabla_{\mathbf{X}}\delta\mathbf{d}) + (\nabla_{\mathbf{X}}^T \delta\mathbf{d})(\nabla_{\mathbf{X}}\mathbf{d} + \mathbf{I})] \\ &= \frac{1}{2} (\nabla_{\mathbf{X}}\delta\mathbf{d} + \nabla_{\mathbf{X}}^T \delta\mathbf{d} + \nabla_{\mathbf{X}}^T \mathbf{d} \nabla_{\mathbf{X}}\delta\mathbf{d} + \nabla_{\mathbf{X}}^T \delta\mathbf{d} \nabla_{\mathbf{X}}\mathbf{d}) \\ &= \frac{1}{2} (\mathbf{D}_{\mathbf{X}}\delta\mathbf{d} + \nabla_{\mathbf{X}}^T \mathbf{d} \nabla_{\mathbf{X}}\delta\mathbf{d} + \nabla_{\mathbf{X}}^T \delta\mathbf{d} \nabla_{\mathbf{X}}\mathbf{d}). \end{aligned} \quad (2.57)$$

Remark 2.5. The expression of \mathbf{E} (2.19) may also be rewritten as:

$$\begin{aligned}\mathbf{E} &= \frac{1}{2} (\mathbf{F}^T \mathbf{F} - \mathbf{I}) \\ &= \frac{1}{2} [(\nabla_{\mathbf{X}}^T \mathbf{d} + \mathbf{I})(\nabla_{\mathbf{X}} \mathbf{d} + \mathbf{I}) - \mathbf{I}] \\ &= \frac{1}{2} (\mathbf{D}_{\mathbf{X}} \mathbf{d} + \nabla_{\mathbf{X}}^T \mathbf{d} \nabla_{\mathbf{X}} \mathbf{d}).\end{aligned}\quad (2.58)$$

One can also get (2.57) from (2.58) due to (2.51).

We are now ready to linearize expression (2.48). Let $\mathcal{F}(\mathbf{d}) = \mathbf{S}(\mathbf{E}) : \delta \mathbf{E}$, linearizing $\mathcal{F}(\mathbf{d})$ at a reference point $\tilde{\mathbf{d}}$ gives

$$\mathcal{F}(\mathbf{d}) = \mathcal{F}(\tilde{\mathbf{d}}) + \delta \mathcal{F}(\tilde{\mathbf{d}}, \mathbf{w}), \quad \mathbf{w} = \mathbf{d} - \tilde{\mathbf{d}}. \quad (2.59)$$

Using the definition of Gâteaux variation and (2.58) (or replacing \mathbf{d} with $\tilde{\mathbf{d}}$ and $\delta \mathbf{d}$ with \mathbf{w} in (2.57)), we have

$$\delta \mathbf{E}(\tilde{\mathbf{d}}; \mathbf{w}) = \frac{1}{2} (\mathbf{D}_{\mathbf{X}} \mathbf{w} + \nabla_{\mathbf{X}}^T \tilde{\mathbf{d}} \nabla_{\mathbf{X}} \mathbf{w} + \nabla_{\mathbf{X}}^T \mathbf{w} \nabla_{\mathbf{X}} \tilde{\mathbf{d}}), \quad (2.60)$$

and using (2.55) we further have

$$\delta^2 \mathbf{E}(\tilde{\mathbf{d}}; \mathbf{w}, \delta \mathbf{d}) = \frac{d}{d\epsilon} \delta \mathbf{E}(\tilde{\mathbf{d}} + \epsilon \mathbf{w}; \delta \mathbf{d}) \Big|_{\epsilon=0} = \frac{1}{2} (\nabla_{\mathbf{X}}^T \mathbf{w} \nabla_{\mathbf{X}} \delta \mathbf{d} + \nabla_{\mathbf{X}}^T \delta \mathbf{d} \nabla_{\mathbf{X}} \mathbf{w}). \quad (2.61)$$

Since $\mathbf{S}(\cdot)$ is a linear operator, then according to (2.52):

$$\delta \mathbf{S}(\mathbf{E}(\tilde{\mathbf{d}}; \mathbf{w})) = \mathbf{S}(\delta \mathbf{E}(\tilde{\mathbf{d}}; \mathbf{w})). \quad (2.62)$$

Substituting (2.60) into (2.62) we get

$$\delta \mathbf{S}(\tilde{\mathbf{d}}; \mathbf{w}) = \delta \mathbf{S}(\mathbf{E}(\tilde{\mathbf{d}}; \mathbf{w})) = \frac{1}{2} \mathbf{S}(\mathbf{D}_{\mathbf{X}} \mathbf{w} + \nabla_{\mathbf{X}}^T \tilde{\mathbf{d}} \nabla_{\mathbf{X}} \mathbf{w} + \nabla_{\mathbf{X}}^T \mathbf{w} \nabla_{\mathbf{X}} \tilde{\mathbf{d}}). \quad (2.63)$$

Using equations (2.61) and (2.63), we further have

$$\begin{aligned}\delta \mathcal{F}(\tilde{\mathbf{d}}, \mathbf{w}) &= \delta \mathbf{S}(\tilde{\mathbf{d}}, \mathbf{w}) : \delta \tilde{\mathbf{E}} + \frac{1}{2} \mathbf{S}(\mathbf{D}_{\mathbf{X}} \tilde{\mathbf{d}} + \nabla_{\mathbf{X}}^T \tilde{\mathbf{d}} \nabla_{\mathbf{X}} \tilde{\mathbf{d}}) : \delta^2 \mathbf{E}(\tilde{\mathbf{d}}; \mathbf{w}, \delta \mathbf{d}) \\ &= \frac{1}{2} \mathbf{S}(\mathbf{D}_{\mathbf{X}} \mathbf{w} + \nabla_{\mathbf{X}}^T \tilde{\mathbf{d}} \nabla_{\mathbf{X}} \mathbf{w} + \nabla_{\mathbf{X}}^T \mathbf{w} \nabla_{\mathbf{X}} \tilde{\mathbf{d}}) : \delta \tilde{\mathbf{E}} \\ &\quad + \frac{1}{2} \mathbf{S}(\mathbf{D}_{\mathbf{X}} \tilde{\mathbf{d}} + \nabla_{\mathbf{X}}^T \tilde{\mathbf{d}} \nabla_{\mathbf{X}} \tilde{\mathbf{d}}) : \frac{1}{2} (\nabla_{\mathbf{X}}^T \mathbf{w} \nabla_{\mathbf{X}} \delta \mathbf{d} + \nabla_{\mathbf{X}}^T \delta \mathbf{d} \nabla_{\mathbf{X}} \mathbf{w}).\end{aligned}\quad (2.64)$$

Following [94], we neglect the last term in equation (2.64) which has a second order Gâteaux variation of Green strain \mathbf{E} . Therefore, substituting $\mathbf{w} = \mathbf{d} - \tilde{\mathbf{d}}$ into equation (2.64), and using the value of $\mathcal{F}(\mathbf{d})$ at $\tilde{\mathbf{d}}$:

$$\mathcal{F}(\tilde{\mathbf{d}}) = \frac{1}{2} \mathbf{S}(\mathbf{D}_{\mathbf{X}} \tilde{\mathbf{d}} + \nabla_{\mathbf{X}}^T \tilde{\mathbf{d}} \nabla_{\mathbf{X}} \tilde{\mathbf{d}}) : \delta \tilde{\mathbf{E}}, \quad (2.65)$$

with

$$\delta\tilde{\mathbf{E}} = \frac{1}{2} \left(D_{\mathbf{X}} \delta \mathbf{d} + \nabla_{\mathbf{X}}^T \tilde{\mathbf{d}} \nabla_{\mathbf{X}} \delta \mathbf{d} + \nabla_{\mathbf{X}}^T \delta \mathbf{d} \nabla_{\mathbf{X}} \tilde{\mathbf{d}} \right), \quad (2.66)$$

$\mathcal{F}(\mathbf{d})$ is then linearized as follows.

$$\mathcal{F}(\mathbf{d}) = \mathbf{S} : \delta \mathbf{E} \approx \mathbf{S} (\tilde{\mathbf{E}}) : \delta \tilde{\mathbf{E}} - \frac{1}{2} \mathbf{S} (\nabla_{\mathbf{X}}^T \tilde{\mathbf{d}} \nabla_{\mathbf{X}} \tilde{\mathbf{d}}) : \delta \tilde{\mathbf{E}}, \quad (2.67)$$

with

$$\tilde{\mathbf{E}} = \frac{1}{2} \left(D_{\mathbf{X}} \mathbf{d} + \nabla_{\mathbf{X}}^T \tilde{\mathbf{d}} \nabla_{\mathbf{X}} \mathbf{d} + \nabla_{\mathbf{X}}^T \mathbf{d} \nabla_{\mathbf{X}} \tilde{\mathbf{d}} \right). \quad (2.68)$$

We finally get the following linearized weak form of solid equation by substituting expression (2.67) and (2.48) into weak form of solid equation (2.41):

$$\begin{aligned} & \int_{\Omega_{\mathbf{X}}^s} \rho_0^s \frac{\partial^2 \mathbf{d}^s}{\partial t^2} \cdot \delta \mathbf{d} d\mathbf{X} + \int_{\Omega_{\mathbf{X}}^s} \mathbf{S} (\tilde{\mathbf{E}}) : \delta \tilde{\mathbf{E}} d\mathbf{X} \\ &= \int_{\Omega_{\mathbf{X}}^s} \frac{1}{2} \mathbf{S} (\nabla_{\mathbf{X}}^T \tilde{\mathbf{d}} \nabla_{\mathbf{X}} \tilde{\mathbf{d}}) : \delta \tilde{\mathbf{E}} d\mathbf{X} + \int_{\Gamma_t} (\boldsymbol{\sigma}^s \mathbf{n}^s) \cdot \delta \mathbf{d} d\Gamma + \int_{\Omega_{\mathbf{X}}^s} \rho_0^s \mathbf{g} \cdot \delta \mathbf{d} d\mathbf{X}. \end{aligned} \quad (2.69)$$

It can be seen from Algorithm 1 that the partitioned methods have to iterate at every time step until the velocity on the interface Γ_t does not change. The convergence is problem dependent, and cannot be guaranteed even if relaxation is adopted, especially in the case where the solid and fluid have a large energy exchange, for example when the solid and fluid have a similar inertia.

2.4.2 Monolithic/Fully-coupled methods

The monolithic methods are regarded to be more robust, which can remove the weakness of the partitioned methods mentioned above, however it transfers the difficulty to solving the discretized linear equation system.

The monolithic methods solve the fluid equations (2.34) and (2.7) in Ω_t^f , the solid equation (2.38) in Ω_t^s and the mesh equation (2.35) in Ω_t^f , together with the consistency equation on Γ_t :

$$\frac{\partial \mathbf{d}^s}{\partial t} = \mathbf{u}^f. \quad (2.70)$$

We use a Lagrange multiplier \mathbf{L} to enforce this condition on Γ_t . Because the finite element method is considered in this thesis, we write down the weak form of these equations with corresponding boundary conditions which are the same as discussed in Section 2.4.1. The unknowns include fluid velocity \mathbf{u}^f and pressure p , solid displacement \mathbf{d}^s , Lagrange multiplier \mathbf{L} and mesh velocity \mathbf{u}_m , with the corresponding test functions being denoted by $\delta \mathbf{u}$, δp , $\delta \mathbf{d}$, $\delta \mathbf{L}$ and $\delta \mathbf{u}_m$. Then the weak form of the solid equation (2.38) is almost the same as (2.69), but

replacing the stress $\sigma^s \mathbf{n}^s$ on Γ_t by a Lagrange multiplier \mathbf{L} , which could be expressed as

$$\begin{aligned} & \int_{\Omega_x^s} \rho_0^s \frac{\partial^2 \mathbf{d}^s}{\partial t^2} \cdot \delta \mathbf{d} d\mathbf{X} + \int_{\Omega_x^s} \mathbf{S}(\tilde{\mathbf{E}}) : \delta \tilde{\mathbf{E}} d\mathbf{X} - \int_{\Gamma_t} \mathbf{L} \cdot \delta \mathbf{d} d\Gamma \\ &= \int_{\Omega_x^s} \frac{1}{2} \mathbf{S}(\nabla_{\mathbf{x}}^T \tilde{\mathbf{d}} \nabla_{\mathbf{x}} \tilde{\mathbf{d}}) : \delta \tilde{\mathbf{E}} d\mathbf{X} + \int_{\Omega_x^s} \rho_0^s \mathbf{g} \cdot \delta \mathbf{d} d\mathbf{X}. \end{aligned} \quad (2.71)$$

The weak form of the fluid equations (2.34) and (2.7), using the constitutive equation (2.8) and considering the Lagrange multiplier \mathbf{L} on Γ_t (replacing the stress $\sigma^f \mathbf{n}^s = \sigma^s \mathbf{n}^s$ on Γ_t by a Lagrange multiplier \mathbf{L} based on the interface boundary condition (2.11)), may be expressed as:

$$\begin{aligned} & \int_{\Omega_t^f} \rho^f \frac{\partial \mathbf{u}^f}{\partial t} \cdot \delta \mathbf{u} d\mathbf{x} + \int_{\Omega_t^f} \rho^f ((\mathbf{u}^f - \mathbf{u}_m) \cdot \nabla) \mathbf{u}^f \cdot \delta \mathbf{u} d\mathbf{x} \\ &+ \int_{\Omega_t^f} \nu^f \mathbf{D}\mathbf{u}^f : \nabla \delta \mathbf{u} d\mathbf{x} - \int_{\Omega_t^f} p \nabla \cdot \delta \mathbf{u} d\mathbf{x} + \int_{\Gamma_t} \mathbf{L} \cdot \delta \mathbf{u} d\Gamma \\ &= \int_{\Gamma_N} \bar{\mathbf{h}} \cdot \delta \mathbf{u} d\mathbf{x} + \int_{\Omega_t^f} \rho^f \mathbf{g} \cdot \delta \mathbf{u} d\mathbf{x}, \end{aligned} \quad (2.72)$$

and

$$-\int_{\Omega_t^f} \delta p \nabla \cdot \mathbf{u}^f d\mathbf{x} = 0. \quad (2.73)$$

The weak form of the consistency equation (2.70) can be expressed as

$$\int_{\Gamma_t} \left(\frac{\partial \mathbf{d}^s}{\partial t} - \mathbf{u}^f \right) \cdot \delta \mathbf{L} d\Gamma = 0. \quad (2.74)$$

Finally, the weak form of the mesh equation (2.35) may be expressed as follows.

$$\frac{\mu}{2} \int_{\Omega_t^f} \mathbf{D}\mathbf{u}_m : \mathbf{D}\delta \mathbf{u}_m d\mathbf{x} - \lambda \int_{\Omega_t^f} (\nabla \cdot \mathbf{u}_m) (\nabla \cdot \delta \mathbf{u}_m) d\mathbf{x} = 0. \quad (2.75)$$

We discretize the time derivatives as follows, which is consistent for displacement and velocity:

$$\frac{\partial \mathbf{u}_{n+1}^f}{\partial t} \approx \frac{\mathbf{u}_{n+1}^f - \mathbf{u}_n^f}{\Delta t}, \quad (2.76)$$

$$\mathbf{u}_{n+1}^s = \frac{\partial \mathbf{d}_{n+1}^s}{\partial t} \approx \frac{\mathbf{d}_{n+1}^s - \mathbf{d}_n^s}{\Delta t}, \quad (2.77)$$

and

$$\frac{\partial^2 \mathbf{d}_{n+1}^s}{\partial t^2} \approx \frac{\mathbf{d}_{n+1}^s - 2\mathbf{d}_n^s + \mathbf{d}_{n-1}^s}{\Delta t^2}. \quad (2.78)$$

Consistency means that when expressing displacement as velocity, equations (2.77) and (2.78)

are consistent with equation (2.76), i.e.:

$$\frac{\partial \mathbf{u}_{n+1}^s}{\partial t} = \frac{\partial^2 \mathbf{d}_{n+1}^s}{\partial t^2} \approx \frac{\mathbf{d}_{n+1}^s - 2\mathbf{d}_n^s + \mathbf{d}_{n-1}^s}{\Delta t^2} = \frac{\frac{\mathbf{d}_{n+1}^s - \mathbf{d}_n^s}{\Delta t} - \frac{\mathbf{d}_n^s - \mathbf{d}_{n-1}^s}{\Delta t}}{\Delta t} = \frac{\mathbf{u}_{n+1}^s - \mathbf{u}_n^s}{\Delta t} \quad (2.79)$$

is consistent with (2.76).

Regarding the nonlinear convection term in (2.72): in order to focus on demonstrating the monolithic method itself, we simply move it to the right-hand side of equation (2.72) and linearize it with a fixed-point iteration. For other methods to treat convection, readers may refer to [108, 163]. Using the arbitrariness of the test functions $\delta\mathbf{u}$, δp , $\delta\mathbf{d}$, $\delta\mathbf{L}$ and $\delta\mathbf{u}_m$, adding up equations (2.71) to (2.75) and substituting into the time approximations (2.76) and (2.78) gives the equivalent expression of the weak forms as follows.

$$\begin{aligned} & \int_{\Omega_t^f} \rho_f^f \frac{\mathbf{u}^f - \mathbf{u}_n^f}{\Delta t} \cdot \delta \mathbf{u} d\mathbf{x} + \frac{1}{2} \int_{\Omega_t^f} \nu^f \mathbf{D}\mathbf{u}^f : \mathbf{D}\delta\mathbf{u} d\mathbf{x} \\ & - \int_{\Omega_t^f} p \nabla \cdot \delta \mathbf{u} d\mathbf{x} - \int_{\Omega_t^f} \delta p \nabla \cdot \mathbf{u}^f d\mathbf{x} \\ & + \int_{\Omega_{\mathbf{X}}^s} \rho_0^s \frac{\mathbf{d}^s - 2\mathbf{d}_n^s + \mathbf{d}_{n-1}^s}{\Delta t^2} \cdot \frac{\delta \mathbf{d}}{\Delta t} d\mathbf{X} + \int_{\Omega_{\mathbf{X}}^s} \mathbf{S}(\tilde{\mathbf{E}}) : \frac{\delta \tilde{\mathbf{E}}}{\Delta t} d\mathbf{X} \\ & - \int_{\Gamma_t(\mathbf{d}_{n+1}^s)} \mathbf{L} \cdot \left(\frac{\delta \mathbf{d}}{\Delta t} - \delta \mathbf{u} \right) d\Gamma - \int_{\Gamma_t(\mathbf{d}_{n+1}^s)} \left(\frac{\mathbf{d}^s - \mathbf{d}_n^s}{\Delta t} - \mathbf{u}^f \right) \cdot \delta \mathbf{L} d\Gamma \\ & + \frac{\mu}{2} \int_{\Omega_t^f} \mathbf{D}\mathbf{u}_m : \mathbf{D}\delta\mathbf{u}_m d\mathbf{x} - \lambda \int_{\Omega_t^f} (\nabla \cdot \mathbf{u}_m) (\nabla \cdot \delta\mathbf{u}_m) d\mathbf{x} \\ & = \int_{\Gamma_N} \bar{\mathbf{h}} \cdot \delta \mathbf{u} d\Gamma + \int_{\Omega_t^f} \rho^f \mathbf{g} \cdot \delta \mathbf{u} d\mathbf{x} + \int_{\Omega_{\mathbf{X}}^s} \rho_0^s \mathbf{g} \cdot \frac{\delta \mathbf{d}}{\Delta t} d\mathbf{X} \\ & - \int_{\Omega_t^f} \rho^f ((\tilde{\mathbf{u}}^f - \tilde{\mathbf{u}}_m) \cdot \nabla) \tilde{\mathbf{u}}^f \cdot \delta \mathbf{u} d\mathbf{x} \\ & + \frac{1}{2} \int_{\Omega_{\mathbf{X}}^s} \mathbf{S}(\nabla_{\mathbf{X}}^T \tilde{\mathbf{d}} \nabla_{\mathbf{X}} \tilde{\mathbf{d}}) : \frac{\delta \tilde{\mathbf{E}}}{\Delta t} d\mathbf{X}, \end{aligned} \quad (2.80)$$

with initial conditions (2.14) and (2.15), boundary conditions (2.12) and (2.13) for the fluid velocity \mathbf{u}^f , and boundary conditions (2.36) and (2.37) for the mesh velocity \mathbf{u}_m . Notice that we divide by Δt on both side of the equation (2.71) before summing up in order to produce the symmetric linear system below. Equation (2.80) gives the following linear algebraic system

after spatial discretization.

$$\begin{bmatrix} \mathbf{F}_{11} & \mathbf{F}_{12} & \mathbf{B}_1 & \mathbf{0} & \mathbf{0} & \mathbf{0} \\ \mathbf{F}_{12}^T & \mathbf{F}_{22} & \mathbf{B}_2 & \mathbf{0} & \mathbf{0} & \mathbf{C}_1 \\ \mathbf{B}_1^T & \mathbf{B}_2^T & \mathbf{0} & \mathbf{0} & \mathbf{0} & \mathbf{0} \\ \mathbf{0} & \mathbf{0} & \mathbf{0} & \mathbf{S}_{11} & \mathbf{S}_{12} & \mathbf{0} \\ \mathbf{0} & \mathbf{0} & \mathbf{0} & \mathbf{S}_{12}^T & \mathbf{S}_{22} & \mathbf{C}_2 \\ \mathbf{0} & \mathbf{C}_1^T & \mathbf{0} & \mathbf{0} & \mathbf{C}_2^T & \mathbf{0} \\ \mathbf{0} & \mathbf{0} & \mathbf{0} & \mathbf{0} & \mathbf{C}_m^T & \mathbf{0} \end{bmatrix} \begin{pmatrix} \mathbf{u}_{in} \\ \mathbf{u}_{on} \\ \mathbf{p} \\ \mathbf{d}_{in} \\ \mathbf{d}_{on} \\ \mathbf{L} \\ \mathbf{u}_m \end{pmatrix} = \begin{pmatrix} \mathbf{f}_1 \\ \mathbf{f}_2 \\ \mathbf{0} \\ \mathbf{g}_1 \\ \mathbf{g}_2 \\ \mathbf{0} \\ \mathbf{0} \end{pmatrix}. \quad (2.81)$$

In the above, $\begin{pmatrix} \mathbf{u}_{in} \\ \mathbf{u}_{on} \end{pmatrix} = \mathbf{u}$, with \mathbf{u}_{on} being the velocity components on boundary Γ_t , and \mathbf{u}_{in} being the velocity components in $\bar{\Omega}_t^f \setminus \Gamma_t$. Similarly $\begin{pmatrix} \mathbf{d}_{in} \\ \mathbf{d}_{on} \end{pmatrix} = \mathbf{d}$, where \mathbf{d}_{on} are the displacement components on boundary Γ_t , and \mathbf{d}_{in} the displacement components in $\bar{\Omega}_t^s \setminus \Gamma_t$. Matrices $\begin{bmatrix} \mathbf{F}_{11} & \mathbf{F}_{12} \\ \mathbf{F}_{12}^T & \mathbf{F}_{22} \end{bmatrix}$ and $\begin{bmatrix} \mathbf{S}_{11} & \mathbf{S}_{12} \\ \mathbf{S}_{12}^T & \mathbf{S}_{22} \end{bmatrix}$ are discretizations of the fluid velocity integrals and the solid displacement integrals respectively (including mass matrices and stiffness matrices). Matrix $\begin{pmatrix} \mathbf{B}_1 \\ \mathbf{B}_2 \end{pmatrix}$ indicates the coupling between fluid velocity and pressure. Matrix \mathbf{C}_1 indicates the coupling between interface Γ_t fluid velocity \mathbf{u}_{on} and the Lagrange multiplier \mathbf{L} . Matrix \mathbf{C}_2 indicates the coupling between interface Γ_t solid displacement \mathbf{d}_{on} and the Lagrange multiplier \mathbf{L} . Matrix \mathbf{K} arises from the discretization of the mesh equation, and matrix \mathbf{C}_m indicates the coupling between the mesh velocity \mathbf{u}_m and interface Γ_t solid displacement \mathbf{d}_{on} due to boundary condition (2.37).

As mentioned at the beginning of this section, the major advantage of the monolithic approach is that it is generally stable and robust because of the fully-coupled system. However this also presents a disadvantage: because one needs a very powerful linear algebraic solver in order to solve this large linear system (2.81).

2.4.3 Monolithic Eulerian method

The monolithic Eulerian method [34, 67, 110] reduces the size of the linear system (2.81) by only solving for one velocity field in the whole fluid-structure domain $\Omega_t^f \cup \Omega_t^s$, however it still has much of the robustness because the system is still fully-coupled and solved simultaneously. The Lagrange multiplier is also unnecessary for this method because there is only one velocity variable defined on the fluid-solid interface as shown in Figure 2.3.

References [34, 67, 110] use a remeshing technique to keep the mesh fitted on the fluid-structure interface. Here we use an ALE mesh to introduce the principle of this method. Let $\mathbf{u} = \begin{cases} \mathbf{u}^f & \text{in } \Omega_t^f \\ \mathbf{u}^s & \text{in } \Omega_t^s \end{cases}$, and use the same test function $\delta\mathbf{u}$ for both the fluid and solid equations

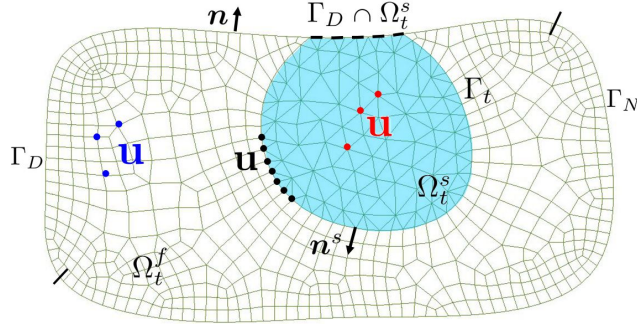


Figure 2.3: Schematic diagram for an interface-fitted mesh, $\Omega = \Omega_t^f \cup \Omega_t^s$, $\Gamma = \Gamma_D \cup \Gamma_N$. Solve for one velocity \mathbf{u} in Ω .

to deduce the weak forms. Then the weak form of this monolithic Eulerian method, using the momentum equation (2.1) and continuity equation (2.7), may be expressed as follows [67].

$$\begin{aligned} & \int_{\Omega_t^f} \rho^f \frac{d\mathbf{u}}{dt} \cdot \delta \mathbf{u} d\mathbf{x} + \int_{\Omega_t^s} \rho^s \frac{d\mathbf{u}}{dt} \cdot \delta \mathbf{u} d\mathbf{x} + \frac{1}{2} \int_{\Omega_t^f} \nu^f \mathbf{D}\mathbf{u} : \mathbf{D}\delta \mathbf{u} d\mathbf{x} \\ & - \int_{\Omega_t^f} p^f \nabla \cdot \delta \mathbf{u} d\mathbf{x} - \int_{\Omega_t^f} \delta p \nabla \cdot \mathbf{u} d\mathbf{x} + \int_{\Omega_t^s} \boldsymbol{\sigma}^s : \nabla \delta \mathbf{u} d\mathbf{x} \\ & = \int_{\Gamma_N} \bar{\mathbf{h}} \cdot \delta \mathbf{u} d\Gamma + \int_{\Omega_t^f} \rho^f \mathbf{g} \cdot \delta \mathbf{u} d\mathbf{x} + \int_{\Omega_t^s} \rho^s \mathbf{g} \cdot \delta \mathbf{u} d\mathbf{x}. \end{aligned} \quad (2.82)$$

If updating the solid with its own velocity, then there is no convection term in Ω_t^s . Using the backward Euler scheme to discretize (2.82) in time and letting $\rho = \begin{cases} \rho^f & \text{in } \Omega_t^f \\ \rho^s & \text{in } \Omega_t^s \end{cases}$, we then have

$$\begin{aligned} & \int_{\Omega} \rho \frac{\mathbf{u} - \mathbf{u}_n}{\Delta t} \cdot \delta \mathbf{u} d\mathbf{x} + \frac{1}{2} \int_{\Omega_{n+1}^f} \nu^f \mathbf{D}\mathbf{u} : \mathbf{D}\delta \mathbf{u} d\mathbf{x} \\ & + \int_{\Omega_{n+1}^f} \rho^f ((\mathbf{u} - \mathbf{u}_m) \cdot \nabla) \mathbf{u} \cdot \delta \mathbf{u} d\mathbf{x} - \int_{\Omega_{n+1}^f} p^f \nabla \cdot \delta \mathbf{u} d\mathbf{x} \\ & - \int_{\Omega_{n+1}^f} \delta p \nabla \cdot \mathbf{u} d\mathbf{x} + \int_{\Omega_{n+1}^s} \boldsymbol{\sigma}^s : \nabla \delta \mathbf{u} d\mathbf{x} \\ & = \int_{\Gamma_N} \bar{\mathbf{h}} \cdot \delta \mathbf{u} d\Gamma + \int_{\Omega} \rho \mathbf{g} \cdot \delta \mathbf{u} d\mathbf{x}, \end{aligned} \quad (2.83)$$

with boundary conditions (2.12) and (2.13). The above equation is coupled with the mesh equation (2.75), boundary conditions (2.36) and

$$\mathbf{u}_m = \mathbf{u} \quad \text{on } \Gamma_t. \quad (2.84)$$

In order to implement the above method, one has to express $\boldsymbol{\sigma}^s$ by displacement and further by velocity. It is straightforward to express displacement in terms of velocity after time

discretization, such as using the backward Euler scheme

$$\mathbf{d}_{n+1} = \mathbf{d}_n + \Delta t \mathbf{u}_{n+1}. \quad (2.85)$$

Because $\boldsymbol{\sigma}^s$ is expressed in terms of \mathbf{F} for either the Saint Venant-Kirchhoff solid model (Section 2.2) or the neo-Hookean solid model (Section 2.3), the remaining task is to express \mathbf{F} in terms of displacement, which can be accomplished by:

$$\mathbf{F} = \mathbf{I} + \nabla \mathbf{d} \mathbf{F} \Rightarrow \mathbf{F}^{-1} = \mathbf{I} - \nabla \mathbf{d}. \quad (2.86)$$

Here we use the incompressible neo-Hookean solid model to present details of expressing the solid stress $\boldsymbol{\sigma}^s$ in terms of velocity in the current configuration. For the compressible case and other solid models, please refer to [34, 67, 109, 110]. Let $\mathbf{B} = \mathbf{F} \mathbf{F}^T$ and neglect J (here it means $J = 1$ which is guaranteed by solving $\nabla \cdot \mathbf{u} = 0$ in the solid domain Ω_t^s), the constitutive equation (2.29) can be expressed as:

$$\boldsymbol{\sigma}^s = \mu^s (\mathbf{B} - \mathbf{I}) - p^s \mathbf{I}. \quad (2.87)$$

According to the Cayley-Hamilton theorem:

$$\mathbf{B}^2 - \text{tr}_{\mathbf{B}} \mathbf{B} + \det_{\mathbf{B}} \mathbf{I} = 0. \quad (2.88)$$

Therefore,

$$\mathbf{B} = \text{tr}_{\mathbf{B}} \mathbf{I} - \mathbf{B}^{-1}, \quad (2.89)$$

due to $\det_{\mathbf{B}} = \det_{\mathbf{F} \mathbf{F}^T} = \det_{\mathbf{F}} \det_{\mathbf{F}^T} = J^2 = 1$. Substituting (2.89) into (2.87) and using (2.86), for $\alpha = \mu^s + p^s - \text{tr}_{\mathbf{B}}$ and $\alpha' = \alpha + \mu^s$, we could express the Cauchy stress in terms of displacement as follows.

$$\begin{aligned} \boldsymbol{\sigma}^s &= \mu^s (\mathbf{B} - \mathbf{I}) - p^s \mathbf{I} \\ &= -\mu^s \mathbf{B}^{-1} - \alpha \mathbf{I} \\ &= -\mu^s (\mathbf{I} - \nabla \mathbf{d})^T (\mathbf{I} - \nabla \mathbf{d}) - \alpha \mathbf{I} \\ &= \mu^s (\nabla^T \mathbf{d} + \nabla \mathbf{d} - \nabla^T \mathbf{d} \nabla \mathbf{d}) - \alpha' \mathbf{I} \\ &= \mu^s (\mathbf{D} \mathbf{d} - \nabla^T \mathbf{d} \nabla \mathbf{d}) - \alpha' \mathbf{I}. \end{aligned} \quad (2.90)$$

Using (2.85), $\boldsymbol{\sigma}^s$ may be further expressed in terms of velocity after time discretization as follows (omit the superscript $n+1$ which indicates the current time step).

$$\begin{aligned} \boldsymbol{\sigma}^s &= \Delta t \mu^s (\mathbf{D} \mathbf{u} - \Delta t \nabla^T \mathbf{u} \nabla \mathbf{u}) \\ &\quad - \Delta t \mu^s (\nabla^T \mathbf{d}^n \nabla \mathbf{u} + \nabla^T \mathbf{u} \nabla \mathbf{d}^n) \\ &\quad + \mu^s \mathbf{D} \mathbf{d}^n - \mu^s \nabla^T \mathbf{d}^n \nabla \mathbf{d}^n - \alpha' \mathbf{I}. \end{aligned} \quad (2.91)$$

Let $p = \begin{cases} p^f & \text{in } \Omega_t^f \\ \alpha' & \text{in } \Omega_t^s \end{cases}$, substituting the above expression (2.91) into (2.83) and neglecting second order term of Δt , solving the incompressibility condition (2.7) $\nabla \cdot \mathbf{u} = 0$ in the solid domain Ω_t^s , gives

$$\begin{aligned} & \int_{\Omega} \rho \frac{\mathbf{u} - \mathbf{u}_n}{\Delta t} \cdot \delta \mathbf{u} d\mathbf{x} + \frac{1}{2} \int_{\Omega_{n+1}^f} \nu^f D\delta \mathbf{u} : D\delta \mathbf{u} d\mathbf{x} + \int_{\Omega_{n+1}^f} \rho^f ((\mathbf{u} - \mathbf{u}_m) \cdot \nabla) \mathbf{u} \cdot \delta \mathbf{u} d\mathbf{x} \\ & - \int_{\Omega} p \nabla \cdot \delta \mathbf{u} d\mathbf{x} - \int_{\Omega} \delta p \nabla \cdot \mathbf{u} d\mathbf{x} + \frac{\Delta t}{2} \int_{\Omega_{n+1}^s} \mu^s D\mathbf{u} : D\delta \mathbf{u} d\mathbf{x} \\ & - \Delta t \int_{\Omega_{n+1}^s} \mu^s (\nabla^T \mathbf{d}^n \nabla \mathbf{u} + \nabla^T \mathbf{u} \nabla \mathbf{d}^n) : \nabla \delta \mathbf{u} d\mathbf{x} = \int_{\Gamma_N} \bar{\mathbf{h}} \cdot \delta \mathbf{u} d\Gamma + \int_{\Omega} \rho \mathbf{g} \cdot \delta \mathbf{u} d\mathbf{x} \\ & - \frac{1}{2} \int_{\Omega_{n+1}^s} \mu^s D\mathbf{d}^n : D\delta \mathbf{u} d\mathbf{x} + \int_{\Omega_{n+1}^s} \mu^s \nabla^T \mathbf{d}^n \nabla \mathbf{d}^n : \nabla \delta \mathbf{u} d\mathbf{x}. \end{aligned} \quad (2.92)$$

According to relation (2.48), the integral related to the solid stress can also be computed in the reference domain $\Omega_{\mathbf{X}}^s$ as follows.

$$\int_{\Omega_t^s} \boldsymbol{\sigma}^s : \nabla \delta \mathbf{u} d\mathbf{x} = \int_{\Omega_{\mathbf{X}}^s} \mathbf{S}(\mathbf{E}) : \delta \dot{\mathbf{E}} d\mathbf{X},$$

where $\delta \dot{\mathbf{E}} = \frac{1}{2} [\mathbf{F}^T (\nabla_{\mathbf{X}} \delta \mathbf{u}) + (\nabla_{\mathbf{X}}^T \delta \mathbf{u}) \mathbf{F}]$. The reader may refer to [67, 110] for more details about that.

2.5 Methods using two meshes

The two-mesh methods generally use one Eulerian mesh to describe the whole domain $\Omega = \Omega_t^f \cup \Omega_t^s$ and a moving Lagrangian mesh to describe the solid in domain Ω_t^s as shown in Figure 2.1. The crucial advantage of the two-mesh methods is that they avoid the need to adjust the mesh in order to fit the fluid-structure interface. However, the disadvantage is also due to the unfitted interface, so that the material properties are smeared out across the interface. Therefore the fluid-structure interface is the main issue for two-mesh methods: one has to take care of this interface in order to maintain stability and accuracy.

For two-mesh methods, the fictitious or artificial fluid refers to the part of the fluid defined in the whole domain/mesh Ω but covered by the solid domain/mesh Ω_t^s . If we assume an incompressible fluid and fictitious fluid, i.e., we solve for $\nabla \cdot \mathbf{u} = 0$ in the whole domain Ω , then it is difficult to discuss a compressible solid, because one has to define a projection P from Ω to Ω_t^s and map a divergence-free velocity \mathbf{u} to \mathbf{u}^s , i.e.:

$$\mathbf{u}^s = P(\mathbf{u}), \quad \nabla \cdot \mathbf{u} = 0, \quad (2.93)$$

such that \mathbf{u}^s satisfies a specified Poisson effect/Poisson's ratio. We know that such a $P(\cdot)$ has

to be nonlinear, or $\nabla \cdot \mathbf{u}^s = 0$. Such a projection is not straightforward to define however. For simplicity, we shall assume an incompressible solid (the incompressible neo-Hookean solid model introduced in Section 2.3) when demonstrating the two-mesh methods in this section. In order to consider a compressible solid, one should only solve for $\nabla \cdot \mathbf{u} = 0$ in the fluid domain Ω_t^f . Section 6.5 will consider this issue in more depth.

2.5.1 Immersed finite element methods

The immersed finite element methods (IFEM) developed from the Immersed Boundary method first introduced by Peskin [107], and has had great success with applications in bioscience and biomedical fields [12, 14]. The classical IFEM does not solve solid equations at all. Instead, the solid equations are arranged on the right-hand side of the fluid equations as an FSI force \mathbf{f} , and these modified fluid equations are solved in the augmented/whole domain (fluid and fictitious fluid). Based upon this idea, the momentum equation of the fluid becomes

$$\rho^f \frac{d\mathbf{u}}{dt} = \nabla \cdot \boldsymbol{\sigma} + \rho^f \mathbf{g} + \mathbf{f}(\mathbf{u}), \quad (2.94)$$

where \mathbf{f} is a singular force that is evaluated from the solid. It can be seen from (2.94) that the idea of the IFEM is very simple, it actually solves a fluid equation but modified to achieve a FSI behaviour. It is only this singular force \mathbf{f} that makes the fictitious fluid behave like a solid. Obviously, the more similar the solid and fluid are (such as a very soft solid), the more suitable the method and the easier the simulation can be accomplished. There are some, specifically designed, IFEM methods that can be applied to a rigid body however they are special case [89, 158].

The IFEM methods solve the fluid equations (2.94) and (2.7) in the whole domain/mesh $\Omega = \Omega_t^f \cup \Omega_t^s$, however the FSI force can only be computed on the solid mesh on Ω_t^s , which may be denoted by \mathbf{f}^s . Therefore, one has to define a function that can properly distribute \mathbf{f}^s evaluated on the solid mesh to the \mathbf{f} which is applied on the background fluid mesh. The following functions are usually adopted to distribute \mathbf{f}^s to \mathbf{f} , and also interpolate the solution value of velocity \mathbf{u} on the background mesh to the solid mesh \mathbf{u}^s in order to accumulate the solid displacement \mathbf{d}^s and further compute \mathbf{f}^s .

1. Discretized δ function [96, 137, 156, 157]:

$$\delta^h(\mathbf{x}) = \frac{1}{h^d} \prod_i^d \phi(x_i), \quad \phi(r) = \begin{cases} \frac{1}{4} \left[1 + \cos \left(\frac{\pi|r|}{2h} \right) \right], & |r| \leq 2h \\ 0, & |r| > 2h \end{cases}, \quad (2.95)$$

with h being the mesh size (uniform mesh) and r being the distance between a solid node and the surrounding fluid node.

2. The shape function used in the Reproducing Kernel Particle Method (RKPM) [136–138, 156, 157] (a type of mesh-free method [95]).

3. The finite element isoparametric interpolation functions [137].

Note that \mathbf{f}^s can be evaluated in Ω_t^s by the following formula [136–138, 156, 157]:

$$\mathbf{f}^s = (\rho^f - \rho^s) \frac{\partial \mathbf{u}^s}{\partial t} + \nabla \cdot \boldsymbol{\sigma}^s - \nabla \cdot \boldsymbol{\sigma}^f + (\rho^s - \rho^f) \mathbf{g}. \quad (2.96)$$

Using the finite element method, \mathbf{f}^s could be computed by the following weak formulation for a given test function $\delta \mathbf{d}$:

$$\begin{aligned} \int_{\Omega_t^s} \mathbf{f}^s \cdot \delta \mathbf{d} d\mathbf{x} &= \int_{\Omega_t^s} (\rho^f - \rho^s) \frac{\partial \mathbf{u}^s}{\partial t} \cdot \delta \mathbf{d} d\mathbf{x} - \int_{\Omega_t^s} \boldsymbol{\sigma}^s : \nabla \delta \mathbf{d} d\mathbf{x} \\ &+ \int_{\Omega_t^s} \boldsymbol{\sigma}^f : \nabla \delta \mathbf{d} d\mathbf{x} + \int_{\Omega_t^s} (\rho^s - \rho^f) \mathbf{g} \cdot \delta \mathbf{d} d\mathbf{x}. \end{aligned} \quad (2.97)$$

The boundary integrals are cancelled out due the boundary condition (2.11). Assuming the solid is incompressible and has the same pressure as the fictitious fluid, and further assuming that $\nu^f \ll \mu^s$, i.e., the fluid deviatoric stress $\boldsymbol{\tau}^f$ can be neglected [157], then the above expression could be simplified as follows:

$$\int_{\Omega_t^s} \mathbf{f}^s \cdot \delta \mathbf{d} d\mathbf{x} = \int_{\Omega_t^s} (\rho^f - \rho^s) \frac{\partial \mathbf{u}^s}{\partial t} \cdot \delta \mathbf{d} d\mathbf{x} - \int_{\Omega_t^s} \boldsymbol{\tau}^s : \nabla \delta \mathbf{d} d\mathbf{x} + \int_{\Omega_t^s} (\rho^s - \rho^f) \mathbf{g} \cdot \delta \mathbf{d} d\mathbf{x}. \quad (2.98)$$

Finally, the solution algorithm for the classic IFEM method is summarized in Algorithm 2 as follows.

Algorithm 2: Immersed Finite Element Method

- 1 Given the solid configuration \mathbf{x}_n^s and the velocity \mathbf{u}_n on the background mesh at time t_n .
 - 2 Compute the FSI force \mathbf{f}_n^s on the solid mesh, using equation (2.98).
 - 3 Distribute \mathbf{f}_n^s to \mathbf{f}_n on the background mesh.
 - 4 Solve the fluid equations (2.94) and (2.7) on the background mesh to get velocity \mathbf{u}_{n+1} .
 - 5 Interpolate the velocity \mathbf{u}_{n+1} to \mathbf{u}_{n+1}^s on the solid mesh.
 - 6 Update the solid mesh and go back to step 1.
-

2.5.2 Modified immersed finite element methods

As can be seen in the previous section, the IFEM method does not solve the solid equation (2.1) or (2.38) at all, instead the solid equation is used to evaluate the FSI force as shown in formula (2.98). The Modified Immersed Finite Element Method (mIFEM) solves the solid equation (2.38) with the following boundary condition on the interface $\Gamma_t = \Gamma_{tD} \cup \Gamma_{tN}$, (Dirichlet boundary Γ_{tD} and Neumann boundary Γ_{tN}) [138]:

$$\mathbf{d}_{n+1}^s = \mathbf{d}_n^s + \Delta t P(\mathbf{u}_n) \quad \text{on } \Gamma_{tD} \quad (2.99)$$

and

$$\boldsymbol{\sigma}_{n+1}^s \mathbf{n}^s = P(\boldsymbol{\sigma}_n) \mathbf{n}^s \quad \text{on } \Gamma_{tN} \quad (2.100)$$

where $P(\cdot)$ is the projection/interpolation from the background mesh to the solid mesh, which could be any one of the three interpolation strategies as discussed in the previous section.

We are able to get the solution algorithm for the mIFEM as follows by modifying the algorithm of the IFEM method in Section 2.5.1.

Algorithm 3: Modified Immersed Finite Element Method

- 1 Given the solid configuration \mathbf{x}_n^s and the velocity \mathbf{u}_n on the background mesh at time t_n ; Compute the stress $\boldsymbol{\sigma}_n$ using (2.8), and further compute $P(\mathbf{u}_n)$ and $P(\boldsymbol{\sigma}_n)$.
 - 2 Solve the solid equation (2.38) with boundary conditions (2.99) and (2.100) to get solid displacement \mathbf{d}_{n+1}^s .
 - 3 Compute the FSI force \mathbf{f}_{n+1}^s on the solid mesh, using equation (2.98).
 - 4 Distribute \mathbf{f}_{n+1}^s to \mathbf{f}_{n+1} on the background mesh.
 - 5 Solve the fluid equations (2.94) and (2.7) on the background mesh to get velocity \mathbf{u}_{n+1} .
 - 6 Update the solid mesh using \mathbf{d}_{n+1}^s and go back to step 1.
-

The IFEM method depends heavily on the fluid equations and usually a small time step is required in order to get an accurate solution. The approximations within the method do not lead to fundamental errors when the solid behaves similarly to the fluid. However, when the solid behaviour is more dominant, the velocity from solving the fluid equation may lead to unrealistic solid deformation. The mIFEM method may present a more reasonable solid deformation by solving the solid equation explicitly, however the boundary conditions for the solid equation still arise from the value of the last time step which is the same as for the IFEM method.

2.5.3 Fictitious domain methods with distributed Lagrange multiplier

There are Fictitious Domain Methods with Distributed Lagrange Multiplier (FDM/DLM) for deformable solids [5, 16–18, 70, 79, 150, 151], and FDM/DLM for rigid solid bodies [58–60, 66, 70, 106, 146]. These methods may be implicitly fully-coupled, such as [17, 18, 70, 79], or split explicitly, such as [58, 60, 150]. Here we take the fully-coupled implicit scheme for a general deformable solid as an example to introduce these FDM/DLM methods [18, 70, 79].

As with the previous introduction of the Monolithic Eulerian method using an interface-fitted mesh in Section 2.4.3, the FDM/DLM we shall present is also fully-coupled. However, compared with the previous weak formulations (2.82) and (2.75), there are three major differences:

1. It is unnecessary to solve a mesh equation (2.75), because two meshes are used here: a static Eulerian mesh for the augmented domain Ω and an updated Lagrangian mesh for the solid domain Ω_t^s .

2. Because the solid displacement and the background velocity are now defined on different meshes (different finite element spaces), the velocity has to be interpolated to the solid mesh in order to apply the Lagrange multiplier. We could use any one of the interpolation (or distribution) functions introduced Section 2.5.1 for the IFEM methods. Let $P(\cdot)$ denote the interpolation from the background mesh Ω to the solid mesh Ω_t^s , and $P^T(\cdot)$ denote the distribution from the solid mesh Ω_t^s to the background mesh Ω .
3. Because we solve for solid displacement as well, there is also a consistency equation (2.70), however this is integrated in the entire domain Ω_t^s rather than on an interface as in the previous equation (2.74).

Let $\mathbf{u} = \begin{cases} \mathbf{u}^f & \text{in } \Omega_t^f \\ \mathbf{u}^s & \text{in } \Omega_t^s \end{cases}$ and $p = \begin{cases} p^f & \text{in } \Omega_t^f \\ p^s & \text{in } \Omega_t^s \end{cases}$, then the weak form corresponding to (2.82), but using the incompressible neo-Hookean model (2.29), can be expressed as

$$\begin{aligned} & \int_{\Omega_t^f} \rho^f \frac{d\mathbf{u}}{dt} \cdot \delta \mathbf{u} d\mathbf{x} + \int_{\Omega_t^s} \rho^s \frac{d\mathbf{u}}{dt} \cdot \delta \mathbf{u} d\mathbf{x} + \frac{1}{2} \int_{\Omega_t^f} \nu^f \mathbf{D}\mathbf{u} : \mathbf{D}\delta \mathbf{u} d\mathbf{x} \\ & - \int_{\Omega} p \nabla \cdot \delta \mathbf{u} d\mathbf{x} - \int_{\Omega} \delta p \nabla \cdot \mathbf{u} d\mathbf{x} + \int_{\Omega_t^s} \boldsymbol{\tau}^s : \delta \mathbf{u} d\mathbf{x} \\ & = \int_{\Gamma_N} \bar{\mathbf{h}} \cdot \delta \mathbf{u} d\Gamma + \int_{\Omega_t^f} \rho^f \mathbf{g} \cdot \delta \mathbf{u} d\mathbf{x} + \int_{\Omega_t^s} \rho^s \mathbf{g} \cdot \delta \mathbf{u} d\mathbf{x}. \end{aligned} \quad (2.101)$$

For simplicity, we assume that the solid has the same viscosity as the fluid, and readers may refer to [18] for a more general case. Then, rewriting the above equation to be only integrated in domain Ω and Ω_t^s gives

$$\begin{aligned} & \int_{\Omega} \rho^f \frac{d\mathbf{u}}{dt} \cdot \delta \mathbf{u} d\mathbf{x} + \int_{\Omega_t^s} \rho^s \frac{d\mathbf{u}}{dt} \cdot \delta \mathbf{u} d\mathbf{x} + \frac{1}{2} \int_{\Omega} \nu^f \mathbf{D}\mathbf{u} : \mathbf{D}\delta \mathbf{u} d\mathbf{x} \\ & - \int_{\Omega} p \nabla \cdot \delta \mathbf{u} d\mathbf{x} - \int_{\Omega} \delta p \nabla \cdot \mathbf{u} d\mathbf{x} + \int_{\Omega_t^s} \boldsymbol{\tau}^s : \nabla \delta \mathbf{u} d\mathbf{x} \\ & = \int_{\Gamma_N} \bar{\mathbf{h}} \cdot \delta \mathbf{u} d\Gamma + \int_{\Omega} \rho^f \mathbf{g} \cdot \delta \mathbf{u} d\mathbf{x} + \int_{\Omega_t^s} \rho^s \mathbf{g} \cdot \delta \mathbf{u} d\mathbf{x}, \end{aligned} \quad (2.102)$$

where $\rho^\delta = \rho^s - \rho^f$. Also consider the consistency equation (2.70), which may be enforced in variational form by introducing a Lagrange multiplier as follows:

$$\int_{\Omega_t^s} \left(\frac{\partial \mathbf{d}^s}{\partial t} - P(\mathbf{u}) \right) \cdot \delta \mathbf{L}(\mathbf{x}) d\mathbf{x} = 0. \quad (2.103)$$

Considering the Lagrange multiplier, we write down the following three equations based on

equation (2.102) :

$$\begin{aligned} & \int_{\Omega} \rho^f \frac{d\mathbf{u}}{dt} \cdot \delta \mathbf{u} d\mathbf{x} + \frac{1}{2} \int_{\Omega} \nu^f \mathbf{D}\mathbf{u} : \mathbf{D}\delta \mathbf{u} d\mathbf{x} - \int_{\Omega} p \nabla \cdot \delta \mathbf{u} d\mathbf{x} \\ & - \int_{\Omega} P^T(\mathbf{L}(\mathbf{x})) \cdot \delta \mathbf{u} d\mathbf{x} = \int_{\Gamma_N} \bar{\mathbf{h}} \cdot \delta \mathbf{u} d\Gamma + \int_{\Omega} \rho^f \mathbf{g} \cdot \delta \mathbf{u} d\mathbf{x}, \end{aligned} \quad (2.104)$$

$$- \int_{\Omega} \delta p \nabla \cdot \mathbf{u} d\mathbf{x} = 0, \quad (2.105)$$

and

$$\begin{aligned} & \int_{\Omega_t^s} \rho^\delta \frac{\partial \mathbf{u}^s}{\partial t} \cdot \delta \mathbf{u} d\mathbf{x} + \mu^s \int_{\Omega_t^s} J^{-1} (\mathbf{F}^T \mathbf{F} - \mathbf{I}) : \nabla \delta \mathbf{u} d\mathbf{x} \\ & + \int_{\Omega_t^s} \mathbf{L}(\mathbf{x}) \cdot \delta \mathbf{u} d\mathbf{x} = \int_{\Omega_t^s} \rho^\delta \mathbf{g} \cdot \delta \mathbf{u} d\mathbf{x}, \end{aligned} \quad (2.106)$$

due to the expression of τ^s of (2.30). Let $\delta \mathbf{d} = \delta \mathbf{u}(\mathbf{x}(\mathbf{X}, t))$, equation (2.106) may be expressed, by integral transformation, as:

$$\begin{aligned} & \int_{\Omega_{\mathbf{X}}^s} \rho^\delta \frac{\partial^2 \mathbf{d}^s}{\partial t^2} \cdot \delta \mathbf{d} d\mathbf{X} + \mu^s \int_{\Omega_{\mathbf{X}}^s} \mathbf{F} : \nabla_{\mathbf{X}} \delta \mathbf{d} d\mathbf{X} - \mu^s \int_{\Omega_t^s} J^{-1} \nabla \cdot \delta \mathbf{u} d\mathbf{x} \\ & + \int_{\Omega_{\mathbf{X}}^s} \mathbf{L}(\mathbf{x}(\mathbf{X}, t)) \cdot \delta \mathbf{d} d\mathbf{X} = \int_{\Omega_{\mathbf{X}}^s} \rho^\delta \mathbf{g} \cdot \delta \mathbf{d} d\mathbf{X}. \end{aligned} \quad (2.107)$$

Remark 2.6. In the continuous case the projection/interpolation P can actually be interpreted as an identity when restricted to domain Ω_t^s , i.e.: $\forall \mathbf{u} \in \Omega$, $P(\mathbf{u}) = \mathbf{u}|_{\Omega_t^s} = \mathbf{u}^s$. For the distribution P^T , $\forall \mathbf{L} \in \Omega_t^s$ (\mathbf{L} may be interpreted as a force vector defined in domain Ω_t^s), $P^T(\mathbf{L})|_{\Omega_t^s} = \mathbf{L}$ and $P^T(\mathbf{L})|_{\Omega_t^f} = \mathbf{0}$. Notice that adding up the three equations (2.104), (2.105) and (2.107) gives equation (2.102).

Using the same time discretization scheme, (2.76) to (2.78), as discussed in Section 2.4.2, we then have the following weak form based on equations (2.103) to (2.107).

$$\begin{aligned} & \int_{\Omega} \rho^f \frac{\mathbf{u} - \mathbf{u}_n}{\Delta t} \cdot \delta \mathbf{u} d\mathbf{x} + \int_{\Omega} \rho^f (\mathbf{u} \cdot \nabla) \mathbf{u} \cdot \delta \mathbf{u} d\mathbf{x} + \frac{1}{2} \int_{\Omega} \nu^f \mathbf{D}\mathbf{u} : \mathbf{D}\delta \mathbf{u} d\mathbf{x} \\ & - \int_{\Omega} p \nabla \cdot \delta \mathbf{u} d\mathbf{x} - \int_{\Omega} \delta p \nabla \cdot \mathbf{u} d\mathbf{x} + \int_{\Omega_{\mathbf{X}}^s} \rho^\delta \frac{\mathbf{d}^s - 2\mathbf{d}_n^s + \mathbf{d}_{n-1}^s}{\Delta t^2} \cdot \frac{\delta \mathbf{d}}{\Delta t} d\mathbf{X} \\ & + \mu^s \int_{\Omega_{\mathbf{X}}^s} \mathbf{F} : \nabla_{\mathbf{X}} \frac{\delta \mathbf{d}}{\Delta t} d\mathbf{X} + \int_{\Omega_{\mathbf{X}}^s} \mathbf{L}(\mathbf{x}(\mathbf{X}, t)) \cdot \frac{\delta \mathbf{d}}{\Delta t} d\mathbf{X} - \int_{\Omega_t^s} P^T(\mathbf{L}(\mathbf{x})) \cdot \delta \mathbf{u} d\mathbf{x} \\ & - \frac{\mu^s}{\Delta t} \int_{\Omega_t^s} J^{-1} \nabla \cdot \delta \mathbf{u} d\mathbf{x} + \int_{\Omega_{\mathbf{X}}^s} \frac{\mathbf{d}^s - \mathbf{d}_n^s}{\Delta t} \cdot \delta \mathbf{L}(\mathbf{x}(t)) d\mathbf{X} - \int_{\Omega_t^s} P(\mathbf{u}) \cdot \delta \mathbf{L}(\mathbf{x}) d\mathbf{x} \\ & = \int_{\Gamma_N} \bar{\mathbf{h}} \cdot \delta \mathbf{u} d\Gamma + \int_{\Omega} \rho^f \mathbf{g} \cdot \delta \mathbf{u} d\mathbf{x} + \int_{\Omega_{\mathbf{X}}^s} \rho^\delta \mathbf{g} \cdot \frac{\delta \mathbf{d}}{\Delta t} d\mathbf{X}. \end{aligned} \quad (2.108)$$

Notice that we also divide by Δt on both sides of equation (2.107) in order to be discretized as a symmetric linear system. We still need to treat the convection term in a special way so that the final linear system can be symmetric, for example, we can arrange the convection term on the right-hand side of the equation or use a suitable splitting scheme to treat the convection separately. In this case, the above equation (2.108) may lead to a similar large linear system as (2.81):

$$\begin{bmatrix} \mathbf{F}_{11} & \mathbf{F}_{12} & \mathbf{B}_1 & \mathbf{0} & \mathbf{0} \\ \mathbf{F}_{12}^T & \mathbf{F}_{22} & \mathbf{B}_2 & \mathbf{0} & \mathbf{P_I C}_1 \\ \mathbf{B}_1^T & \mathbf{B}_2^T & \mathbf{0} & \mathbf{0} & \mathbf{0} \\ \mathbf{0} & \mathbf{0} & \mathbf{0} & \mathbf{S} & \mathbf{C}_2 \\ \mathbf{0} & \mathbf{C}_1^T \mathbf{P}_I^T & \mathbf{0} & \mathbf{C}_2^T & \mathbf{0} \end{bmatrix} \begin{pmatrix} \mathbf{u}^f \\ \mathbf{u}^s \\ \mathbf{p} \\ \mathbf{d}^s \\ \mathbf{L} \end{pmatrix} = \begin{pmatrix} \mathbf{f}_1 \\ \mathbf{f}_2 \\ \mathbf{0} \\ \mathbf{g}^s \\ \mathbf{0} \end{pmatrix}. \quad (2.109)$$

In the above, $\begin{pmatrix} \mathbf{u}^f \\ \mathbf{u}^s \end{pmatrix} = \mathbf{u}$, where \mathbf{u}^f includes the velocity components in domain Ω_t^f , and \mathbf{u}^s are the remaining velocity components which may also have some components in domain Ω_t^f because the interface is not fitted. \mathbf{d}^s is the solid displacement in domain Ω_t^s . Matrices $\begin{bmatrix} \mathbf{F}_{11} & \mathbf{F}_{12} \\ \mathbf{F}_{12}^T & \mathbf{F}_{22} \end{bmatrix}$ and \mathbf{S} are the discretization of fluid velocity integrals and solid displacement integrals respectively (including mass matrices and stiffness matrices). Matrix $\begin{pmatrix} \mathbf{B}_1 \\ \mathbf{B}_2 \end{pmatrix}$ indicates the coupling between fluid velocity and pressure. Matrix $\mathbf{P}_I \mathbf{C}_1$ indicates the coupling between the fictitious fluid velocity \mathbf{u}^s and the Lagrange multiplier \mathbf{L} . Matrix \mathbf{C}_2 indicates the coupling between the solid displacement \mathbf{d}^s and the Lagrange multiplier \mathbf{L} . Notice that matrix \mathbf{P}_I is a discretization of the interpolation function $P(\cdot)$.

2.6 Methods using one mesh without interface fitting

A single Eulerian mesh without interface fitting is widely adopted to solve multi-phase flow problems [2, 19, 23, 31, 56, 119]. When using this pure Eulerian approach for the fluid-structure interaction problem, as shown in Figure 2.4, [90] uses the level set method to capture the fluid-structure interface, and a Lagrangian multiplier and penalty method to couple the fluid and solid. [43, 54, 116, 117, 142] use an Initial Points Set to capture the fluid-structure interface. After getting the position of the interface, [43, 116, 117, 142] use a characteristic function to smooth stress and velocity across the interface. Alternatively [54, 55] modify the local finite elements in order to capture jumps sharply, and [124, 134] use an XFEM-like method to enrich the shape functions locally in order to capture the discontinuity.

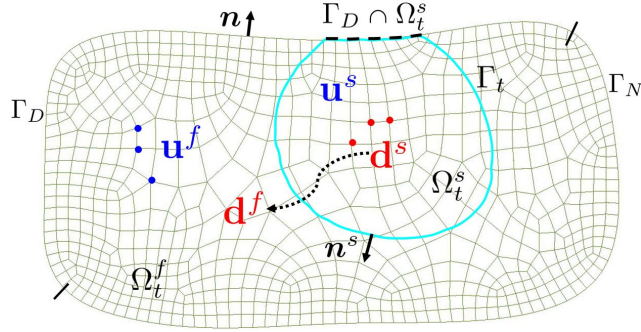


Figure 2.4: Schematic diagram for a mesh without interface fitting, $\Omega = \Omega_t^f \cup \Omega_t^s$, $\Gamma = \Gamma_D \cup \Gamma_N$.

2.6.1 A fully Eulerian formulation

In this section, by way of an example, we introduce the method in [43] which uses the following characteristic function to smooth the variables across the interface:

$$\chi^f(\mathbf{x}) = \begin{cases} 1, & \mathbf{x} - \mathbf{d} \in \Omega_0^f \setminus \Gamma_t \\ 0, & \mathbf{x} - \mathbf{d} \in \Omega_0^s \end{cases}, \quad \chi^s(\mathbf{x}) = 1 - \chi^f(\mathbf{x}), \quad (2.110)$$

where \mathbf{d} is defined in the whole domain $\Omega = \Omega_t^f \cup \Omega_t^s$, which is a smooth extension of the solid displacement \mathbf{d}^s in Ω_t^s as shown in Figure 2.4. $\frac{d\mathbf{d}^s}{dt} = \mathbf{u}^s$, but generally $\frac{d\mathbf{d}^f}{dt} \neq \mathbf{u}^f$. Let

$$\frac{d\mathbf{d}}{dt} = \frac{\partial \mathbf{d}}{\partial t} + (\mathbf{w} \cdot \nabla) \mathbf{d} = \mathbf{w}, \quad (2.111)$$

then the extension is defined by velocity \mathbf{w} as follows (harmonic continuation of the solid velocity) [43]:

$$\int_{\Omega} \chi^s (\mathbf{u}^s - \mathbf{w}) \cdot \delta \mathbf{w} d\mathbf{x} + \alpha_{\mathbf{u}} \int_{\Omega} \chi^f \nabla \mathbf{w} : \nabla \delta \mathbf{w} d\mathbf{x} = 0, \quad (2.112)$$

where $\alpha_{\mathbf{u}}$ is a small positive constant, and $\delta \mathbf{w}$ is a given test function. It can be seen that the above three equations are coupled with each other: χ is related to \mathbf{d} in (2.110), which depends on \mathbf{w} according to (2.111), which again depends on χ due to (2.112). These may be combined with the fluid and solid momentum equations, which are the same as (2.101) for the neo-Hookean solid model or (2.82) for the St Venant-Kirchhoff solid model. By introducing $\rho = \chi^f \rho^f + \chi^s \rho^s$ and $\boldsymbol{\sigma} = \chi^f \boldsymbol{\sigma}^f + \chi^s \boldsymbol{\sigma}^s$, we rewrite equation (2.101) and (2.82) as follows.

For the neo-Hookean solid model:

$$\int_{\Omega} \rho \frac{d\mathbf{u}}{dt} \cdot \delta \mathbf{u} d\mathbf{x} + \int_{\Omega} \boldsymbol{\sigma} : \delta \mathbf{u} d\mathbf{x} - \int_{\Omega} \delta p \nabla \cdot \mathbf{u} d\mathbf{x} = \int_{\Gamma_N} \bar{\mathbf{h}} \cdot \delta \mathbf{u} d\Gamma + \int_{\Omega} \rho \mathbf{g} \cdot \delta \mathbf{u} d\mathbf{x}, \quad (2.113)$$

and for the St Venant-Kirchhoff solid model:

$$\begin{aligned} & \int_{\Omega} \rho \frac{d\mathbf{u}}{dt} \cdot \delta \mathbf{u} d\mathbf{x} + \int_{\Omega} \boldsymbol{\sigma} : \delta \mathbf{u} d\mathbf{x} - \int_{\Omega} \chi^f \delta p \nabla \cdot \mathbf{u} d\mathbf{x} \\ & - \alpha_p \int_{\Omega} \chi^s \nabla p : \nabla \delta \mathbf{u} d\mathbf{x} = \int_{\Gamma_N} \bar{\mathbf{h}} \cdot \delta \mathbf{u} d\Gamma + \int_{\Omega} \rho \mathbf{g} \cdot \delta \mathbf{u} d\mathbf{x}, \end{aligned} \quad (2.114)$$

where α_p is a small positive constant. One could solve for a displacement \mathbf{d} , a velocity \mathbf{u} , an additional velocity \mathbf{w} and a pressure p in the whole domain Ω based on equations from (2.110) to (2.114).

Remark 2.7. $\alpha_{\mathbf{u}}$ in (2.112) controls the extension of the solid velocity from the solid domain Ω_t^s to the fluid domain Ω_t^f . In the compressible case, α_p in (2.114) controls the extension of the fluid pressure in the fluid domain Ω_t^f to the solid domain Ω_t^s . Usually choosing $\alpha_{\mathbf{u}} = \alpha_{\mathbf{u}}^0 h^2$ and $\alpha_p = \alpha_p^0 h$, where h is the local mesh size with $\alpha_{\mathbf{u}}^0 = \alpha_p^0 \sim 0.01$ [117].

This fully Eulerian formulation looks elegant, however it transfers the difficulty to a later stage. First, it has to solve enlarged velocity \mathbf{u} and displacement \mathbf{d} fields and an additional velocity field \mathbf{w} . Second, it has to solve a strongly nonlinear system even though both the fluid and solid model may be linear, which can be observed from equation (2.110) to (2.112). Third, there is one more convection equation (2.111) which may lead to an unsymmetric linear algebraic system. Readers may refer to [43] for more discussion and consideration of the discretization in time and space.

2.7 Summary

In this chapter, we first present the governing partial differential equations for the problem of fluid-structure interactions (FSI), and a compressible and an incompressible hyperelastic solid model. Based upon the governing equations and the two solid models, existing numerical methods for FSI problems are introduced in the framework of the finite element method. We focus on the finite element weak formulation, the linearization, and the solution algorithm, instead of giving details of finite element discretization and methods for solving the final linear algebraic system, since the latter are very standard finite element procedures and could be easily found in the literature. Important and relevant details are presented in the following chapters. We categorized the existing numerical methods into different types and found that there were many potential types although they have not all been observed in the literature by us so far. This includes the proposed approach which will be introduced in the following chapter.

Chapter 3

A one-field fictitious domain method for fluid-structure interactions

In this chapter, we first present the weak formulation for the proposed one-field fictitious domain method (one-field FDM) in Section 3.1, based on an incompressible neo-Hookean solid model introduced in Section 2.3. The time and space discretizations are presented in sections 3.2 and 3.3 respectively. Finally, the stability is analyzed by an energy estimate in Section 3.4.

In order to discuss stability of the proposed scheme in a general framework we modify the neo-Hookean solid model by adding a viscous stress as presented in [18]. Based upon this and expression (2.29), the constitutive equation of a viscous incompressible neo-Hookean solid model may be expressed in the form of a Kelvin-Voigt material:

$$\boldsymbol{\sigma}^s = \mu^s J^{-1} (\mathbf{FF}^T - \mathbf{I}) - p^s \mathbf{I} + \nu^s \mathbf{D}\mathbf{u}^s, \quad (3.1)$$

where ν^s is the solid viscosity.

3.1 The weak formulation of finite element method

In the following context, let $L^2(\omega)$ be the space of square integrable functions in domain ω , endowed with norm $\|u\|_{0,\omega}^2 = \int_\omega |u|^2$ ($u \in L^2(\omega)$). Let $H^1(\omega) = \{u : u, \nabla u \in L^2(\omega)\}$ with the norm denoted by $\|u\|_{1,\omega}^2 = \|u\|_{0,\omega}^2 + \|\nabla u\|_{0,\omega}^2$. We also denote by $H_0^1(\omega)$ the subspace of $H^1(\omega)$ whose functions have zero values on the boundary of ω , and denote by $L_0^2(\omega)$ the subspace of $L^2(\omega)$ whose functions have zero mean value.

Given $\mathbf{v} \in H_0^1(\Omega)^d$, we perform the following symbolic operations:

$$\int_{\Omega_t^f} \text{Eq.(2.1)} \cdot \mathbf{v} d\mathbf{x} + \int_{\Omega_t^s} \text{Eq.(2.1)} \cdot \mathbf{v} d\mathbf{x}.$$

Integrating the stress terms by parts, the above operation gives:

$$\begin{aligned} & \int_{\Omega_t^f} \rho^f \frac{d\mathbf{u}}{dt} \cdot \mathbf{v} d\mathbf{x} + \frac{1}{2} \int_{\Omega_t^f} \boldsymbol{\sigma}^f : \mathbf{D}\mathbf{v} d\mathbf{x} + \int_{\Gamma_t} \mathbf{n}^s \boldsymbol{\sigma}^f \cdot \mathbf{v} d\Gamma \\ & + \int_{\Omega_t^s} \rho^s \frac{d\mathbf{u}}{dt} \cdot \mathbf{v} d\mathbf{x} + \frac{1}{2} \int_{\Omega_t^s} \boldsymbol{\sigma}^s : \mathbf{D}\mathbf{v} d\mathbf{x} - \int_{\Gamma_t} \mathbf{n}^s \boldsymbol{\sigma}^s \cdot \mathbf{v} d\Gamma \\ & = \int_{\Omega_t^f} \rho^f \mathbf{g} \cdot \mathbf{v} d\mathbf{x} + \int_{\Omega_t^s} \rho^s \mathbf{g} \cdot \mathbf{v} d\mathbf{x} + \int_{\Gamma_N} \bar{\mathbf{h}} \cdot \mathbf{v} d\Gamma. \end{aligned} \quad (3.2)$$

Let $p = \begin{cases} p^f & \text{in } \Omega_t^f \\ p^s & \text{in } \Omega_t^s \end{cases}$. Using the fluid constitutive equation (2.8), solid constitutive equation (3.1) and boundary condition (2.11) we further have:

$$\begin{aligned} & \int_{\Omega} \rho^f \frac{d\mathbf{u}}{dt} \cdot \mathbf{v} d\mathbf{x} + \frac{1}{2} \int_{\Omega} \nu^f \mathbf{D}\mathbf{u} : \mathbf{D}\mathbf{v} d\mathbf{x} - \int_{\Omega} p \nabla \cdot \mathbf{v} d\mathbf{x} \\ & + \int_{\Omega_t^s} \rho^{\delta} \frac{d\mathbf{u}}{dt} \cdot \mathbf{v} d\mathbf{x} + \frac{1}{2} \int_{\Omega_t^s} \nu^{\delta} \mathbf{D}\mathbf{u} : \mathbf{D}\mathbf{v} d\mathbf{x} + \int_{\Omega_t^s} \mu^s J^{-1} (\mathbf{F}\mathbf{F}^T - \mathbf{I}) : \nabla \mathbf{v} d\mathbf{x} \\ & = \int_{\Omega} \rho^f \mathbf{g} \cdot \mathbf{v} d\mathbf{x} + \int_{\Omega_t^s} \rho^{\delta} \mathbf{g} \cdot \mathbf{v} d\mathbf{x} + \int_{\Gamma_N} \bar{\mathbf{h}} \cdot \mathbf{v} d\Gamma, \end{aligned} \quad (3.3)$$

where $\rho^{\delta} = \rho^s - \rho^f$ and $\nu^{\delta} = \nu^s - \nu^f$. Note that the integrals on the interface Γ_t are cancelled out using boundary condition (2.11). This is not surprising because they are internal forces for the whole FSI system considered here. Let us do the following two integral transforms:

$$\int_{\Omega_t^s} J^{-1} \mathbf{F}\mathbf{F}^T : \nabla \mathbf{v} d\mathbf{x} = \int_{\Omega_t^s} J^{-1} \mathbf{F} : (\nabla \mathbf{v} \mathbf{F}) d\mathbf{x} = \int_{\Omega_{\mathbf{x}}^s} \mathbf{F} : (\nabla_{\mathbf{x}} \mathbf{v}) d\mathbf{x}, \quad (3.4)$$

and

$$\int_{\Omega_t^s} \rho^{\delta} \mathbf{g} \cdot \mathbf{v} d\mathbf{x} = \int_{\Omega_t^s} J^{-1} \rho_0^{\delta} \mathbf{g} \cdot \mathbf{v} d\mathbf{x} = \int_{\Omega_{\mathbf{x}}^s} \rho_0^{\delta} \mathbf{g} \cdot \mathbf{v} d\mathbf{x}, \quad (3.5)$$

where $\rho_0^{\delta} = \rho_0^s - \rho_0^f$. Because we consider both an incompressible fluid and solid, and we use a constant density throughout the domain for all time $t \in [0, T]$, there is actually no need to distinguish ρ_0^s (or ρ_0^f) and ρ^s (or ρ^f). However for a numerical scheme which cannot guarantee incompressibility ($J = 1$) exactly, the integral of (3.5) in the reference domain may be accurate.

The above equations (3.3), (3.4) and (3.5), combined with the following symbolic operations for $q \in L^2(\Omega)$,

$$-\int_{\Omega_t^f} \text{Eq.(2.2)} q d\mathbf{x} - \int_{\Omega_t^s} \text{Eq.(2.2)} q d\mathbf{x},$$

leads to the weak form of the FSI system as follows.

Problem 3.1. Given \mathbf{u}_0 and Ω_0^s , for $t \in (0, T]$, find $\mathbf{u}(t) \in \{\mathbf{u}_D + H_0^1(\Omega)^d\}$, $p(t) \in L_0^2(\Omega)$ and Ω_t^s , such that $\forall \mathbf{v} \in H_0^1(\Omega)^d$, $\forall q \in L^2(\Omega)$, the following two equations hold:

$$\begin{aligned} & \int_{\Omega} \rho^f \frac{\partial \mathbf{u}}{\partial t} \cdot \mathbf{v} d\mathbf{x} + \int_{\Omega} \rho^f (\mathbf{u} \cdot \nabla) \mathbf{u} \cdot \mathbf{v} d\mathbf{x} + \frac{1}{2} \int_{\Omega} \nu^f \mathbf{D}\mathbf{u} : \mathbf{D}\mathbf{v} d\mathbf{x} - \int_{\Omega} p \nabla \cdot \mathbf{v} d\mathbf{x} \\ & + \int_{\Omega_t^s} \rho^\delta \frac{\partial \mathbf{u}}{\partial t} \cdot \mathbf{v} d\mathbf{X} + \frac{1}{2} \int_{\Omega_t^s} \nu^\delta \mathbf{D}\mathbf{u} : \mathbf{D}\mathbf{v} d\mathbf{X} + \int_{\Omega_t^s} \mu^s \mathbf{F} : \nabla_{\mathbf{X}} \mathbf{v} d\mathbf{X} \\ & = \int_{\Omega_t^s} \mu^s J^{-1} \nabla \cdot \mathbf{v} d\mathbf{x} + \int_{\Omega} \rho^f \mathbf{g} \cdot \mathbf{v} d\mathbf{x} + \int_{\Omega_t^s} \rho^\delta \mathbf{g} \cdot \mathbf{v} d\mathbf{X} + \int_{\Gamma_N} \bar{\mathbf{h}} \cdot \mathbf{v} d\Gamma, \end{aligned} \quad (3.6)$$

and

$$- \int_{\Omega} q \nabla \cdot \mathbf{u} d\mathbf{x} = 0. \quad (3.7)$$

In the above, $\{\mathbf{u}_D + H_0^1(\Omega)^d\}$ is the subspace of $H^1(\Omega)^d$ which satisfies the Dirichlet boundary condition (2.12).

Remark 3.1. Because domain Ω is stationary the Eulerian description will be used. However Ω_t^s is transient, being updated by its own velocity, so the updated Lagrangian description is used. Hence there is a convection term from the total derivative of time in Ω , but there is no convection term in Ω_t^s (or $\Omega_{\mathbf{X}}^s$).

Remark 3.2. In the literature of the IFEM method, the viscous term $-\frac{1}{2} \int_{\Omega_t^s} \nu^f \mathbf{D}\mathbf{u} : \mathbf{D}\mathbf{v}$ is neglected [18, 157], which is equivalent to $\nu^s = \nu^f$ or $\nu^\delta = 0$ in the formulation (3.6). This makes no big difference if $\nu^f \ll \mu^s$, but may be unreasonable when $\nu^f \sim \mu^s$. Here we consider the viscous term generally by introducing a viscosity ν^s in the solid (also see [18]). However we shall argue that the problem may not be well posed when $\nu^\delta < 0$, (see Remark 3.4 and numerical tests in Section 4.5).

3.2 Discretization in time

We may use the backward Euler method to discretize Problem 3.1, and update coordinates of the solid by $\mathbf{x}_{n+1} = \mathbf{x}_n + \Delta t \mathbf{u}_{n+1}$. As a result, \mathbf{F} is updated by $\mathbf{F}_{n+1} = \mathbf{F}_n + \Delta t \nabla_{\mathbf{X}} \mathbf{u}_{n+1}$, and so,

$$\int_{\Omega_{\mathbf{X}}^s} \mathbf{F}_{n+1} : \nabla_{\mathbf{X}} \mathbf{v} d\mathbf{X} = \int_{\Omega_{\mathbf{X}}^s} \mathbf{F}_n : \nabla_{\mathbf{X}} \mathbf{v} d\mathbf{X} + \Delta t \int_{\Omega_{\mathbf{X}}^s} \nabla_{\mathbf{X}} \mathbf{u}_{n+1} : \nabla_{\mathbf{X}} \mathbf{v} d\mathbf{X}. \quad (3.8)$$

Using equation (3.8), the discretized weak form corresponding to Problem 3.1 may be expressed as:

Problem 3.2. Given \mathbf{u}_n , p_n and Ω_n^s , find $\mathbf{u}_{n+1} \in \{\mathbf{u}_D + H_0^1(\Omega)^d\}$, $p_{n+1} \in L_0^2(\Omega)$ and Ω_{n+1}^s ,

such that $\forall \mathbf{v} \in H_0^1(\Omega)^d$, $\forall q \in L^2(\Omega)$, the following four relations hold:

$$\begin{aligned} & \int_{\Omega} \rho^f \frac{\mathbf{u}_{n+1} - \mathbf{u}_n}{\Delta t} \cdot \mathbf{v} d\mathbf{x} + \int_{\Omega} \rho^f (\mathbf{u}_{n+1} \cdot \nabla) \mathbf{u}_{n+1} \cdot \mathbf{v} d\mathbf{x} \\ & + \frac{1}{2} \int_{\Omega} \nu^f D\mathbf{u}_{n+1} : D\mathbf{v} d\mathbf{x} - \int_{\Omega} p_{n+1} \nabla \cdot \mathbf{v} d\mathbf{x} \\ & + \int_{\Omega_{\mathbf{x}}^s} \rho^{\delta} \frac{\mathbf{u}_{n+1} - \mathbf{u}_n}{\Delta t} \cdot \mathbf{v} d\mathbf{X} + \frac{1}{2} \int_{\Omega_{n+1}^s} \nu^{\delta} D\mathbf{u}_{n+1} : D\mathbf{v} d\mathbf{X} \\ & + \Delta t \int_{\Omega_{\mathbf{x}}^s} \mu^s \nabla_{\mathbf{x}} \mathbf{u}_{n+1} : \nabla_{\mathbf{x}} \mathbf{v} d\mathbf{X} = \int_{\Omega_{n+1}^s} \mu^s J_{n+1}^{-1} \nabla \cdot \mathbf{v} d\mathbf{x} \\ & - \int_{\Omega_{\mathbf{x}}^s} \mu^s \mathbf{F}_n \nabla_{\mathbf{x}} \mathbf{v} d\mathbf{X} + \int_{\Omega} \rho^f \mathbf{g} \cdot \mathbf{v} d\mathbf{x} + \int_{\Omega_{\mathbf{x}}^s} \rho^{\delta} \mathbf{g} \cdot \mathbf{v} d\mathbf{X} + \int_{\Gamma_N} \bar{\mathbf{h}} \cdot \mathbf{v} d\Gamma, \end{aligned} \quad (3.9)$$

$$- \int_{\Omega} q \nabla \cdot \mathbf{u}_{n+1} d\mathbf{x} = 0, \quad (3.10)$$

$$\Omega_{n+1}^s = \{\mathbf{x} : \mathbf{x} = \mathbf{x}_n + \Delta t \mathbf{u}_{n+1}, \mathbf{x}_n \in \Omega_n^s\}, \quad (3.11)$$

and

$$\mathbf{F}_{n+1} = \mathbf{F}_n + \Delta t \nabla_{\mathbf{x}} \mathbf{u}_{n+1}. \quad (3.12)$$

Remark 3.3. In Problem 3.2 the solid deformation tensor \mathbf{F} is updated. We can also update the solid stress $\boldsymbol{\sigma}^s$ as described in Appendix A (only for an explicit scheme). As noted by the author of [110], in which the solid displacement \mathbf{d}^s is updated: maybe updating an unsymmetric tensor (four components in 2D and nine components in 3D) \mathbf{F} is less accurate than updating a symmetric tensor $\boldsymbol{\sigma}^s$ (three components in 2D and six components in 3D) or the displacement \mathbf{d}^s (two components in 2D and three components in 3D). However this needs further investigation, and we add more discussion about these in Appendix F.

Remark 3.4. We can see that (3.9) contains a bilinear form $\Delta t \int_{\Omega_{\mathbf{x}}^s} \mu^s \nabla_{\mathbf{x}} \mathbf{u}_{n+1} : \nabla_{\mathbf{x}} \mathbf{v} d\mathbf{X}$ which is coercive. However the coercivity could be destroyed by adding term $\frac{1}{2} \int_{\Omega_{n+1}^s} \nu^{\delta} D\mathbf{u}_{n+1} : D\mathbf{v} d\mathbf{x}$ if $\nu^{\delta} < 0$ and $\Delta t \rightarrow 0$, in which case Problem 3.2 may not be well-posed. We can argue similarly for the inertia term related to ρ^{δ} . Although it is difficult to prove the well-posedness of Problem 3.2 (there is an initial attempt in Section 6.1 which relies on stronger assumptions than we would ideally wish), we shall numerically solve for these cases in Section 4.5.

3.3 Discretization in space

We shall use a fixed Eulerian mesh for Ω and an updated Lagrangian mesh for Ω_{n+1}^s to discretize Problem 3.2. First, we discretize Ω as Ω^h with the corresponding finite element spaces as

$$V^h(\Omega^h) = \text{span} \{\varphi_1, \dots, \varphi_{N^u}\} \subset H_0^1(\Omega)$$

and

$$L^h(\Omega^h) = \text{span} \{ \phi_1, \dots, \phi_{N^p} \} \subset L^2(\Omega).$$

Notice that the number of prescribed Dirichlet data points is not included in N^u . Suppose the discretized Dirichlet boundary Γ_D has N_D^u nodes, and let $\{\varphi_{N^u+1}, \dots, \varphi_{N^u+N_D^u}\}$ be the corresponding shape functions with these nodes, then the approximated solution \mathbf{u}^h can be expressed in terms of these basis functions as

$$\mathbf{u}^h(\mathbf{x}) = \sum_{i=1}^{N^u} \mathbf{u}(\mathbf{x}_i) \varphi_i(\mathbf{x}) + \sum_{i=N^u+1}^{N^u+N_D^u} \bar{\mathbf{u}}(\mathbf{x}_i) \varphi_i(\mathbf{x}), \quad (3.13)$$

with the corresponding space denoted by $\{\bar{\mathbf{u}}^h + V^h(\Omega^h)^d\}$. The approximated solution p^h can be expressed in terms of the basis functions as

$$p^h(\mathbf{x}) = \sum_{i=1}^{N^p} p(\mathbf{x}_i) \phi_i(\mathbf{x}). \quad (3.14)$$

We further discretize Ω_0^s as Ω_0^{sh} with the corresponding finite element spaces as:

$$V^{sh}(\Omega_0^{sh}) = \text{span} \{ \varphi_1^s, \dots, \varphi_{N^s}^s \} \subset H^1(\Omega_0^s),$$

and move the vertices of each element of Ω_n^{sh} by their own velocities to get Ω_{n+1}^{sh} . Notice that after moving the vertices, the basis functions of space $V^{sh}(\Omega_{n+1}^{sh})$ are different from $V^{sh}(\Omega_n^{sh})$. For notational simplicity, $\{\varphi_1^s, \dots, \varphi_{N^s}^s\}$ will be used to denote the basis functions for all $V^{sh}(\Omega_n^{sh})$ ($n = 0, 1, 2, \dots$). We then approximate $\mathbf{u}^h(\mathbf{x})|_{\mathbf{x} \in \Omega_{n+1}^{sh}}$ as:

$$\mathbf{u}^{sh}(\mathbf{x}) = \sum_{i=1}^{N^s} \mathbf{u}^h(\mathbf{x}_i^s) \varphi_i^s(\mathbf{x}) = \sum_{i=1}^{N^s} \sum_{j=1}^{N^u+N_D^u} \mathbf{u}(\mathbf{x}_j) \varphi_j(\mathbf{x}_i^s) \varphi_i^s(\mathbf{x}), \quad (3.15)$$

where \mathbf{x}_i^s is the nodal coordinate of the solid mesh. Notice that the above approximation defines a projection/interpolation P_{n+1} from $V^h(\Omega^h)^d$ to $V^{sh}(\Omega_{n+1}^{sh})^d$: $P_{n+1}(\mathbf{u}^h(\mathbf{x})) = \mathbf{u}^{sh}(\mathbf{x})$. We then discretize Problem 3.2 in space as follows.

Problem 3.3. Given \mathbf{u}_n^h , p_n^h and Ω_n^{sh} , find $\mathbf{u}_{n+1}^h \in \{\bar{\mathbf{u}}^h + V^h(\Omega^h)^d\}$, $p_{n+1}^h \in L^h(\Omega^h)$ and Ω_{n+1}^{sh} ,

such that $\forall \mathbf{v} \in V^h(\Omega^h)^d$, $\forall q \in L^h(\Omega^h)$, the following four relations hold:

$$\begin{aligned} & \int_{\Omega^h} \rho^f \frac{\mathbf{u}_{n+1}^h - \mathbf{u}_n^h}{\Delta t} \cdot \mathbf{v} d\mathbf{x} + \int_{\Omega^h} \rho^f (\mathbf{u}_{n+1}^h \cdot \nabla) \mathbf{u}_{n+1}^h \cdot \mathbf{v} d\mathbf{x} \\ & + \frac{1}{2} \int_{\Omega^h} \nu^f \mathbf{D}\mathbf{u}_{n+1}^h : \mathbf{D}\mathbf{v} d\mathbf{x} - \int_{\Omega^h} p_{n+1}^h \nabla \cdot \mathbf{v} d\mathbf{x} \\ & + \int_{\Omega_{\mathbf{X}}^{sh}} \rho^\delta \frac{\mathbf{u}_{n+1}^{sh} - \mathbf{u}_n^{sh}}{\Delta t} \cdot \mathbf{v}^s d\mathbf{X} + \frac{1}{2} \int_{\Omega_{\mathbf{X}}^{sh}} \nu^\delta \mathbf{D}\mathbf{u}_{n+1}^{sh} : \mathbf{D}\mathbf{v}^s d\mathbf{X} \\ & + \Delta t \int_{\Omega_{\mathbf{X}}^{sh}} \mu^s \nabla_{\mathbf{X}} \mathbf{u}_{n+1}^{sh} : \nabla_{\mathbf{X}} \mathbf{v}^s d\mathbf{X} = \int_{\Omega_{n+1}^{sh}} \mu^s J_{n+1}^{-1} \nabla \cdot \mathbf{v}^s d\mathbf{x} \\ & - \int_{\Omega_{\mathbf{X}}^{sh}} \mu^s \mathbf{F}_n^{sh} : \nabla_{\mathbf{X}} \mathbf{v}^s d\mathbf{X} + \int_{\Omega^h} \rho^f \mathbf{g} \cdot \mathbf{v} d\mathbf{x} + \int_{\Omega_{\mathbf{X}}^{sh}} \rho^\delta \mathbf{g} \cdot \mathbf{v}^s d\mathbf{X} + \int_{\Gamma_N^h} \bar{\mathbf{h}} \cdot \mathbf{v} d\Gamma, \end{aligned} \quad (3.16)$$

$$- \int_{\Omega} q \nabla \cdot \mathbf{u}_{n+1}^h d\mathbf{x} = 0, \quad (3.17)$$

$$\Omega_{n+1}^{sh} = \left\{ \mathbf{x} : \mathbf{x} = \mathbf{x}_n + \Delta t \mathbf{u}_{n+1}^{sh}, \mathbf{x}_n \in \Omega_n^{sh} \right\}, \quad (3.18)$$

and

$$\mathbf{F}_{n+1}^{sh} = \mathbf{F}_n^{sh} + \Delta t \nabla_{\mathbf{X}} \mathbf{u}_{n+1}^{sh}, \quad (3.19)$$

where $\mathbf{u}^{sh} = P_{n+1}(\mathbf{u}^h)$ and $\mathbf{v}^s = P_{n+1}(\mathbf{v})$.

Remark 3.5. According to equation (3.15), P_{n+1} is the finite element isoparametric interpolation. Readers may refer to Appendix C for more details of the computation of P_{n+1} .

3.4 Stability by energy estimate

In this section, we analyze the stability of the proposed scheme based on the following assumption.

Assumption 3.1. We consider an enclosed flow ($\mathbf{u} \cdot \mathbf{n} = 0$ on Γ), and assume that there is no external boundary force ($\bar{\mathbf{h}} = 0$) and body force ($\mathbf{g} = 0$). We assume that both the fluid and solid densities are constants, and the solid density is not less than the fluid density ($\rho^\delta \geq 0$). We also assume a constant viscosity ($\nu^\delta = 0$) throughout the domain Ω and a constant material parameter μ^s for the solid.

3.4.1 Energy conservation in the continuous case

In this subsection we shall prove that the weak forms (3.6) and (3.7), associated with Problem 3.1, preserve energy based upon Assumption 3.1.

Lemma 3.1. *The energy function $\Psi(\mathbf{F})$ (2.31) for the hyperelastic stress satisfies:*

$$\mu^s \int_0^t \int_{\Omega_{\mathbf{x}}^s} \mathbf{F} : \nabla_{\mathbf{x}} \mathbf{u} d\mathbf{X} - \mu^s \int_0^t \int_{\Omega_t^s} J^{-1} \nabla \cdot \mathbf{u} d\mathbf{x} = \int_{\Omega_{\mathbf{x}}^s} \Psi(\mathbf{F}) d\mathbf{X} - \int_{\Omega_{\mathbf{x}}^s} \Psi(\mathbf{F}_0) d\mathbf{X}, \quad (3.20)$$

where \mathbf{F}_0 is the initial solid deformation.

Proof. According to formula (2.27) (the compressible case), the derivative of the energy function $\Psi(\mathbf{F})$ (2.31) can be expressed as:

$$\frac{\partial \Psi(\mathbf{F})}{\partial \mathbf{F}} = \mu^s (\mathbf{F} - \mathbf{F}^{-T}), \quad (3.21)$$

which is the incompressible case, i.e. without term $\frac{\lambda^s}{2} \ln^2(J)$ in expression (2.25). We then have:

$$\begin{aligned} \frac{d}{dt} \int_{\Omega_{\mathbf{x}}^s} \Psi(\mathbf{F}) d\mathbf{X} &= \int_{\Omega_{\mathbf{x}}^s} \frac{\partial \Psi}{\partial \mathbf{F}} : \frac{d\mathbf{F}}{dt} d\mathbf{X} \\ &= \mu^s \int_{\Omega_{\mathbf{x}}^s} (\mathbf{F} - \mathbf{F}^{-T}) : \frac{d}{dt} (\mathbf{I} + \nabla_{\mathbf{x}} \mathbf{d}) d\mathbf{X} \\ &= \mu^s \int_{\Omega_{\mathbf{x}}^s} \mathbf{F} : \nabla_{\mathbf{x}} \mathbf{u} d\mathbf{X} - \mu^s \int_{\Omega_t^s} J^{-1} \nabla \cdot \mathbf{u} d\mathbf{x}, \end{aligned} \quad (3.22)$$

where \mathbf{d} is the displacement of the solid at time t . The following integral transform is used in the above proof:

$$\begin{aligned} \int_{\Omega_{\mathbf{x}}^s} \mathbf{F}^{-T} : \nabla_{\mathbf{x}} \mathbf{u} d\mathbf{X} &= \int_{\Omega_{\mathbf{x}}^s} \text{tr}(\nabla_{\mathbf{x}} \mathbf{u} \mathbf{F}^{-1}) d\mathbf{X} \\ &= \int_{\Omega_{\mathbf{x}}^s} \text{tr}(\nabla \mathbf{u}) d\mathbf{X} = \int_{\Omega_t^s} J^{-1} \nabla \cdot \mathbf{u} d\mathbf{x}. \end{aligned} \quad (3.23)$$

We get (3.20) by integrating (3.22) from 0 up to time t .

□

Lemma 3.2. *If (\mathbf{u}, p) is the solution pair of Problem 3.1, then*

$$\int_{\Omega} (\mathbf{u} \cdot \nabla) \mathbf{u} \cdot \mathbf{u} d\mathbf{x} = 0. \quad (3.24)$$

Proof. First,

$$\int_{\Omega} (\mathbf{u} \cdot \nabla) \mathbf{u} \cdot \mathbf{u} d\mathbf{x} = \int_{\Omega} \nabla(\mathbf{u} \otimes \mathbf{u}) \cdot \mathbf{u} d\mathbf{x} - \int_{\Omega} |\mathbf{u}|^2 \nabla \cdot \mathbf{u} d\mathbf{x}. \quad (3.25)$$

The following tensor form of the above equation (3.25) is straightforward to understand, which

can actually be used as a proof for (3.25):

$$\int_{\Omega} u_j \frac{\partial u_i}{\partial x_j} u_i d\mathbf{x} = \int_{\Omega} \frac{\partial (u_i u_j)}{\partial x_j} u_i d\mathbf{x} - \int_{\Omega} u_i u_i \frac{\partial u_j}{\partial x_j} d\mathbf{x}. \quad (3.26)$$

Note that i and j are automatically summed if they are repeated in one term. Integrating by parts, we have:

$$\int_{\Omega} \nabla(\mathbf{u} \otimes \mathbf{u}) \cdot \mathbf{u} d\mathbf{x} = \int_{\Gamma} |\mathbf{u}|^2 \mathbf{u} \cdot \mathbf{n} d\Gamma - \int_{\Omega} (\mathbf{u} \cdot \nabla) \mathbf{u} \cdot \mathbf{u} d\mathbf{x}, \quad (3.27)$$

which may also be explained by the following tensor form:

$$\int_{\Omega} \frac{\partial (u_i u_j)}{\partial x_j} u_i d\mathbf{x} = \int_{\Gamma} (u_i u_j) n_j u_i d\Gamma - \int_{\Omega} u_i u_j \frac{\partial u_i}{\partial x_j} d\mathbf{x}. \quad (3.28)$$

According to a Sobolev imbedding theorem [99, Theorem 6 in Chapter 5] and the inclusion between L^p spaces ($L^q \subset L^p$ if $p < q$), we know $H^1(\Omega) \subset L^4(\Omega)$ (for both 2D and 3D). Therefore $\mathbf{u} \in L^4(\Omega)$, i.e., $\int_{\Omega} |\mathbf{u}|^4 d\mathbf{x} < \infty$. That is to say $|\mathbf{u}|^2 \in L^2(\Omega)$. Then we have $\int_{\Omega} |\mathbf{u}|^2 \nabla \cdot \mathbf{u} = 0$ from (3.7). We also have $\int_{\Gamma} |\mathbf{u}|^2 \mathbf{u} \cdot \mathbf{n} = 0$ due to the Assumption (3.1) of an enclosed flow. Substituting these two equations into (3.25) and (3.27), we get

$$\int_{\Omega} (\mathbf{u} \cdot \nabla) \mathbf{u} \cdot \mathbf{u} d\mathbf{x} = - \int_{\Omega} (\mathbf{u} \cdot \nabla) \mathbf{u} \cdot \mathbf{u} d\mathbf{x}, \quad (3.29)$$

which gives equation (3.24). \square

Proposition 3.1 (Energy Conservation). Let (\mathbf{u}, p) be the solution pair of Problem 3.1, then

$$\begin{aligned} & \frac{\rho^f}{2} \int_{\Omega} |\mathbf{u}|^2 d\mathbf{x} + \frac{\nu^f}{2} \int_0^t \int_{\Omega} \mathbf{D}\mathbf{u} : \mathbf{D}\mathbf{u} d\mathbf{x} \\ & + \frac{\rho^\delta}{2} \int_{\Omega_{\mathbf{x}}^s} |\mathbf{u}|^2 d\mathbf{X} + \int_{\Omega_{\mathbf{x}}^s} \Psi(\mathbf{F}) d\mathbf{X} = \mathbf{0}. \end{aligned} \quad (3.30)$$

Proof. First let $\mathbf{v} = \mathbf{u}$ in (3.6) and use Assumption 3.1, we have:

$$\begin{aligned} & \rho^f \int_{\Omega} \frac{\partial \mathbf{u}}{\partial t} \cdot \mathbf{u} d\mathbf{x} + \rho^f \int_{\Omega} (\mathbf{u} \cdot \nabla) \mathbf{u} \cdot \mathbf{u} d\mathbf{x} + \frac{\nu^f}{2} \int_{\Omega} \mathbf{D}\mathbf{u} : \mathbf{D}\mathbf{u} d\mathbf{x} - \int_{\Omega} p \nabla \cdot \mathbf{u} d\mathbf{x} \\ & + \rho^\delta \int_{\Omega_{\mathbf{x}}^s} \frac{\partial \mathbf{u}}{\partial t} \cdot \mathbf{u} d\mathbf{X} + \mu^s \int_{\Omega_{\mathbf{x}}^s} \mathbf{F} : \nabla_{\mathbf{X}} \mathbf{u} d\mathbf{X} - \mu^s \int_{\Omega_t^s} J^{-1} \nabla \cdot \mathbf{u} d\mathbf{x} = 0, \end{aligned} \quad (3.31)$$

then let $q = p$ in (3.7), we have:

$$\int_{\Omega} p \nabla \cdot \mathbf{u} d\mathbf{x} = 0. \quad (3.32)$$

Notice that

$$\frac{d}{dt} |\mathbf{u}|^2 = 2 \frac{\partial \mathbf{u}}{\partial t} \cdot \mathbf{u}. \quad (3.33)$$

Finally substituting (3.32) into (3.31) and integrating from time 0 to t gives the energy conservation (3.30) due to Lemma 3.1 and 3.2. \square

3.4.2 Stability analysis after discretization in time

We next demonstrate a similar energy stability result for Problem 3.2.

Lemma 3.3. *The trace function $\frac{1}{2} \text{tr}(\mathbf{F}\mathbf{F}^T)$ satisfies:*

$$\frac{1}{2} \text{tr}(\mathbf{F}_{n+1}\mathbf{F}_{n+1}^T) - \frac{1}{2} \text{tr}(\mathbf{F}_n\mathbf{F}_n^T) = \Delta t \mathbf{F}_{n+1} : \nabla_{\mathbf{X}} \mathbf{u}_{n+1} - \frac{\Delta t^2}{2} |\nabla_{\mathbf{X}} \mathbf{u}_{n+1}|^2, \quad (3.34)$$

where $|\mathbf{A}|^2 = \sum_{ij} a_{ij}^2$ for a square matrix $\mathbf{A} = [a_{ij}]$.

Proof.

$$\begin{aligned} & \mathbf{F}_{n+1}\mathbf{F}_{n+1}^T - \mathbf{F}_n\mathbf{F}_n^T \\ &= \mathbf{F}_{n+1}\mathbf{F}_{n+1}^T - (\mathbf{F}_{n+1} - \Delta t \nabla_{\mathbf{X}} \mathbf{u}_{n+1})(\mathbf{F}_{n+1} - \Delta t \nabla_{\mathbf{X}} \mathbf{u}_{n+1})^T \\ &= \Delta t \mathbf{F}_{n+1} \nabla_{\mathbf{X}}^T \mathbf{u}_{n+1} + \Delta t \nabla_{\mathbf{X}} \mathbf{u}_{n+1} \mathbf{F}_{n+1}^T - \Delta t^2 \nabla_{\mathbf{X}} \mathbf{u}_{n+1} \nabla_{\mathbf{X}}^T \mathbf{u}_{n+1}. \end{aligned} \quad (3.35)$$

Notice that

$$\text{tr}(\mathbf{F}_{n+1} \nabla_{\mathbf{X}}^T \mathbf{u}_{n+1}) = \text{tr}(\nabla_{\mathbf{X}} \mathbf{u}_{n+1} \mathbf{F}_{n+1}^T) = \nabla_{\mathbf{X}} \mathbf{u}_{n+1} : \mathbf{F}_{n+1}, \quad (3.36)$$

because of $\text{tr}(\mathbf{A}) = \text{tr}(\mathbf{A}^T)$ and $\text{tr}(\mathbf{AB}^T) = \mathbf{A} : \mathbf{B}$ for arbitrary square matrices \mathbf{A} and \mathbf{B} . Therefore, Lemma 3.3 holds by taking the trace on both sides of equation (3.35). \square

Lemma 3.4. *The log-determinant function $\ln(\det \mathbf{F})$ satisfies:*

$$\ln(\det \mathbf{F}_{n+1}) - \ln(\det \mathbf{F}_n) \geq \Delta t \nabla \cdot \mathbf{u}_{n+1} - \frac{\Delta t^2}{2} |\mathbf{F}_{n+1}^{-1} \nabla_{\mathbf{X}} \mathbf{u}_{n+1}|^2. \quad (3.37)$$

Proof. We will use the fact that function $\ln(\det \mathbf{Y})$ is concave over the set of positive definite matrices [22, Chapter 3]. Let $\mathbf{B} = \mathbf{F}\mathbf{F}^T$, $\mathcal{F}(\mathbf{B}) = \frac{1}{2} \ln(\det \mathbf{B}) = \ln(\det \mathbf{F})$ and $w(\xi) = \mathcal{F}(\mathbf{B}_n + \xi(\mathbf{B}_{n+1} - \mathbf{B}_n))$. Noticing that \mathbf{B} is symmetric and $\frac{\partial(\det \mathbf{B})}{\partial \mathbf{B}} = (\det \mathbf{B}) \mathbf{B}^{-T}$ (see (2.26), a special case of Jacobi's formula [97]), then

$$w'(\xi) = \frac{d\mathcal{F}}{d\mathbf{B}} : (\mathbf{B}_{n+1} - \mathbf{B}_n) = \frac{1}{2} (\mathbf{B}_n + \xi(\mathbf{B}_{n+1} - \mathbf{B}_n))^{-1} : (\mathbf{B}_{n+1} - \mathbf{B}_n). \quad (3.38)$$

According to the property of concave functions, we have $w(1) - w(0) \geq w'(1)$, this is to say:

$$\begin{aligned}
& \ln(\det \mathbf{F}_{n+1}) - \ln(\det \mathbf{F}_n) = \mathcal{F}(\mathbf{B}_{n+1}) - \mathcal{F}(\mathbf{B}_n) \\
& \geq \frac{1}{2} \mathbf{B}_{n+1}^{-1} : (\mathbf{B}_{n+1} - \mathbf{B}_n) = \frac{1}{2} \operatorname{tr} (\mathbf{I} - \mathbf{B}_{n+1}^{-1} \mathbf{B}_n) \\
& = \frac{1}{2} \operatorname{tr} (\mathbf{I} - \mathbf{B}_{n+1}^{-1} (\mathbf{F}_{n+1} - \Delta t \nabla_{\mathbf{X}} \mathbf{u}_{n+1}) (\mathbf{F}_{n+1}^T - \Delta t \nabla_{\mathbf{X}}^T \mathbf{u}_{n+1})) \\
& = \frac{\Delta t}{2} \operatorname{tr} (\mathbf{F}_{n+1}^{-T} \nabla_{\mathbf{X}}^T \mathbf{u}_{n+1} + \mathbf{F}_{n+1}^{-T} \mathbf{F}_{n+1}^{-1} \nabla_{\mathbf{X}} \mathbf{u}_{n+1} \mathbf{F}_{n+1}^T) \\
& \quad - \frac{\Delta t^2}{2} \operatorname{tr} (\mathbf{F}_{n+1}^{-T} \mathbf{F}_{n+1}^{-1} \nabla_{\mathbf{X}} \mathbf{u}_{n+1} \nabla_{\mathbf{X}}^T \mathbf{u}_{n+1}) \\
& = \frac{\Delta t}{2} \operatorname{tr} (\nabla^T \mathbf{u}_{n+1}) + \frac{\Delta t}{2} \operatorname{tr} (\mathbf{F}_{n+1}^{-1} \nabla_{\mathbf{X}} \mathbf{u}_{n+1}) \\
& \quad - \frac{\Delta t^2}{2} \operatorname{tr} (\mathbf{F}_{n+1}^{-1} \nabla_{\mathbf{X}} \mathbf{u}_{n+1} (\mathbf{F}_{n+1}^{-1} \nabla_{\mathbf{X}} \mathbf{u}_{n+1})^T) \\
& = \frac{\Delta t}{2} \operatorname{tr} (\nabla^T \mathbf{u}_{n+1}) + \frac{\Delta t}{2} \operatorname{tr} (\nabla \mathbf{u}_{n+1}) - \frac{\Delta t^2}{2} |\mathbf{F}_{n+1}^{-1} \nabla_{\mathbf{X}} \mathbf{u}_{n+1}|^2 \\
& = \Delta t \nabla \cdot \mathbf{u}_{n+1} - \frac{\Delta t^2}{2} |\mathbf{F}_{n+1}^{-1} \nabla_{\mathbf{X}} \mathbf{u}_{n+1}|^2.
\end{aligned}$$

In the above, we use the trace property of cyclic permutations: $\operatorname{tr}(\mathbf{A}_1 \mathbf{A}_2 \mathbf{A}_3) = \operatorname{tr}(\mathbf{A}_2 \mathbf{A}_3 \mathbf{A}_1) = \operatorname{tr}(\mathbf{A}_3 \mathbf{A}_1 \mathbf{A}_2)$ (a special case: $\operatorname{tr}(\mathbf{A}_1 \mathbf{A}_2) = \operatorname{tr}(\mathbf{A}_2 \mathbf{A}_1)$). \square

From the above two lemmas, we have:

Proposition 3.2. The energy function $\Psi(\mathbf{F})$ (2.31) for the hyperelastic stress satisfies:

$$\begin{aligned}
& \int_{\Omega_{\mathbf{X}}^s} \Psi(\mathbf{F}_{n+1}) d\mathbf{X} - \int_{\Omega_{\mathbf{X}}^s} \Psi(\mathbf{F}_n) d\mathbf{X} \\
& \leq \Delta t \mu^s \int_{\Omega_{\mathbf{X}}^s} \mathbf{F}_{n+1} : \nabla_{\mathbf{X}} \mathbf{u}_{n+1} d\mathbf{X} - \Delta t \mu^s \int_{\Omega_{n+1}^s} J_{n+1}^{-1} \nabla \cdot \mathbf{u}_{n+1} d\mathbf{x} + R_{n+1},
\end{aligned} \tag{3.39}$$

where

$$R_{n+1} = \frac{\mu^s \Delta t^2}{2} \int_{\Omega_{\mathbf{X}}^s} \left(|\mathbf{F}_{n+1}^{-1} \nabla_{\mathbf{X}} \mathbf{u}_{n+1}|^2 - |\nabla_{\mathbf{X}} \mathbf{u}_{n+1}|^2 \right) d\mathbf{X}. \tag{3.40}$$

Proof. According to the definition of energy function $\Psi(\mathbf{F})$ (2.31):

$$\begin{aligned}
& \Psi(\mathbf{F}_{n+1}) d\mathbf{X} - \Psi(\mathbf{F}_n) d\mathbf{X} \\
& = \frac{\mu^s}{2} \operatorname{tr} (\mathbf{F}_{n+1} \mathbf{F}_{n+1}^T) - \frac{\mu^s}{2} \operatorname{tr} (\mathbf{F}_n \mathbf{F}_n^T) - \mu^s (\ln(\det \mathbf{F}_{n+1}) - \ln(\det \mathbf{F}_n)).
\end{aligned} \tag{3.41}$$

We get Proposition 3.2 due to Lemma 3.3 and Lemma 3.4. \square

Similarly to Lemma 3.2, we have:

Lemma 3.5. *If $(\mathbf{u}_{n+1}, p_{n+1})$ is the solution pair of Problem 3.2, then*

$$\int_{\Omega} (\mathbf{u}_{n+1} \cdot \nabla) \mathbf{u}_{n+1} \cdot \mathbf{u}_{n+1} d\mathbf{x} = 0. \quad (3.42)$$

Proof. The proof is the same as Lemma 3.2 by changing \mathbf{u} to \mathbf{u}_{n+1} in the proof of Lemma 3.2. \square

Proposition 3.3 (Energy Nonincreasing). Let $(\mathbf{u}_{n+1}, p_{n+1})$ be the solution pair of Problem 3.2, then

$$\begin{aligned} & \frac{\rho^f}{2} \int_{\Omega} |\mathbf{u}_{n+1}|^2 d\mathbf{x} + \frac{\rho^\delta}{2} \int_{\Omega_{\mathbf{X}}^s} |\mathbf{u}_{n+1}|^2 d\mathbf{X} + \int_{\Omega_{\mathbf{X}}^s} \Psi(\mathbf{F}_{n+1}) d\mathbf{X} \\ & + \frac{\Delta t \nu^f}{2} \sum_{k=1}^{n+1} \int_{\Omega} \mathbf{D}\mathbf{u}_k : \mathbf{D}\mathbf{u}_k d\mathbf{x} \\ & \leq \frac{\rho^f}{2} \int_{\Omega} |\mathbf{u}_n|^2 d\mathbf{x} + \frac{\rho^\delta}{2} \int_{\Omega_{\mathbf{X}}^s} |\mathbf{u}_n|^2 d\mathbf{X} + \int_{\Omega_{\mathbf{X}}^s} \Psi(\mathbf{F}_n) d\mathbf{X} \\ & + \frac{\Delta t \nu^f}{2} \sum_{k=1}^n \int_{\Omega} \mathbf{D}\mathbf{u}_k : \mathbf{D}\mathbf{u}_k d\mathbf{x} + R_{n+1}, \end{aligned} \quad (3.43)$$

where R_{n+1} is defined in equation (3.40).

Proof. Under the Assumption 3.1 ($\nu^\delta = 0$), let $\mathbf{v} = \mathbf{u}_{n+1}$ in (3.9):

$$\begin{aligned} & \rho^f \int_{\Omega} \frac{\mathbf{u}_{n+1} - \mathbf{u}_n}{\Delta t} \cdot \mathbf{u}_{n+1} d\mathbf{x} + \rho^f \int_{\Omega} (\mathbf{u}_{n+1} \cdot \nabla) \mathbf{u}_{n+1} \cdot \mathbf{u}_{n+1} d\mathbf{x} \\ & + \frac{\nu^f}{2} \int_{\Omega} \mathbf{D}\mathbf{u}_{n+1} : \mathbf{D}\mathbf{u}_{n+1} d\mathbf{x} - \int_{\Omega} p_{n+1} \nabla \cdot \mathbf{u}_{n+1} d\mathbf{x} \\ & + \rho^\delta \int_{\Omega_{\mathbf{X}}^s} \frac{\mathbf{u}_{n+1} - \mathbf{u}_n}{\Delta t} \cdot \mathbf{u}_{n+1} d\mathbf{X} + \Delta t \mu^s \int_{\Omega_{\mathbf{X}}^s} \nabla_{\mathbf{X}} \mathbf{u}_{n+1} : \nabla_{\mathbf{X}} \mathbf{u}_{n+1} d\mathbf{X} \\ & = \mu^s \int_{\Omega_{n+1}^s} J_{n+1}^{-1} \nabla \cdot \mathbf{u}_{n+1} d\mathbf{x} - \mu^s \int_{\Omega_{\mathbf{X}}^s} \mathbf{F}_n \nabla_{\mathbf{X}} \mathbf{u}_{n+1} d\mathbf{X}. \end{aligned} \quad (3.44)$$

Let $q = p_{n+1}$ in (3.10):

$$\int_{\Omega} p_{n+1} \nabla \cdot \mathbf{u}_{n+1} d\mathbf{x} = 0. \quad (3.45)$$

Substituting (3.42) and (3.45) into equation (3.44) and multiplying by Δt on both sides of the

equation, we then, using equation (3.8), have:

$$\begin{aligned} & \rho^f \int_{\Omega} (\mathbf{u}_{n+1} - \mathbf{u}_n) \cdot \mathbf{u}_{n+1} d\mathbf{x} + \frac{\Delta t \nu^f}{2} \int_{\Omega} \mathbf{D}\mathbf{u}_{n+1} : \mathbf{D}\mathbf{u}_{n+1} d\mathbf{x} \\ & + \rho^\delta \int_{\Omega_{\mathbf{X}}^s} (\mathbf{u}_{n+1} - \mathbf{u}_n) \cdot \mathbf{u}_{n+1} d\mathbf{X} \\ & + \mu^s \Delta t \int_{\Omega_{\mathbf{X}}^s} \mathbf{F}_{n+1} : \nabla_{\mathbf{X}} \mathbf{u}_{n+1} d\mathbf{X} - \mu^s \Delta t \int_{\Omega_{n+1}^s} J_{n+1}^{-1} \nabla \cdot \mathbf{u}_{n+1} d\mathbf{x} = 0. \end{aligned} \quad (3.46)$$

Using the Cauchy-Schwarz inequality and the fact $ab \leq \frac{a^2+b^2}{2}$, we have:

$$\int_{\omega} \mathbf{u}_n \cdot \mathbf{u}_{n+1} d\mathbf{x} \leq \|\mathbf{u}_n\|_{0,\omega} \|\mathbf{u}_{n+1}\|_{0,\omega} \leq \frac{\|\mathbf{u}_n\|_{0,\omega}^2 + \|\mathbf{u}_{n+1}\|_{0,\omega}^2}{2}, \quad (3.47)$$

where $\omega = \Omega$ or Ω_{n+1}^s . Substituting the above relation into (3.46), we get (3.43) due to Proposition 3.2. \square

Remark 3.6. Notice that the above estimate (3.47) cannot be applied to the proof without the assumption that $\rho^\delta \geq 0$ in Assumption 3.1.

Remark 3.7. Relation (3.43) does not exactly show energy nonincreasing, because we do not know whether R_{n+1} is greater or less than 0. However, R_{n+1} is $O(\Delta t^2)$ if

$$\int_{\Omega_{\mathbf{X}}^s} \left(|\mathbf{F}_{n+1}^{-1} \nabla_{\mathbf{X}} \mathbf{u}_{n+1}|^2 - |\nabla_{\mathbf{X}} \mathbf{u}_{n+1}|^2 \right) d\mathbf{X} < \infty, \quad (3.48)$$

which may need more assumption such as Assumption 6.3. We shall demonstrate $R_{n+1} = O(\Delta t^2)$ in Section 4.4 by numerical tests. In order to test the energy property, let us use the following notation for the different contributions to the total energy in (3.43).

(1) Kinetic energy of fluid plus fictitious fluid:

$$E_k(\Omega) = \frac{\rho^f}{2} \int_{\Omega} |\mathbf{u}_n|^2 d\mathbf{x}. \quad (3.49)$$

(2) Kinetic energy of solid minus fictitious fluid:

$$E_k(\Omega_{\mathbf{X}}^s) = \frac{\rho^\delta}{2} \int_{\Omega_{\mathbf{X}}^s} |\mathbf{u}_n|^2 d\mathbf{X}. \quad (3.50)$$

(3) Viscous dissipation:

$$E_d(\Omega) = \frac{\Delta t \nu^f}{2} \sum_{k=1}^n \int_{\Omega} \mathbf{D}\mathbf{u}_k : \mathbf{D}\mathbf{u}_k d\mathbf{x}. \quad (3.51)$$

(4) Potential energy of the solid:

$$E_p(\Omega_{\mathbf{X}}^s) = \int_{\Omega_{\mathbf{X}}^s} \Psi(\mathbf{F}_n) d\mathbf{X}. \quad (3.52)$$

Denote the total energy as:

$$E_{total}(t_n) = E_k(\Omega) + E_k(\Omega_{\mathbf{X}}^s) + E_d(\Omega) + E_p(\Omega_{\mathbf{X}}^s), \quad (3.53)$$

and the energy ratio as:

$$E_{ratio} = \frac{E_{total}(t_n)}{E_{total}(t_0)}. \quad (3.54)$$

We shall numerically demonstrate that E_{ratio} is nonincreasing in Section 4.4.

3.4.3 Stability analysis after discretization in space

As with the previous stability estimate (Proposition 3.3) after time discretization, we have the following estimate after space discretization.

Proposition 3.4. Let $(\mathbf{u}_{n+1}^h, p_{n+1}^h)$ be the solution pair of Problem 3.3, then

$$\begin{aligned} & \frac{\rho^f}{2} \int_{\Omega^h} |\mathbf{u}_{n+1}^h|^2 d\mathbf{x} + \frac{\rho^\delta}{2} \int_{\Omega_{\mathbf{X}}^{sh}} |\mathbf{u}_{n+1}^{sh}|^2 d\mathbf{X} + \int_{\Omega_{\mathbf{X}}^{sh}} \Psi(\mathbf{F}_{n+1}^{sh}) d\mathbf{X} \\ & + \frac{\Delta t \nu^f}{2} \sum_{k=1}^{n+1} \int_{\Omega^h} \mathbf{D}\mathbf{u}_k^h : \mathbf{D}\mathbf{u}_k^h d\mathbf{x} \\ & \leq \frac{\rho^f}{2} \int_{\Omega^h} |\mathbf{u}_n^h|^2 d\mathbf{x} + \frac{\rho^\delta}{2} \int_{\Omega_{\mathbf{X}}^{sh}} |\mathbf{u}_n^h|^2 d\mathbf{X} + \int_{\Omega_{\mathbf{X}}^{sh}} \Psi(\mathbf{F}_n^{sh}) d\mathbf{X} \\ & + \frac{\Delta t \nu^f}{2} \sum_{k=1}^n \int_{\Omega^h} \mathbf{D}\mathbf{u}_k^h : \mathbf{D}\mathbf{u}_k^h d\mathbf{x} + R_{n+1}^h, \end{aligned} \quad (3.55)$$

where

$$R_{n+1}^h = \frac{\mu^s \Delta t^2}{2} \int_{\Omega_{\mathbf{X}}^{sh}} \left(\left| (\mathbf{F}_{n+1}^{sh})^{-1} \nabla_{\mathbf{X}} \mathbf{u}_{n+1}^{sh} \right|^2 - \left| \nabla_{\mathbf{X}} \mathbf{u}_{n+1}^{sh} \right|^2 \right) d\mathbf{X}. \quad (3.56)$$

Proof. Let $\mathbf{v} = \mathbf{u}_{n+1}^h$ in (3.16) and multiply by Δt on both sides of the equation, and then let $q = p_{n+1}^h$ in (3.17) and substitute into equation (3.16), we get:

$$\begin{aligned} & \rho^f \int_{\Omega^h} (\mathbf{u}_{n+1}^h - \mathbf{u}_n^h) \cdot \mathbf{u}_{n+1}^h d\mathbf{x} + \frac{\Delta t \nu^f}{2} \int_{\Omega^h} \mathbf{D}\mathbf{u}_{n+1}^h : \mathbf{D}\mathbf{u}_{n+1}^h d\mathbf{x} \\ & + \rho^\delta \int_{\Omega_{\mathbf{X}}^{sh}} (\mathbf{u}_{n+1}^{sh} - \mathbf{u}_n^{sh}) \cdot \mathbf{u}_{n+1}^{sh} d\mathbf{X} \\ & + \mu^s \Delta t \int_{\Omega_{\mathbf{X}}^{sh}} \mathbf{F}_{n+1}^{sh} : \nabla_{\mathbf{X}} \mathbf{u}_{n+1}^{sh} d\mathbf{X} - \mu^s \Delta t \int_{\Omega_{n+1}^{sh}} \nabla \cdot \mathbf{u}_{n+1}^{sh} d\mathbf{x} = 0. \end{aligned} \quad (3.57)$$

Using the Cauchy-Schwarz inequality and the fact $ab \leq \frac{a^2+b^2}{2}$, we have:

$$\int_{\omega} \mathbf{u}_n \cdot \mathbf{u}_{n+1} d\mathbf{x} \leq \|\mathbf{u}_n\|_{0,\omega} \|\mathbf{u}_{n+1}\|_{0,\omega} \leq \frac{\|\mathbf{u}_n\|_{0,\omega}^2 + \|\mathbf{u}_{n+1}\|_{0,\omega}^2}{2},$$

where $\omega = \Omega^h$ or Ω_{n+1}^{sh} . Notice that Lemmas 3.3 to 3.5 still hold after space discretization, then substituting the above relation into (3.57) gives (3.55). \square

3.5 Summary

Details of the one-field fictitious domain method, from the continuous formulation to discretization in time and space, are presented in this chapter. The energy stability is proved based upon Assumption 3.1. Let us discuss these specific assumptions in Assumption 3.1 again as follows.

1. If the flow is not enclosed, i.e. $(\mathbf{u} \cdot \mathbf{n} \neq 0)$, then it can be seen from the proof of Lemma 3.2 that equation (3.24) becomes:

$$\int_{\Omega} (\mathbf{u} \cdot \nabla) \mathbf{u} \cdot \mathbf{u} d\mathbf{x} = \frac{1}{2} \int_{\Gamma} |\mathbf{u}|^2 \mathbf{u} \cdot \mathbf{n} d\Gamma. \quad (3.58)$$

The above term will appear in the energy estimate relation (3.30) or (3.43).

2. The assumptions of $\bar{\mathbf{h}} = 0$ and $\mathbf{g} = 0$ are not essential, but are a convenience for the proof (see a general estimate (3.59) below).
3. The assumption $\nu^\delta = 0$ is because of the argument about coercivity in Remark 3.4.
4. The assumption $\rho^\delta \geq 0$ is necessary due to the use of the Cauchy-Schwarz inequality in the proof of Proposition 3.3 (see Remark 3.6).

In short, the first two assumptions are not necessary, while the last two are important. For a general case ($\mathbf{u} \cdot \mathbf{n} \neq 0$, $\bar{\mathbf{h}} \neq 0$ and $\mathbf{g} \neq 0$), the energy estimate (3.43) becomes (the energy estimates (3.30) and (3.55) follow similar principles although it is not necessary to state them here again):

$$\begin{aligned} & \frac{\rho^f}{2} \int_{\Omega} |\mathbf{u}_{n+1}|^2 d\mathbf{x} + \frac{\rho^\delta}{2} \int_{\Omega_{\mathbf{x}}^s} |\mathbf{u}_{n+1}|^2 d\mathbf{X} + \int_{\Omega_{\mathbf{x}}^s} \Psi(\mathbf{F}_{n+1}) d\mathbf{X} \\ & + \frac{\Delta t \nu^f}{2} \sum_{k=1}^{n+1} \int_{\Omega} \mathbf{D}\mathbf{u}_k : \mathbf{D}\mathbf{u}_k d\mathbf{x} + \Delta t \sum_{k=1}^{n+1} E_k^{external} \\ & \leq \frac{\rho^f}{2} \int_{\Omega} |\mathbf{u}_n|^2 d\mathbf{x} + \frac{\rho^\delta}{2} \int_{\Omega_{\mathbf{x}}^s} |\mathbf{u}_n|^2 d\mathbf{X} + \int_{\Omega_{\mathbf{x}}^s} \Psi(\mathbf{F}_n) d\mathbf{X} \\ & + \frac{\Delta t \nu^f}{2} \sum_{k=1}^n \int_{\Omega} \mathbf{D}\mathbf{u}_k : \mathbf{D}\mathbf{u}_k d\mathbf{x} + \Delta t \sum_{k=1}^n E_k^{external} + R_{n+1}, \end{aligned} \quad (3.59)$$

where

$$E_k^{external} = \frac{1}{2} \int_{\Gamma} |\mathbf{u}_k|^2 \mathbf{u}_k \cdot \mathbf{n} d\Gamma - \int_{\Omega} \rho^f \mathbf{g} \cdot \mathbf{u}_k d\mathbf{x} - \int_{\Omega_{\mathbf{x}}^s} \rho^\delta \mathbf{g} \cdot \mathbf{u}_k d\mathbf{x} - \int_{\Gamma_N} \bar{\mathbf{h}} \cdot \mathbf{u}_k d\Gamma \quad (3.60)$$

is the input/output energy.

Problem 3.3 requires iterations in order to construct the current domain Ω_{n+1}^{sh} and build the interpolation function P_{n+1} . If the iterations can be proved to converge, then the solution existence for Problem 3.3 is proved (an alternative approach is to prove Problem 3.3 is well posed by comparing it with the standard Stokes equation. Refer to Section 6.1 for more discussion). At the moment we have only proved the energy convergence as demonstrated above, the solution existence may be proved based on this energy convergence in the future.

Chapter 4

An implicit implementation

Some implementation details of the proposed scheme are presented in this chapter. The treatment of convection is presented in Section 4.1, and a simple preconditioned iterative solver is described in Section 4.2. The overall algorithm is summarized in Section 4.3 and numerical tests are presented in Section 4.4 and 4.5.

All the simulation codes used in this thesis were constructed with the aid of the software package pFEPG (parallel Finite Element Programme Generator) [94]. Please refer to website “<http://www.yuanjisuan.cn>” for more information.

4.1 Treatment of convection

There are four non-linear elements in equation (3.16): the convection, the changing domain Ω_{n+1}^{sh} , the interpolation P_{n+1} and the term J_{n+1}^{-1} . All these non-linear elements are considered in one fixed point iteration. For low Reynolds number flow, as considered in this chapter, we arrange the convection term on the right-hand side of the equation and use the fixed point iteration to solve the non-linear system at each time step. For other methods to treat convection, readers may refer to [108, 163]. Notice that no artificial diffusion terms are added in this case, and we can measure the system energy exactly using the energy functions defined in Remark 3.7.

4.2 Iterative linear algebra solver

Using the linearization described in Section 4.1, Problem 3.3 leads to the following linear equation system (for details of assembling this global matrix and the right-hand side vector, please refer to Appendix B):

$$\begin{bmatrix} \mathbf{A} & \mathbf{B} \\ \mathbf{B}^T & \mathbf{0} \end{bmatrix} \begin{pmatrix} \mathbf{u} \\ \mathbf{p} \end{pmatrix} = \begin{pmatrix} \mathbf{b} \\ \mathbf{0} \end{pmatrix}, \quad (4.1)$$

where

$$\mathbf{A} = \mathbf{M}/\Delta t + \mathbf{K} + \mathbf{D}^T (\mathbf{M}^s/\Delta t + \mathbf{K}^s) \mathbf{D}, \quad (4.2)$$

and

$$\mathbf{b} = \mathbf{f} + \mathbf{D}^T \mathbf{f}^s + \mathbf{M} \mathbf{u}_n/\Delta t + \mathbf{D}^T \mathbf{M}^s \mathbf{D} \mathbf{u}_n/\Delta t. \quad (4.3)$$

In the above, matrix \mathbf{D} is the isoparametric interpolation matrix derived from equation (3.15) which can be expressed as

$$\mathbf{D} = \text{diag} \left(\underbrace{\mathbf{P}^T, \dots, \mathbf{P}^T}_d \right), \quad \mathbf{P}_{ij} = \varphi_i(\mathbf{x}_j^s). \quad (4.4)$$

Please refer to Appendix C for details of computing \mathbf{D} . All the other matrices and vectors arise from standard FEM discretization of equation (3.16): \mathbf{M} and \mathbf{M}^s are mass matrices from discretization of the terms

$$\int_{\Omega^h} \rho^f \mathbf{u}_{n+1}^h \cdot \mathbf{v} d\mathbf{x} \quad \text{and} \quad \int_{\Omega_{\mathbf{X}}^{sh}} \rho^\delta \mathbf{u}_{n+1}^{sh} \cdot \mathbf{v}^s d\mathbf{X}$$

respectively, and similarly the stiffness matrices \mathbf{K} and \mathbf{K}^s are from the terms

$$\frac{1}{2} \int_{\Omega^h} \nu^f \mathbf{D} \mathbf{u}_{n+1}^h : \mathbf{D} \mathbf{v} d\mathbf{x} \quad \text{and} \quad \frac{1}{2} \int_{\tilde{\Omega}_{n+1}^{sh}} \nu^\delta \mathbf{D} \mathbf{u}_{n+1}^h : \mathbf{D} \mathbf{v} d\mathbf{x} + \Delta t \int_{\Omega_{\mathbf{X}}^{sh}} \mu^s \nabla_{\mathbf{X}} \mathbf{u}_{n+1}^{sh} : \nabla_{\mathbf{X}} \mathbf{v}^s d\mathbf{X}$$

respectively. \mathbf{B} is from discretization of

$$-\int_{\Omega} q \nabla \cdot \mathbf{u}_{n+1}^h d\mathbf{x}.$$

The force vectors \mathbf{f} and \mathbf{f}^s come from discretization of right-hand sides

$$\int_{\Omega^h} \rho^f \mathbf{g} \cdot \mathbf{v} d\mathbf{x} + \int_{\Gamma_N^h} \bar{\mathbf{h}} \cdot \mathbf{v} d\Gamma - \int_{\Omega^h} \rho^f (\tilde{\mathbf{u}}_{n+1}^h \cdot \nabla) \tilde{\mathbf{u}}_{n+1}^h \cdot \mathbf{v} d\mathbf{x}$$

and

$$\int_{\Omega_{\mathbf{X}}^{sh}} \rho^\delta \mathbf{g} \cdot \mathbf{v}^s d\mathbf{X} + \int_{\tilde{\Omega}_{n+1}^{sh}} \mu^s \tilde{J}_{n+1}^{-1} \nabla \cdot \mathbf{v}^s d\mathbf{x} - \int_{\Omega_{\mathbf{X}}^{sh}} \mu^s \mathbf{F}_n^{sh} : \nabla_{\mathbf{X}} \mathbf{v}^s d\mathbf{X}$$

respectively. In the above, $\tilde{\mathbf{u}}_{n+1}^h$, \tilde{J}_{n+1}^{-1} and $\tilde{\Omega}_{n+1}^{sh}$ are approximations to \mathbf{u}_{n+1}^h , J_{n+1}^{-1} and Ω_{n+1}^{sh} from the previous fixed point iteration. To solve system (4.1) we use the preconditioned MinRes algorithm [46]. The block matrix $\begin{bmatrix} \mathbf{M}/\Delta t + \mathbf{K} & \mathbf{0} \\ \mathbf{0}^T & \mathbf{M}_p/\Delta t \end{bmatrix}$ is adopted as a preconditioner (\mathbf{M}_p is the pressure mass matrix), approximated by an incomplete Cholesky decomposition with no fill-in. A stable convergence performance can be observed, although this is not the topic of this thesis.

Remark 4.1. When implementing the one-field FDM algorithm, it is unnecessary to perform the matrix multiplication $\mathbf{D}^T \mathbf{K}^s \mathbf{D}$ in (4.2) globally, because the FEM interpolation is locally based. All the matrix operations can be computed based on the local element matrices only (refer to Appendix D for details). Alternatively, if an iterative solver is used, it is actually unnecessary to compute $\mathbf{D}^T \mathbf{K}^s \mathbf{D}$. What an iterative step needs is to compute $(\mathbf{D}^T \mathbf{K}^s \mathbf{D}) \mathbf{u}$ for a given vector \mathbf{u} , therefore one can compute $\mathbf{D}\mathbf{u}$ first, then $\mathbf{K}^s(\mathbf{D}\mathbf{u})$, and last $\mathbf{D}^T(\mathbf{K}^s\mathbf{D}\mathbf{u})$.

4.3 Solution algorithm

The solution algorithm for each implicit time step is summarized in Algorithm 4.

Algorithm 4: The implicit algorithm for the one-field FDM

- 1 Given the solid configuration Ω_n^s and velocity field $\mathbf{u}_n = \begin{cases} \mathbf{u}_n^f & \text{in } \Omega_n^f \\ \mathbf{u}_n^s & \text{in } \Omega_n^s \end{cases}$ at time step n .
Let $\mathbf{u}_{n+1}^0 = \mathbf{u}_n$, $\mathbf{u}_{n+1}^{s,0} = \mathbf{u}_n^s$, $\Omega_{n+1}^{s,0} = \Omega_n^s$ and tol be a tolerance.
 - 2 Let $k = 0$:
 - (i) Compute the interpolation matrix \mathbf{D} and solve equation (4.1) get velocity field \mathbf{u}_{n+1}^{k+1} and p .
 - (ii) Compute solid velocity $\mathbf{u}_{n+1}^{s,k+1} = \mathbf{D}\mathbf{u}_{n+1}^{k+1}$ and update the solid mesh by
$$\Omega_{n+1}^{s,k+1} = \left\{ \mathbf{x}_{n+1} : \mathbf{x}_{n+1} = \mathbf{x}_n + \mathbf{u}_{n+1}^{s,k+1} \Delta t \right\}, \text{ for all } \mathbf{x}_n \in \Omega_n^s.$$
 - (iii) Compute the variation of the velocity norm: $error = \frac{\|\mathbf{u}_{n+1}^{k+1} - \mathbf{u}_{n+1}^k\|}{\|\mathbf{u}_{n+1}^0\|}$. If $error < tol$, let $n = n + 1$ go to “step 1” for the next time step; else: let $k = k + 1$ go to “step (i)” for next iteration.
-

4.4 Numerical tests for energy conservation

In this section, we focus on validation of the energy stability of the proposed numerical method on the condition of Assumption 3.1. We shall use linear triangles (2D) or linear tetrahedra (3D) to discretize the solid domain Ω_0^s . In domain Ω , the $P_2/(P_1 + P_0)$ elements will be used, i.e., the standard *Taylor-Hood* element P_2/P_1 is enriched by a constant P_0 for approximation of the pressure. This element has the property of local mass conservation and the constant P_0 may better capture the element-based jump of pressure [3, 16]. We shall demonstrate the improvement of mass conservation and energy conservation by using the $P_2/(P_1 + P_0)$ elements compared to the more usual P_2/P_1 elements. We shall also validate that the total energy is nonincreasing as stated in Proposition 3.3 (or Proposition 3.4) and Remark 3.7.

Remark 4.2. All variables are interpreted as dimensional in the numerical tests throughout this thesis. If the unit of a variable is not given in a test, this means it could be any unit as

long as all the variables use consistent units. For example, the following two groups of units are considered consistent:

length	time	velocity	acceleration	mass	force	pressure/stress/ μ^s	density	viscosity
m	s	m/s	m/s^2	kg	N	N/m^2	kg/m^3	$N \cdot s/m^2$
cm	s	cm/s	cm/s^2	g	$dyne$	$dyne/cm^2$	g/cm^3	$dyne \cdot s/cm^2$

Table 4.1: Two groups of consistent units ($1dyne = 10^{-5}N$, $1N = 1kg \cdot m/s^2$).

4.4.1 Test1-2D (activated disc): Oscillating disc driven by an initial kinetic energy

In this test, we consider an enclosed flow ($\mathbf{n} \cdot \mathbf{u} = 0$) in $\Omega = [0, 1] \times [0, 1]$ with a periodic boundary condition. A solid disc is initially located in the middle of the square Ω and has a radius of 0.2. The initial velocity of the fluid and solid are prescribed by the following stream function

$$\Psi = \Psi_0 \sin(ax) \sin(by),$$

where $\Psi_0 = 5.0 \times 10^{-2}$ and $a = b = 2\pi$. In this test, $\rho^f = 1$, $\nu^f = 0.01$, $\rho^s = 1.5$ and $\mu^s = 1$. Taking the maximum initial velocity $2\pi\Psi_0 = \hat{U}$ and the height of domain Ω , $\hat{H} = 1$, as the characteristic velocity and length respectively, the Reynolds number is: $Re = \frac{\rho^f \hat{U} \hat{H}}{\nu^f} = 10\pi$. In order to visualize the flow a snapshot ($t = 0.25$) of the velocity and deformation fields is presented in Figure 4.1, and the evolution of energy is presented in Figure 4.2 using a 50×50 mesh (biquadratic squares for the fluid velocity and 3052 linear triangles for the solid velocity).

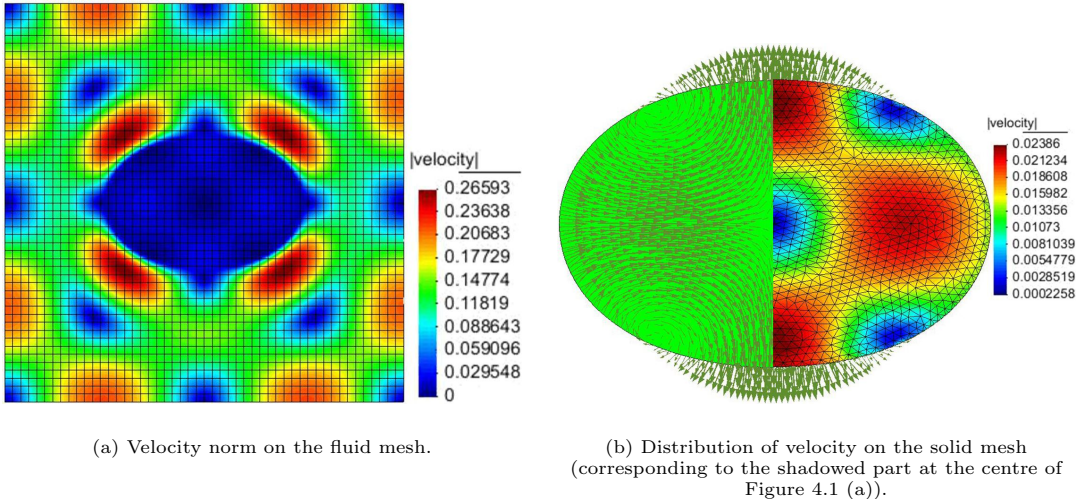


Figure 4.1: Snapshot at $t = 0.25$ for Test1-2D (activated disc) in Section 4.4.1 using a time step of $\Delta t = 5.0 \times 10^{-3}$.

We commence by comparing P_2/P_1 elements and $P_2/(P_1 + P_0)$ elements. The evolution of mass variation and energy ratio are demonstrated in Figure 4.3, from which it can be seen that

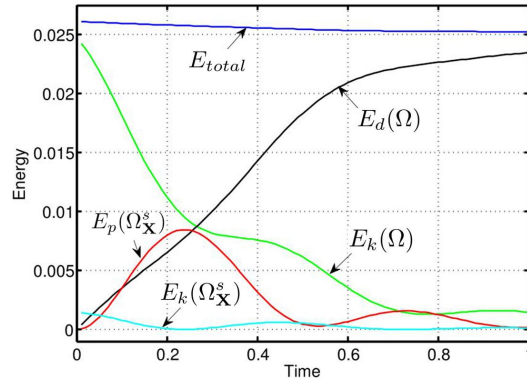


Figure 4.2: Evolution of energy for Test1-2D (activated disc) in Section 4.4.1, $\Delta t = 5.0 \times 10^{-3}$. The peaks of the red curve (curve of $E_p(\Omega_X^s)$) indicate the time when the disc is maximally stretched. The first peak is horizontally stretched and the second peak is vertically stretched. The troughs of the red curve touch line $E_p(\Omega_X^s) = 0$, which are the stress-free stages.

the enrichment of the pressure field by a constant P_0 has an effect of stabilizing the mass and energy evolution. In addition, this enrichment of the pressure field dramatically improves the mass conservation, although the effect for energy conservation is not obvious. Furthermore, using element $P_2/(P_1 + P_0)$, time convergence of the total energy can be observed in Figure 4.4 (a). From this a nonincreasing energy and a first order time convergence can also be observed. It can be seen from Figure 4.4 (b) that the residual term defined in (3.40) is very small and converges rapidly to zero when reducing Δt ($\sim O(\Delta t^2)$).

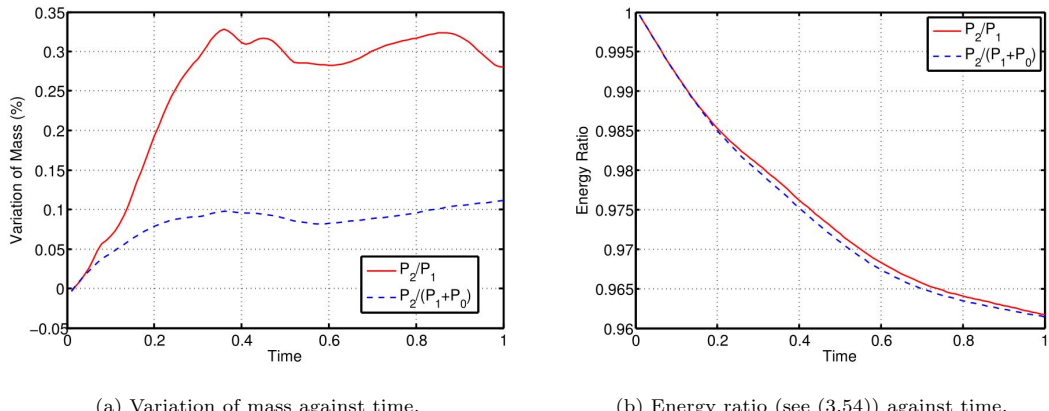
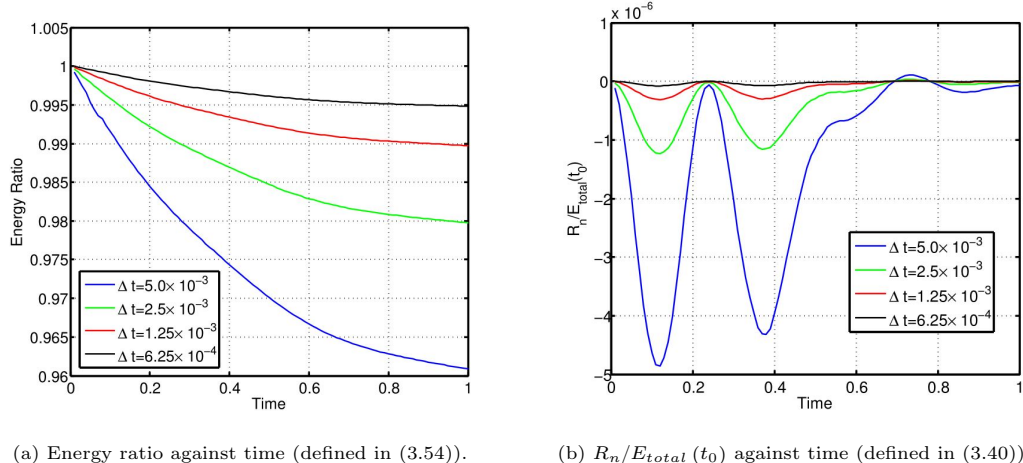


Figure 4.3: Variation of mass and energy for Test1-2D (activated disc) in Section 4.4.1 using a time step of $\Delta t = 5.0 \times 10^{-3}$.



(a) Energy ratio against time (defined in (3.54)).

(b) $R_n/E_{total}(t_0)$ against time (defined in (3.40)).Figure 4.4: Evolution of the energy ratio and residual R_n for Test1-2D (activated disc) in Section 4.4.1.

4.4.2 Test2-2D (stretched disc): Oscillating disc driven by an initial potential energy

In the previous example, the disc oscillates because a kinetic energy is prescribed for the FSI system at the beginning. In this test, we shall stretch the disc and create a potential energy in the solid, then release it causing the disc to oscillate due to this potential energy. The computational domain is again the square $\Omega = [0, 1] \times [0, 1]$. One quarter of a solid disc of radius 0.5 is located in the left-bottom corner of the square, and initially stretched as an ellipse as shown in Figure 4.5. Notice the equation of an ellipse $\frac{x^2}{a^2} + \frac{y^2}{b^2} = 1$ and its area πab , hence we ensure that this stretch does not change mass of the solid.

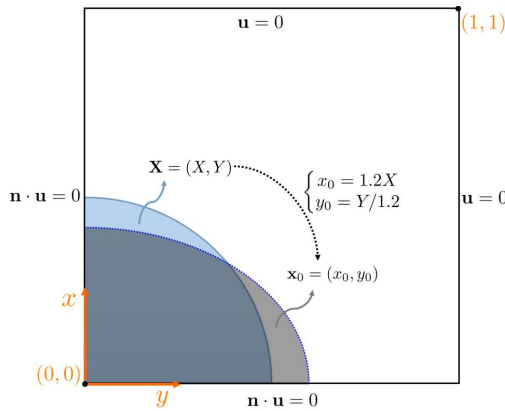


Figure 4.5: Computational domain and boundary conditions for Test2-2D (stretched disc) in Section 4.4.2.

We choose $\rho^f = 1$, $\nu^f = 0.01$, $\rho^s = 2$ and $\mu^s = 2$. Taking a maximum velocity $\hat{U} = 0.16$ (approximately, observed from the numerical result) and the height of domain Ω , $\hat{H} = 1$, as the

characteristic velocity and length respectively, the Reynolds number is: $Re = \frac{\rho^f \hat{U} \hat{H}}{\nu^f} = 16$. The fluid adopts a mesh of 66×66 biquadratic squares, and the solid has similar node density (8206 linear triangles) as the fluid. A snapshot of pressure on the fluid mesh and corresponding solid deformation with its velocity norm are displayed in Figure 4.6, and the evolution of energy is presented in Figure 4.7. It can be seen from Figure 4.8 (a) that the total energy is nonincreasing, and from Figure 4.8 (b) that the residual term defined in (3.40) is very small and converges rapidly to zero when reducing Δt .

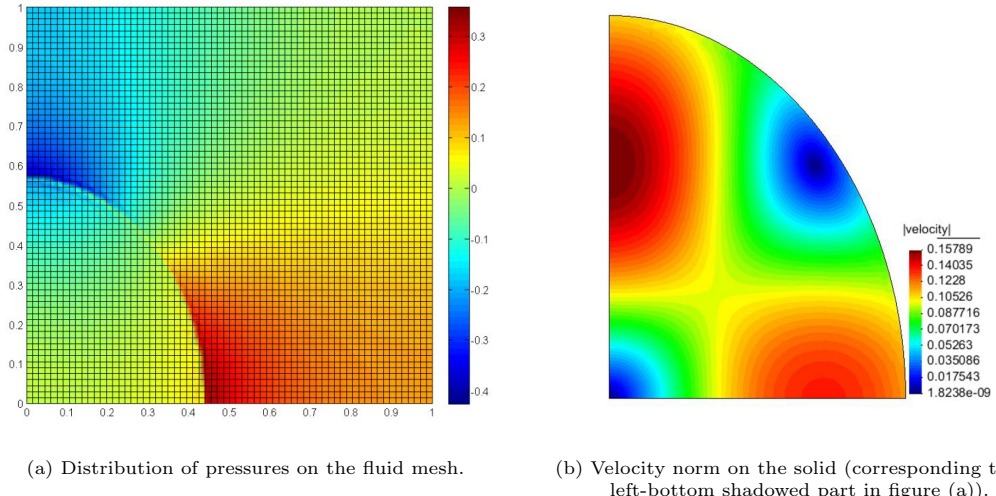


Figure 4.6: A snapshot at $t = 1$ for Test2-2D (stretched disc) in Section 4.4.2 using a time step of $\Delta t = 5.0 \times 10^{-3}$.

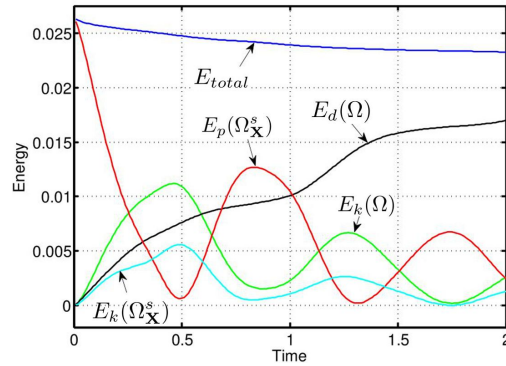
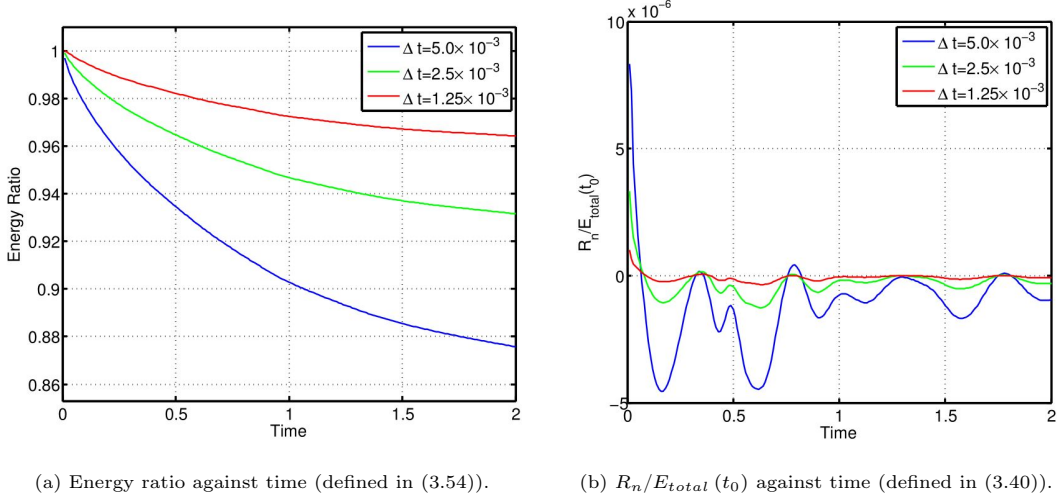


Figure 4.7: Evolution of energy for Test2-2D (stretched disc) in Section 4.4.2, $\Delta t = 5.0 \times 10^{-3}$. The peaks of the red curve (curve of $E_p(\Omega_X^s)$) indicate the time when the disc is maximally stretched. The first and third peaks are corresponding to the time when the disc is horizontally stretched and the second and fourth peaks are corresponding to the time when the disc is vertically stretched. The troughs of the red curve touch line $E_p(\Omega_X^s) = 0$ (numerical error could be observed from the first rough which does not touches line $E_p(\Omega_X^s) = 0$), which are the stress-free stages.



(a) Energy ratio against time (defined in (3.54)).

(b) $R_n/E_{total}(t_0)$ against time (defined in (3.40)).Figure 4.8: Evolution of the energy ratio and residual R_n for Test2-2D (stretched disc) in Section 4.4.2.

4.4.3 Test3-3D (activated ball): Oscillating ball driven by an initial kinetic energy

In this section, we consider a 3D oscillating ball, which is an extension of the example in Section 4.4.1 (same Reynolds number). The ball is initially located at the center of $\Omega = [0, 1] \times [0, 1] \times [0, 0.6]$ with a radius of 0.2. Using the property of symmetry this computation is carried out on 1/8 of domain Ω : $[0, 0.5] \times [0, 0.5] \times [0, 0.3]$. The initial velocities of x and y components are the same as that used in Section 4.4.1 and the z component is set to be 0 at the beginning. We adopt the same parameter and mesh size defined in Section 4.4.1 (with the same mesh size in the z direction). A snapshot of the 1/8 solid ball and the corresponding fluid velocity norm are presented in Figure 4.9, and the nonincreasing energy property is presented in Figure 4.10.

4.5 Limitation of the proposed method

In Section 6.1 we assume that $\rho^\delta \geq 0$, $\nu^\delta = 0$ and have proved the well-posedness based on some additional assumptions (Assumption 6.1 to 6.3). Furthermore, the nonincreasing energy property is tested in the previous Section 4.4 under the condition of $\rho^\delta \geq 0$, $\nu^\delta = 0$. In this section, we aim to analyze and test the cases of $\rho^\delta < 0$ or $\nu^\delta < 0$, and we shall draw a conclusion that the proposed method may not be stable or well-posed in these cases. It can be seen from the analysis in Section 6.1 that a crucial condition for the well-posedness is the coercivity of the bilinear form (6.22):

$$a^h(\mathbf{u}^h, \mathbf{v}^h) = a^f(\mathbf{u}^h, \mathbf{v}^h) + a^s(\mathbf{u}^{sh}, \mathbf{v}^{sh}),$$

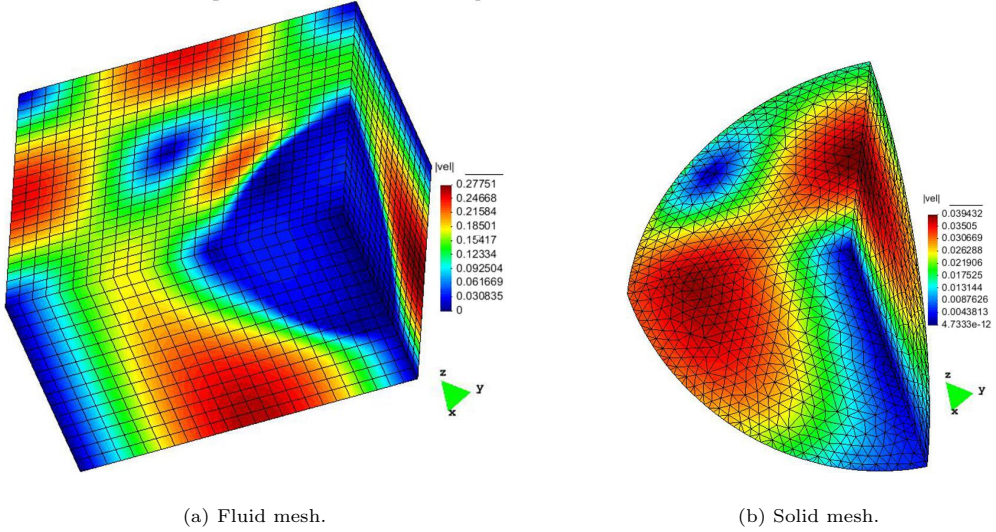
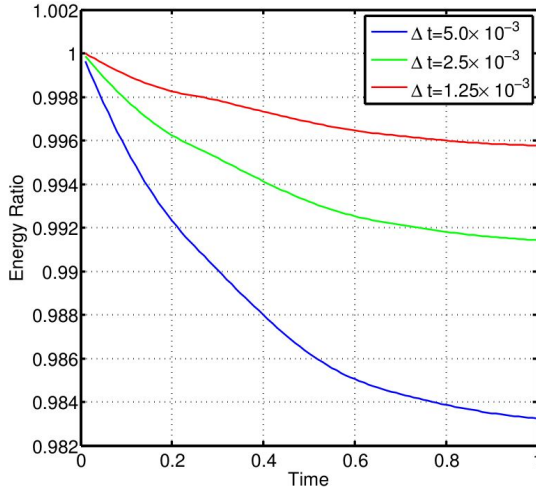
Figure 4.9: Velocity norm at $t = 0.2$ for Test3-3D (activated ball) in Section 4.4.3.

Figure 4.10: Evolution of the energy ratio (defined in (3.54)) for Test3-3D (activated ball) in Section 4.4.3.

where

$$a^f(\mathbf{u}^h, \mathbf{v}^h) = \alpha \int_{\Omega^h} \mathbf{u}^h \cdot \mathbf{v}^h d\mathbf{x} + \frac{\nu^f}{2} \int_{\Omega^h} D\mathbf{u}^h : D\mathbf{v}^h d\mathbf{x}, \quad (4.5)$$

and

$$\begin{aligned} a^s(\mathbf{u}^{sh}, \mathbf{v}^{sh}) &= \beta \int_{\Omega_X^{sh}} \mathbf{u}^{sh} \cdot \mathbf{v}^{sh} d\mathbf{x} \\ &+ \frac{\nu^\delta}{2} \int_{\Omega_{n+1}^{sh}} D\mathbf{u}^{sh} : D\mathbf{v}^{sh} d\mathbf{x} + \gamma \int_{\Omega_X^{sh}} \nabla_{\mathbf{X}} \mathbf{u}^{sh} : \nabla_{\mathbf{X}} \mathbf{v}^{sh} d\mathbf{X}, \end{aligned} \quad (4.6)$$

where $\alpha = \rho^f/\Delta t$, $\beta = \rho^\delta/\Delta t$ and $\gamma = \mu^s\Delta t$. Under the conditions $\beta = \rho^\delta/\Delta t \geq 0$ and $\nu^\delta = 0$, the coercivity of $a^h(\mathbf{u}^h, \mathbf{v}^h)$ can be directly proved by the coercivity of $a^f(\mathbf{u}^h, \mathbf{v}^h)$. However, the coercivity may be destroyed in the case of $\rho^\delta < 0$ or/and $\nu^\delta < 0$ as discussed in Remark 3.4, and it is difficult to analyze the well-posedness in these cases. We shall numerically test to consider the case of $\rho^\delta < 0$ or/and $\nu^\delta < 0$ in this section. Before showing the simulations, let us first write down the main results of the observations as follows:

Observation 4.1. In the case of $\rho^\delta \geq 0$ and $\nu^\delta < 0$: when μ^s is small (soft solid), instability is observed quickly when reducing the time step; for a large μ^s (hard solid) a smaller time is possible before instability is seen. We could define the following indication parameter:

$$\mu_c = \mu^s \Delta t + \nu^\delta. \quad (4.7)$$

Then the above observation may be stated as: μ_c should be positive and sufficient large, or instability will occur.

Observation 4.2. In the case of $\rho^\delta < 0$ and $\nu^\delta = 0$, we have not observed instability even for a very high fluid-solid density ratio $\frac{\rho^f}{\rho^s}$.

Observation 4.3. The cases of $\nu^\delta > 0$ have also been tested, and instability has not been observed.

The $P_2/(P_1 + P_0)$ element (discussed and tested in Section 4.4) will be used in the following numerical tests.

4.5.1 Test4-2D (rotating disc): A rotating disc

This test is taken from [67]. The computational domain is the area between two concentric circles (R_0 and R_1) as shown in Figure 4.11. A constant angular velocity ($\omega = U/R_1 = 0.6$) is prescribed at the outer boundary. This velocity first induces the fluid initially at rest to rotate, and then gradually drags the solid to rotate as well. Oscillation of the solid can be observed at the beginning, which is subsequently damped by numerical dissipation and viscosity as time evolves. Using the property of symmetry, this problem can be reduced to a one dimensional equation when considered in a polar coordinate system (r, θ) [67]:

$$\rho^f \frac{\partial u_\theta}{\partial t} = \frac{1}{r} \nu^f \frac{\partial}{\partial r} \left(r \frac{\partial u_\theta}{\partial r} \right), \quad R \leq r < R_1 \quad (4.8)$$

and

$$\rho^s \frac{\partial u_\theta}{\partial t} = \frac{1}{r} \mu^s \frac{\partial}{\partial r} \left(r \frac{\partial d_\theta}{\partial r} \right), \quad \frac{\partial d_\theta}{\partial t} = u_\theta, \quad R_0 < r \leq R, \quad (4.9)$$

where u_r and u_θ are the velocity components in the radial and tangential directions respectively. We shall use this example to test the stability and mesh convergence of the proposed method, and compare our results (which use two meshes) with a fitted-one-mesh method used in [67].

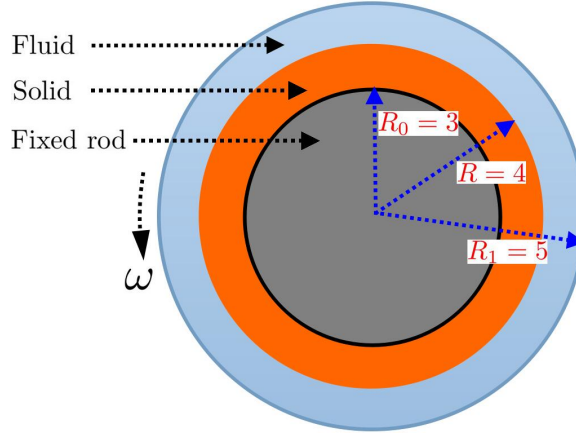
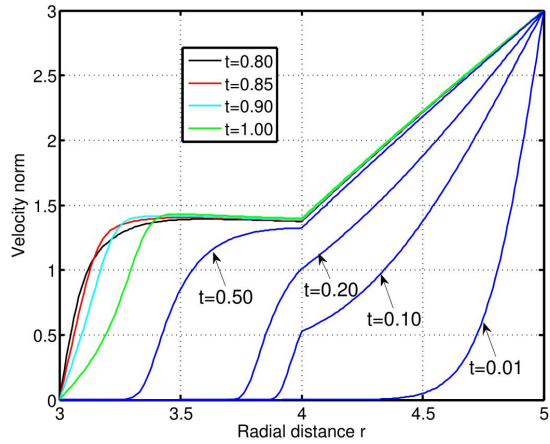


Figure 4.11: Sketch of Test4-2D (rotating disc) in Section 4.5.1.

Figure 4.12: Revolution of the velocity norm for Test4-2D (rotating disc) in Section 4.5.1 (results of the 1D equation, using 200 linear elements and $\Delta t = 1.0 \times 10^{-3}$).

A distinctive feature of this test is that the geometry does not change, and we can always integrate on the original mesh by just updating the solid displacement independently. We implement the fitted-mesh method in [67] using an ALE mesh (see Section 2.4.3) and compare it with our unfitted-mesh method. We first choose the same parameters as used in [67]: $\rho^f = 1$, $\rho^s = 2$, $\nu^f = 2$, $\nu^s = 0$ and $\mu^s = 4$ (note the very large viscosity ν^f and the same magnitude of solid parameter μ^s , which will cause problem for the proposed method when $\nu^s = 0$. Refer to formula (4.7)). Using the value of velocity U and length R_1 as references, the Reynolds number is: $Re = \frac{\rho^f U R_1}{\nu^f} = 7.5$. Solving the reduced one dimensional equation (4.8) and (4.9), one can get the results of an evolving velocity in Figure 4.12. A coarse structured biquadratic fluid mesh (720 nodes and 160 elements) and a coarse unstructured linear solid mesh (654 nodes and 1090 elements) are displayed in Figure 4.14. Other, medium and fine meshes, are obtained based upon one or two refinements of these coarse meshes. Using a time step 5.0×10^{-3} , then

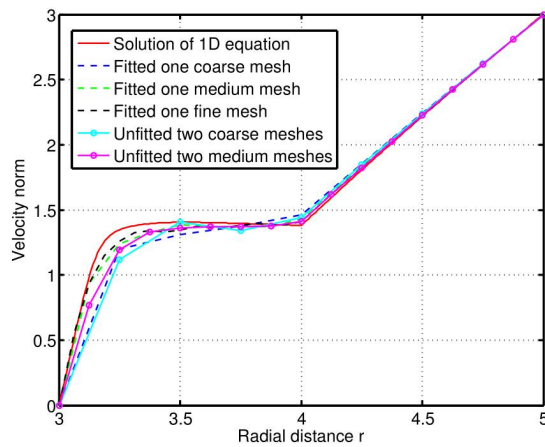
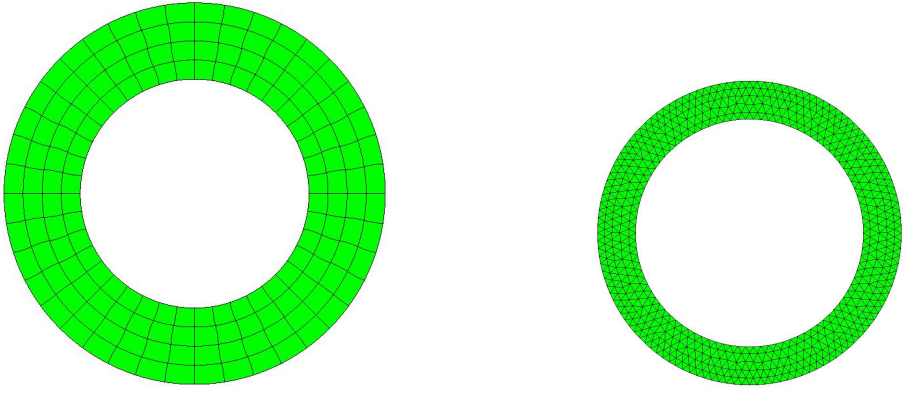


Figure 4.13: Comparison between the one-field FDM, the fitted mesh method in [67] and the semi-analytic solution at $t = 0.85$. Test4-2D (rotating disc) in Section 4.5.1.



(a) Structured biquadratic fluid mesh. (b) Unstructured bilinear solid mesh.

Figure 4.14: Coarse meshes for Test4-2D (rotating disc) in Section 4.5.1.

$\mu_c = \mu^s \Delta t + \nu^\delta = -1.8$ for the above parameters. Instability is observed for this case, however we find that the finer the solid mesh is, the later the simulation fails. We can manage to get a partially stable result using a fine solid mesh combined with a coarse (stable until $t = 1.1$) and a medium (stable until $t = 0.9$) fluid mesh respectively. The result is compared with the fitted mesh method and the solution of 1D equation at $t = 0.85$ (Figure 4.13), which is the first maximum rotation of the solid. The distribution of the pressure and velocity norm on the fluid mesh are presented in Figure 4.15, and the velocity norm is also presented on the solid mesh in Figure 4.16. We can see from Figure 4.16 that a very fine solid mesh is used. However we point out here that this is not a typical choice, and a similar size of fluid and solid mesh is sufficient for both accuracy and stability, which will be explained in the following context. Since the proposed method is based upon updating the solid deformation tensor \mathbf{F} (\mathbf{F} -scheme, see Appendix F), the distribution of \mathbf{F} is also demonstrated in Figure 4.18.

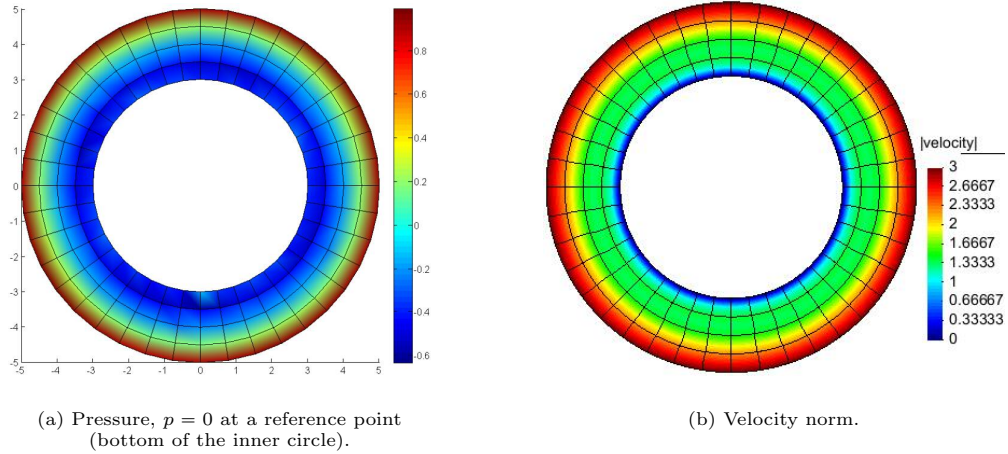


Figure 4.15: Pressure and velocity on the fluid mesh at $t = 0.85$ for Test4-2D (rotating disc) in Section 4.5.1.

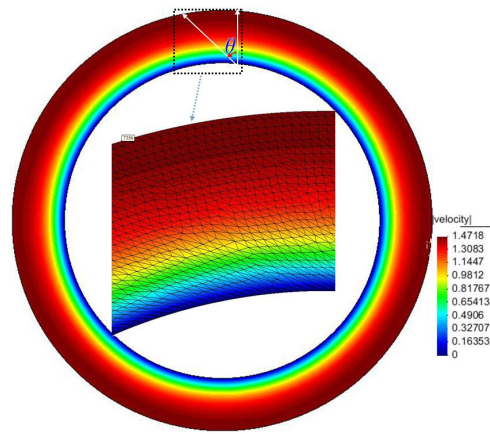


Figure 4.16: Velocity norm on the solid mesh at $t = 1$ using Parameter 1 in Table 4.2, the rotation angle of the disc is $\theta = 16.17^\circ$. Test4-2D (rotating disc) in Section 4.5.1.

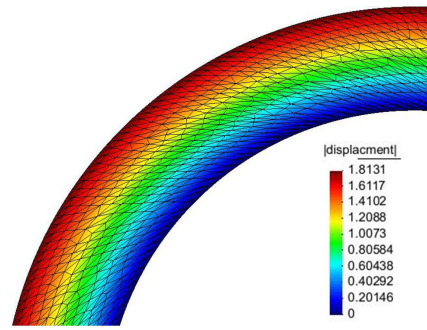


Figure 4.17: Displacement on the solid mesh at $t = 2$ for Parameter 8 in Table 4.2, the rotation angle of the disc is $\theta = 25.97^\circ$. Test4-2D (rotating disc) in Section 4.5.1.

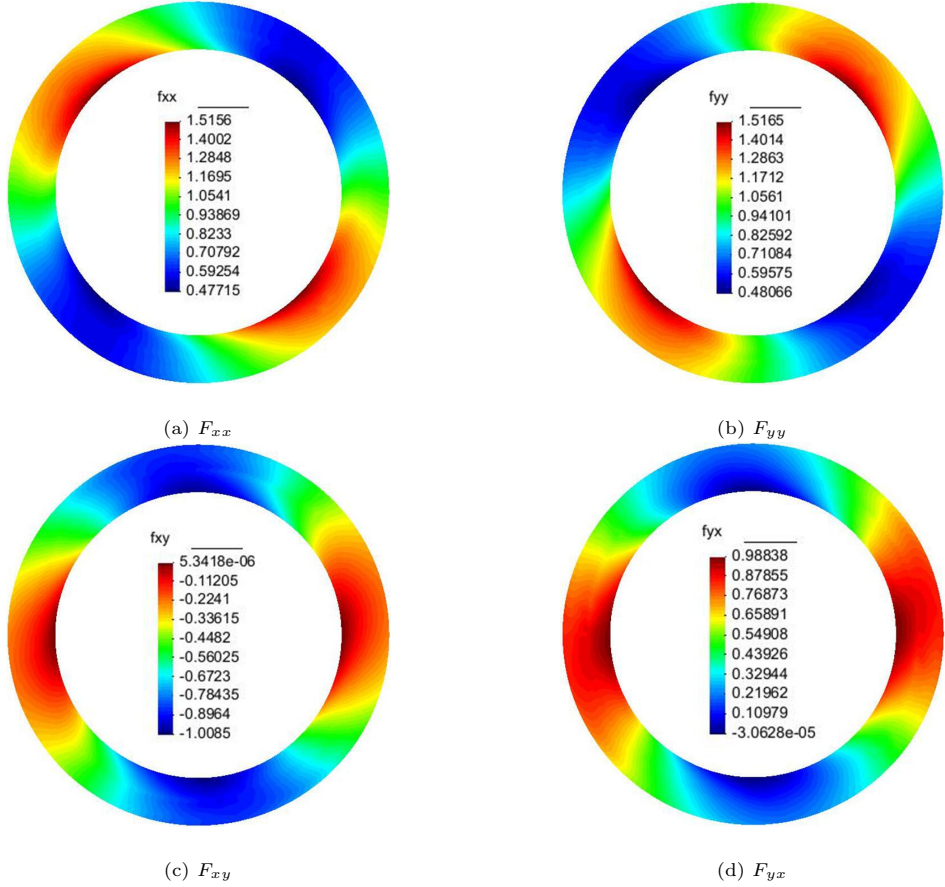


Figure 4.18: Deformatioin tensor \mathbf{F} at $t = 0.85$ for Test4-2D (rotating disc) in Section 4.5.1.

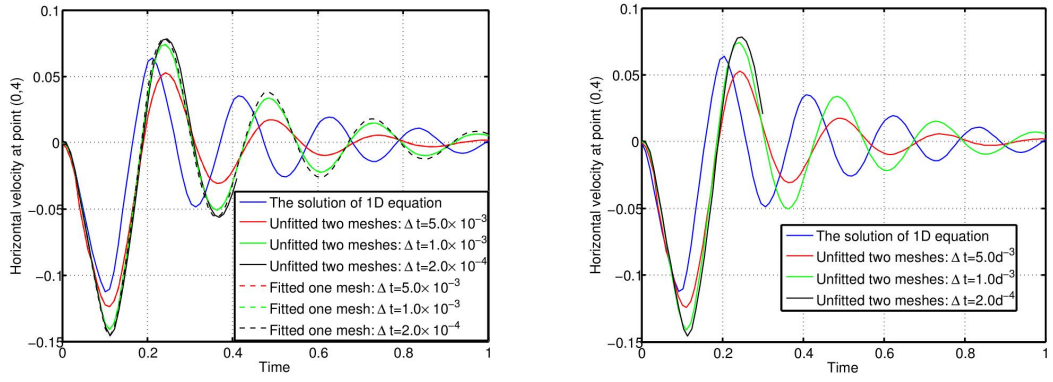


Figure 4.19: Evolustion of velocity for Parameters 2 in Table 4.2. 200 linear elements are used for the one dimensional equation with $\Delta t = 1.0 \times 10^{-4}$. Test4-2D (rotating disc) in Section 4.5.1.

Parameter sets	ρ^f	ρ^s	ν^f	ν^s	μ^s	Δt	μ_c	Stability
Parameter 1	1	2	2	0	4	5.0×10^{-3}	-1.98	✗
						5.0×10^{-3}	3	✓
Parameter 2	1	2	2	0	10^3	1.0×10^{-3}	-1	✓
						2.0×10^{-4}	-1.8	✗
						2.0×10^{-4}	-0.8	✓
						4.0×10^{-5}	-0.96	✓
Parameter 3	1	2	2	1	10^3	8.0×10^{-6}	-0.992	✓
						1.0×10^{-6}	-0.999	✗
						5.0×10^{-3}	-	✓
						5.0×10^{-3}	-	✓
Parameter 4	1	2	2	2	4	5.0×10^{-3}	-	✓
Parameter 5	1	0.5	2	2	4	5.0×10^{-3}	-	✓
Parameter 6	1	0.1	2	2	4	5.0×10^{-3}	-	✓
Parameter 7	1	0.01	2	2	4	5.0×10^{-3}	-	✓
Parameter 8	1	0.001	2	2	4	5.0×10^{-3}	-	✓

Table 4.2: Parameter sets for Test4-2D (rotating disc) in Section 4.5.1 with $\mu_c = \mu^s \Delta t + \nu^\delta$. “✗” means instability is observed (“✓” means not) during $t = 0$ to 1, and “–” means μ_c is not an indication for stability in the case $\nu^\delta \geq 0$.

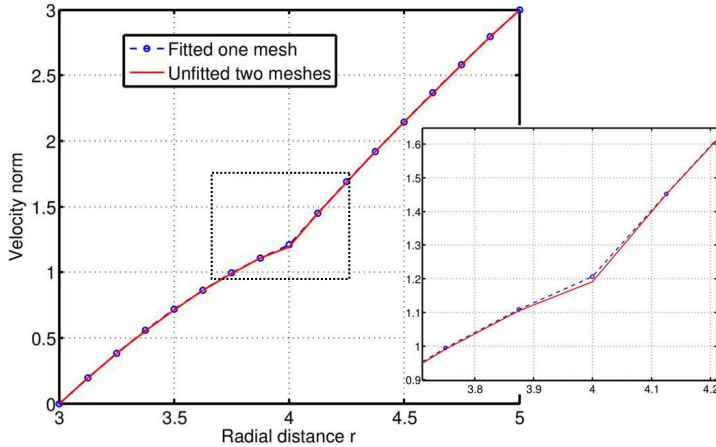


Figure 4.20: Velocity norm at $t = 0.85$ for Parameter 4 in Table 4.2. Test4-2D (rotating disc) in Section 4.5.1.

For this problem, we also tested other parameters as summarized in Table 4.2 with corresponding stability results, from which it can be seen that when $\nu^\delta < 0$ instability always occurs eventually if we keep reducing the time step. For parameter set 2 and 3 (hard solid), the solid velocity oscillates frequently and approaches a small constant as shown in Figure 4.19. We cannot see a big difference between results of the fitted one mesh and the unfitted two meshes, however we do not know the reason that there is gap between the solution in 1D and 2D. For the case of $\nu^\delta = 0$ and $\rho^\delta < 0$, we have not observed any instability up to $t = 2$, even for a very small solid density. As an example, a quarter of the solid mesh is displayed in Figure 4.17 for the case of $\rho^s = 0.001$. Although it is difficult to justify accuracy of the result after such a long run (the solid mesh is extremely stretched), we can see the robustness of the algorithm in this

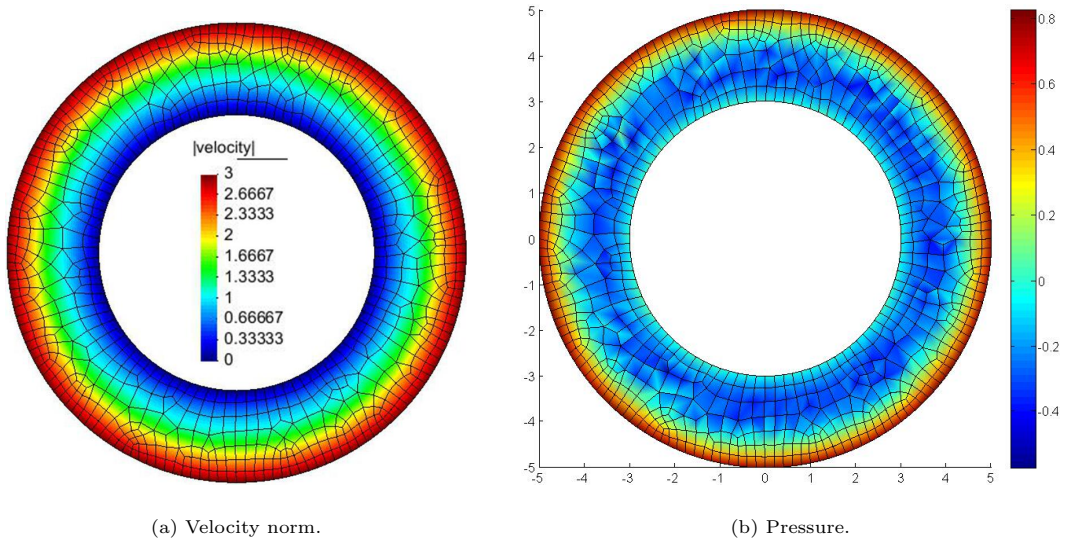


Figure 4.21: Velocity norm and pressure at $t = 0.85$ for Parameter 4 in Table 4.2 using a coarse mesh. Test4-2D (rotating disc) in Section 4.5.1.

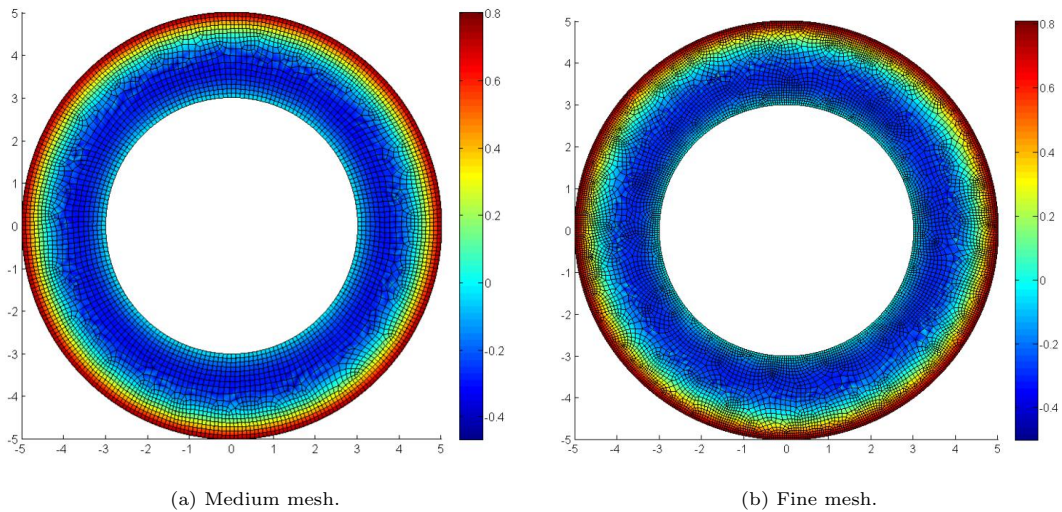


Figure 4.22: Pressure at $t = 0.85$ for Parameter 4 in Table 4.2. Test4-2D (rotating disc) in Section 4.5.1.

case. Figure 4.20 plots the velocity norm for the fitted and unfitted mesh methods, from which we cannot see a big difference. This good agreement maybe because the boundary between the unfitted two meshes still matches in the normal direction. To investigate this further, we use an unstructured fluid mesh, as shown in Figure 4.21, which is a coarse and poor quality mesh (for this problem). This poor choice is deliberate in order to test robustness of the proposed scheme. Based on this coarse mesh (3542 nodes), a medium mesh (18114 nodes) and fine mesh (41764 nodes) are use to repeat the test. Convergence of velocity across the disc at $\theta = \pi/2$ is plotted in Figure 4.23, and from Figure 4.22 we may observe that the oscillation of pressure

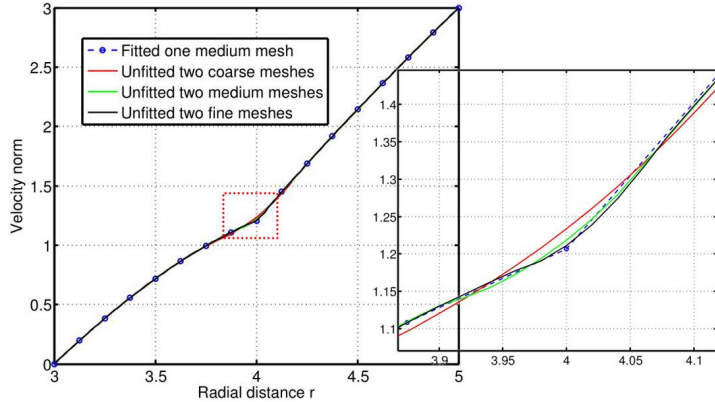


Figure 4.23: Mesh convergence for an unstructured fluid mesh. Test4-2D (rotating disc) in Section 4.5.1.

only happens near the interface between the fluid and solid when refining the mesh.

4.5.2 Test5-2D (elastic wall): Cavity flow with an elastic solid wall

This example is taken from [160]. The computational domain is a $L \times L$ square with a rectangular solid at the bottom of this square as shown in Figure 4.24, where $L = 2$ and $H = 0.5$ for this test problem. The velocities are fixed to be zero on all boundaries except the top lid, which is prescribed as follows:

$$u_x = \begin{cases} \sin^2(\pi x / 0.6) & x \in [0, 0.3] \\ 1 & x \in (0.3, 1.7) \\ \sin^2(\pi(x - 2) / 0.6) & x \in [1.7, 2] \end{cases} \quad (4.10)$$

Taking the maximum velocity $\hat{U} = 1$ at the top of the cavity and the cavity height $\hat{H} = 1$ as the characteristic velocity and length respectively, the Reynolds number is: $Re = \frac{\rho^f \hat{U} \hat{H}}{\nu^f} = 5$.

We first use the same parameters as used in [160], i.e. $\rho^f = \rho^s = 1$, $\nu^f = \nu^s = 0.2$ and $\mu^s = 0.2$, and compare the proposed one-field FDM which use two meshes and the Monolithic Eulerian method using one fitted ALE mesh [67]. A plot of pressure on the fluid mesh and velocity on the deformed solid mesh are presented in Figure 4.25, which uses a coarse mesh (400×400 elements). The velocity and mesh displacement using an ALE mesh are displayed in Figure 4.26. Using the same time step $\Delta t = 5.0 \times 10^{-3}$, a comparison between these two different methods via the interface position and the solid area is demonstrated in Figure 4.27, from which it can be seen that the two-mesh method and the fitted-ALE-mesh method give almost the same accuracy.

We then extend to the case of $\nu^\delta < 0$ to test the stability as shown in Table 4.3, which indicates that small time steps Δt will again cause instability. It may also be observed from the result of Parameter 4 ($\Delta t = 4.0 \times 10^{-2}$) that too large time step can also lead to instability, because the solid mesh may be distorted or flip over locally when updated by its own velocity.

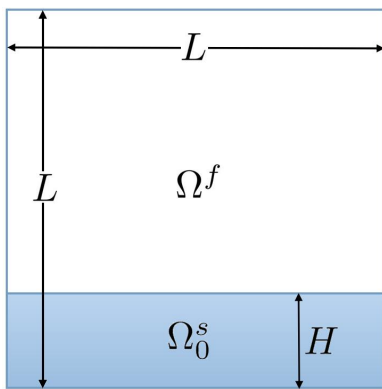


Figure 4.24: Computational domain for Test5-2D (elastic wall) in Section 4.5.2.

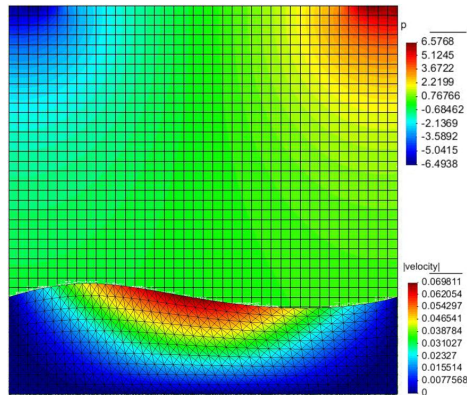
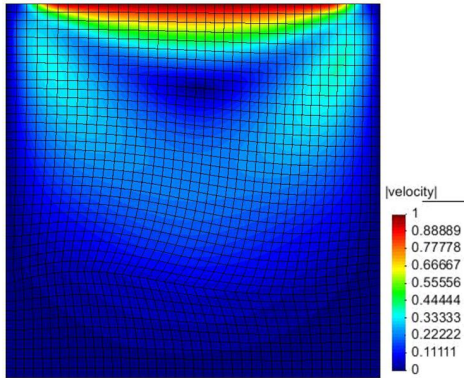
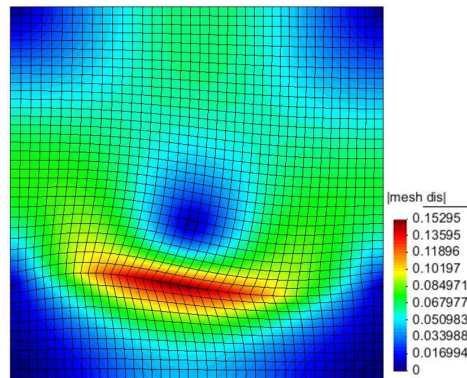


Figure 4.25: Distribution of pressure on the fluid mesh and velocity norm on the deformed solid mesh at $t = 2$. Test5-2D (elastic wall) in Section 4.5.2.



(a) Velocity norm.



(b) Displacement of the mesh.

Figure 4.26: Velocity and mesh displacement using an ALE mesh at $t = 2$ for Test5-2D (elastic wall) in Section 4.5.2.

4.5.3 Test6-2D (rising bar): A rising bar

In this test, we consider a rising bar in a container of dense fluid with gravity. We first test the limitation of the density ratio of two materials when $\nu^s = \nu^f$, and then test the case $\nu^s = 0$ and investigate any limitation of time step. We note here that the mesh quality of a bar can be maintained more easily than the mesh of a disc when updating their position, so we consider a bar (very soft) rather than a disc.

The computational domain is the box as illustrated in Figure 4.28 with boundary conditions shown. $Re = \frac{\rho^f \hat{U} \hat{H}}{\nu^f} = 12$ if using the maximum velocity $\hat{U} = 4$ (approximately) which is observed from numerical result and the channel height $\hat{H} = 3$ as the characteristic velocity and length respectively. All the parameter sets and stability results are displayed in Table 4.4, which supports what we discussed in Observations 4.1 to 4.3. We can see from parameter sets 1 to 8 that it is always stable when $\nu^\delta = \nu^s - \nu^f \geq 0$, even for a very high fluid-solid density ratio $\frac{\rho^f}{\rho^s}$.

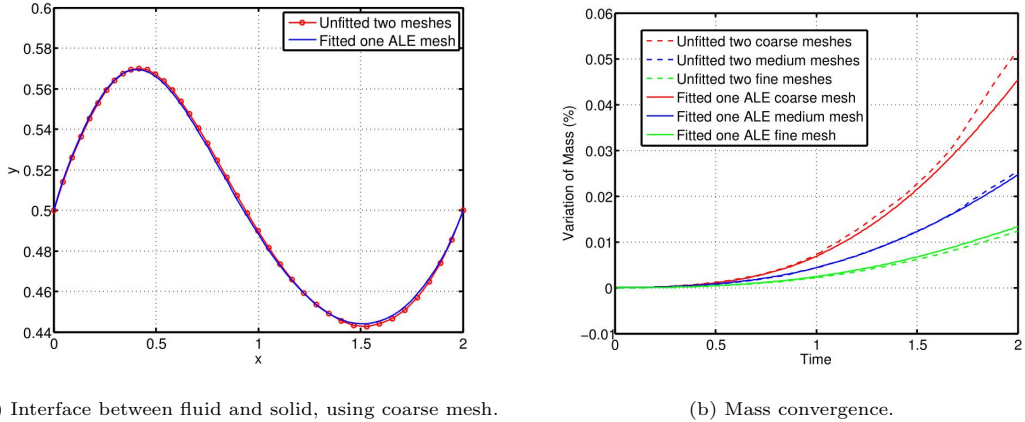


Figure 4.27: Comparison between the two-mesh method and the fitted-mesh method for Test5-2D (elastic wall) in Section 4.5.2, using a time step of $\Delta t = 5.0 \times 10^{-3}$.

Parameter sets	ρ^f	ρ^s	ν^f	ν^s	μ^s	Δt	μ_c	Stability
Parameter 1	1	1	0.2	0.2	0.2	5.0×10^{-3}	—	✓
Parameter 2	1	1	0.2	0.1	0.2	5.0×10^{-3}	-0.099	✗
						1.0×10^{-2}	-0.098	✗
						2.0×10^{-2}	-0.096	✗
						4.0×10^{-2}	-0.092	✗
Parameter 3	1	1	0.2	0	0.2	5.0×10^{-3}	-0.199	✗
						1.0×10^{-2}	-0.198	✗
						2.0×10^{-2}	-0.196	✗
						4.0×10^{-2}	-0.192	✗
Parameter 4	1	1	0.2	0.1	1	5.0×10^{-3}	-0.0995	✗
						1.0×10^{-2}	-0.099	✓
						2.0×10^{-2}	-0.098	✓
						4.0×10^{-2}	-0.096	✗

Table 4.3: Parameter sets for Test5-2D (elastic wall) in Section 4.5.2 with $\mu_c = \mu^s \Delta t + \nu^\delta$. “✗” means instability is observed (“✓” means not) during $t = 0$ to 2, and “—” means μ_c is not an indicator for stability in the case $\nu^\delta \geq 0$.

While from the last four parameter sets we can see that it is unstable when using small time steps due to $\nu^\delta < 0$. In order to visualize evolution of the solid bar, results using Parameter 1 are demonstrated in Figure 4.29 and Figure 4.30 on fluid mesh and solid mesh respectively. It can be seen from Figure 4.30 that using a structured solid mesh or an unstructured solid mesh makes no qualitative difference. We only focus on the test for stability, without evaluating the accuracy here, because the solid meshes are distorted at two ends of the bar (see Figure 4.30).

4.5.4 Test7-2D (cavity with disc): Cavity flow with a solid disc

This example is taken from [161]. A sketch of the problem and boundary conditions are shown in Figure 4.31. $Re = \frac{\rho^f \hat{U} \hat{H}}{\nu^f} = 100$ if taking the maximum velocity $\hat{U} = 1$ at the top of the

Parameter sets	ρ^f	ρ^s	ν^f	ν^s	μ^s	Δt	μ_c	Stability
Parameter 1	1	0.5	1	2	100	2.0×10^{-3}	—	✓
Parameter 2	1	0.1	1	2	100	2.0×10^{-3}	—	✓
Parameter 3	1	0.05	1	2	100	2.0×10^{-3}	—	✓
Parameter 4	1	0.01	1	2	100	2.0×10^{-3}	—	✓
Parameter 5	1	0.5	1	1	100	2.0×10^{-3}	—	✓
Parameter 6	1	0.1	1	1	100	2.0×10^{-3}	—	✓
Parameter 7	1	0.05	1	1	100	2.0×10^{-3}	—	✓
Parameter 8	1	0.01	1	1	100	2.0×10^{-3}	—	✓
Parameter 9	1	0.5	1	0	100	1.0×10^{-3}	-0.9	✗
Parameter 10	1	0.5	1	0	100	2.0×10^{-3}	-0.8	✗
Parameter 11	1	0.5	1	0	100	5.0×10^{-3}	-0.5	✓
Parameter 12	1	0.5	1	0	100	1.0×10^{-2}	0	✓

Table 4.4: Parameter sets for Test6-2D (rising bar) in Section 4.5.3. “✗” means instability is observed (“✓” means not) before the bar moves out of the cup, and “—” means μ_c is not an indicator for stability in the case $\nu^\delta \geq 0$. $\mu_c = \mu^s \Delta t + \nu^\delta$ and gravity acceleration is 980.

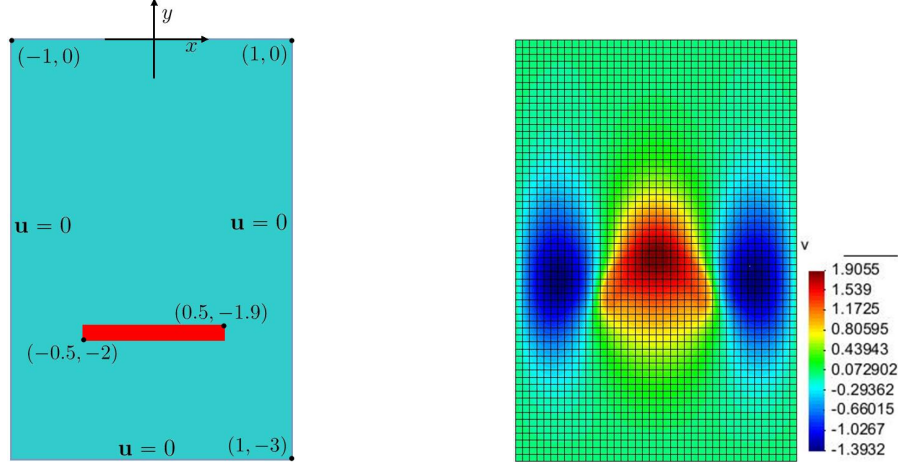


Figure 4.28: Sketch of Test6-2D (rising bar) in Section 4.5.3. Figure 4.29: Vertical velocity on the background mesh at $t = 0.6$ for Test6-2D (rising bar) in Section 4.5.3.

cavity and the height $\hat{H} = 1$ of the cavity as the characteristic velocity and length respectively. We consider the parameter sets displayed in Table 4.5, and the results also support what we discussed in Observations 4.1 and 4.2. In the tests of Parameter set 1 to 6, we choose $\nu^s = \nu^f$ and change the solid density from soft ($\mu^s = 0.1$) to hard ($\mu^s = 100$) solid. All these simulations are stable after a long run (up to $t = 20$). We also test several cases of $\nu^s > \nu^f$ (not shown in the table) and the simulations are always stable. In the tests of Parameter set 7 to 11, we again observe instability, when reducing the time step, because of $\nu^s < \nu^f$. It is not surprising that instability also occurs for Parameter set 7, because the time step is too large to maintain a good quality of mesh (the mesh of the disc is distorted when it arrives at the top of the cavity). As an example to show the evolution of the solid disc, the velocity norm on the fluid mesh and

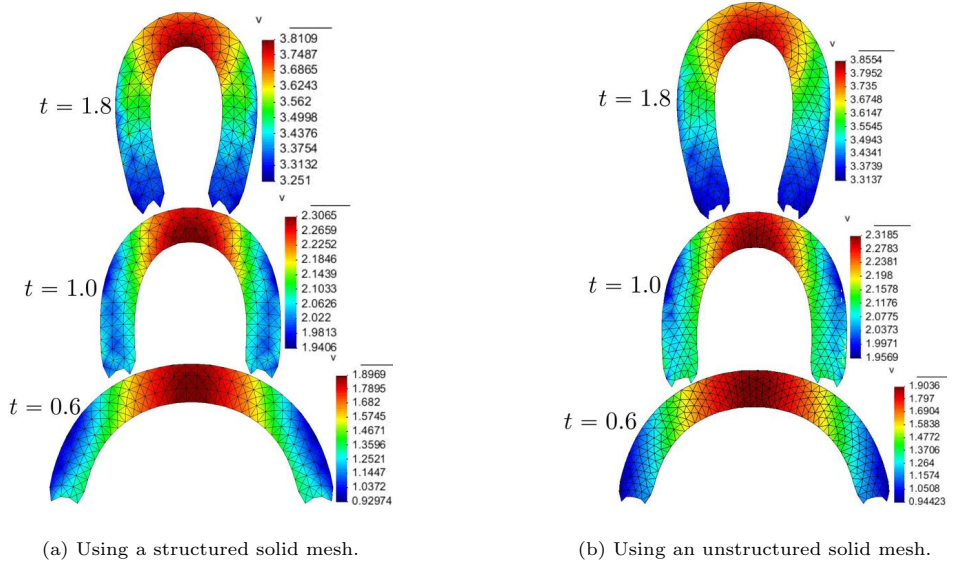


Figure 4.30: Evolution of the solid for Test6-2D (rising bar) in Section 4.5.3.

the solid mesh for Parameter 1 are presented in Figure 4.32 and Figure 4.33 respectively.

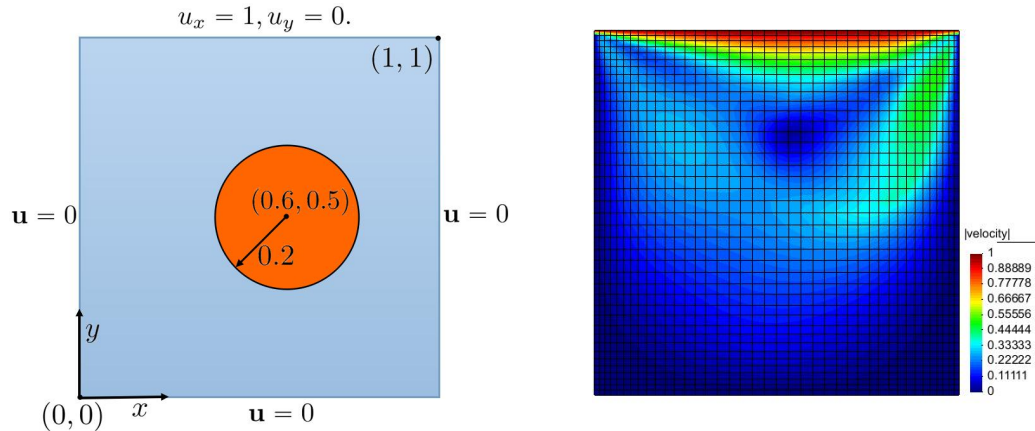


Figure 4.31: Sketch of the cavity with a solid disc for Test7-2D (cavity with disc) in Section 4.5.4.

Figure 4.32: Velocity norm on the fluid mesh at $t = 20$ for Test7-2D (cavity with disc) in Section 4.5.4.

4.5.5 Conclusion

In this section we present a brief summary of the stability tests. The following conclusions are based on the underlying assumption that no solid element distorts or flips over when updating the solid mesh, so that a finite element approximation on the solid mesh is accurate enough. Let us recall that $\nu^\delta = \nu^s - \nu^f$ and $\rho^\delta = \rho^s - \rho^f$, and define a ratio of the fluid and solid mesh size: $r_m = (\text{local solid nodes})/(\text{local fluid nodes})$.

Parameter sets	ρ^f	ρ^s	ν^f	ν^s	μ^s	Δt	μ_c	Stability
Parameter 1	1	1	0.01	0.01	0.1	1.0×10^{-3}	—	✓
Parameter 2	1	1	0.01	0.01	1	1.0×10^{-3}	—	✓
Parameter 3	1	1	0.01	0.01	10	1.0×10^{-3}	—	✓
Parameter 4	1	1	0.01	0.01	100	1.0×10^{-3}	—	✓
Parameter 5	1	0.5	0.01	0.01	1	1.0×10^{-3}	—	✓
Parameter 6	1	0.2	0.01	0.01	1	1.0×10^{-3}	—	✓
Parameter 7	1	2	0.01	0	1	1.0×10^{-3}	-0.009	✗
Parameter 8	1	2	0.01	0	1	5.0×10^{-3}	-0.005	✓
Parameter 9	1	1	0.01	0	1	5.0×10^{-3}	-0.005	✓
Parameter 10	1	0.5	0.01	0	1	5.0×10^{-3}	-0.005	✗
Parameter 11	1	0.2	0.01	0	1	5.0×10^{-3}	-0.005	✗

Table 4.5: Parameter sets for Test7-2D (cavity with disc) in Section 4.5.4 with $\mu_c = \mu^s \Delta t + \nu^\delta$. “✗” means instability is observed (“✓” means not) up to $t = 20$, and “—” means μ_c is not an indicator for stability in the case of $\nu^\delta \geq 0$.

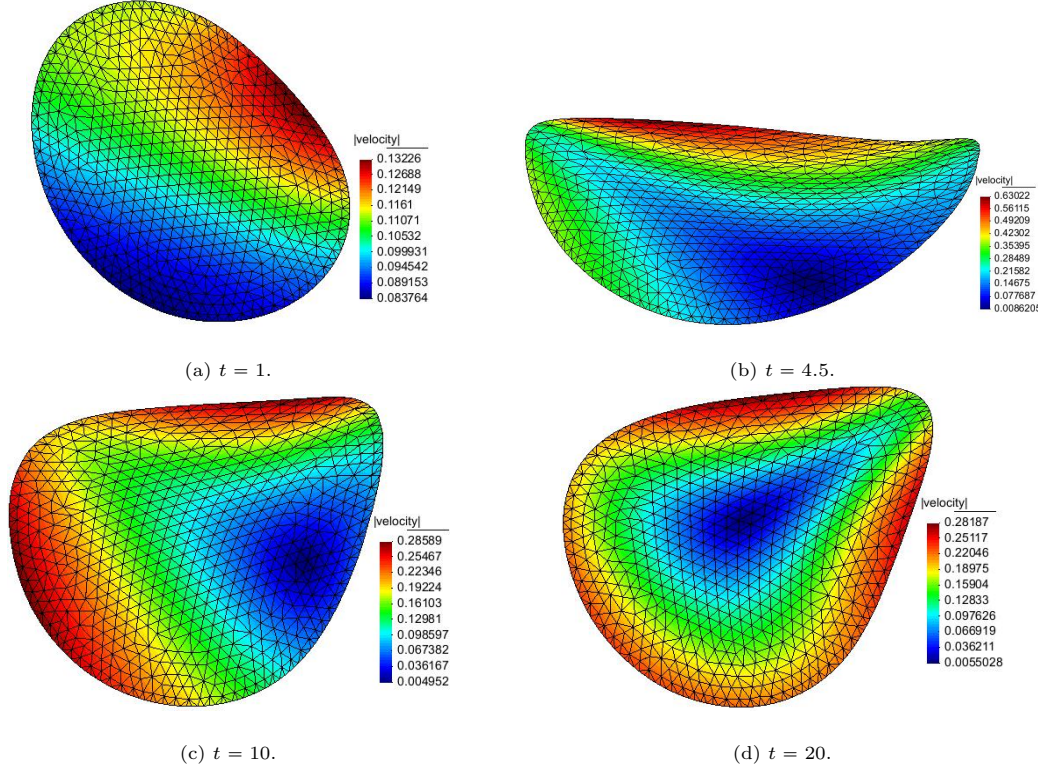


Figure 4.33: Velocity norm on the solid mesh (Parameter 1) for Test7-2D (cavity with disc) in Section 4.5.4.

1. If $\nu^\delta = 0$ and $\rho^\delta \geq 0$, we proved, under some assumptions in Section 6.1, that the proposed scheme is stable for any Δt . In this case, a similar fluid and solid mesh size ($r_m \approx 1$) is sufficient to give an accurate result.

2. If $\nu^\delta \geq 0$ and $\rho^\delta < 0$, we have not observed instability problems for the above (or any other) numerical tests, even for a very small density ratio ($\rho^s/\rho^f = 0.001$). In this case, $r_m \approx 1$ is also sufficient to give an accurate result and the stability is not sensitive to r_m .
3. If $\nu^\delta < 0$, our scheme is always unstable if using a sufficiently small time step. In this case $\mu_c = \mu^s \Delta t + \nu^\delta$ is an empirical indicator for instability: i.e. the scheme is still possible to be stable if $\mu_c \approx 0$ or $\mu_c > 0$. In this case, the stability is also sensitive to r_m . Numerical tests show that a larger r_m has a positive effect on stabilization. Nevertheless, the fact that it is not possible to take the limit $\Delta t \rightarrow 0$ means that we cannot recommend our scheme when $\nu^\delta < 0$.

4.6 Summary

An implicit implementation of the one-field FDM is introduced in this chapter, followed by numerical tests for different purposes: three numerical experiments are presented in order to demonstrate the energy property proved in Section 4.4; four numerical experiments are presented in order to show the limitation of the proposed method, and a conclusion about this is clearly drawn in Section 4.5.5. In the next chapter, three explicit schemes for the one-field FDM will be introduced based upon different splitting methods.

The numerical tests implemented in this chapter all use the $P_2/(P_1 + P_0)$ element after a comparison with the P_2/P_1 element in Test1-2D (Section 4.4.1), which shows that the mass conservation is dramatically improved by using $P_2/(P_1 + P_0)$. Local mass conservation of the $P_2/(P_1 + P_0)$ element is proved by [16]. However, we would not say the $P_2/(P_1 + P_0)$ element is necessarily the best choice, even though it improves the mass conservation. First, it is expensive since we add the piecewise constant P_0 through the whole domain although the discontinuity of pressure usually only happens across the fluid-solid interface. Second, the energy conservation is not improved from Test1-2D (stability may be improved but the improvement of accuracy is not obvious). Third, as will be considered in Chapter 5, in the case of a thin solid (Test8-2D: a leaflet and Test9-2D: a flag) interacting with a fluid our iterative linear solver (see Section 4.2) struggles to converge when using the $P_2/(P_1 + P_0)$ element. The reason may be that too many redundant unknowns P_0 are added through the domain, and the pressure is only discontinuous across the thin solid. However, we do not lose accuracy when using P_2/P_1 element in this case, because our results agree well with the ALE fitted mesh method at the first few steps (before the ALE method fails) and also agrees well with results from the literature.

Chapter 5

Explicit splitting schemes

In the previous chapter, the case of low Reynolds number flow is considered. An implicit scheme is utilized to solve the whole FSI system by arranging the convection term on the right-hand side of the equation and applying a fixed point iteration. In this chapter, the case of higher Reynolds number will be considered as well, and explicit splitting schemes are adopted to treat the convection separately.

We shall introduce three types of splitting schemes. The purpose of splitting is to decouple the highly non-linear implicit one-field FDM formulation (see Chapter 3), such that every step/subproblem can be efficiently solved without losing significant accuracy. A 2-step splitting scheme and a 3-step splitting scheme are introduced in Section 5.1 and 5.3 respectively. Numerical experiments are presented in Sections 5.2 and 5.4, for testing these two different schemes respectively, which indicate that both are energy non-increasing. A 4-step splitting method (projection method) is also introduced in Section 5.5, however the same numerical tests (in Section 5.6) show that this scheme is energy non-increasing for a mixed-element (P_2/P_1 or $P_2/(P_1 + P_0)$) but not for the equal-order element (P_1).

There are 14 numerical tests implemented in this thesis, numbered from Test1 to Test14. Five of these are used in this chapter (highlighted **in blue and bold** in Table 5.1): Test1-2D (activated disc), Test2-2D (stretched disc), Test3-3D (stretched ball), Test7-2D (cavity with disc) and Test8-2D (leaflet) are used through this chapter to compare the three types of splitting schemes. Other tests may also be added to a specific scheme in order to compare with IFEM, ALE method, laboratory experiment or other existing methods.

Some of our numerical tests use P_2/P_1 element while others use $P_2/(P_1 + P_0)$ element. A general explanation of this choice is presented in Section 4.6. Also notice that there is no need to use $P_2/(P_1 + P_0)$ element for the 4-step splitting scheme, because it is redundant to add a piecewise constant to the shape function in order to solve the Poisson equation. Some tests use an adaptive mesh with hanging nodes, while others use a uniform mesh. The purpose of using the adaptive mesh is to improve computational efficiency and to show the robustness of

the proposed method. The scheme does not rely on the use of an adaptive mesh (however brief implementation details may be found in appendix E). We summarize the choice of the element ($P_2/(P_1 + P_0)$ or P_2/P_1) and the mesh (adaptive or uniform) in Table 5.1, in which the method (Least-squares or Taylor-Galerkin) for treating the convection step is also illustrated.

When implementing the proposed one-field FDM, one could update the deformation tensor \mathbf{F} (for both the implicit and explicit scheme) as illustrated in formula (3.8) or (3.12), alternatively one may also update the deviatoric part of solid stress $\boldsymbol{\sigma}$ (only for the explicit scheme) as discussed in Appendix A. It is interesting that for Test8-2D (leaflet) we implemented both schemes, and found that the \mathbf{F} -scheme could not converge (mesh distorted at some stage, see Appendix A for more discussion of this). For Test4-2D (rotating disc) and Test7-2D (cavity with disc) the two schemes present similar results (see Figure 5.11). It is worth comparing these two scheme more thoroughly, which however has not been done in thesis and is left as future work. We just display the choice of \mathbf{F} -scheme and/or $\boldsymbol{\sigma}$ -scheme in Table 5.1.

Numerical tests	Element type	Mesh type	Convection	\mathbf{F} and/or $\boldsymbol{\sigma}$ -scheme
Test1-2D (activated disc)	$P_2/(P_1 + P_0)$	uniform	LS/TG	F
Test2-2D (stretched disc)	$P_2/(P_1 + P_0)$	uniform	LS/TG	F
Test3-3D (stretched ball)	$P_2/(P_1 + P_0)$	uniform	LS	F
Test4-2D (rotating disc)	$P_2/(P_1 + P_0)$	uniform	-	F/ $\boldsymbol{\sigma}$
Test5-2D (elastic wall)	$P_2/(P_1 + P_0)$	uniform	-	F
Test6-2D (rising bar)	$P_2/(P_1 + P_0)$	uniform	-	$\boldsymbol{\sigma}$
Test7-2D (cavity with disc)	$P_2/(P_1 + P_0)$	uniform	LS	F/ $\boldsymbol{\sigma}$
Test8-2D (leaflet)	P_2/P_1	adaptive and uniform	LS/TG	$\boldsymbol{\sigma}$
Test9-2D (thin flag)	P_2/P_1	adaptive	LS	$\boldsymbol{\sigma}$
Test10-2D (channel with solids)	P_2/P_1	adaptive	LS	$\boldsymbol{\sigma}$
Test11-2D (thick flag)	P_2/P_1	uniform	TG	$\boldsymbol{\sigma}$
Test12-3D (cylinder)	P_2/P_1	uniform	LS	$\boldsymbol{\sigma}$
Test13-2D (one particle)	P_2/P_1	adaptive	-	$\boldsymbol{\sigma}$
Test14-2D (two particle)	P_2/P_1	adaptive	-	$\boldsymbol{\sigma}$

Table 5.1: The choice of element and mesh in all the numerical tests. LS: Least-squares method, TG: Taylor-Galerkin method. “-”: low Reynolds number flow, the convection is either neglected or moved to the right-hand side of the equation as a force term.

Based on the discussion of the limitations of the proposed one-field FDM in Section 4.5.5, we know that the proposed scheme may be unstable when $\nu^\delta < 0$ (or $\nu^s < \nu^f$). In this chapter we only consider the case of $\nu^\delta = 0$, i.e. the solid viscosity is the same as the fluid viscosity ($\nu^s = \nu^f$). Although the case of $\nu^\delta > 0$ (or $\nu^s > \nu^f$) is also stable, however we consider this to be of relatively little interest. Please also refer to Section 7.2 for more discussion about why we only choose $\nu^\delta = 0$.

5.1 A 2-step splitting scheme

Using the splitting method of [163, Chapter 3] and [58], equation (3.9) can be expressed as the following two fractional steps.

(1) Convection step:

$$\int_{\Omega} \frac{\mathbf{u}_{n+1/2} - \mathbf{u}_n}{\Delta t} \cdot \mathbf{v} d\mathbf{x} + \int_{\Omega} (\mathbf{u}_{n+1/2} \cdot \nabla) \mathbf{u}_{n+1/2} \cdot \mathbf{v} d\mathbf{x} = 0. \quad (5.1)$$

(2) Diffusion step:

$$\begin{aligned} & \rho^f \int_{\Omega} \frac{\mathbf{u}_{n+1} - \mathbf{u}_{n+1/2}}{\Delta t} \cdot \mathbf{v} d\mathbf{x} + \frac{\nu^f}{2} \int_{\Omega} \mathbf{D}\mathbf{u}_{n+1} : \mathbf{D}\mathbf{v} d\mathbf{x} \\ & - \int_{\Omega} p_{n+1} \nabla \cdot \mathbf{v} d\mathbf{x} + \rho^\delta \int_{\Omega_{\mathbf{x}}^s} \frac{\mathbf{u}_{n+1} - \mathbf{u}_n}{\Delta t} \cdot \mathbf{v} d\mathbf{x} \\ & + \mu^s \Delta t \int_{\Omega_{\mathbf{x}}^s} \nabla_{\mathbf{X}} \mathbf{u}_{n+1} : \nabla_{\mathbf{X}} \mathbf{v} d\mathbf{X} = \mu^s \int_{\Omega_n^s} J_n^{-1} \nabla \cdot \mathbf{v} d\mathbf{x} \\ & - \mu^s \int_{\Omega_{\mathbf{x}}^s} \mathbf{F}_n : \nabla_{\mathbf{X}} \mathbf{v} d\mathbf{X} + \rho^f \int_{\Omega} \mathbf{g} \cdot \mathbf{v} d\mathbf{x} + \rho^\delta \int_{\Omega_{\mathbf{x}}^s} \mathbf{g} \cdot \mathbf{v} d\mathbf{x} + \int_{\Gamma_N} \bar{\mathbf{h}} \cdot \mathbf{v} d\Gamma, \end{aligned} \quad (5.2)$$

and

$$- \int_{\Omega} q \nabla \cdot \mathbf{u}_{n+1} d\mathbf{x} = 0, \quad (5.3)$$

with Dirichlet boundary condition (2.12), i.e.:

$$\mathbf{u}_{n+1} = \bar{\mathbf{u}} \quad \text{on} \quad \Gamma_D. \quad (5.4)$$

For this explicit scheme the domain Ω_n^s is fixed, so the above diffusion step becomes a linear equation at each time step. We focus on linearization of the convection step and the FEM discretization of the diffusion step in the following subsections respectively.

Remark 5.1. Summing the equations (5.1) and (5.2) and comparing with the implicit scheme (3.9), we can see that the 2-step scheme can actually be interpreted as evaluating the convection term in (3.9) by an intermediate value $\mathbf{u}_{n+1/2}$. How to get the value $\mathbf{u}_{n+1/2}$ depends on how the convection step is treated.

5.1.1 Treatment of the convection step

There are a variety of numerical methods to treat the pure convection equation (5.1), such as wave-like methods [58], characteristic based schemes [58, 67, 163], upwind schemes (including the Streamline Upwind Petrov Galerkin (SUPG) method) [58, 163] or the Least-squares method [94, 163]. In this section, two methods are considered to treat the convection equation: the Least-squares method and the Taylor-Galerkin method [86] (a particular, simplest, case of the wave-like method [58]). Readers may refer to [58] for more details of these methods.

Least-squares method

It is possible to linearize (5.1) using the value of \mathbf{u} from the last time step:

$$(\mathbf{u}_{n+1/2} \cdot \nabla) \mathbf{u}_{n+1/2} \approx (\mathbf{u}_{n+1/2} \cdot \nabla) \mathbf{u}_n + (\mathbf{u}_n \cdot \nabla) \mathbf{u}_{n+1/2} - (\mathbf{u}_n \cdot \nabla) \mathbf{u}_n. \quad (5.5)$$

Substituting (5.5) into equation (5.1) gives,

$$\begin{aligned} & \int_{\Omega} (\mathbf{u}_{n+1/2} + \Delta t (\mathbf{u}_{n+1/2} \cdot \nabla) \mathbf{u}_n + \Delta t (\mathbf{u}_n \cdot \nabla) \mathbf{u}_{n+1/2}) \cdot \mathbf{v} d\mathbf{x} \\ &= \int_{\Omega} (\mathbf{u}_n + \Delta t (\mathbf{u}_n \cdot \nabla) \mathbf{u}_n) \cdot \mathbf{v} d\mathbf{x}. \end{aligned} \quad (5.6)$$

For the Least-squares method [15], we may choose the test function in the following form:

$$\mathbf{v} = L(\mathbf{w}) = \mathbf{w} + \Delta t ((\mathbf{w} \cdot \nabla) \mathbf{u}_n + (\mathbf{u}_n \cdot \nabla) \mathbf{w}), \quad (5.7)$$

where $\mathbf{w} \in H_0^1(\Omega)$. In such a case, the weak form of (5.1) is:

$$\int_{\Omega} L(\mathbf{u}_{n+1/2}) \cdot L(\mathbf{w}) d\mathbf{x} = \int_{\Omega} (\mathbf{u}_n + \Delta t (\mathbf{u}_n \cdot \nabla) \mathbf{u}_n) \cdot L(\mathbf{w}) d\mathbf{x}. \quad (5.8)$$

A standard biquadratic finite element space is used to discretize equation (5.8) directly, although other spaces could be used.

Taylor-Galerkin method

Equation (5.1) is a backward discretization of the following pure convection equation:

$$\frac{\partial \mathbf{u}}{\partial t} = -(\mathbf{u} \cdot \nabla) \mathbf{u}. \quad (5.9)$$

The Taylor-Galerkin scheme is a second order approximation of the above equation [86]. First consider a 3-term Taylor series expansion of $\mathbf{u}_{n+1/2}$ at \mathbf{u}_n :

$$\mathbf{u}_{n+1/2} = \mathbf{u}_n + \Delta t \frac{\partial \mathbf{u}_n}{\partial t} + \frac{\Delta t^2}{2} \frac{\partial^2 \mathbf{u}_n}{\partial t^2}. \quad (5.10)$$

The second order derivative could be computed from the first order derivative (5.9):

$$\frac{\partial^2 \mathbf{u}}{\partial t^2} = -\left(\frac{\partial \mathbf{u}}{\partial t} \cdot \nabla\right) \mathbf{u} - (\mathbf{u} \cdot \nabla) \frac{\partial \mathbf{u}}{\partial t} = \{[(\mathbf{u} \cdot \nabla) \mathbf{u}] \cdot \nabla\} \mathbf{u} + (\mathbf{u} \cdot \nabla) [(\mathbf{u} \cdot \nabla) \mathbf{u}]. \quad (5.11)$$

We then get the following approximation of $\mathbf{u}_{n+1/2}$ by substituting equations (5.9) and (5.11) into (5.10):

$$\frac{\mathbf{u}_{n+1/2} - \mathbf{u}_n}{\Delta t} = -(\mathbf{u}_n \cdot \nabla) \mathbf{u}_n + \frac{\Delta t}{2} \{[(\mathbf{u}_n \cdot \nabla) \mathbf{u}_n] \cdot \nabla\} \mathbf{u}_n + \frac{\Delta t}{2} (\mathbf{u}_n \cdot \nabla) [(\mathbf{u}_n \cdot \nabla) \mathbf{u}_n]. \quad (5.12)$$

Notice there is a second order derivative in the last term of the above equation (5.12). In practice, one does not need to calculate the second order derivative. Instead, integration by parts may be used to reduce the order. It is convenient to use the tensor form to deduce the following formula, for a test function \mathbf{v} and a general vector \mathbf{w} ,

$$\int_{\Omega} (\mathbf{w} \cdot \nabla) [(\mathbf{w} \cdot \nabla) \mathbf{w}] \cdot \mathbf{v} d\mathbf{x} = \int_{\Omega} w_j \frac{\partial}{\partial x_j} \left(w_k \frac{\partial w_i}{\partial x_k} \right) v_i dx. \quad (5.13)$$

As previously i, j and k are automatically summed if they are repeated in one term. Therefore, we have when $\frac{\partial w_j}{\partial x_j} = \nabla \cdot \mathbf{w} = 0$ (true for $\mathbf{w} = \mathbf{u}_n$ due to incompressibility):

$$\int_{\Omega} w_j \frac{\partial}{\partial x_j} \left(w_k \frac{\partial w_i}{\partial x_k} \right) v_i dx = \int_{\Omega} \frac{\partial}{\partial x_j} \left(w_j w_k \frac{\partial w_i}{\partial x_k} \right) v_i dx. \quad (5.14)$$

Integrating by parts:

$$\int_{\Omega} \frac{\partial}{\partial x_j} \left(w_j w_k \frac{\partial w_i}{\partial x_k} \right) v_i dx = \int_{\Gamma} n_j w_j w_k \frac{\partial w_i}{\partial x_k} v_i d\Gamma - \int_{\Omega} w_j w_k \frac{\partial w_i}{\partial x_k} \frac{\partial v_i}{\partial x_j} dx. \quad (5.15)$$

Finally, let $\mathbf{w} = \mathbf{u}_n$ and use boundary condition (5.4) to get:

$$\begin{aligned} & \int_{\Omega} (\mathbf{u}_n \cdot \nabla) [(\mathbf{u}_n \cdot \nabla) \mathbf{u}_n] \cdot \mathbf{v} d\mathbf{x} \\ &= \int_{\Gamma_D} (\mathbf{n} \cdot \bar{\mathbf{u}}) (\bar{\mathbf{u}} \cdot \nabla) \bar{\mathbf{u}} \cdot \mathbf{v} d\Gamma - \int_{\Omega} [(\mathbf{u}_n \cdot \nabla) \mathbf{u}_n] \cdot [(\mathbf{u}_n \cdot \nabla) \mathbf{v}] d\mathbf{x}. \end{aligned} \quad (5.16)$$

Substituting (5.16) into equation (5.12), we may approximate (5.12) as:

$$\begin{aligned} & \int_{\Omega} \frac{\mathbf{u}_{n+1/2} - \mathbf{u}_n}{\Delta t} \cdot \mathbf{v} d\mathbf{x} + \int_{\Omega} (\mathbf{u}_n \cdot \nabla) \mathbf{u}_n \cdot \mathbf{v} d\mathbf{x} \\ &= \frac{\Delta t}{2} \int_{\Omega} \{[(\mathbf{u}_n \cdot \nabla) \mathbf{u}_n] \cdot \nabla\} \mathbf{u}_n \cdot \mathbf{v} - \frac{\Delta t}{2} \int_{\Omega} [(\mathbf{u}_n \cdot \nabla) \mathbf{u}_n] \cdot [(\mathbf{u}_n \cdot \nabla) \mathbf{v}] d\mathbf{x} \\ &+ \frac{\Delta t}{2} \int_{\Gamma_D} (\mathbf{n} \cdot \bar{\mathbf{u}}) (\bar{\mathbf{u}} \cdot \nabla) \bar{\mathbf{u}} \cdot \mathbf{v} d\Gamma. \end{aligned} \quad (5.17)$$

or

$$\begin{aligned} \int_{\Omega} \mathbf{u}_{n+1/2} \cdot \mathbf{v} d\mathbf{x} &= \int_{\Omega} \mathbf{u}_n \cdot \mathbf{v} d\mathbf{x} - \Delta t \int_{\Omega} (\mathbf{u}_n \cdot \nabla) \mathbf{u}_n \cdot \mathbf{v} d\mathbf{x} \\ &+ \frac{\Delta t^2}{2} \int_{\Omega} \{[(\mathbf{u}_n \cdot \nabla) \mathbf{u}_n] \cdot \nabla\} \mathbf{u}_n \cdot \mathbf{v} - \frac{\Delta t^2}{2} \int_{\Omega} [(\mathbf{u}_n \cdot \nabla) \mathbf{u}_n] \cdot [(\mathbf{u}_n \cdot \nabla) \mathbf{v}] d\mathbf{x} \\ &+ \frac{\Delta t^2}{2} \int_{\Gamma_D} (\mathbf{n} \cdot \bar{\mathbf{u}}) (\bar{\mathbf{u}} \cdot \nabla) \bar{\mathbf{u}} \cdot \mathbf{v} d\Gamma. \end{aligned} \quad (5.18)$$

Remark 5.2. It is important to use a distributed/consistent mass matrix (instead of a lumped mass matrix) when implementing (5.18). The results of using these two types of mass matrix are compared in Test1-2D (activated disc in Section 5.2.1) and Test2-2D (stretched disc in Section 5.2.2). A study and comparison of the consistent and lumped mass matrix can also be found in [61].

5.1.2 FEM discretization of the diffusion step

We only describe here the discretization for the diffusion step, since the convection step just follows a very standard FEM discretization procedure [94, 163]. A mixed finite element method to discretize equation (5.2) and (5.3) gives the following linear algebraic system (for details of assembling this global matrix and the right-hand side vector, please refer to Appendix B):

$$\begin{bmatrix} \mathbf{A} & \mathbf{B} \\ \mathbf{B}^T & \mathbf{0} \end{bmatrix} \begin{pmatrix} \mathbf{u} \\ \mathbf{p} \end{pmatrix} = \begin{pmatrix} \mathbf{b} \\ \mathbf{0} \end{pmatrix}, \quad (5.19)$$

where

$$\mathbf{A} = \mathbf{M}/\Delta t + \mathbf{K} + \mathbf{D}^T (\mathbf{M}^s/\Delta t + \mathbf{K}^s) \mathbf{D}, \quad (5.20)$$

and

$$\mathbf{b} = \mathbf{f} + \mathbf{D}^T \mathbf{f}^s + \mathbf{M} \mathbf{u}_{n+1/2}/\Delta t + \mathbf{D}^T \mathbf{M}^s \mathbf{D} \mathbf{u}_n/\Delta t. \quad (5.21)$$

In the above, all the matrices and vectors have the same meaning as those in Section 4.2 except vector \mathbf{f} , which does not include the convection term because it is treated in a separate step.

5.1.3 The 2-step splitting algorithm

We now describe the solution algorithm for the 2-step splitting method at each time step in Algorithm 5.

Algorithm 5: The explicit 2-step splitting algorithm for the one-field FDM

- 1 Given the solid configuration Ω_n^s and velocity field $\mathbf{u}_n = \begin{cases} \mathbf{u}_n^f & \text{in } \Omega_n^f \\ \mathbf{u}_n^s & \text{in } \Omega_n^s \end{cases}$ at time step n .
 - 2 Discretize the convection equation using (5.8) or (5.18) and solve it to get an intermediate velocity $\mathbf{u}_{n+1/2}$.
 - 3 Compute the interpolation matrix and solve equation (5.19) using $\mathbf{u}_{n+1/2}$ and \mathbf{u}_n^s as initial values to get velocity field \mathbf{u}_{n+1} .
 - 4 Compute solid velocity $\mathbf{u}_{n+1}^s = \mathbf{D}\mathbf{u}_{n+1}$ and update the solid mesh by $\Omega_{n+1}^s = \{\mathbf{x}_{n+1} : \mathbf{x}_{n+1} = \mathbf{x}_n + \mathbf{u}_{n+1}^s \Delta t\}$, for all $\mathbf{x}_n \in \Omega_n^s$, then go to step 1 for the next time step.
-

5.2 Numerical tests for the 2-step splitting scheme

In this section, we present some numerical examples that have been selected to allow us to assess the accuracy and the versatility of the proposed 2-step splitting scheme. We demonstrate convergence in time and space. Furthermore, we favourably compare results with those obtained using FDM [5, 79, 150], IFEM [137, 156] and ALE method [133], as well as comparing against results from laboratory experiment [70, 156].

In order to improve the computational efficiency, an adaptive spatial mesh with hanging nodes is used in some of the following numerical experiments (mainly for thin solids). However, we shall not discuss details of this adaptive mesh in this thesis, which is not the core of the proposed method. Readers can refer to [7, 56, 62, 152] and Appendix E for details of the treatment of hanging nodes.

5.2.1 Test1-2D (activated disc): Oscillating disc driven by an initial kinetic energy

We use the same test as in Section 4.4.1 to compare the energy growth between the implicit scheme and this 2-step explicit splitting scheme. The deformed solid, with velocity norm, at $t = 0.7$ are compared in Figure 5.1, from which it can be seen that the difference of velocity norm between these two schemes decreases when reducing the size time step. The evolution of the energy ratio (see (3.54)) is plotted in Figure 5.2, from which it can be seen that the Least squares method converges similarly to the implicit scheme, and the error between them becomes smaller with reducing time step. The same figure also shows that the Taylor-Galerkin method, if using a lumped mass matrix, stops converging as Δt is reduced, but however converges almost the same as the Least squares method if using a distributed mass matrix. This indicates the importance of using a distributed mass matrix when implementing the convection step (5.1) as discussed in Remark 5.2.

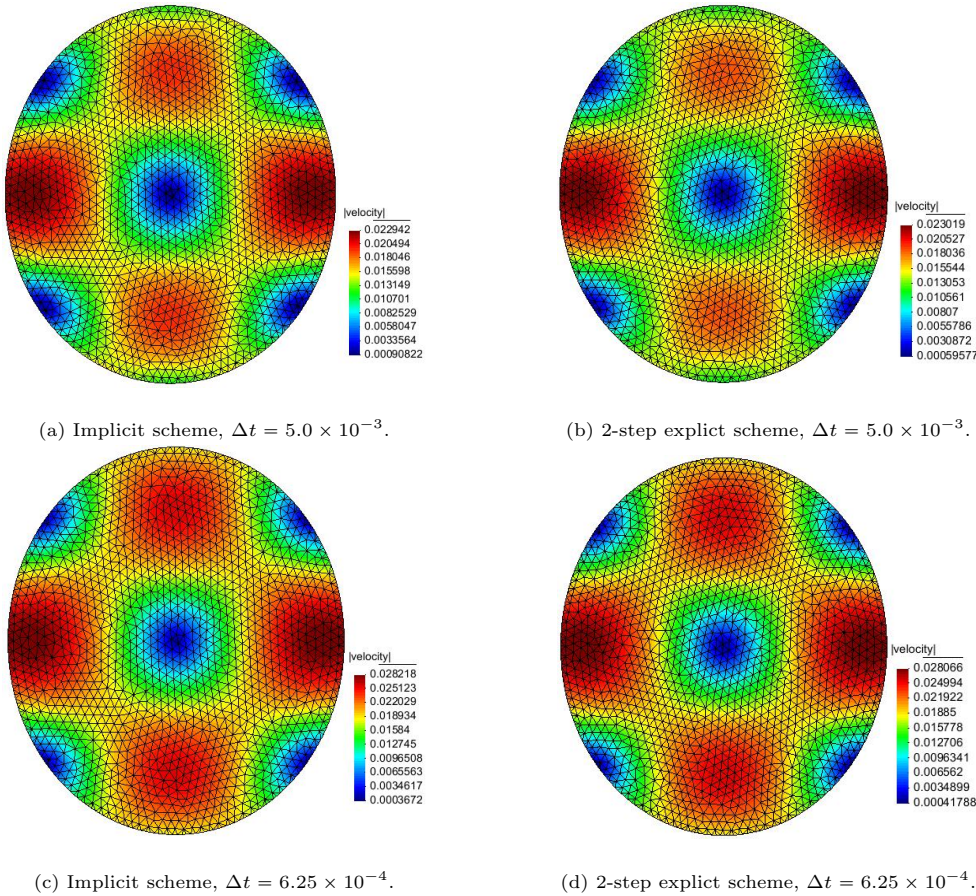


Figure 5.1: Configuration of solid at $t = 0.7$ for Test1-2D (activated disc) in Section 5.2.1 (Least-squares method for convection).

5.2.2 Test2-2D (stretched disc): Oscillating disc driven by an initial potential energy

We next investigate the numerical test of Section 4.4.2 in order to compare the results between the implicit scheme and this 2-step explicit splitting scheme. The configurations of solid with velocity norm at time $t = 0.9$ and $t = 2$ are compared in Figures 5.3 and 5.4 respectively. From these it can be seen that the difference of velocity norm between the two schemes again decreases when reducing the size of time step. The evolution of total energy ratio (defined in (3.54)) is plotted in Figure 5.5, from which it can be seen that both the implicit and the Least-squares 2-step explicit splitting schemes converge at a similar rate (which is approximately first order). However when using a lumped mass matrix the order of the Taylor-Galerkin 2-step explicit splitting scheme converges slightly slower, and when using a distributed mass matrix the order of the Taylor-Galerkin method converges almost the same as that using the Least squares method. This again suggests that using a distributed mass matrix is better than using

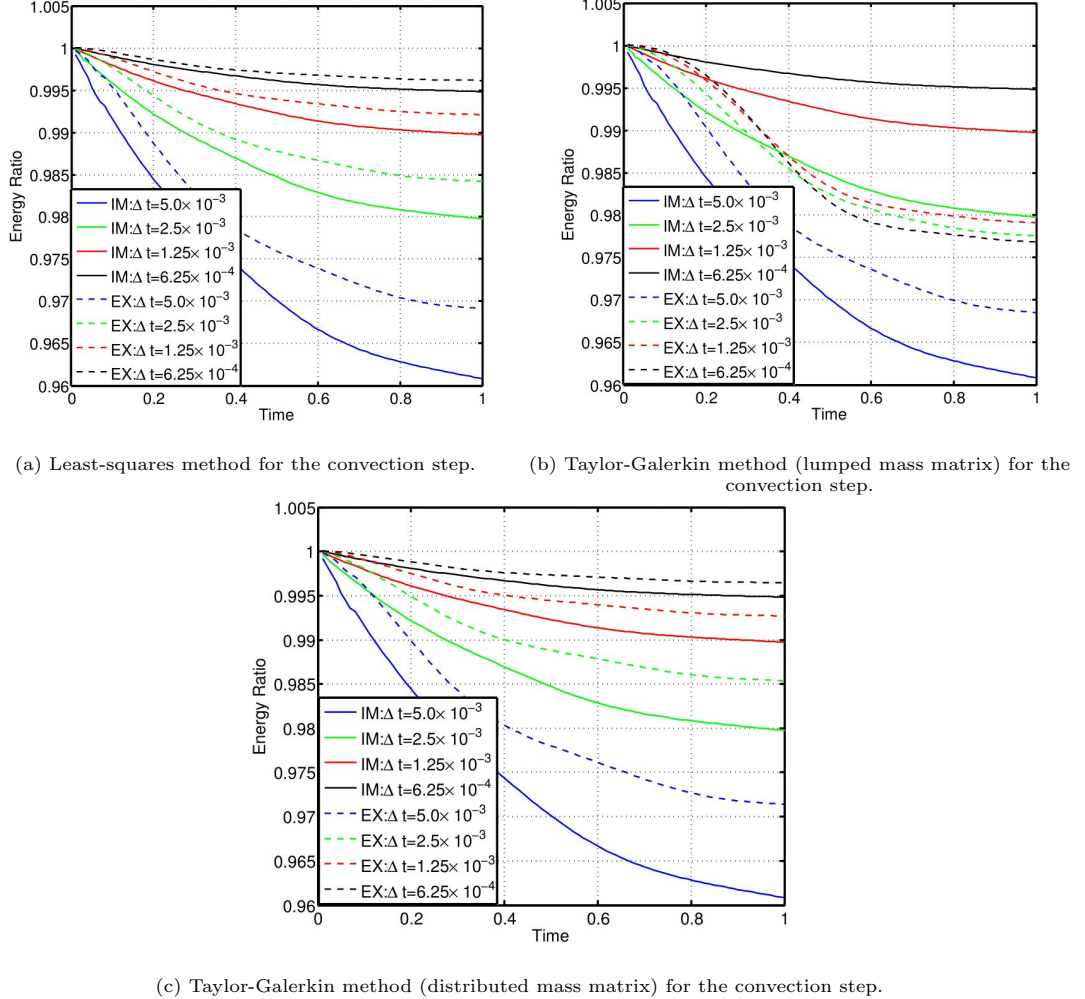


Figure 5.2: Evolution of the energy ratio (defined in (3.54)) for Test1-2D (activated disc) in Section 5.2.1.

a lumped mass matrix when implementing the convection step (5.1).

5.2.3 Test3-3D (activated ball): Oscillating ball driven by an initial kinetic energy

In this test we revisit the oscillating ball discussed in Section 4.4.3 and compare the energy of the 2-step splitting scheme with the implicit scheme. The comparison of energy evolution is shown in Figure 5.6, from which it can be seen that the implicit scheme and this 2-step splitting scheme give very similar energy behaviour. This, and the previous 2D results suggest that the 2-step splitting scheme could present very accurate results, at least in the case of low Reynolds number.

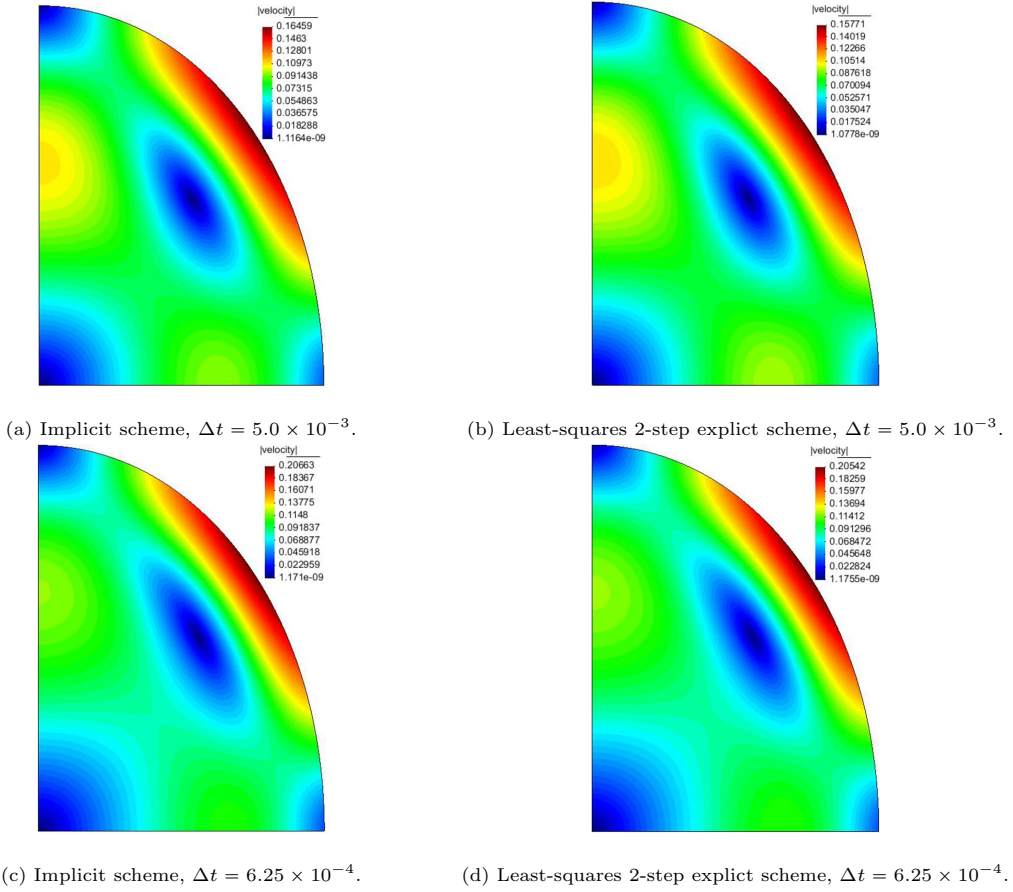


Figure 5.3: Configuration of solid at $t = 0.9$ for Test2-2D (stretched disc) in Section 5.2.2 (the solid is maximum stretched to the y direction).

5.2.4 Test7-2D (cavity with disc): Cavity flow with a solid disc (Parameter 1-3)

We use the numerical example which has already been studied in Section 4.5.4 (the first three parameter sets are considered here) to compare with the IFEM method [137, 161]. In order to compare in detail, we also implement the IFEM by using the isoparametric FEM interpolation function, which is suggested to be capable of producing a sharp interface in [137]. Please refer to [156, 157] for other interpolation functions such as the discretized delta function and RKPM function.

We use the same mesh for the proposed one-field FDM method and IFEM method, and a time step of $\Delta t = 1.0 \times 10^{-3}$. Figure 5.7 shows the configuration of the deformed disc at two different stages, from which we do not observe significant differences of the velocity norm even for a long run as shown in Figure 5.7 (b).

We also test different densities, and the cases of $\mu^s = 1.0$ and $\mu^s = 100$ (see Figure 5.8 and

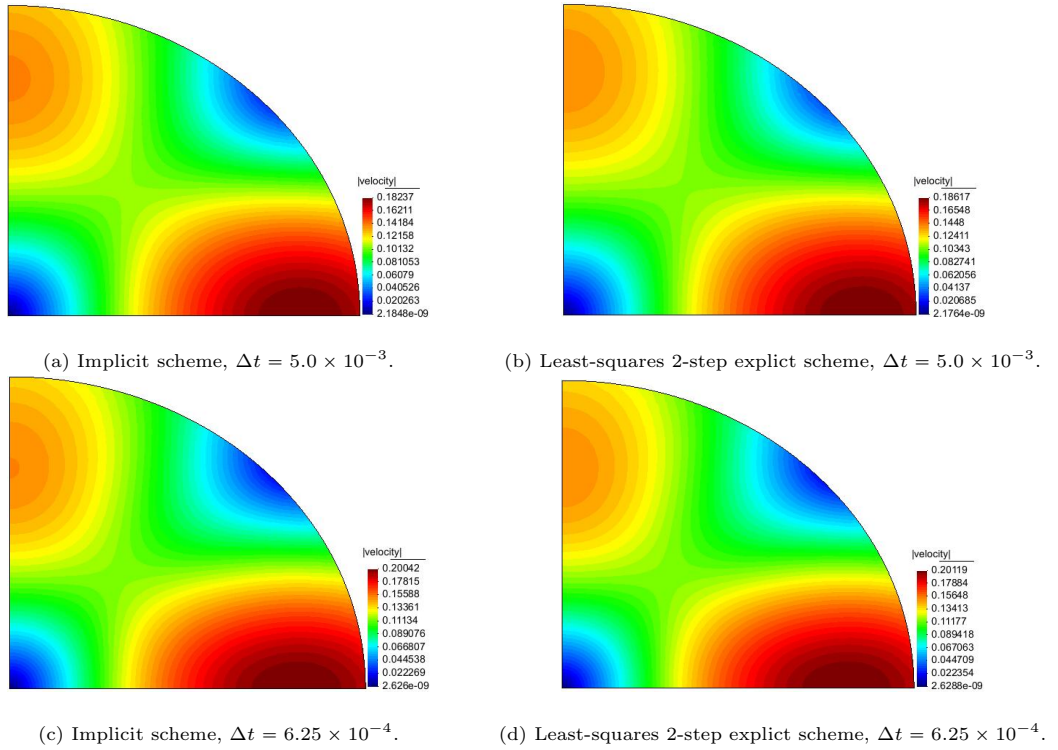


Figure 5.4: Configuration of solid at $t = 2.0$ for Test2-2D (stretched disc) in Section 5.2.2.

5.9 respectively). For the proposed method we can use $\mu^s = 100$ or larger in order to make the solid behave like a rigid body without changing time step. This is not possible for the IFEM for which the simulation breaks down for $\mu^s = 100$, even for very small the time step, due to the huge FSI force on the right-hand side of the IFEM system.

Let us we compare the solid deformation between the implicit and the 2-step splitting schemes in Figure 5.10 after a long run ($t = 20$). It can be observed that the results of these two schemes match very well. Finally we compare the **F**-scheme and **σ** -scheme via the solid deformation as shown in Figure 5.11, from which it can been seen that both schemes present similar results.

5.2.5 Test8-2D (leaflet): An oscillating leaflet

This numerical example is used by [5, 79, 150] to validate their methods. We first use the same parameters as used in the above three publications in order to compare results and test convergence in time and space. We then use a wide range of parameters to show the robustness of the proposed one-field FDM. The computational domain is a $L \times H$ channel with a $h \times w$ leaflet located across it as shown in Figure 5.12. A periodic flow condition is prescribed on the inlet and outlet boundaries, given by $u_x = 15.0y(2 - y)\sin(2\pi t)$. Gravity is not considered in

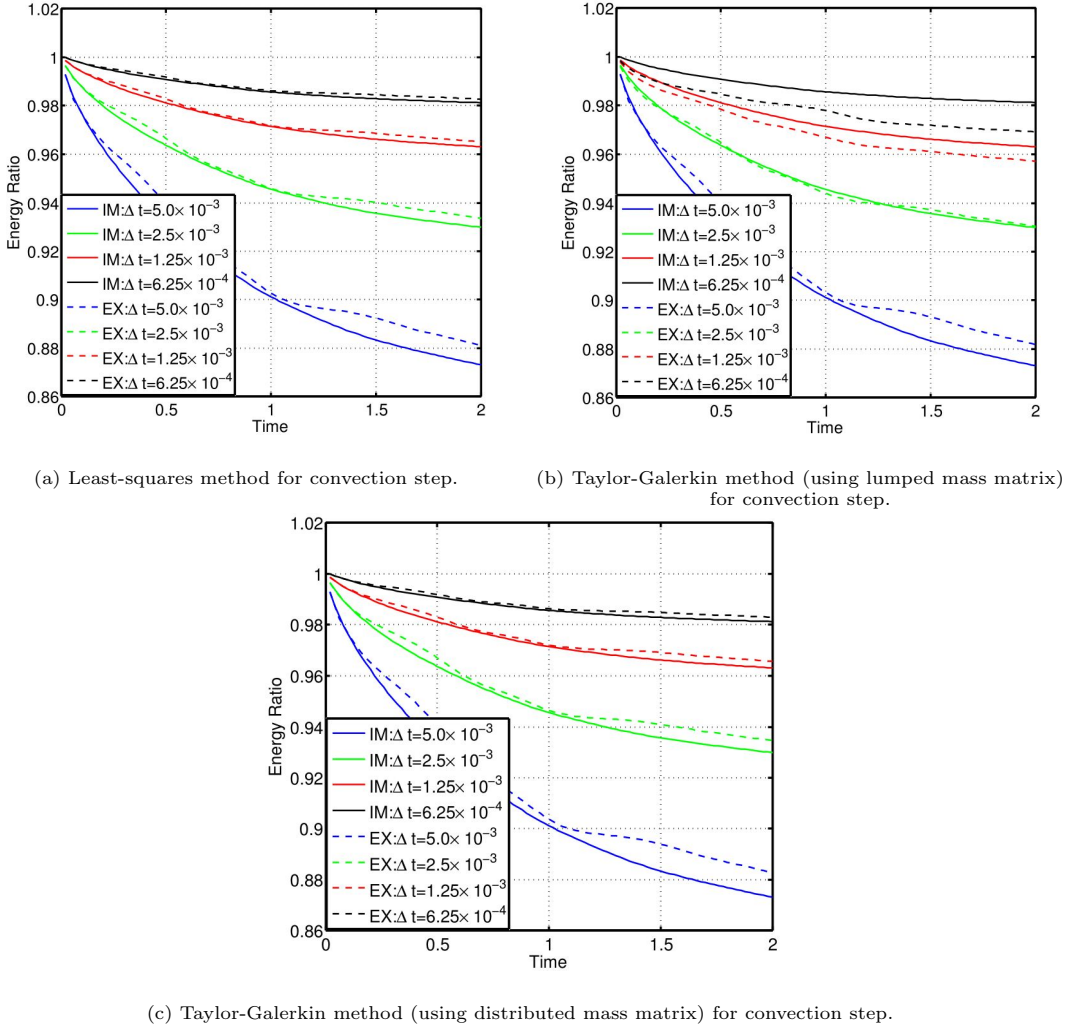


Figure 5.5: Evolution of the energy ratio (defined in (3.54)) for Test2-2D (stretched disc) in Section 5.2.2.

the first test case (i.e. $\mathbf{g} = 0$), and other fluid and solid properties are presented in Table 5.2. Taking the average velocity $\bar{U} = \int_0^H u_x dy = 10$ and the channel height H as the characteristic velocity and length respectively, the Reynolds number is: $Re = \frac{\rho^f \bar{U} H}{\nu^f} = 100$.

Fluid	Leaflet
$L = 4.0 \text{ m}$	$w = 0.0212 \text{ m}$
$H = 1.0 \text{ m}$	$h = 0.8 \text{ m}$
$\rho^f = 100 \text{ kg/m}^3$	$\rho^s = 100 \text{ kg/m}^3$
$\nu^f = 10 \text{ N} \cdot \text{s/m}^2$	$\mu^s = 10^7 \text{ N/m}^2$

Table 5.2: Properties and domain size for Test8-2D (leaflet) in Section 5.2.5 with a leaflet oriented across the flow direction.

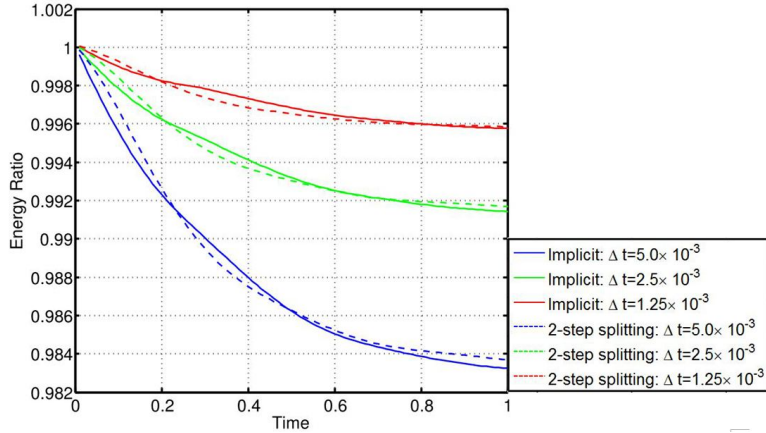


Figure 5.6: Evolution of energy ratio (defined in (3.54)) for Test3-3D (activated ball) in Section 5.2.3.

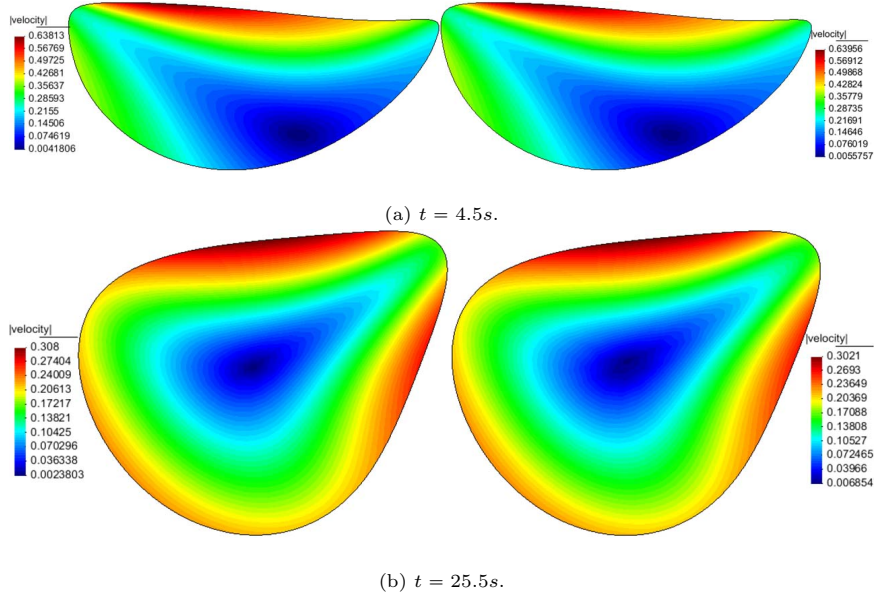


Figure 5.7: Velocity norm for a soft solid ($\mu^s = 0.1$) using the one-field FDM (left) and IFEM (right). Test7-2D (cavity with disc) in Section 5.2.4

The leaflet is approximated with 1200 linear triangles with 794 nodes (medium mesh size), and the corresponding fluid mesh is adapted in the vicinity of the leaflet so that it has a similar size. A stable time step $\Delta t = 5.0 \times 10^{-4}$ is used in the simulations illustrated in Figure 5.13, which shows the configuration of the leaflet for different times.

Previously published numerical results are qualitatively similar to those in Figure 5.13 but show some quantitative variations. For example, [5] solved a fully-coupled system but the coupling is limited to a line, and the solid in their results (Figure 7 (l) in [5]) behaves as if it is slightly harder. Alternatively, [150] used a fractional step scheme to solve the FSI equations

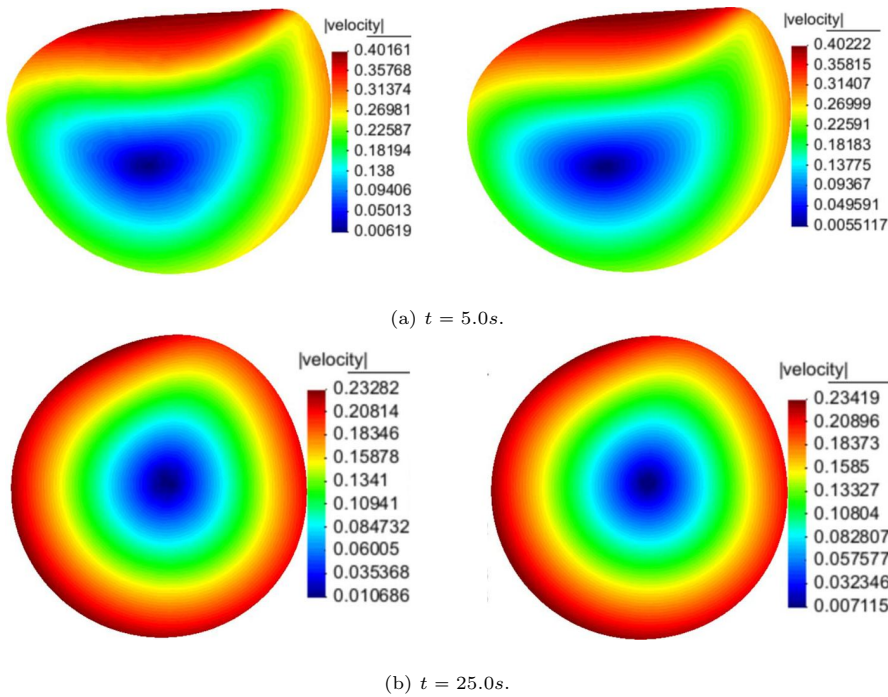
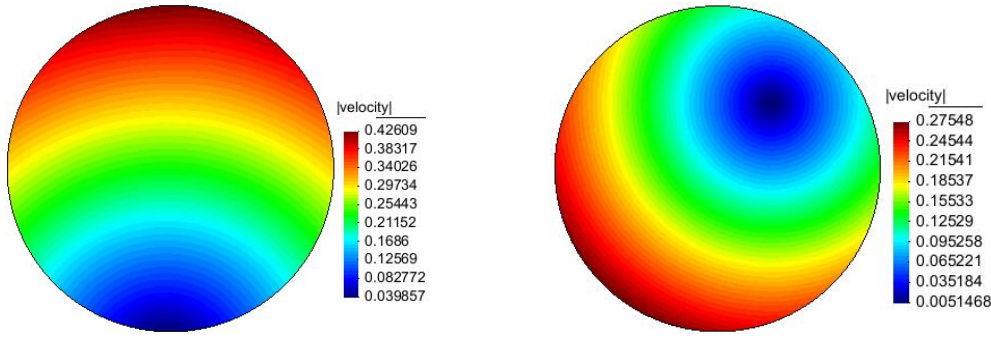


Figure 5.8: Velocity norm for a soft solid ($\mu^s = 1.0$) using the one-field FDM (left) and IFEM (right). Test7-2D (cavity with disc) in Section 5.2.4.



(a) $t = 5.0\text{s}$ (The disc arrives at the top of the cavity). (b) $t = 30.0\text{s}$.

Figure 5.9: Velocity norm for a hard solid ($\mu^s = 100$) using the one-field FDM. Test7-2D (cavity with disc) in Section 5.2.4.

combined with a penalty method to enforce the incompressibility condition. In their results (Fig. 3(h) in [150]) the leaflet behaves as if it is slightly softer than [5] and harder than [79]. In [79] a beam formulation is used to describe the solid. The fluid mesh is locally refined using hierarchical B-Splines, and the FSI equation is solved monolithically. The leaflet in their results (Fig. 34 in [79]) behaves as softer than the other two considered here. Our results in Figure 5.13 are most similar to those of [79]. This may be seen more precisely by inspection of the

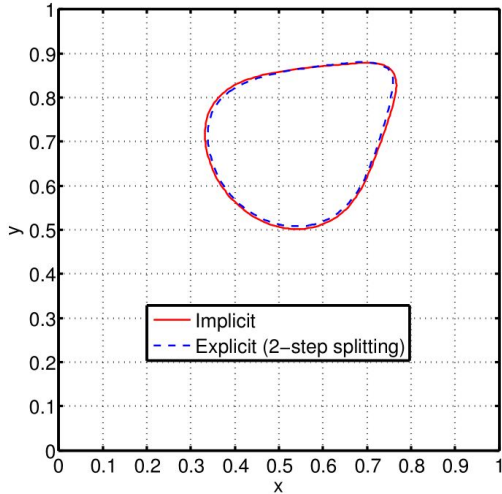


Figure 5.10: Comparison of the solid deformation at $t = 20s$ for Test7-2D (cavity with disc) in Section 5.2.4, using the same mesh size and time step $\Delta t = 1.0 \times 10^{-3}$.

graphs of the oscillatory motion of the leaflet tip in Figure 5.14, corresponding to Fig. 32 in [79]. Having validated our results for this example against the work of others, we shall use this test case to further explore more details of our method.

We commence by testing the influence of the ratio of fluid and solid mesh sizes: $r_m = (\text{local solid nodes})/(\text{local fluid nodes})$. Fixing the fluid mesh size, three different solid mesh sizes are chosen: coarse (640 linear triangles with 403 nodes $r_m \approx 0.5$), medium (1200 linear triangles with 794 nodes $r_m \approx 1$) and fine (2560 linear triangles with 1445 nodes $r_m \approx 2$), and a stable time step $\Delta t = 5.0 \times 10^{-4}s$ is used throughout. From these tests we observe that there is a slight difference in the solid configuration for different meshes, as illustrated at $t = 0.6$ in Figure 5.15. Significantly however, the difference in displacement decreases as the solid mesh becomes finer. Further, we found that $r_m \approx 1$ ensures the accuracy of the proposed approach, which can be confirmed from the comparison with the monolithic approach from Figure 5.14. This is similar to comparison with IFEM in Section 5.2.4: Test7-2D (cavity with disc), with fitted ALE method in Section 5.2.6: Test9-2D (thin flag) or with laboratory results in Section 5.2.7: Test10-2D (channel with solids), all of which use a mesh ratio of $r_m \approx 1$ and achieve the same accuracy of their results.

We next consider convergence tests undertaken for refinement of both the fluid and solid meshes with the fixed ratio of mesh sizes $r_m \approx 1$. Four different levels of meshes are used, the solid meshes are: coarse (584 linear triangles with 386 nodes), medium (1200 linear triangles with 794 nodes), fine (2560 linear triangles with 1445 nodes), and very fine (3780 linear triangles with 2085 nodes). The fluid meshes, at their maximum refinement level, have the corresponding sizes to the solid mesh. As can be seen in Figure 5.16 and Table 5.3, the velocity is converging as the mesh becomes finer.

In addition, we consider tests of convergence in time using a fixed ratio of fluid and solid

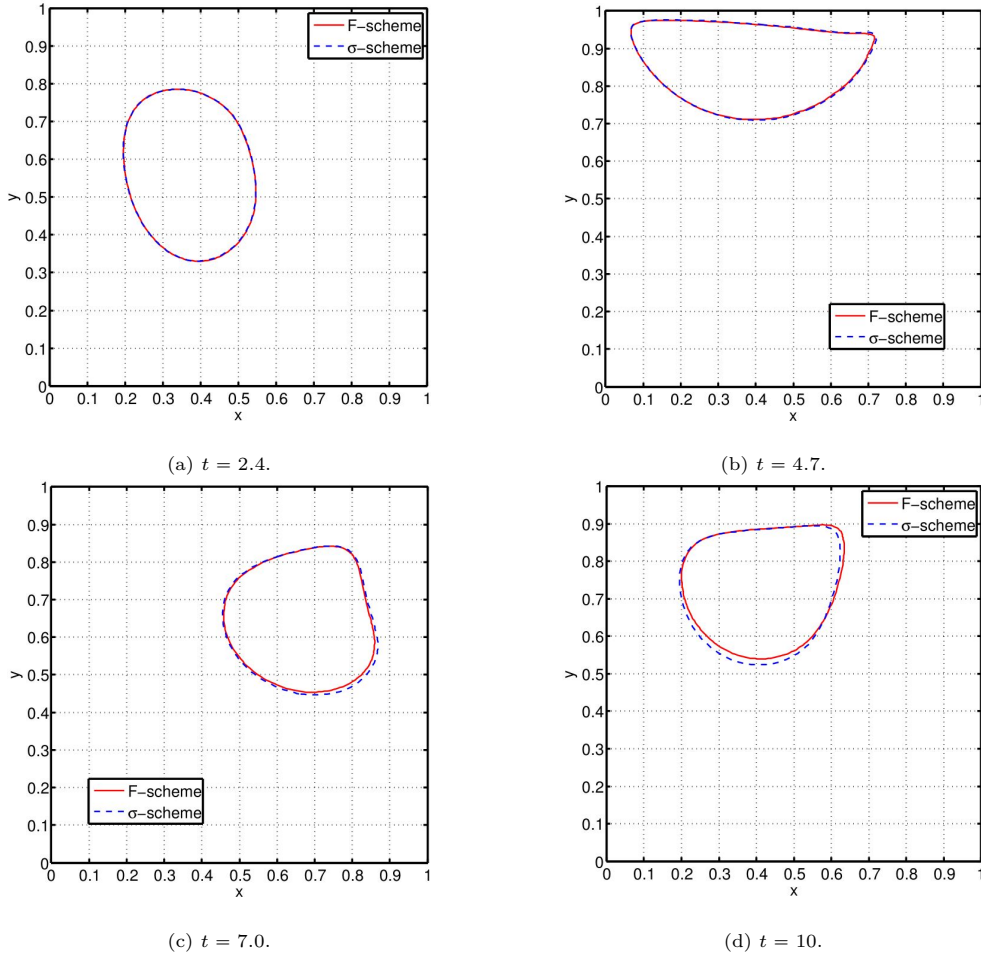


Figure 5.11: Solid deformation for Parameter 1 in Test7-2D (cavity with disc) in Section 5.2.4.

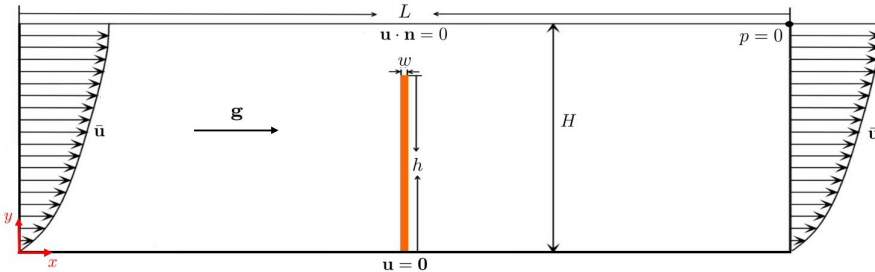


Figure 5.12: Computational domain and boundary conditions for Test8-2D (leaflet) in Section 5.2.5.

mesh sizes $r_m \approx 1$. Using the medium solid mesh size and the same fluid mesh size as above, results are shown in Figure 5.17 and Table 5.4. From these it can be seen that the velocities are converging as the time step decreases.

Finally, in order to assess the robustness of our approach, we vary each of the physical

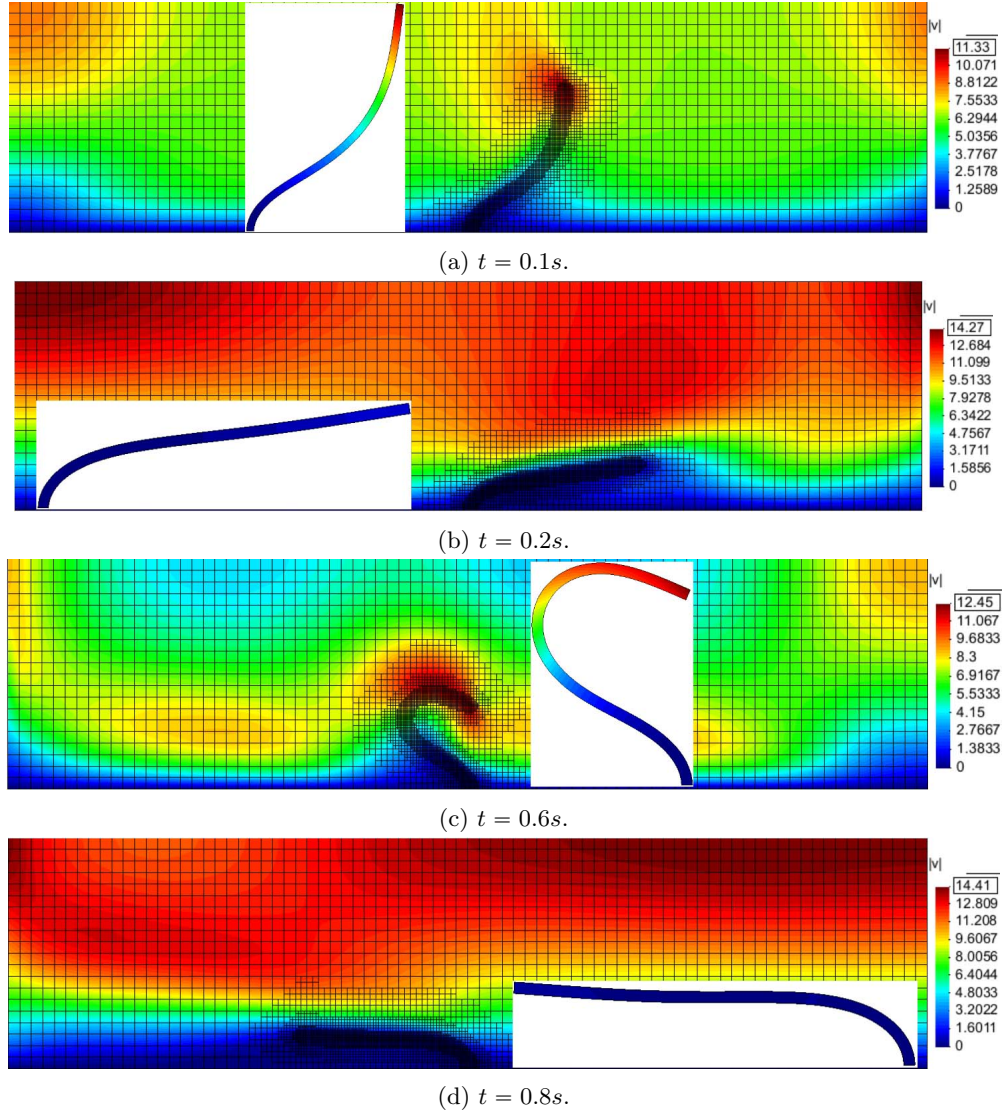


Figure 5.13: Configuration of the leaflet and magnitude of velocity on the adaptive fluid mesh for Test8-2D (leaflet) in Section 5.2.5.

Between different mesh sizes	Difference of maximum horizontal velocity at $t = 0.5s$
coarse and medium	0.01497
medium and fine	0.00214
fine and very fine	0.00190

Table 5.3: Comparison of maximum velocity for different meshes. Test8-2D (leaflet) in Section 5.2.5.

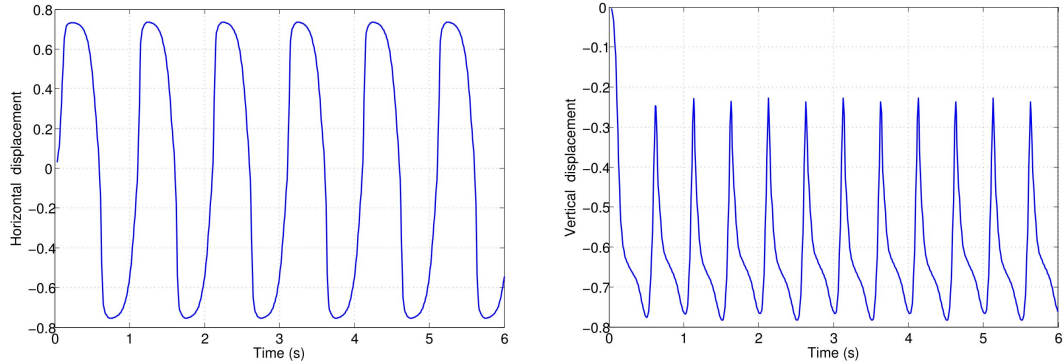


Figure 5.14: Evolution of horizontal and vertical displacement at top right corner of the leaflet ($r_m \approx 1$) for Test8-2D (leaflet) in Section 5.2.5.

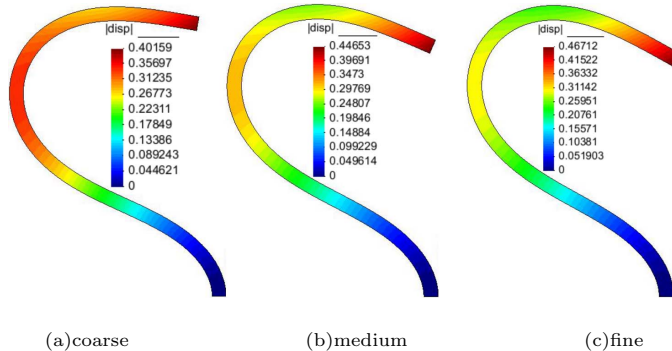


Figure 5.15: Configuration of leaflet for different mesh ratio r_m , and contour plots of displacement magnitude at $t = 0.6$ for Test8-2D (leaflet) in Section 5.2.5.

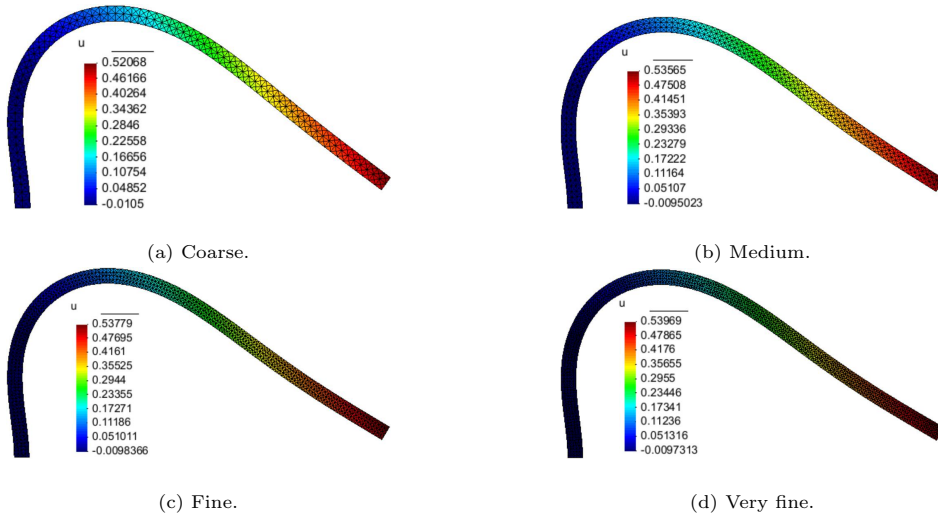


Figure 5.16: Contour plots of the horizontal velocity at $t = 0.5s$ for Test8-2D (leaflet) in Section 5.2.5, using different sizes of mesh.

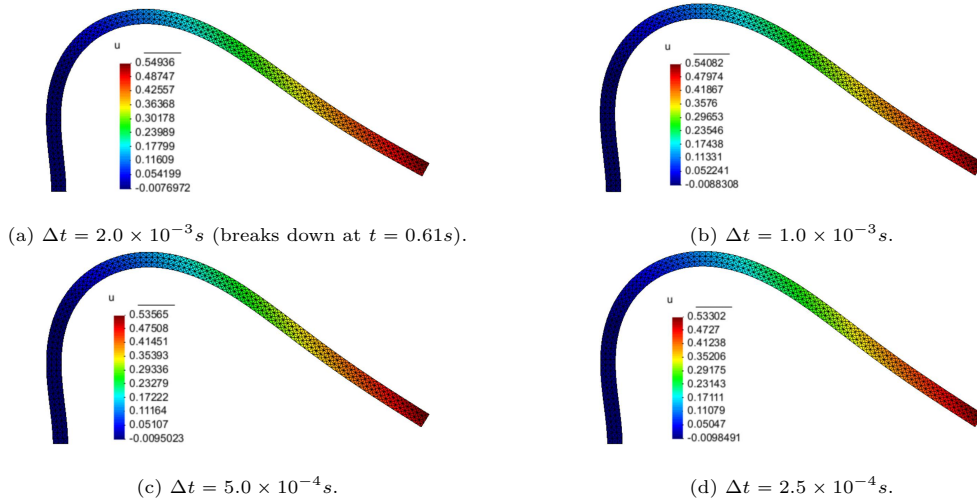


Figure 5.17: Contour plots of the horizontal velocity at $t = 0.5s$ for Test8-2D (leaflet) in Section 5.2.5, using different time steps and a medium size of mesh.

Steps sizes compared	Difference of maximum horizontal velocity at $t = 0.5s$
$\Delta t = 2.0 \times 10^{-3}$ and $\Delta t = 1.0 \times 10^{-3}$	0.00854
$\Delta t = 1.0 \times 10^{-3}$ and $\Delta t = 5.0 \times 10^{-4}$	0.00517
$\Delta t = 5.0 \times 10^{-4}$ and $\Delta t = 2.5 \times 10^{-4}$	0.00263

Table 5.4: Comparison of maximum velocity for different time step size. Test8-2D (leaflet) in Section 5.2.5.

parameters using three different cases as shown in Figure 5.18. A medium mesh size with fixed $r_m \approx 1$ is used to undertake all of these tests. The dimensionless parameters shown in Figure 5.18 are defined as: $\rho^r = \frac{\rho^s}{\rho^f}$, $\bar{\mu}^s = \frac{\mu^s}{\rho^f U^2}$, $Re = \frac{\rho^f U H}{\nu^f}$ and $Fr = \frac{g H}{U^2}$, where the average velocity $U = 10$ in this example. The period of inlet flow is $T = 1$.

It can be seen from the results of group (a) that the larger the value of shear modulus $\bar{\mu}^s$ the harder the solid behaves, however a smaller time step is required. For the case of $\bar{\mu}^s = 10^9$, the solid behaves almost like a rigid body, as we would expect. From the results of group (b) it is clear that the Reynolds Number (Re) has a large influence on the behaviour of the solid. The density and gravity have relatively less influence on the behaviour of the solid in this problem which can be seen from the results of group (c) and group (d) respectively.

5.2.6 Test9-2D (thin flag): An oscillating thin flag

The following test problem is taken from [133], which describes an implementation on an ALE fitted mesh. It has since been used as a benchmark to validate different numerical schemes [70, 79]. The computational domain is a rectangle with a block cut off and a flag attached behind it as shown in Figure 5.19, in which the size of geometry and the boundary conditions

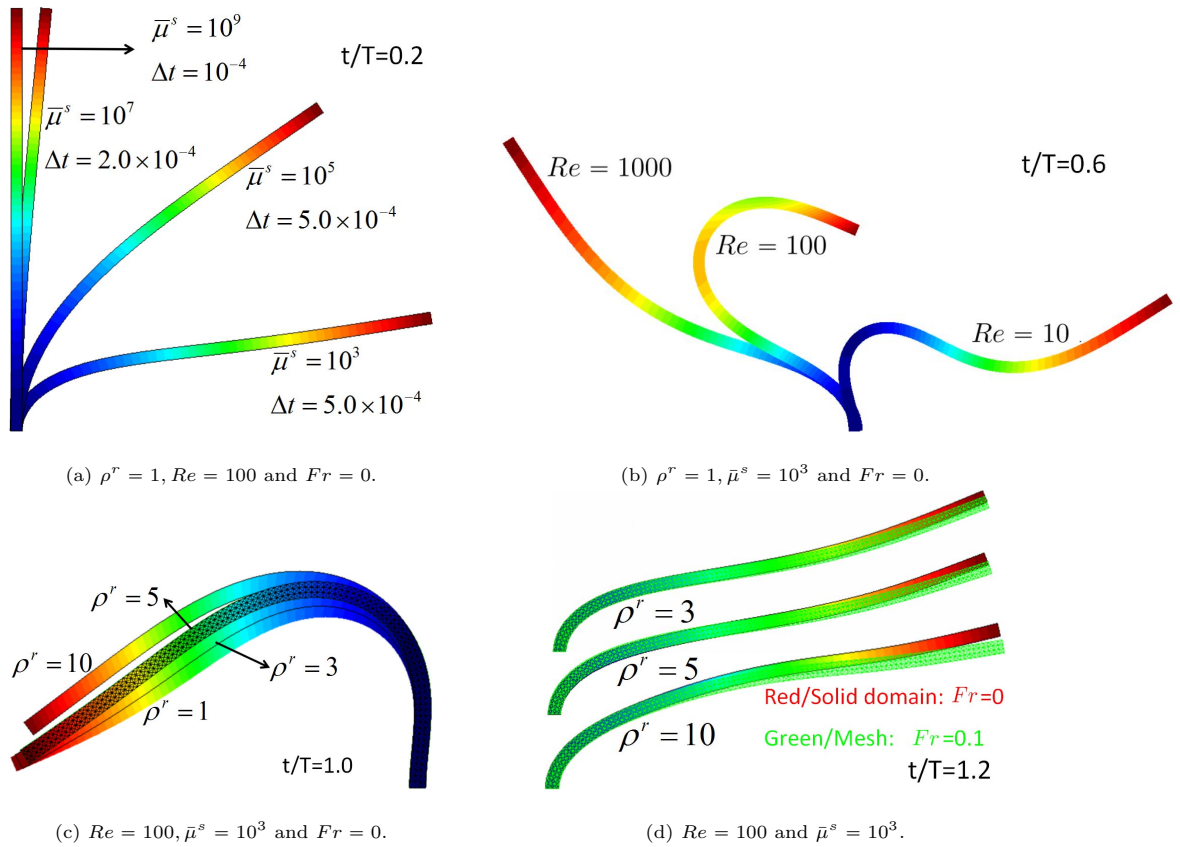


Figure 5.18: Parameters sets and results for Group (b)~(d) of Test8-2D (leaflet) in Section 5.2.5, using a time step of $\Delta t = 5.0 \times 10^{-4}$ s.

are displayed as well.

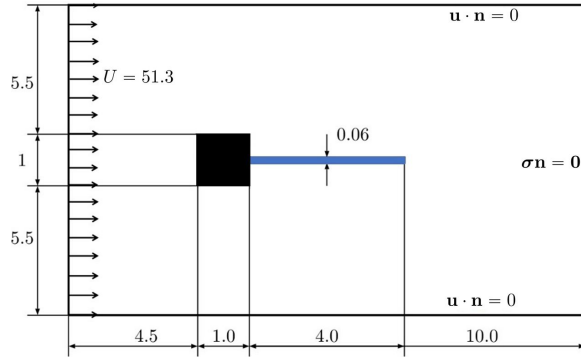
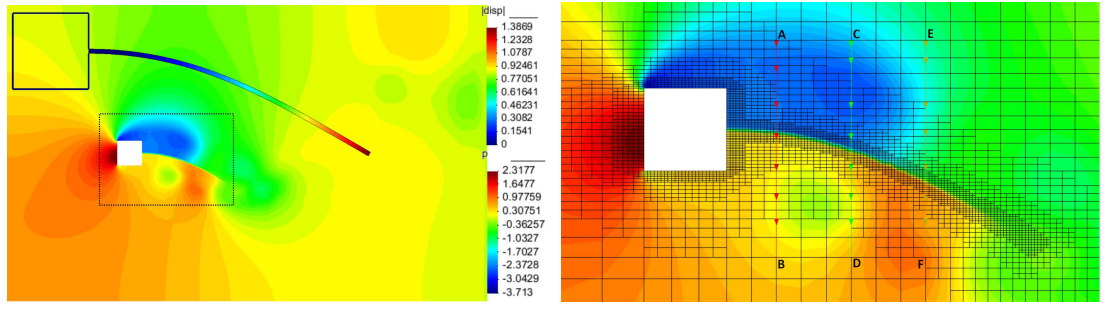


Figure 5.19: Computational domain and boundary condition for Test9-2D (thin flag) in Section 5.2.6.

For the fluid, the viscosity and density are $\nu^f = 1.82 \times 10^{-4}$ and $\rho^f = 1.18 \times 10^{-3}$ respectively. For the solid, we use shear modulus $\mu^s = 9.2593 \times 10^5$ and density $\rho^s = 0.1$. Taking the inlet



(a) Leaflet displacement and fluid pressure.

(b) Mesh refinement near the structure.

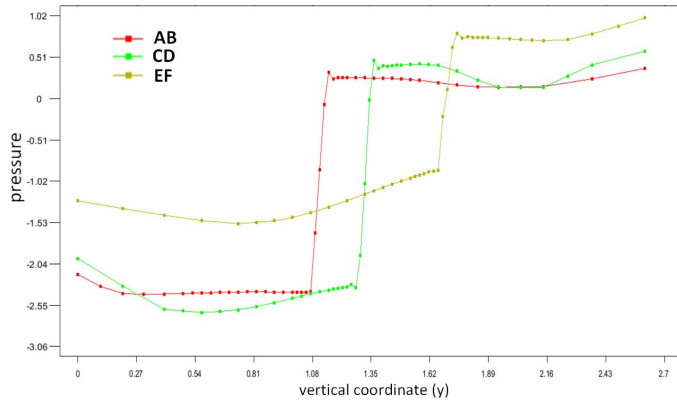
Figure 5.20: Contour plots of leaflet displacement and fluid pressure at $t = 5.44s$ for Test9-2D (thin flag) in Section 5.2.6.

Figure 5.21: Distribution of pressure across the leaflet on the three lines in Figure 5.20 (b) for Test9-2D (thin flag) in Section 5.2.6.

velocity $U = 51.3$ and the height of the block ($H = 1$) as the characteristic velocity and length respectively, the Reynolds number is: $Re = \frac{\rho f U H}{\nu f} = 333$. The leaflet is discretized by 1063 three-node linear triangles with 666 nodes, and the corresponding fluid mesh locally has a similar node density to the leaflet ($r_m \approx 1$). Snapshots of the leaflet deformation and fluid pressure at $t = 5.44s$ are illustrated in Figure 5.20. In Figure 5.21, the distributions of pressure across the leaflet corresponding to the three lines (AB, CD and EF) in Figure 5.20 (b) are plotted. From this we can observe that the sharp jumps of pressure across the leaflet are captured.

The evolution of the vertical displacement of the leaflet tip with respect to time is plotted in Figure 5.22. Both the magnitude (1.34) and the frequency (2.94) have a good agreement with the result of [133], using a fitted ALE mesh and of [79], using a monolithic unfitted mesh approach. These results are all within the range of values in [79, Table 4] (magnitude: $1.1 \sim 1.4$ and frequency: $2.78 \sim 3.22$). Note that since the initial condition before oscillation for these simulations is an unstable equilibrium, the first perturbation from this regime is due to numerical disturbances.

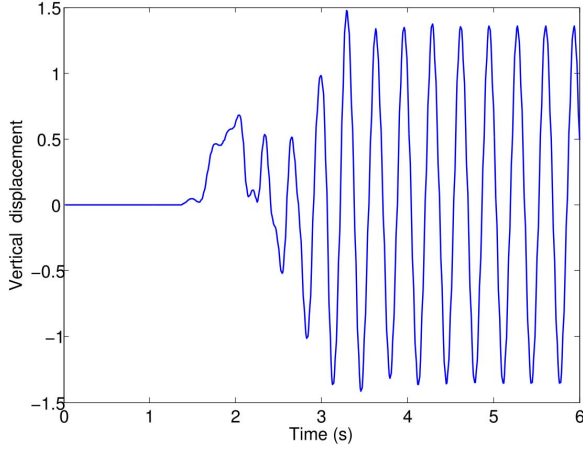


Figure 5.22: Displacement of the leaflet tip as a function of time for Test9-2D (thin flag) in Section 5.2.6.

5.2.7 Test10-2D (channel with solids): Solids in a channel with gravity

We first simulate a falling disc due to gravity in order to further validate the accuracy of the one-field FDM. We then show a simulation of the evolution of different shapes of solids falling and rising in a channel in order to show the flexibility and robustness of the proposed method.

The test of a falling disc in a channel is cited by [70, 156] in order to validate the IFEM and a monolithic method respectively. The computational domain is a vertical channel with a disc placed at the top of the channel as illustrated in Figure 5.23, and computational parameters are shown in Table 5.5. The fluid velocity is fixed to be 0 on all boundaries except the top one on which no boundary condition is imposed ($\sigma\mathbf{n} = \mathbf{0}$).

Fluid	Disc
$W = 2.0 \text{ cm}$	$d = 0.0125 \text{ cm}$
$H = 4.0 \text{ cm}$	$h = 0.5 \text{ cm}$
$\rho^f = 1.0 \text{ g/cm}^3$	$\rho^s = 1.2 \text{ g/cm}^3$
$\nu^f = 1.0 \text{ dyne}\cdot\text{s}/\text{cm}^2$	$\mu^s = 10^8 \text{ dyne}/\text{cm}^2$
$g = 980 \text{ cm/s}^2$	$g = 980 \text{ cm/s}^2$

Table 5.5: Fluid and material properties of a single falling disc for Test10-2D (channel with solids) in Section 5.2.7.

There is an empirical solution of a rigid ball falling in a viscous fluid [70], for which the terminal velocity, u_t , under gravity is given by

$$u_t = \frac{(\rho^s - \rho^f) gr^2}{4\nu^f} \left(\ln \left(\frac{L}{r} \right) - 0.9157 + 1.7244 \left(\frac{r}{L} \right)^2 - 1.7302 \left(\frac{r}{L} \right)^4 \right), \quad (5.22)$$

where ρ^s and ρ^f are the density of solid and fluid respectively, ν^f is viscosity of the fluid,

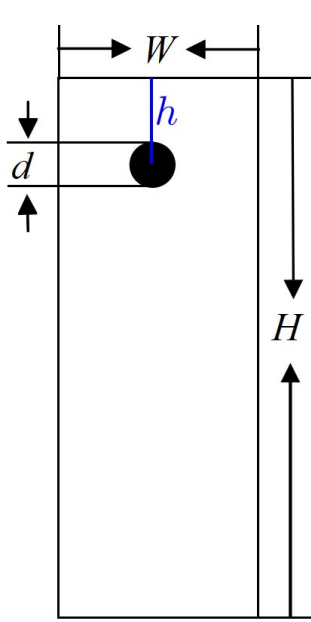


Figure 5.23: Computational domain for Test10-2D (channel with solids) in Section 5.2.7: a single falling disc.

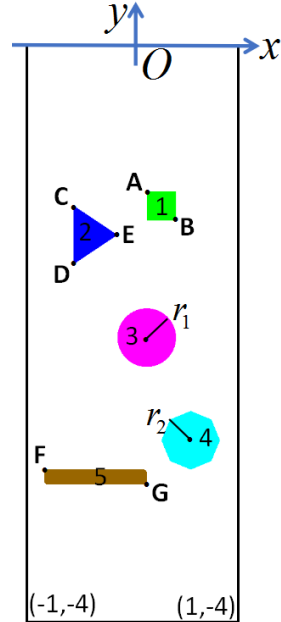


Figure 5.24: Computational domain for different shapes of solids with different properties. Test10-2D (channel with solids) in Section 5.2.7.

$g = 980 \text{ cm/s}^2$ is acceleration due to gravity, $L = W/2$ and r is the radius of the falling ball. We choose $\mu^s = 10^8 \text{ dyne/cm}^2$ to simulate a rigid body here. $\mu^s = 10^{12} \text{ dyne/cm}^2$ is also applied, which gives virtually identical results.

Three different meshes are used: the disc boundary is represented with 28 nodes (coarse), 48 nodes (medium), or 80 nodes (fine). The fluid mesh near the solid boundary has the same mesh size, and a stable time step $t = 0.005s$ is used for all the three cases. The Least-squares method is used to treat the convection step in all these tests. A local snapshot of the vertical velocity with the adaptive mesh is shown in Figure 5.25. From the fluid velocity pattern around the disc, we can observe that the disc behaves like a rigid body as expected. In addition, the evolution of the velocity of the mid-point of the disc is shown in Figure 5.26, from which it can be seen that the numerical solution converges from below to the empirical solution.

Reference [70] uses a monolithic method to simulate multiple rigid and deformable discs in a gravity channel. We have implemented this example and obtain very similar results. Rather than replicate these here however, we instead show a more complex example, as illustrated in Figure 5.24. The computational domain, boundary conditions and the fluid properties are the same as the above one-disc test. All the solids are numbered at their initial positions are as shown in Figure 5.24 with $A(0, -1)$, $B(0.2, -1.2)$, $C(-0.5, -1.1)$, $D(-0.5, -1.5)$, $E(-0.2, -1.3)$, $F(-0.7, -2.9)$ and $\mu^s(0, -3)$. The center and radius (r_1) of the 3rd solid (circle) are $(0, -2)$ and 0.2 respectively, and the center and radius (r_2) of the 4th solid (octagon) are $(0.3, -2.7)$ and 0.2 respectively. The solid properties are illustrated in Table 5.6.

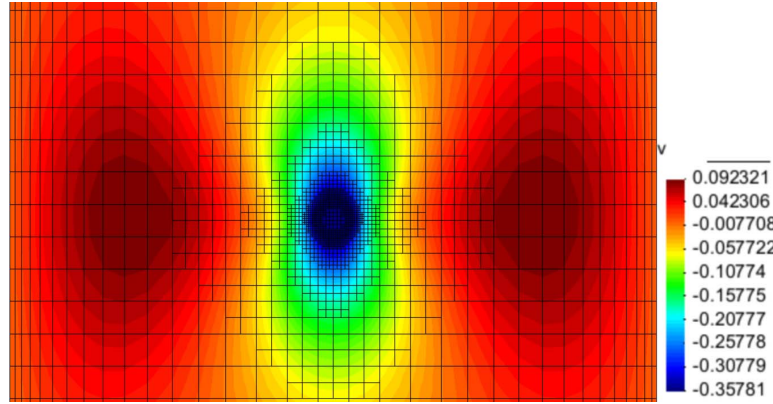


Figure 5.25: Contour of vertical velocity at $t = 1\text{s}$ (fine mesh) for Test10-2D (channel with solids) in Section 5.2.7.

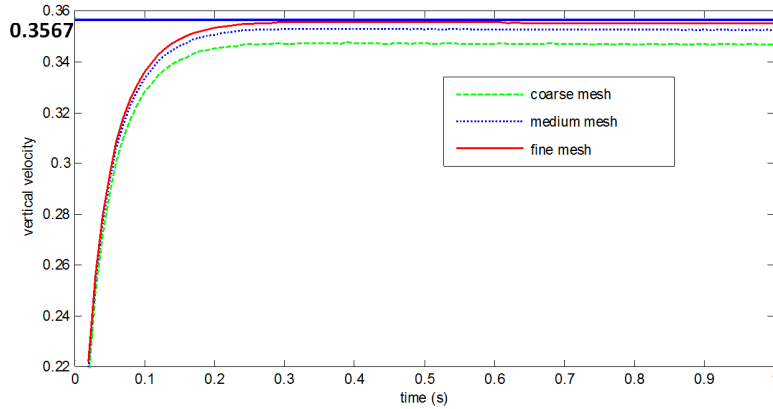


Figure 5.26: Evolution of velocity at the center of a falling disc for Test10-2D (channel with solids) in Section 5.2.7. (The blue solid line represents the empirical solution from formula (5.22).)

No. of solid	Density (g/cm^3)	Shear modulus (dyne/cm^2)
1	1.3	10^4
2	1.2	10^3
3	1.0	10
4	0.8	10^6
5	0.7	10^2

Table 5.6: Properties for multi-solids falling in a channel as shown in Figure 5.24. Test10-2D (channel with solids) in Section 5.2.7.

A high resolution of each solid boundary is used in this simulation, as shown in Figure 5.27 (a), which can guarantee the mesh quality during the whole process of evolution, and a stable time step $t = 0.002\text{s}$ is used. Snapshots of the solids at different times are shown in Figure 5.27.

The 2-step splitting scheme decouples the convection and diffusion of the Navier-Stokes equation, leaving the fluid-structure coupling only in a modified Stokes equation (modified by

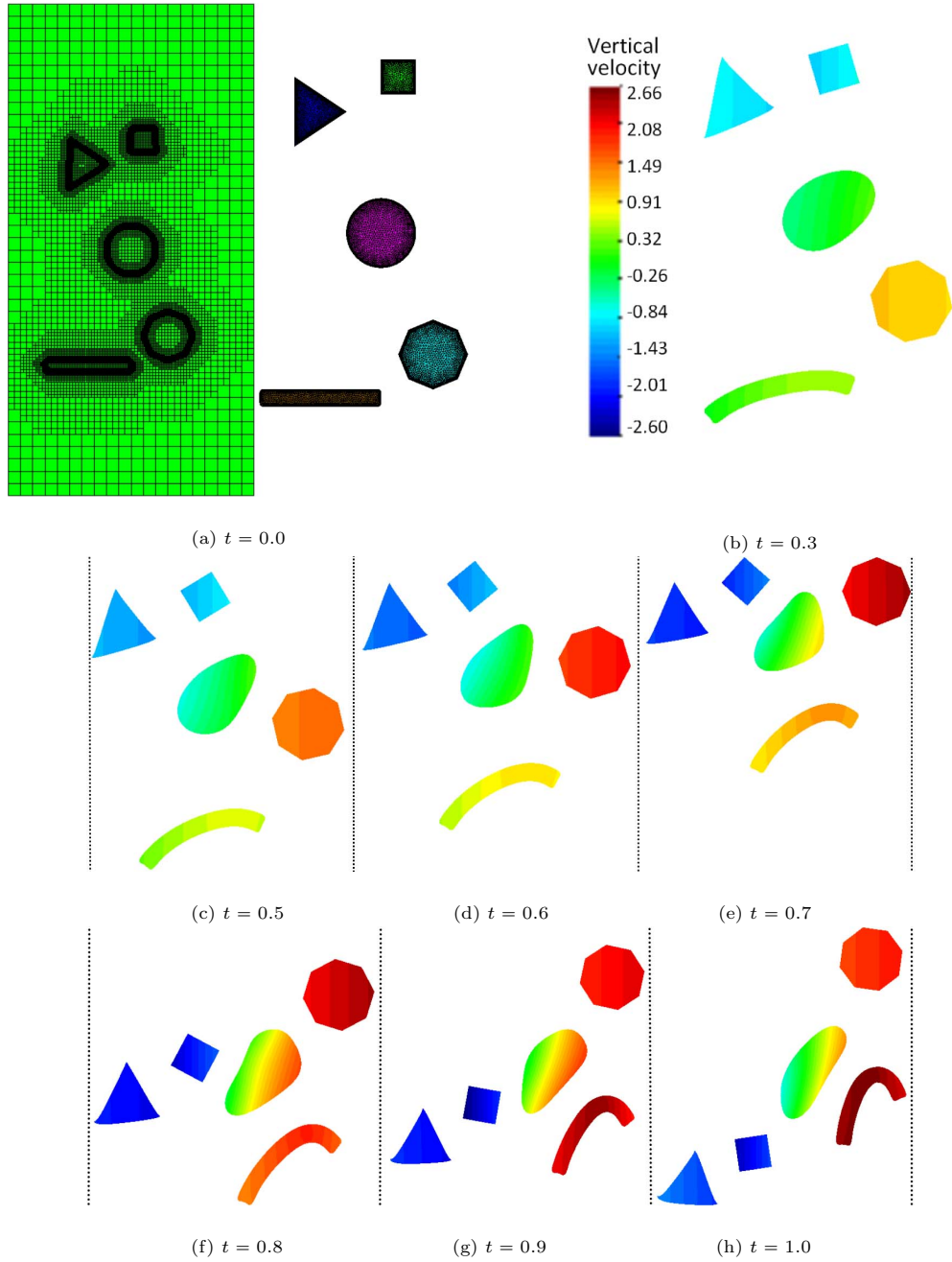


Figure 5.27: Contours of vertical velocity at different times for multi-solids falling in a channel. Test10-2D (channel with solids) in Section 5.2.7.

adding the solid equation). The modified Stokes equation leads to a saddle-point linear system, which is still a challenge to solve (with our iterative solver struggling to converge in some cases, see Remark 5.6). In the following section, we further split the modified Stokes equation into a

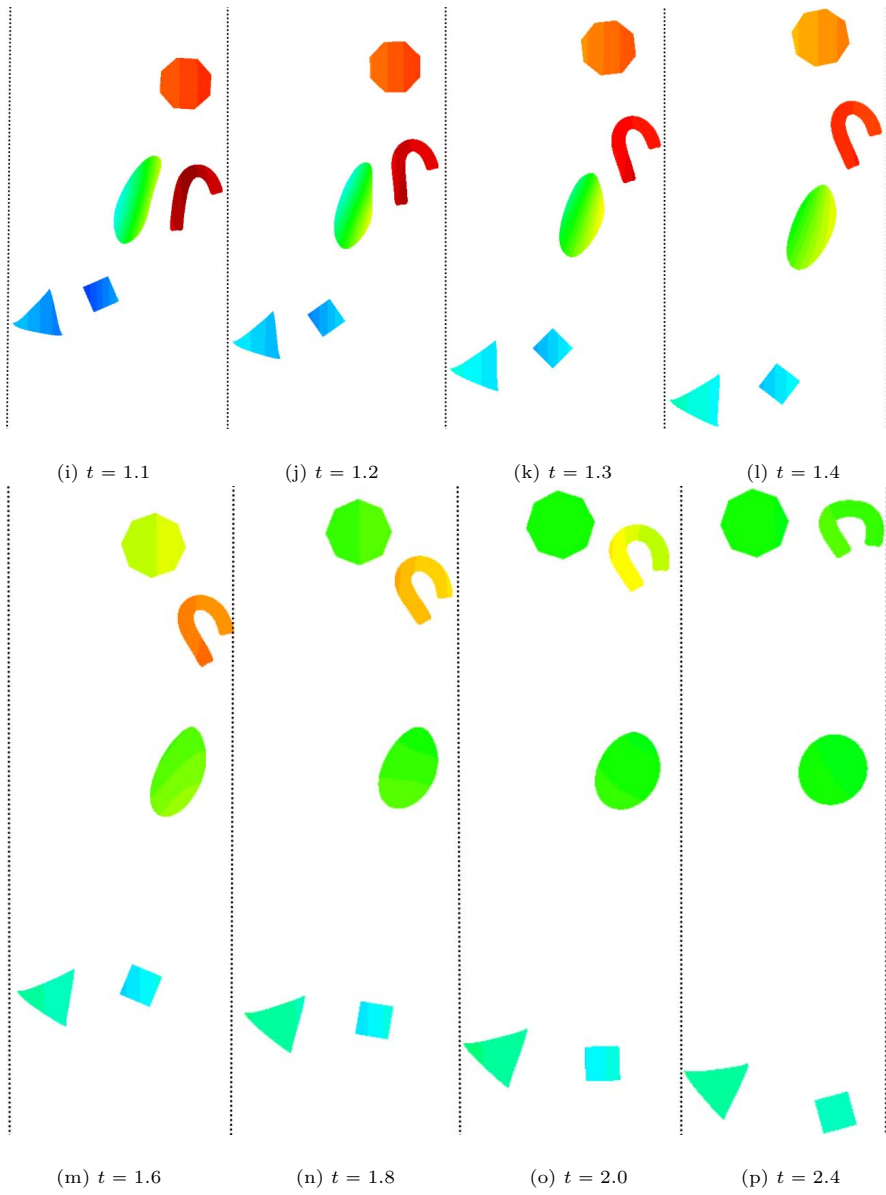


Figure 5.27 (continued).

“Degenerate” Stokes equation (which may be efficiently preconditioned and solved, see section 5.3.1) and a Poisson-like equation (which can also be efficiently solved using the Conjugate Gradient method, see Section 5.3.2). In this case, the saddle-point system only exists in the former and the fluid-solid interaction only exists in the latter, and each subproblem becomes easier.

5.3 A 3-step splitting scheme

As discussed above, we can produce a 3-step splitting scheme by decoupling the diffusion step in Section 5.1. Equation (5.2) can be further split into two fractional steps, which therefore gives a 3-step splitting method as follows. Readers may refer to [58] for more discussion of splitting schemes.

(1) Convection step:

$$\int_{\Omega} \frac{\mathbf{u}_{n+1/3} - \mathbf{u}_n}{\Delta t} \cdot \mathbf{v} d\mathbf{x} + \int_{\Omega} (\mathbf{u}_{n+1/3} \cdot \nabla) \mathbf{u}_{n+1/3} \cdot \mathbf{v} d\mathbf{x} = 0. \quad (5.23)$$

(2) “Degenerate” Stokes step:

$$\rho^f \int_{\Omega} \frac{\mathbf{u}_{n+2/3} - \mathbf{u}_{n+1/3}}{\Delta t} \cdot \mathbf{v} d\mathbf{x} - \frac{1}{2} \int_{\Omega} p_{n+2/3} \nabla \cdot \mathbf{v} d\mathbf{x} = 0, \quad (5.24)$$

and

$$-\int_{\Omega} q \nabla \cdot \mathbf{u}_{n+2/3} d\mathbf{x} = 0, \quad (5.25)$$

with Dirichlet boundary condition:

$$\mathbf{u}_{n+2/3} = \bar{\mathbf{u}} \quad \text{on} \quad \Gamma_D. \quad (5.26)$$

This step is called a “Degenerate” Stokes problem in [58, Section 34] since the integral of the viscous term is missing.

(3) Diffusion step:

$$\begin{aligned} & \rho^f \int_{\Omega} \frac{\mathbf{u}_{n+1} - \mathbf{u}_{n+2/3}}{\Delta t} \cdot \mathbf{v} d\mathbf{x} + \frac{\nu^f}{2} \int_{\Omega} \mathbf{D}\mathbf{u}_{n+1} : \mathbf{D}\mathbf{v} d\mathbf{x} \\ & + \rho^{\delta} \int_{\Omega_{\mathbf{X}}^s} \frac{\mathbf{u}_{n+1} - \mathbf{u}_n}{\Delta t} \cdot \mathbf{v} d\mathbf{x} + \mu^s \Delta t \int_{\Omega_{\mathbf{X}}^s} \nabla_{\mathbf{X}} \mathbf{u}_{n+1} : \nabla_{\mathbf{X}} \mathbf{v} d\mathbf{X} \\ & = \mu^s \int_{\Omega_n^s} J_n^{-1} \nabla \cdot \mathbf{v} d\mathbf{x} - \mu^s \int_{\Omega_{\mathbf{X}}^s} \mathbf{F}_n : \nabla_{\mathbf{X}} \mathbf{v} d\mathbf{X} + \rho^f \int_{\Omega} \mathbf{g} \cdot \mathbf{v} d\mathbf{x} \\ & + \rho^{\delta} \int_{\Omega_n^s} \mathbf{g} \cdot \mathbf{v} d\mathbf{x} + \int_{\Gamma_N} \bar{\mathbf{h}} \cdot \mathbf{v} d\Gamma + \frac{1}{2} \int_{\Omega} p_{n+2/3} \nabla \cdot \mathbf{v} d\mathbf{x}, \end{aligned} \quad (5.27)$$

with Dirichlet boundary condition:

$$\mathbf{u}_{n+1} = \bar{\mathbf{u}} \quad \text{on} \quad \Gamma_D. \quad (5.28)$$

Remark 5.3. As noted in Remark 5.1, this 3-step splitting scheme is not equivalent to the 2-step scheme, and neither is equivalent to the previous implicit scheme (3.9) and (3.10). However, if we add up equations (5.23), (5.24) and (5.27), and compare with equation (3.9), it can be seen that the 3-step splitting scheme may be interpreted as evaluating the convection term

using value $\mathbf{u}_{n+1/3}$. At the same time, pressure $p_{n+2/3}$ is determined by the velocity $\mathbf{u}_{n+2/3}$ rather than \mathbf{u}_{n+1} based on (5.25). Therefore, the last velocity \mathbf{u}_{n+1} is not divergence free, but however is controlled by a divergence free velocity $\mathbf{u}_{n+2/3}$.

Remark 5.4. One may swap the order of solving step (2) and step (3) so that the last velocity could be divergence free (let us call it divergence free 3-step splitting in this case), and gain better mass conservation. However, this divergence free 3-step splitting is empirically observed to increase the total energy, which can be seen from Test1-2D (activated disc) in Section 5.4.1 and Test2-2D (stretched disc) in Section 5.4.2. The accuracy (or equivalently the solid deformation) of a specific problem depends on both the mass and energy conservation. Therefore, solving step (2) or step (3) first depends on which part (the mass conservation or the energy conservation) is important in an application. For example, from numerical results we can clearly see that the mass conservation is more important (based on the solid deformation) for the Test7-2D (cavity with disc) in Section 5.4.4.

5.3.1 “Degenerate” Stokes step

A nice property of this degenerated Stokes problem is that the solid equation is decoupled in this step, which gives the following discretized linear system:

$$\begin{bmatrix} \mathbf{M} & \mathbf{B} \\ \mathbf{B}^T & \mathbf{0} \end{bmatrix} \begin{pmatrix} \mathbf{u} \\ \mathbf{p} \end{pmatrix} = \begin{pmatrix} \mathbf{b} \\ \mathbf{0} \end{pmatrix}, \quad (5.29)$$

where \mathbf{M} is a diagonal (lumped) mass matrix, in which case one may compute the Schur complement $\mathbf{S} = \mathbf{B}^T \mathbf{M}^{-1} \mathbf{B}$ exactly. This only needs to be computed once at the first time step if using an unchanging uniform mesh. An alternative is to use $\begin{bmatrix} \mathbf{M} & \\ & \mathbf{M}_p \end{bmatrix}$ as a preconditioner, whose inverse can also be computed directly if \mathbf{M} and \mathbf{M}_p are both lumped mass matrices (our numerical tests show that using distributed pressure mass matrix does not improve the speed of convergence). One can also use $\begin{bmatrix} \mathbf{M} & \\ & \Delta_p \end{bmatrix}$ as a preconditioner, where Δ_p is the stiffness matrix from the pressure Poisson equation as will be discussed in Section 5.5. It is observed from numerical tests that the latter performs much better than the former. As mentioned above, from (5.29) we can derive a Schur complement in the form of $\mathbf{S} = \mathbf{B}^T \mathbf{M}^{-1} \mathbf{B}$. The operators that are discretized in this form imply that \mathbf{S} will be spectrally equivalent to a discrete Laplacian. Hence we expect that the latter preconditioner will be effective for this system, similarly to analysis for Stokes equation [46].

5.3.2 Diffusion step

Compared with equation (5.19), the diffusion step of this 3-step splitting scheme is reduced as follows after FEM discretization.

$$\mathbf{A}\mathbf{u} = \mathbf{b}, \quad (5.30)$$

where

$$\mathbf{A} = \mathbf{M}/\Delta t + \mathbf{K} + \mathbf{D}^T (\mathbf{M}^s/\Delta t + \mathbf{K}^s) \mathbf{D}, \quad (5.31)$$

and

$$\mathbf{b} = \mathbf{f} + \mathbf{D}^T \mathbf{f}^s + \mathbf{M}\mathbf{u}_{n+2/3}/\Delta t + \mathbf{D}^T \mathbf{M}^s \mathbf{D}\mathbf{u}_n/\Delta t. \quad (5.32)$$

A preconditioned Conjugate Gradient method can efficiently solve equation (5.30). We use the incomplete Cholesky decomposition of matrix $\mathbf{M}/\Delta t + \mathbf{K}$ as a preconditioner in order to solve equation (5.30). Very good convergence performance can be observed from our numerical tests (although the precise performance of the linear algebraic solver is not the topic of this thesis).

5.4 Numerical tests for the 3-step splitting scheme

In this section we test the 3-step splitting scheme using some of the numerical examples considered previously. We shall also add two new examples to show the flexibility of this 3-step splitting scheme: it decouples the fluid-structure interaction into a diffusion step, which can be solved cheaply by a Conjugate Gradient method; although we still have to solve a saddle-point equation for the “Degenerate” Stokes step. That is a pure fluid problem however, which can be solved as discussed in Section 5.3.1.

5.4.1 Test1-2D (activated disc): Oscillating disc driven by an initial kinetic energy

The total energy ratio as a function of time is plotted in Figure 5.28, from which we can observe that both the error of the total energy and the difference between the implicit scheme and the 3-step explicit splitting scheme decrease when reducing the time step. Compared with the results of the 2-step splitting scheme in Figure 5.2 (a), we know that the 3-step splitting scheme converges more slowly. However, it is important to note that both schemes converge.

As noted in Remark 5.4, if using the divergence free 3-step splitting (swap the step (2) and step (3) introduced in Section 5.3), one can gain better mass conservation as shown in Figure 5.29 (a): the divergence free 3-step splitting can conserve mass as accurately as the 2-step splitting scheme. However the total energy increases at some times (see Figure 5.29) (b), which may cause stability problems. In this test, both the mass and energy are conserved better using the divergence free splitting (although it is not a non-increasing energy). It is not surprising therefore to see, from Figure 5.30, that the solid deformation is more accurate in this case.

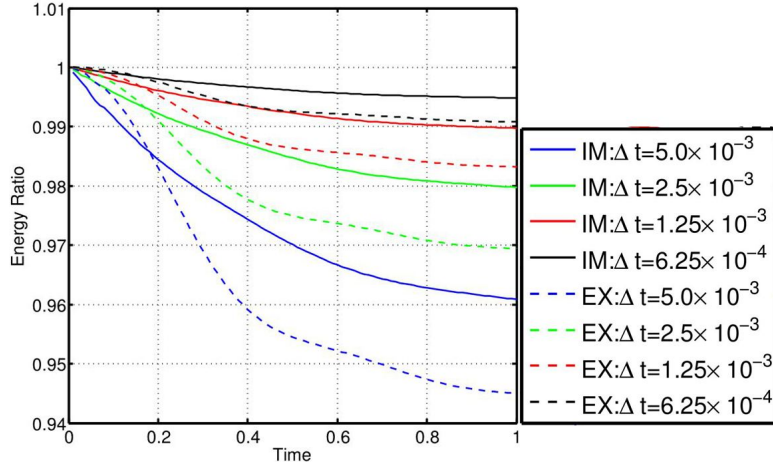


Figure 5.28: The energy ratio against time for Test1-2D (activated disc) in Section 5.4.1: comparison between implicit and explicit scheme.

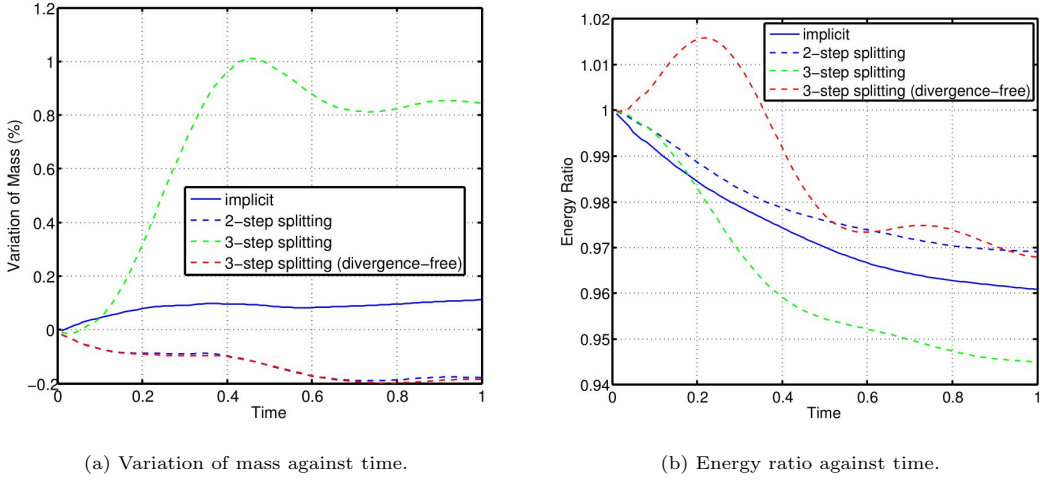


Figure 5.29: Convergence of mass and energy for Test1-2D (activated disc) in Section 5.4.1 using $\Delta t = 5.0 \times 10^{-3}$: comparing with the divergence free 3-step splitting.

5.4.2 Test2-2D (stretched disc): Oscillating disc driven by an initial potential energy

We plot energy ratio as a function of time here in Figure 5.31, from which it can be seen that error of the total energy converges when reducing the time step, and the difference between the two schemes decreases when the time step decreases. As previously, it is not surprising that the 3-step splitting scheme converges slower than the 2-step splitting scheme by comparing Figure 5.31 and Figure 5.5 (a), but the important point is that both schemes converge.

As noted in Remark 5.4, if using the divergence free 3-step splitting (swap step (2) and step (3) as introduced in Section 5.3), we could gain better mass conservation as shown in Figure

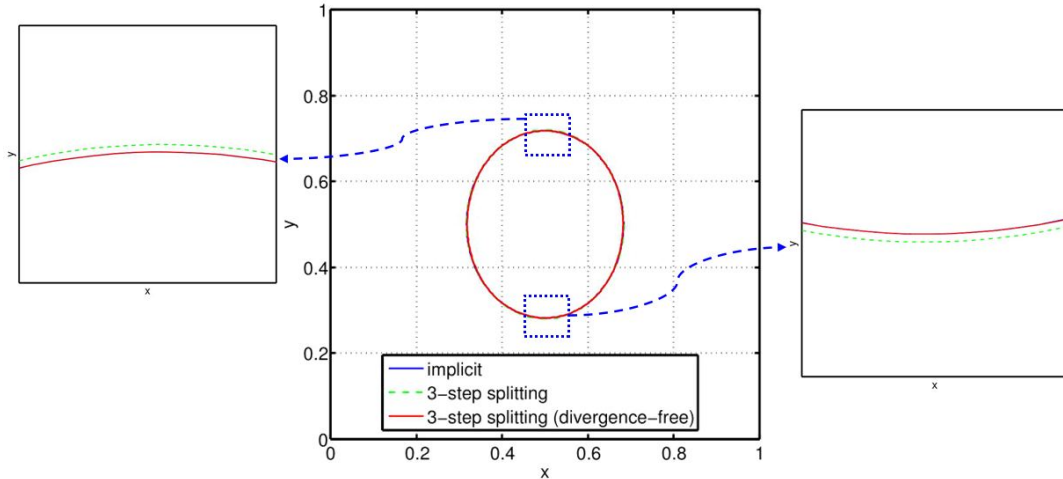


Figure 5.30: The solid deformation at $t = 0.74$ (the disc is maximally stretched in the vertical direction) for Test1-2D (activated disc) in Section 5.4.1. The curve of the divergence free splitting (solid red) overlaps with the curve of the implicit scheme (solid blue).

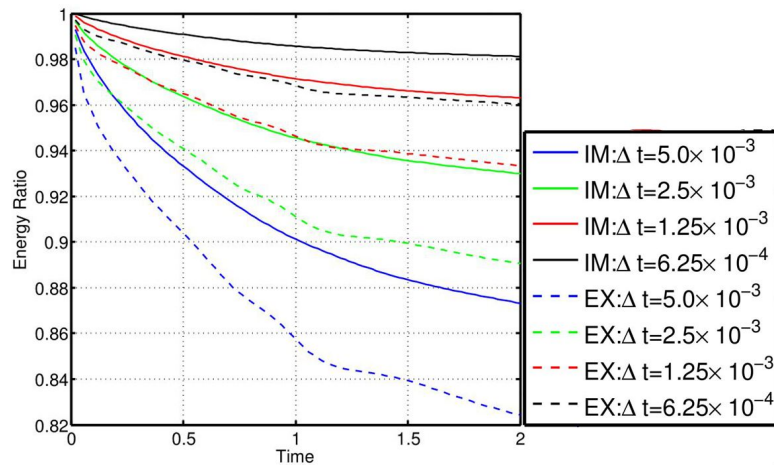


Figure 5.31: The energy ratio against time for Test2-2D (stretched disc) in Section 5.4.2: comparison between implicit and explicit scheme.

5.32 (a). However, the energy is not non-increasing as shown in Figure 5.32 (b). In order to see which effect is significant for this problem, in Figure 5.33 we plot the solid deformation at $t = 1$ when the disc is maximally stretched in the vertical direction. It can be observed that the divergence free splitting does not improve the accuracy of the solid deformation, instead it reduces the accuracy although improving the mass conservation.

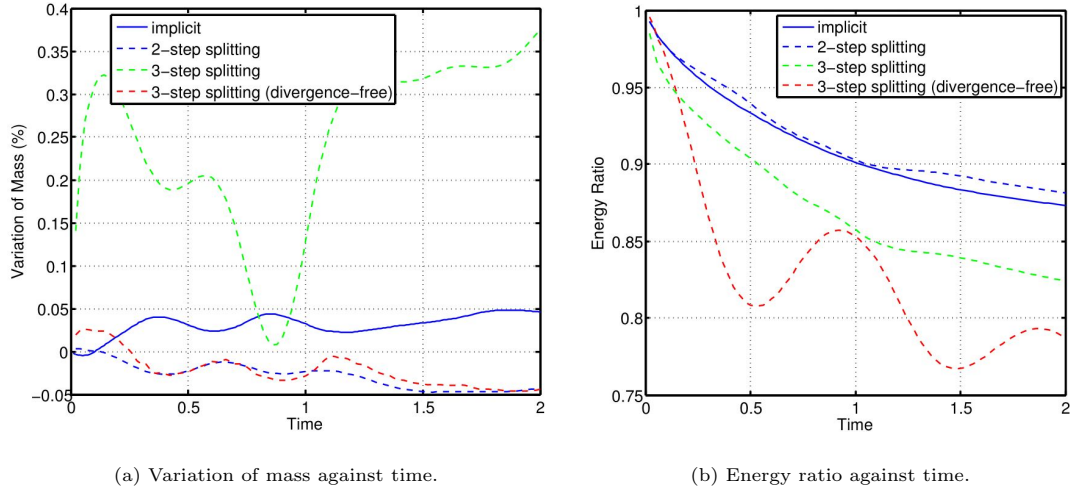


Figure 5.32: Convergence of mass and energy for Test2-2D (stretched disc) in Section 5.4.2 using $\Delta t = 5.0 \times 10^{-3}$: comparing with the divergence free 3-step splitting.

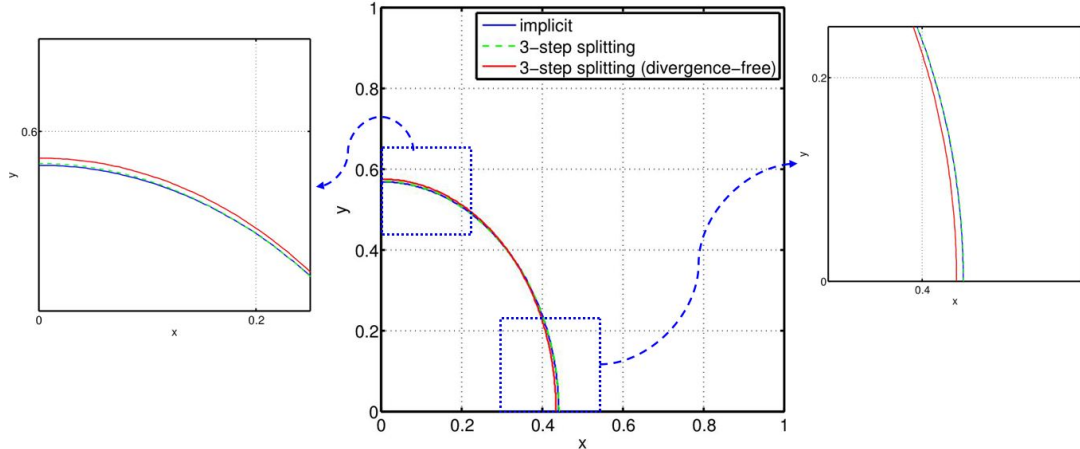


Figure 5.33: The solid deformation at $t = 1$ (the disc is maximally stretched in the vertical direction) for Test2-2D (stretched disc) in Section 5.4.2. The curve of the 3-step splitting (dashed green) overlaps with the curve of the implicit scheme (solid blue).

5.4.3 Test3-3D (activated ball): Oscillating ball driven by an initial kinetic energy

We revisit the oscillating ball discussed in Section 4.4.3 and compare the energy of this 3-step splitting scheme with the implicit scheme. The comparison of energy evolution is shown in Figure 5.34, from which it can be observed that both schemes converge in time although the 3-step splitting is less accurate. It is also less accurate than the 2-step splitting scheme through comparing to Figure 5.6. This could be accepted because we solve a computationally cheaper problem as shown from the analysis in Section 5.3.1 and 5.3.2.

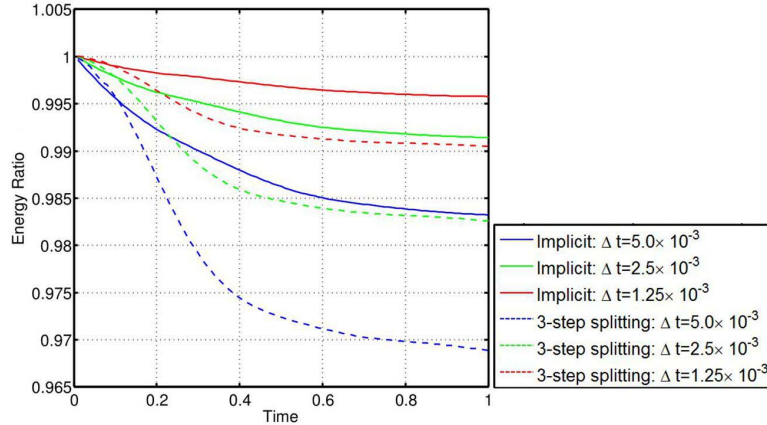


Figure 5.34: Evolution of the energy ratio for Test3-3D (activated ball) in Section 5.4.3: comparison between implicit and explicit scheme.

5.4.4 Test7-2D (cavity with disc): Cavity flow with a solid disc (Parameter 1)

The cavity flow with a solid disc is tested again in this section using the 3-step splitting scheme. We plot the contour of the deformed solid in Figure 5.35, from which it may be seen that the 3-step splitting scheme is worse than the 2-step splitting scheme in terms of preserving mass (the reason may be that $\nabla \cdot \mathbf{u}_{n+1} = 0$ is not enforced, see Remark 5.3). However this can be improved by reducing the time step, which is observed from variation of the mass ratio in Figure 5.36 (a) and solid deformation in Figure 5.36 (b) using a smaller time step.

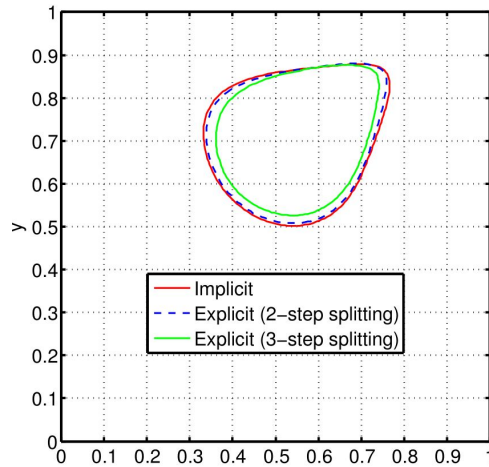


Figure 5.35: Comparison of the solid deformation at $t = 20$ for Test7-2D (cavity with disc) in Section 5.4.4, using a time step of $\Delta t = 1.0 \times 10^{-3}$.

For this test, if we swap the step (2) and step (3) in Section 5.3 (the divergence free splitting), the accuracy is clearly improved, as seen by comparing the solid deformation shown in Figure

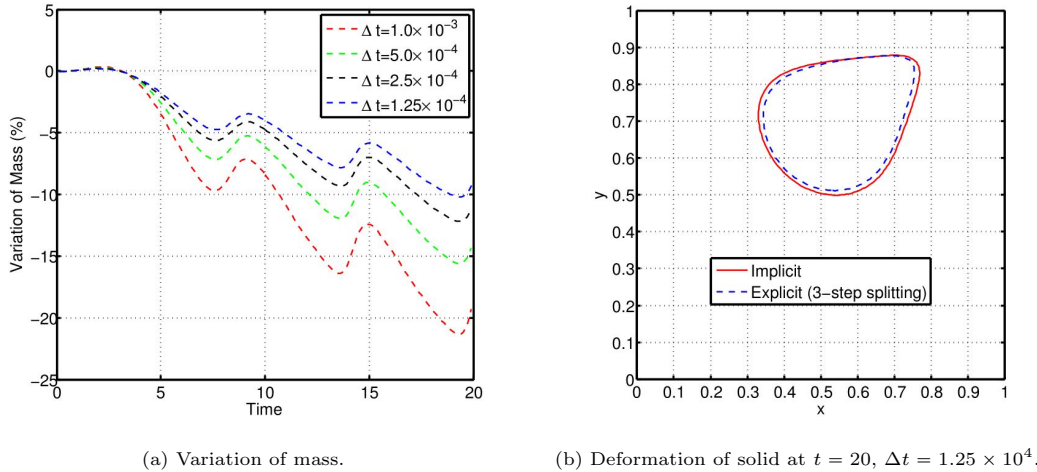


Figure 5.36: Convergence of mass for Test7-2D (cavity with disc) in Section 5.4.4, using the 3-step splitting scheme.

5.37.

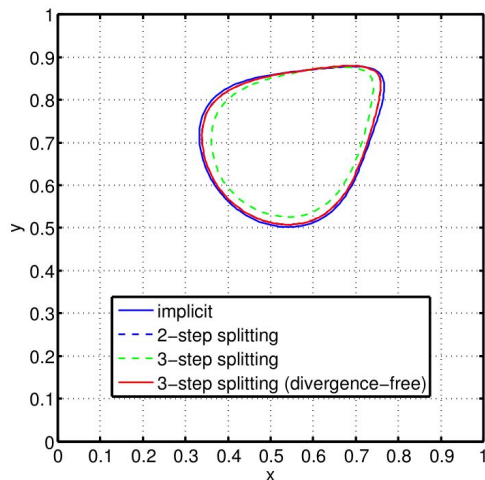
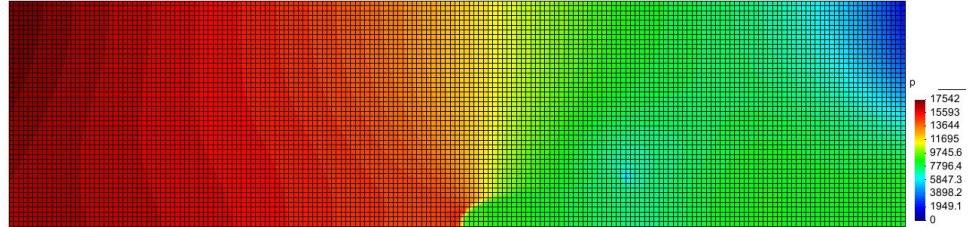


Figure 5.37: The solid deformation at $t = 20$ for Test7-2D (cavity with disc) in Section 5.4.4 with $\Delta t = 1.0 \times 10^{-3}$. The curve of the divergence free 3-step splitting (solid red) overlaps with the curve of the 2-step splitting scheme (dashed blue).

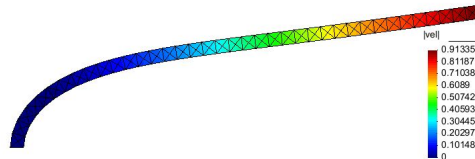
5.4.5 Test8-2D (leaflet): An oscillating leaflet (Parameter 1)

In this test we revisit the oscillation of a flexible leaflet oriented across the flow direction, and use the 3-step step splitting scheme based upon a uniform mesh and the result is compared with an ALE fitted mesh method (see Section 2.4.3 for the ALE method). In order to show the meshes, the pressure on the fluid mesh and velocity on the deformed solid mesh are presented in Figure 5.38. The same mesh size is adopted for the ALE method as shown in Figure 5.39, from

which it can be seen that the ALE mesh cannot be trusted after around $t = 0.12$ if we check the mesh closely at the tip and bottom of the leaflet. However we can carry on the simulation using the proposed two-mesh method, and the accuracy can be compared with the ALE method before $t = 0.12$ which is very good (see Figure 5.40 to 5.42).

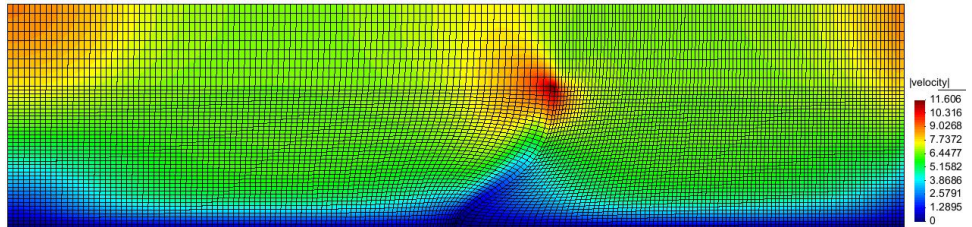


(a) P_2/P_1 elements for velocity and pressure, the size of one element is the same as the width of the solid leaflet (0.0212).

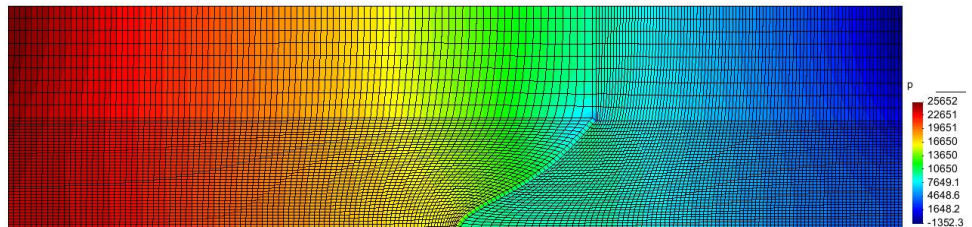


(b) Bilinear solid mesh.

Figure 5.38: Distribution of pressure on the fluid mesh and velocity norm on the solid mesh at $t = 1.0$ for Test8-2D (leaflet) in Section 5.4.5.

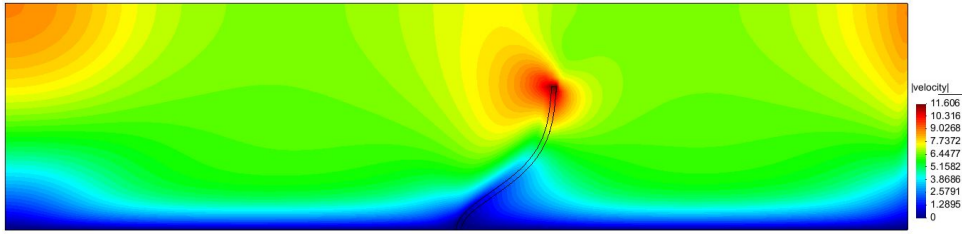


(a) velocity norm at $t = 0.1$.

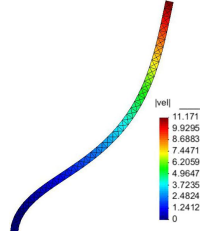


(b) Pressure at $t = 0.12$,

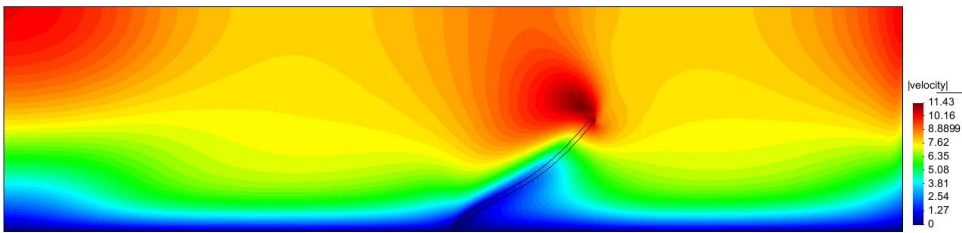
Figure 5.39: Distribution of pressure and velocity norm using an ALE mesh (same mesh as in Figure 5.38 (a)) for Test8-2D (leaflet) in Section 5.4.5.



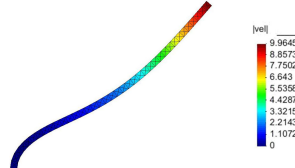
(a) Deformation of leaflet using a fitted ALE mesh.



(b) Defomation of the solid leaflet using the proposed two-mesh method.

Figure 5.40: Comparison of the leaflet deformation at $t = 0.1$ for Test8-2D (leaflet) in Section 5.4.5.

(a) Deformation of the leaflet using a fitted ALE mesh.



(b) Defomation of the solid leaflet using the proposed two-mesh method.

Figure 5.41: Comparison of the leaflet deformation at $t = 0.12$ for Test8-2D (leaflet) in Section 5.4.5.

Remark 5.5. For this test using the $P_2/(P_1 + P_0)$ element, the “Degenerate” Stokes step does not converge using the iterative linear solver introduced in Section 5.3.1, which however does converge using the P_2/P_1 element. This may because too many unknowns P_0 have been added in the domain, because we know the pressure only jumps across the leaflet.

Remark 5.6. The 2-step scheme (when using the preconditioned MinRes linear solver for the diffusion step, which is the same as the solver discussed in Section 4.2) does not converge for either $P_2/(P_1 + P_0)$ or P_2/P_1 element. We also found that the preconditioned MinRes linear

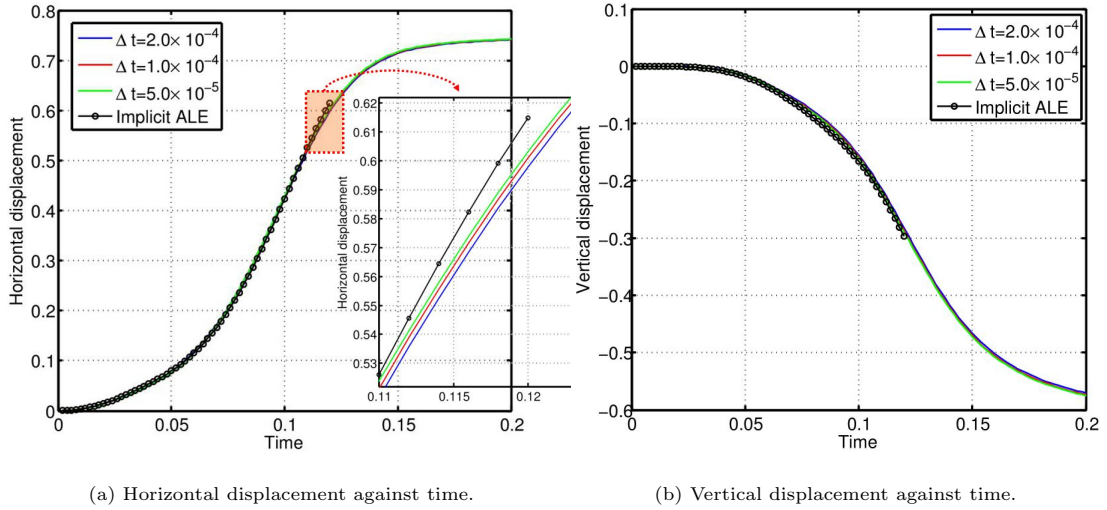


Figure 5.42: Comparison of displacement at the leaflet tip (top-left corner) for Test8-2D (leaflet) in Section 5.4.5. The implicit ALE method uses a stable/converged time step of $\Delta t = 1.0 \times 10^{-4}$.

solver could not converge for this pure fluid problem. The above two facts suggest that the reason that the 2-step splitting scheme fails to converge is because the original preconditioned MinRes algorithm is problem dependent (which should be investigated in the future), rather than because the solid information is not used in the preconditioner.

5.4.6 Test11-2D (thick flag): An oscillating thick flag

In this section, we use a uniform mesh and test a thick flag attached to a cylinder, which has been studied in [30, 67, 115, 117]. We shall compare these results with the 3-step splitting scheme. The computational domain is a rectangle ($L \times H$) with a cut hole of radius r and center (c, c) as shown in Figure 5.43. A leaflet of size $l \times h$ is attached to the boundary of the hole (the mesh of the leaflet is fitted to the boundary of the hole, see the solid mesh in Figure 5.44). In this test, $L = 2.5$, $H = 0.41$, $l = 0.35$, $h = 0.02$, $c = 0.2$ and $r = 0.05$. The fluid and solid parameters are as follows: $\rho^f = \rho^s = 10^3$, $\nu^f = \nu^s = 1$ and $\mu^s = 2.0 \times 10^6$. The inlet flow is prescribed as:

$$\bar{u}_x = \frac{12y}{H^2} (H - y), \quad \bar{u}_y = 0. \quad (5.33)$$

This example is actually very similar to Test8-2D (leaflet). However we test it here because first, it is also used as a benchmark in the FSI literature [30, 67, 115, 117], but the solid is wider and softer than for Test8-2D (leaflet). Second, the channel is narrower in Test11-2D (thick flag); the type of boundary conditions on the top and bottom of the channel are different in these two cases: wall boundary condition in Test11-2D (thick flag) and sliding boundary condition in Test8-2D (leaflet); Third, the amplitude of the oscillation is smaller than that of the thin flag in Test8-2D (leaflet), so that an ALE mesh could be easily adopted. Therefore, we choose this

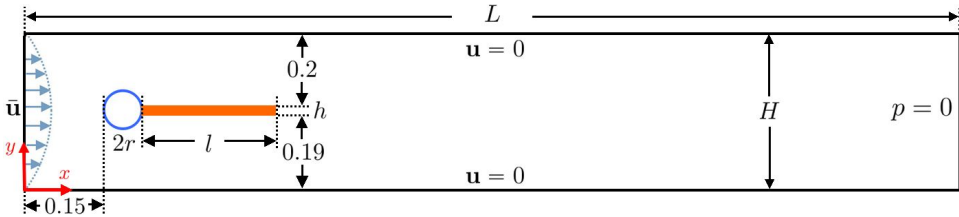


Figure 5.43: Computational domain and boundary conditions for Test11-2D (thick flag) in Section 5.4.6.

test to show the flexibility of our numerical scheme in this section.

Taking $\bar{U} = \int_0^H \bar{u}_x dy = 2H$ and the channel height H as the characteristic velocity and length respectively, the Reynolds number is: $Re = \frac{\rho f \bar{U} H}{\nu f} = 336.2$. We use a uniform mesh of size 0.1×0.1 for the fluid and a similar mesh density for the solid. A snapshot of the velocity field is displayed in Figure 5.44 and the vertical displacement at the tip of leaflet is plotted in Figure 5.45 using a stable time step $\Delta t = 2.5 \times 10^{-3}$. Both the frequency (5.3) and magnitude (0.03) have a good agreement with the published results [30, 67].

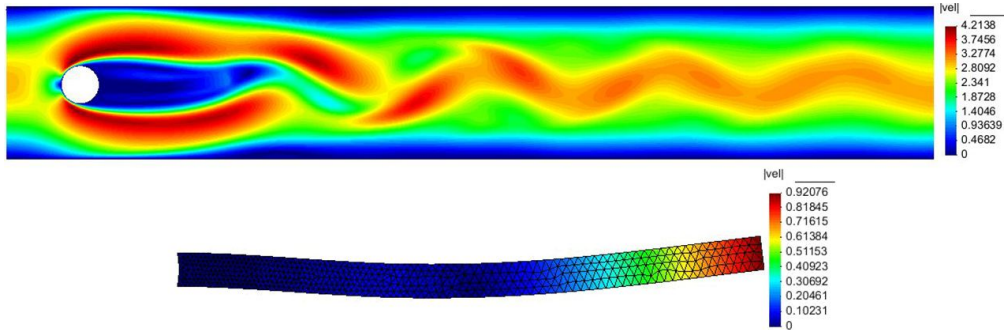


Figure 5.44: A snap shot of the velocity norms in the fluid domain and on the solid mesh at $t=6$. Test11-2D (thick flag) in Section 5.4.6.

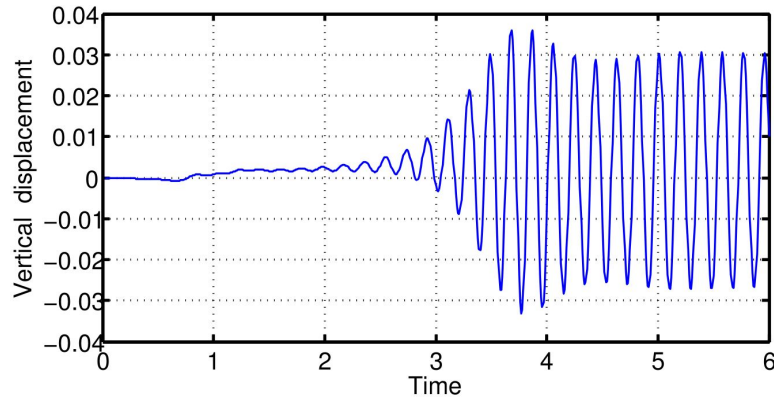


Figure 5.45: Vertical displacement at the tip of the leaflet versus time for Test11-2D (thick flag) in Section 5.4.6. The frequency and amplitude are around 5.3 and 0.03 respectively.

5.4.7 Test12-3D (cylinder): An oscillating cylinder

In this test, we consider a cylindrical pillar oscillating in a cuboid channel as shown in Figure 5.46. The size of the cuboid is: length $L = 3$, height $H = 1$ and width $W = 1$. The cylinder is located at the center of the cuboid, with base's radius of $r = 0.05$ and height $h = 0.8$. Notice that this test problem is a 3D extension of the Test8-2D (leaflet) ($Re = 100$). The corresponding 2D geometry is shown in Figure 5.47, which is not exactly the same as that used in the Test8-2D (leaflet): the leaflet in Figure 5.47 is wider and the channel is shorter (thus reducing the problem size in the 3D case). We use a symmetry boundary condition on the top, front and back surfaces of the cuboid, all the velocity components are fixed to be zero at the bottom of the cuboid, and the inlet and outlet flow are defined by:

$$u_x = 15y(2 - y) \sin(2\pi t), \quad u_y = u_z = 0. \quad (5.34)$$

This is then a natural extension of the corresponding 2D problem with the same Reynolds number, and therefore we shall compare the 3D oscillating cylinder with the corresponding 2D oscillating leaflet.

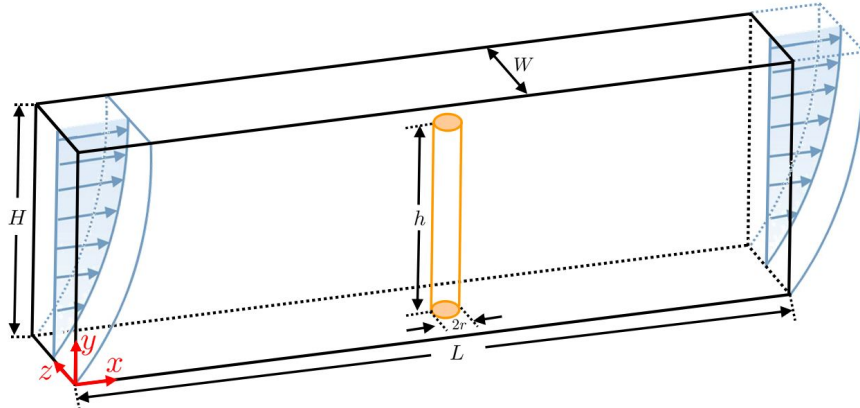


Figure 5.46: Sketch of the oscillating cylinder in a cuboid. Test12-3D (cylinder) in Section 5.4.7.

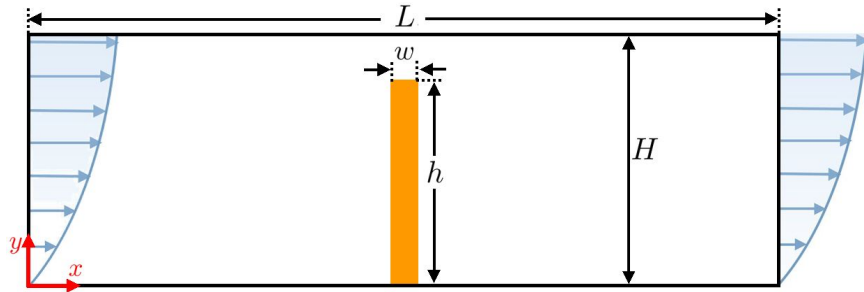


Figure 5.47: Computational domain of the corresponding 2D problem ($w = 2r$, corresponding to Figure 5.46) for Test12-3D (cylinder) in Section 5.4.7.

We use a uniform mesh of size of 0.05 in all directions and stable time step $\Delta t = 1.0 \times 10^{-4}$ for both the 2D and 3D tests. In order to visualize the results of this simulation, snapshots of the velocity norm on the background mesh and the solid deformations are presented in Figure 5.48 and 5.49 respectively. The displacement at point $(1.55, 0.8, 0.5)$, at the top of the cylinder, is plotted in Figure 5.50 as a function of time in order to compare with the results of the corresponding 2D problem. It is not surprising that a very similar oscillating patterns of the 3D cylinder and the corresponding 2D leaflet could be observed from these figures.

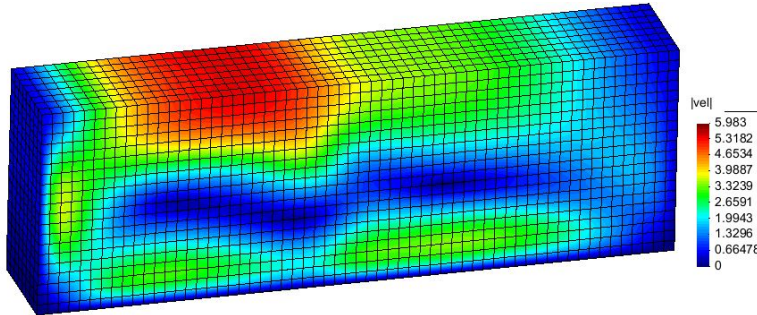


Figure 5.48: Velocity norm at $t = 2.0$ for Test12-3D (cylinder) in Section 5.4.7.

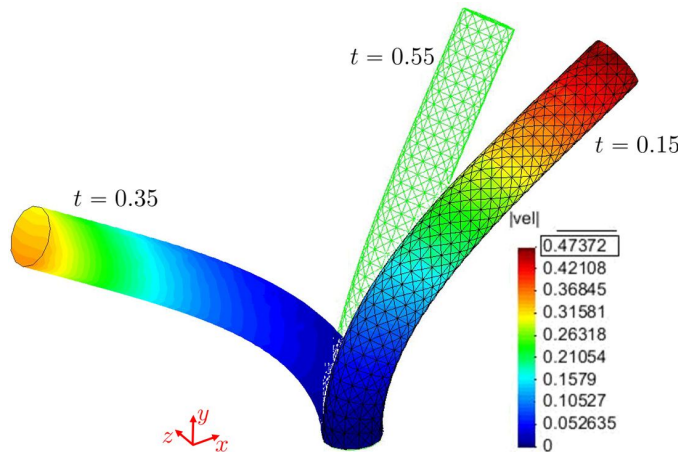


Figure 5.49: Solid deformation at three different stages for Test12-3D (cylinder) in Section 5.4.7.

5.5 A 4-step splitting scheme

The “Degenerate” Stokes step in Section 5.3 may further be split into a pressure Poisson step and an update step (Chorin’s projection method) [58]. Noting that the test function \mathbf{v} satisfies the homogeneous boundary condition, the strong form corresponding to equation (5.24) and (5.25) is:

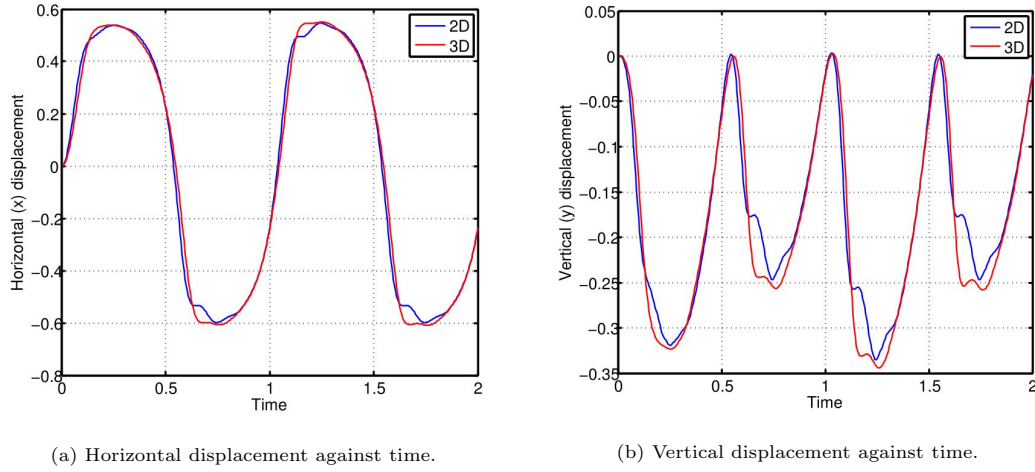


Figure 5.50: Displacement at point $(1.55, 0.8, 0.5)$ in the 3D case and point $(1.55, 0.8)$ in the 2D case. Test12-3D (cylinder) in Section 5.4.7.

$$\rho^f \frac{\mathbf{u}_{n+2/3} - \mathbf{u}_{n+1/3}}{\Delta t} + \frac{1}{2} \nabla p_{n+2/3} = 0 \quad (5.35)$$

and

$$\nabla \cdot \mathbf{u}_{n+2/3} = 0. \quad (5.36)$$

Taking the divergence on both sides of equation (5.35) and using equation (5.36), we have the following pressure Poisson equation:

$$\nabla^2 p_{n+2/3} = 2\rho^f \frac{\nabla \cdot \mathbf{u}_{n+1/3}}{\Delta t}. \quad (5.37)$$

Using the Dirichlet boundary condition (5.26) and equation (5.35), we have the boundary condition for the above pressure Poisson equation:

$$\frac{\partial p_{n+2/3}}{\partial \mathbf{n}} = 2\rho^f \frac{\bar{\mathbf{u}} - \mathbf{n} \cdot \mathbf{u}_{n+1/3}}{\Delta t} = 0 \quad \text{on } \Gamma_D. \quad (5.38)$$

Using (5.35), the velocity is finally updated by

$$\mathbf{u}_{n+2/3} = \mathbf{u}_{n+1/3} - \frac{\Delta t}{2\rho^f} \nabla p_{n+2/3}. \quad (5.39)$$

Hence step (2) (the ‘‘Degenerate’’ Stokes step) in Section 5.3 can further be expressed as the following two substeps.

(2.1) Pressure Poisson step:

$$\nabla^2 p_{n+2/3} = \frac{2\rho^f}{\Delta t} \nabla \cdot \mathbf{u}_{n+1/3}, \quad (5.40)$$

with boundary condition

$$\frac{\partial p_{n+2/3}}{\partial \mathbf{n}} = 0 \quad \text{on } \Gamma_D \cup \Gamma_N. \quad (5.41)$$

The corresponding weak form is

$$\int_{\Omega} \nabla q \cdot \nabla p_{n+2/3} = -\frac{2\rho^f}{\Delta t} \int_{\Omega} q \nabla \cdot \mathbf{u}_{n+1/3}. \quad (5.42)$$

(2.2) Update step:

$$\mathbf{u}_{n+2/3} = \mathbf{u}_{n+1/3} - \frac{\Delta t}{2\rho^f} \nabla p_{n+2/3}. \quad (5.43)$$

Rather than updating the velocity point by point, we shall solve the following finite element problem, which gives better energy conservation.

$$\rho^f \int_{\Omega} \frac{\mathbf{u}_{n+2/3} - \mathbf{u}_{n+1/3}}{\Delta t} \cdot \mathbf{v} - \frac{1}{2} \int_{\Omega} p_{n+2/3} \nabla \cdot \mathbf{v} = 0. \quad (5.44)$$

Remark 5.7. Generally we do not have the Neumann condition $\frac{\partial P_{n+2/3}}{\partial \mathbf{n}} = 0$, and this false boundary condition introduces an error in the form of a numerical boundary layer of thickness $O(\sqrt{\nu^f \Delta t})$. However, for an enclosed flow ($\mathbf{n} \cdot \mathbf{u} = 0$ on $\Gamma_D = \Gamma$) this issue is avoided. The major advantage of Chorin's projection method is that it decouples the velocity and pressure, therefore removing the need for the *inf-sup* condition to be satisfied. Furthermore, this scheme is also unconditionally stable and "extremely" robust [58, Section 37]. Readers may refer to [58, Section 37] for more comments about this scheme.

Remark 5.8. It is also possible to solve the "Degenerate" Stokes problem (here, the Pressure Poisson step (2.1) and the Update step (2.2)) in the last step. In this case, one can achieve better mass conservation so that the accuracy may be improved, such as Test7-2D (cavity with disc) in Section 5.6.4. However, the total energy may increase, hence the scheme may be unstable.

5.6 Numerical tests for the 4-step splitting scheme

In this section we shall use Test1-2D (activated disc), Test2-2D (stretched disc) and Test3-3D (activated ball) again to check the energy convergence for the 4-step splitting scheme. It is interesting that the energy converges for the mixed element (P_2/P_1) but diverges for the equal-order element (P_1), although the latter is widely used for the pure fluid problems [58]. Based upon the these three tests and two more tests Test7-2D (cavity with disc) and Test8-2D (leaflet), we comment on the importance of the energy conservation and its influence on the solid deformation.

5.6.1 Test1-2D (activated disc): Oscillating disc driven by an initial kinetic energy

The time convergence of the error in the total energy is presented in Figure 5.51 and compared with the implicit scheme. From this it can be seen that the two different types of finite element discretization give quite different results: the error of the total energy converges (although slowly) with the time step for the P_2/P_1 element (in Figure 5.51 (a)), however the error of the total energy diverges for the P_1 elements, as shown in Figure 5.51 (b). We plot the corresponding solid deformation in Figure 5.52 and 5.53 to show the importance of the energy conservation for this test, because it has a significant influence on the solid deformation. It may be observed from Figure 5.53 that the difference of the solid deformation between the implicit and the 4-step splitting scheme increases when reducing the time step, which indicates that the 4-step splitting scheme does not converge in time when using this equal-order (P_1) element.

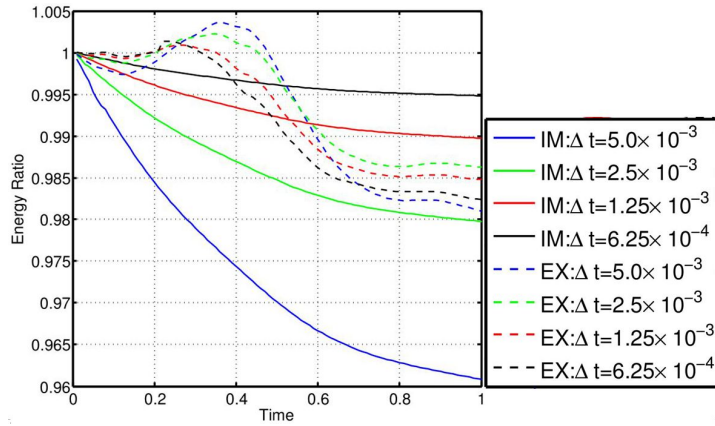
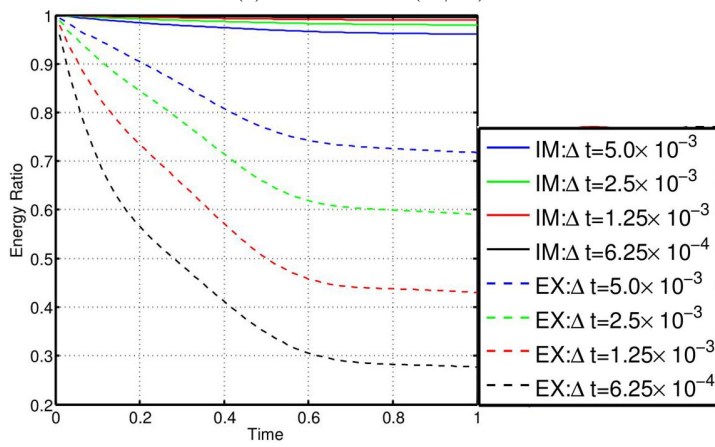
(a) Mixed element (P_2/P_1).(b) Equal-order element (P_1), mesh is twice finer than that in (a) (same number of nodes).

Figure 5.51: The energy ratio against time for Test1-2D (activated disc) in Section 5.6.1.

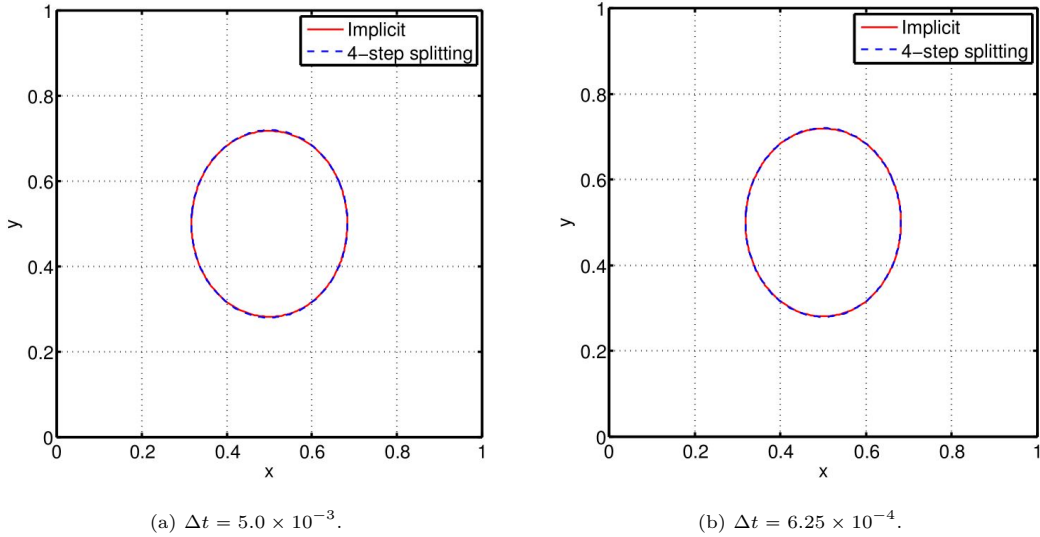


Figure 5.52: The solid deformation at $t = 0.74$ when the solid is maximally stretched along y direction, for Test1-2D (activated disc) in Section 5.6.1 using the mixed element (P_2/P_1).

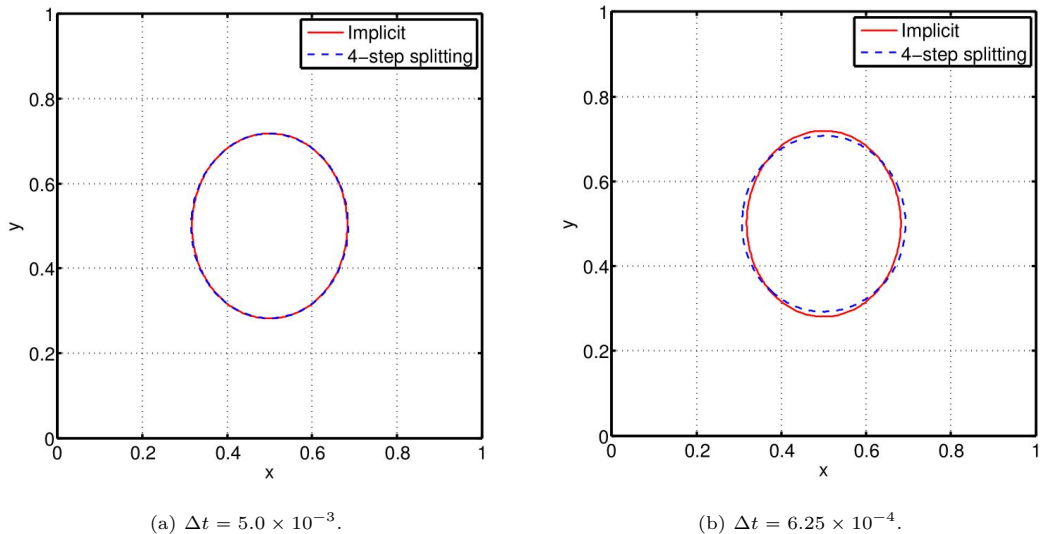


Figure 5.53: The solid deformation at $t = 0.74$ when the solid is maximally stretched along y direction for Test1-2D (activated disc) in Section 5.6.1. The equal-order element (P_1) is used, and the mesh is twice finer (same number of nodes) than the mixed element (P_2/P_1).

The area of the solid disc is plotted in Figure 5.54 as a function of time, from which it is apparent that mass converges in time for both the P_2/P_1 element and the P_1 element. This further indicates that divergence of the energy in Figure 5.51 (b) and divergence of the solid deformation in Figure 5.53 (b) is not because of mass increase or decrease. By looking at the different kinds of energy contribution (defined in Remark 3.7) in Figure 5.55, we could see that the kinetic energy $E_k(\Omega)$ and viscous dissipation $E_d(\Omega)$ evaluated on the background mesh

decrease much quicker, when reducing the time step, than the other two energy components $E_k(\Omega_X^s)$ and $E_p(\Omega_X^s)$ evaluated on the solid mesh. This could be the reason that the total energy does not converge in time, which may further be due to the use of the equal-order element (P_1) for the background mesh. However it still requires further study to explain why the P_1 element damps the kinetic energy $E_k(\Omega)$ so quickly (especially for small time steps) and does not preserve energy. As a comparison, the mixed element (P_2/P_1) behaves quite differently, as shown in Figure 5.56.

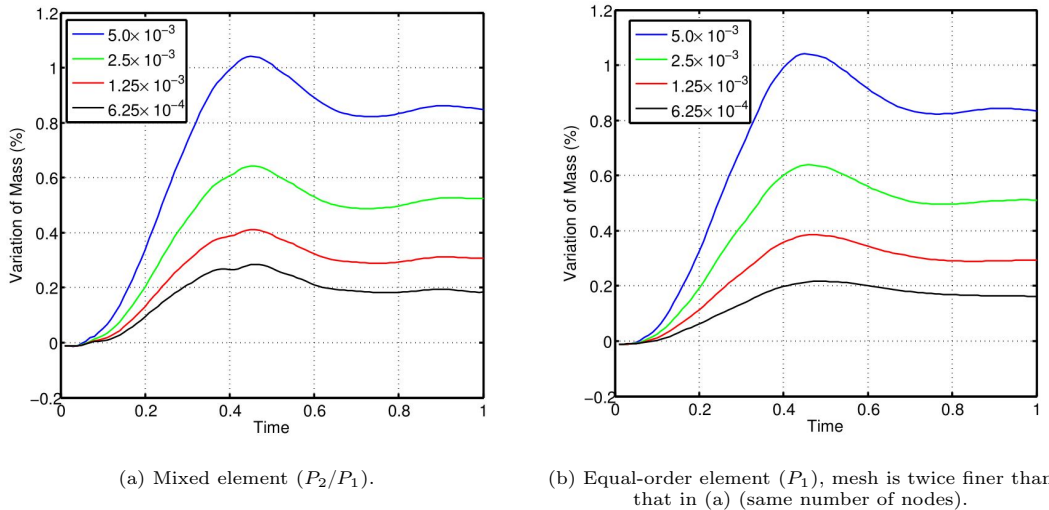


Figure 5.54: Variation of mass as a function of time for Test1-2D (activated disc) in Section 5.6.1.

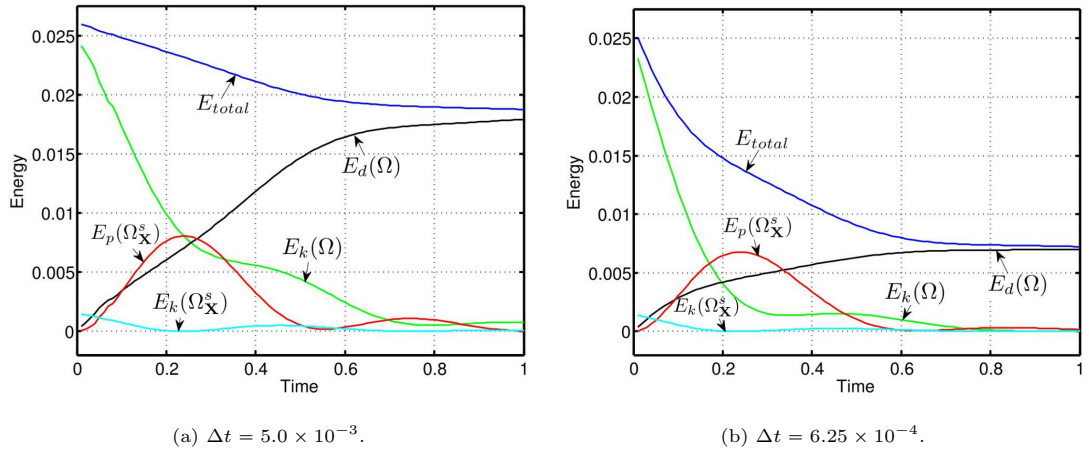


Figure 5.55: Evolution of all energy contributions, using equal-order element (P_1), for Test1-2D (activated disc) in Section 5.6.1.

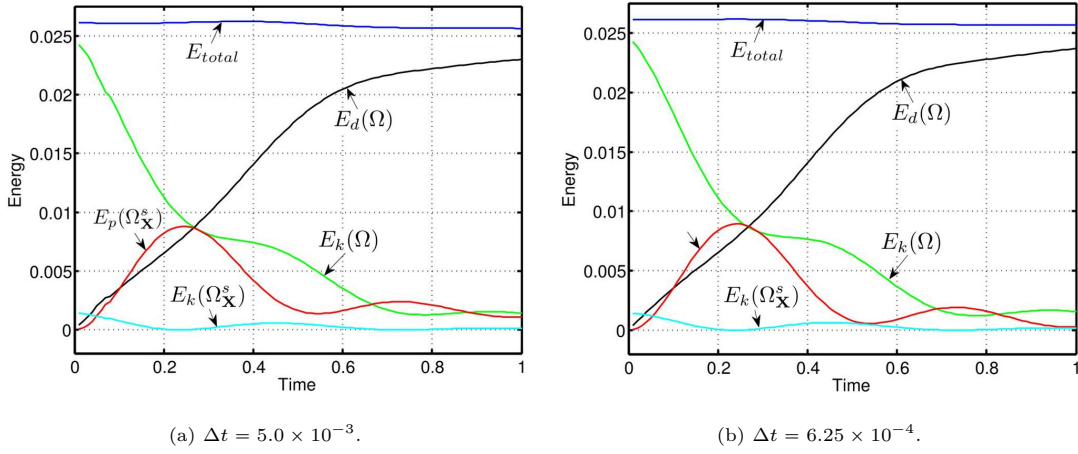


Figure 5.56: Evolution of all energy contributions, using mixed element (P_1), for Test1-2D (activated disc) in Section 5.6.1.

5.6.2 Test2-2D (stretched disc): Oscillating disc driven by an initial potential energy

The time convergence of the error in the total energy is presented in Figure 5.57 and compared with the implicit scheme. From this it can be seen that the total energy converges with reducing time step for the P_2/P_1 element (in Figure 5.57 (a)), however the error in the total energy diverges for the P_1 element, as shown in Figure 5.57 (b). As can be seen from the comparison in Figure 5.58, using the equal-order P_1 elements, the divergence of energy is related to the divergence of the solid deformation, although the reason behind this still needs further study. All the other figures, such as the mass convergence and energy evolution, provide very similar conclusions to those discussed in the above Section 5.6.1. Consequently these are not plotted here.

5.6.3 Test3-3D (activated ball): Oscillating ball driven by an initial kinetic energy

In this section, we use the 4-step splitting scheme to compute the oscillating ball discussed in Section 4.4.3 again, and compare the energy of the 4-step splitting scheme with the implicit scheme. Both the mixed finite element and the equal-order finite element are tested, and again we observe quite different behaviour of these two elements: it can be seen from Figure 5.59 that the former converges while the latter diverges in time.

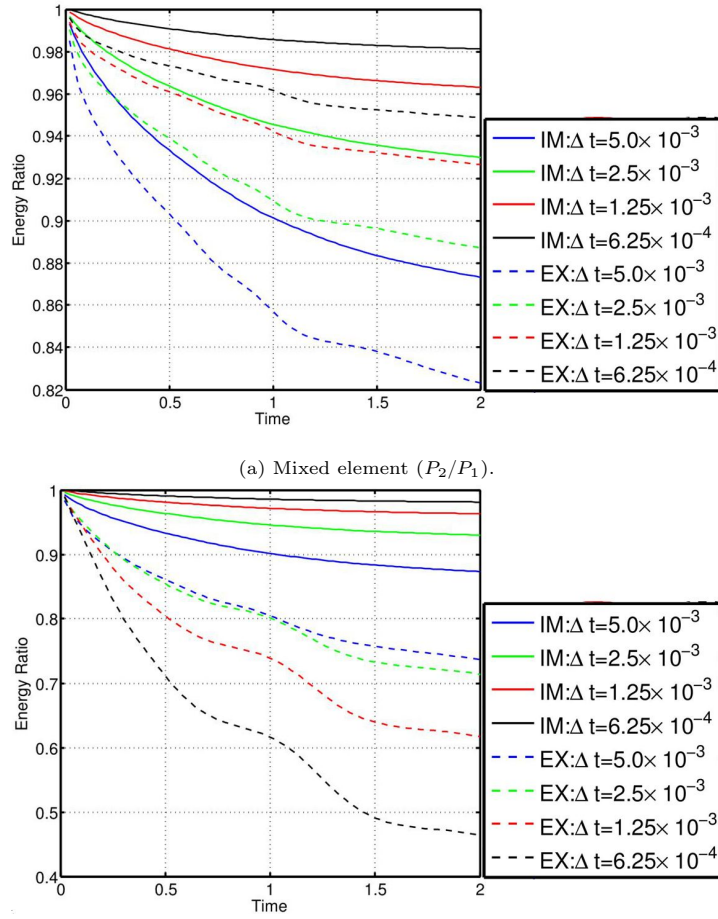
(b) Equal-order element (P_1), mesh is twice finer than that in (a) (same number of nodes).

Figure 5.57: The energy ratio against time for Test2-2D (stretched disc) in Section 5.6.2.

5.6.4 Test7-2D (cavity with disc): Cavity flow with a solid disc (Parameter 1)

We revisit the cavity flow with a solid disc using this 4-step splitting scheme and compare the result with the previous results as demonstrated in Figure 5.60. The mixed element ($P_2/(P_1 + P_0)$) is used, and we also test the case of swapping steps (2) (including step (2.1) and (2.2)) and (3) as discussed in Remark 5.8. It can be seen from Figure 5.60 that the 4-step and 3-step splitting schemes yield almost the same accuracy in terms of the solid deformation.

5.6.5 Test8-2D (leaflet): An oscillating leaflet (Parameter 1)

The displacement of the leaflet tip, using the equal-order element (P_1 element), is presented in Figure 5.61 corresponding to the Figure 5.42 computed by the 3-step splitting scheme. Although

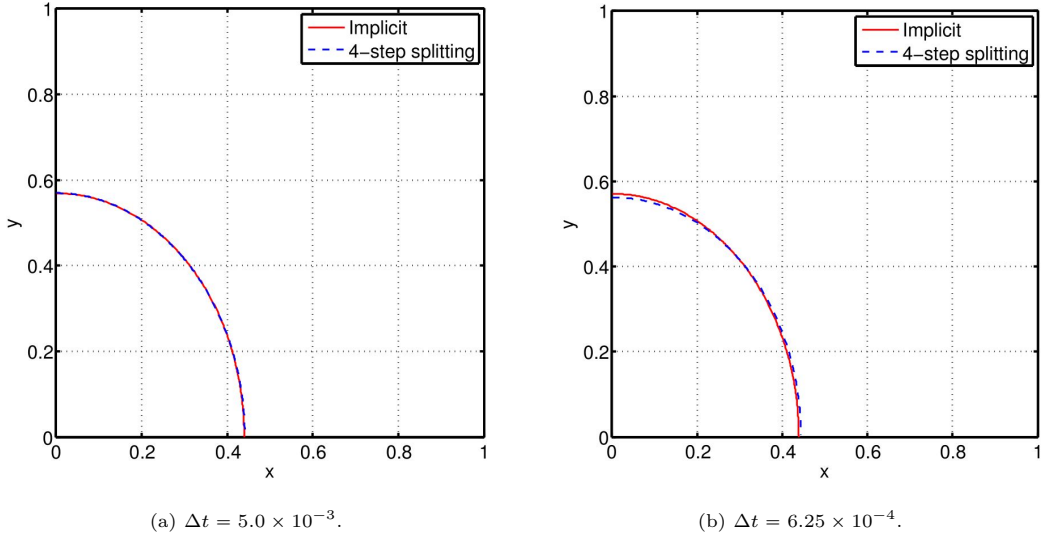


Figure 5.58: The solid deformation at $t = 1.0$ for Test2-2D (stretched disc) in Section 5.6.2. The equal-order element (P_1) is used, and the mesh is twice finer (same number of nodes) than the mixed element (P_2/P_1).

Figure 5.61 and Figure 5.42 look similar, we can observe that the result of the 4-step splitting scheme does not converge in time. However it could be seen from Figure 5.62 that the results converge when using the mixed element (P_2/P_1 element). These results confirm that the energy conservation of the whole FSI system is important, which is directly related to the deformation of the solid.

5.7 Discussion of different splitting schemes

Looking at the fully-coupled FSI equations (3.6) and (3.7), there are three major difficulties: (1) the non-linear convection, (2) the saddle-point problem arising from the incompressibility condition and (3) the fluid-solid interaction in a moving domain. The splitting schemes decouple these three difficulties step by step, so that each subproblem could be more easily solved, accepting the fact of losing accuracy from the 2-step splitting to the 4 step splitting.

The 2-step splitting is accurate, even for the case of large Reynolds number flow. The drawbacks are primarily associated with the diffusion step. (1) It is hard for the preconditioner to use the solid mesh information (for all the tests we have done, the preconditioner is based on the fluid matrix only and works well: so in practice this is not a practical drawback). (2) The preconditioned (incomplete LU factorization as discussed in Section 4.2) MinRes algorithm does not work well for every problem. For example, the preconditioned MinRes algorithm [46] cannot converge for Test8-2D (leaflet) and Test11-2D (thick flag) (even for a pure fluid problem without a solid).

The subproblem of the “Degenerate” Stokes equation in the 3-step splitting scheme can be effectively preconditioned (see Section 5.3.1), and one does not need to know the boundary

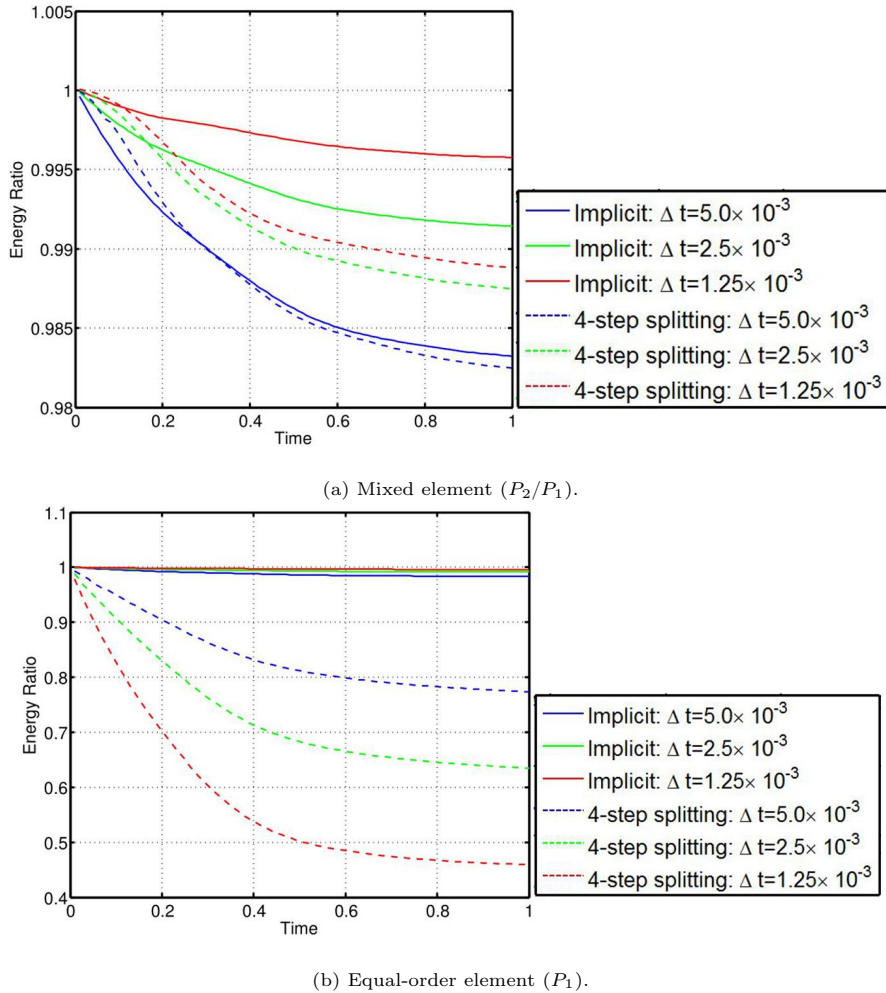


Figure 5.59: Evolution of the energy ratio for Test3-3D (activated ball) in Section 5.6.3.

condition for pressure. The fluid and solid are coupled in the diffusion step, which may also be effectively solved by the preconditioned CG algorithm. This 3-step splitting can solve all the test problems in this thesis and presents accurate results at a reasonable computational cost, which is then recommended.

The major advantage of the 4-step splitting (projection method) is that the *inf-sup* condition is removed and the equal-order element can be used, although the pressure boundary condition is a problem. However our tests show that this equal-order element does not converge in energy. Although it is beyond the scope of the current work, it would be interesting to investigate the reasons behind this in the future.

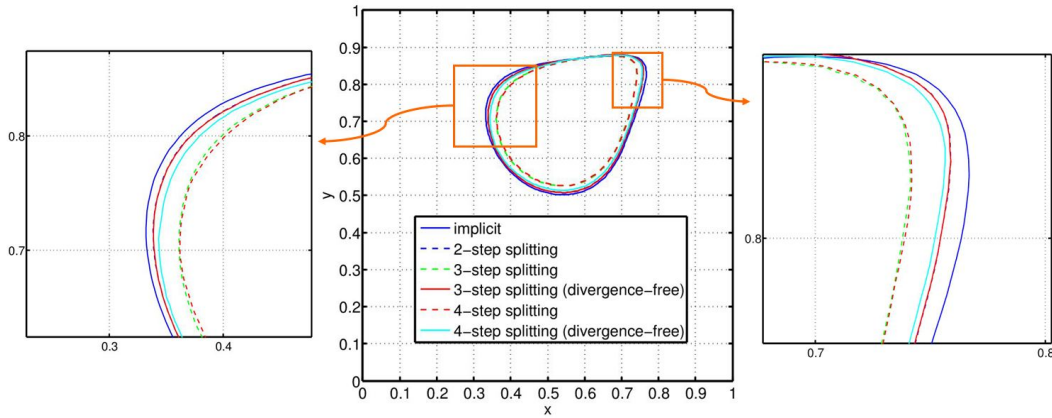


Figure 5.60: The solid deformation at $t = 20$ for Test7-2D (cavity with disc) in Section 5.6.4 using $\Delta t = 1.0 \times 10^{-3}$.

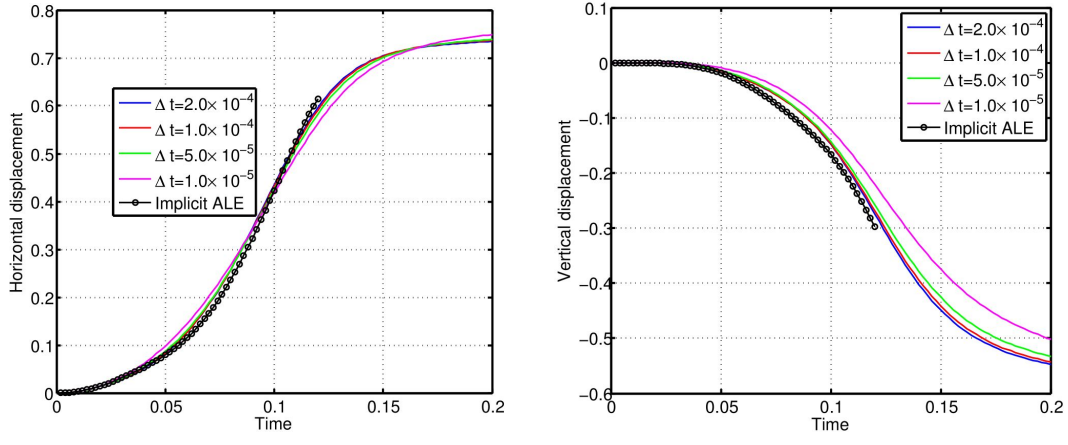


Figure 5.61: Comparison of displacement at the leaflet tip (top-left corner) for Test8-2D (leaflet) in Section 5.6.5. The ALE method is implicit and uses P_2/P_1 element. The 4-step splitting scheme uses the equal-order element (P_1), however whose mesh is twice finer than the ALE mesh (same number of nodes).

5.8 Energy analysis for the explicit splitting schemes

In this section, we estimate the energy of the FSI system for the explicit splitting schemes. We shall see that additional “artificial energy terms” are introduced in these splitting schemes, which consequently introduces errors due to the splitting. However, we shall see that these “artificial energy terms” are proportional to Δt in the following, thus not compromising the convergence of the methods.

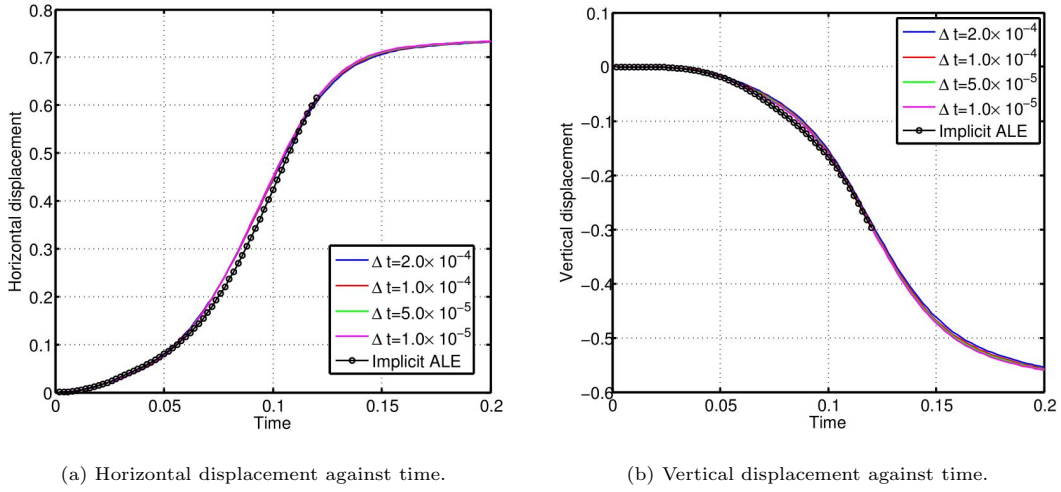


Figure 5.62: Comparison of displacement at the leaflet tip (top-left corner) for Test8-2D (leaflet) in Section 5.6.5. Both the ALE method and the 4-step splitting scheme use the mixed element (P_2/P_1).

5.8.1 2-step splitting scheme

As with the previous analysis for the implicit scheme, if we let $\mathbf{v} = \mathbf{u}_{n+1}$ in equations (5.1), (5.2) and (5.3), adding up these three equations gives:

$$\begin{aligned}
 & \rho^f \int_{\Omega} (\mathbf{u}_{n+1} - \mathbf{u}_n) \cdot \mathbf{u}_{n+1} d\mathbf{x} + \frac{\Delta t \nu^f}{2} \int_{\Omega} D\mathbf{u}_{n+1} : D\mathbf{u}_{n+1} d\mathbf{x} \\
 & + \boxed{\rho^f \Delta t \int_{\Omega} (\mathbf{u}_{n+1/2} \cdot \nabla) \mathbf{u}_{n+1/2} \cdot \mathbf{u}_{n+1} d\mathbf{x}} \\
 & + \rho^\delta \int_{\Omega_{\mathbf{x}}^s} (\mathbf{u}_{n+1} - \mathbf{u}_n) \cdot \mathbf{u}_{n+1} d\mathbf{x} \\
 & + \Delta t \mu^s \int_{\Omega_{\mathbf{x}}^s} \mathbf{F}_{n+1} : \nabla_{\mathbf{x}} \mathbf{u}_{n+1} d\mathbf{X} - \Delta t \mu^s \int_{\Omega_{\mathbf{x}}^s} \nabla \cdot \mathbf{u}_{n+1} d\mathbf{X} \\
 & + \boxed{\Delta t \mu^s \int_{\Omega_{\mathbf{x}}^s} (\nabla \cdot \mathbf{u}_{n+1} - \nabla_n \cdot \mathbf{u}_{n+1}) d\mathbf{X}} = 0.
 \end{aligned} \tag{5.45}$$

Similarly to the proof for the energy estimate of the implicit scheme in Section 3.4.2, we further have the following energy estimate for the 2-step splitting scheme:

$$E_{total}(t_{n+1}) \leq E_{total}(t_n) + R_{n+1}^{im} + R_{2-step}^{conv} + R_{2-step}^{div}, \tag{5.46}$$

where $R_{n+1}^{im} = R_{n+1}$ as defined in (3.40), and E_{total} is defined in Remark 3.7. R_{2-step}^{conv} and R_{2-step}^{div} are from the boxed terms in (5.45), i.e.:

$$R_{2-step}^{conv} = -\Delta t \rho^f \int_{\Omega} (\mathbf{u}_{n+1/2} \cdot \nabla) \mathbf{u}_{n+1/2} \cdot \mathbf{u}_{n+1} d\mathbf{x} \tag{5.47}$$

and

$$R_{2-step}^{div} = \Delta t \mu^s \int_{\Omega_X^s} (\nabla_n \cdot \mathbf{u}_{n+1} - \nabla \cdot \mathbf{u}_{n+1}) d\mathbf{X}. \quad (5.48)$$

We can deduce from this that the growth in the total energy is bounded by its initial value plus terms of order Δt .

5.8.2 3-step splitting scheme

For the 3-step splitting, we choose $\mathbf{v} = \mathbf{u}_{n+1}$ in equation (5.23), (5.24) and (5.27), and choose $q = p_{n+2/3}$ in (5.25). Adding up these four equations gives:

$$\begin{aligned} & \rho^f \int_{\Omega} (\mathbf{u}_{n+1} - \mathbf{u}_n) \cdot \mathbf{u}_{n+1} d\mathbf{x} + \frac{\Delta t \nu^f}{2} \int_{\Omega} \mathbf{D}\mathbf{u}_{n+1} : \mathbf{D}\mathbf{u}_{n+1} d\mathbf{x} \\ & + \boxed{\rho^f \Delta t \int_{\Omega} (\mathbf{u}_{n+1/3} \cdot \nabla) \mathbf{u}_{n+1/3} \cdot \mathbf{u}_{n+1} d\mathbf{x}} \\ & + \boxed{\Delta t \int_{\Omega} p_{n+2/3} (\nabla \cdot \mathbf{u}_{n+2/3} - \nabla \cdot \mathbf{u}_{n+1}) d\mathbf{x}} \\ & + \rho^\delta \int_{\Omega_X^s} (\mathbf{u}_{n+1} - \mathbf{u}_n) \cdot \mathbf{u}_{n+1} d\mathbf{x} \\ & + \Delta t \mu^s \int_{\Omega_X^s} \mathbf{F}_{n+1} : \nabla_{\mathbf{X}} \mathbf{u}_{n+1} d\mathbf{X} - \Delta t \mu^s \int_{\Omega_X^s} \nabla \cdot \mathbf{u}_{n+1} d\mathbf{X} \\ & + \boxed{\Delta t \mu^s \int_{\Omega_X^s} (\nabla \cdot \mathbf{u}_{n+1} - \nabla_n \cdot \mathbf{u}_{n+1}) d\mathbf{X}} = 0, \end{aligned} \quad (5.49)$$

and the energy estimate relation may be expressed as:

$$E_{total}(t_{n+1}) \leq E_{total}(t_n) + R_{n+1}^{im} + R_{3-step}^{conv} + R_{3-step}^{div-p} + R_{3-step}^{div}, \quad (5.50)$$

where

$$R_{3-step}^{conv} = -\Delta t \rho^f \int_{\Omega} (\mathbf{u}_{n+1/3} \cdot \nabla) \mathbf{u}_{n+1/3} \cdot \mathbf{u}_{n+1} d\mathbf{x} \quad (5.51)$$

$$R_{3-step}^{div-p} = \Delta t \int_{\Omega} p_{n+2/3} (\nabla \cdot \mathbf{u}_{n+1} - \nabla \cdot \mathbf{u}_{n+2/3}) d\mathbf{x}, \quad (5.52)$$

and $R_{3-step}^{div} = R_{2-step}^{div}$.

5.8.3 4-step splitting scheme

Finally, let $\mathbf{v} = \mathbf{u}_{n+1}$ in equation (5.23), (5.27) and (5.44), and choose $q = p_{n+2/3}$ in (5.42). Adding up these four equation gives:

$$\begin{aligned}
& \rho^f \int_{\Omega} (\mathbf{u}_{n+1} - \mathbf{u}_n) \cdot \mathbf{u}_{n+1} d\mathbf{x} + \frac{\Delta t \nu^f}{2} \int_{\Omega} \mathbf{D}\mathbf{u}_{n+1} : \mathbf{D}\mathbf{u}_{n+1} d\mathbf{x} \\
& + \boxed{\rho^f \Delta t \int_{\Omega} (\mathbf{u}_{n+1/3} \cdot \nabla) \mathbf{u}_{n+1/3} \cdot \mathbf{u}_{n+1} d\mathbf{x}} \\
& + \boxed{\Delta t \int_{\Omega} p_{n+2/3} (\nabla \cdot \mathbf{u}_{n+1/3} - \nabla \cdot \mathbf{u}_{n+1}) d\mathbf{x}} \\
& - \boxed{\frac{\Delta t}{2\rho^f} \int_{\Omega} \nabla p_{n+2/3} \cdot \nabla p_{n+2/3} d\mathbf{x}} \\
& + \rho^\delta \int_{\Omega_{\mathbf{X}}^s} (\mathbf{u}_{n+1} - \mathbf{u}_n) \cdot \mathbf{u}_{n+1} d\mathbf{x} \\
& + \Delta t \mu^s \int_{\Omega_{\mathbf{X}}^s} \mathbf{F}_{n+1} : \nabla_{\mathbf{X}} \mathbf{u}_{n+1} d\mathbf{X} - \Delta t \mu^s \int_{\Omega_{\mathbf{X}}^s} \nabla \cdot \mathbf{u}_{n+1} d\mathbf{X} \\
& + \boxed{\Delta t \mu^s \int_{\Omega_{\mathbf{X}}^s} (\nabla \cdot \mathbf{u}_{n+1} - \nabla_n \cdot \mathbf{u}_{n+1}) d\mathbf{X}} = 0,
\end{aligned} \tag{5.53}$$

and the energy estimate is as follows:

$$E_{total}(t_{n+1}) \leq E_{total}(t_n) + R_{n+1}^{im} + R_{4-step}^{conv} + R_{4-step}^{div-p} + R_{4-step}^{press} + R_{4-step}^{div}, \tag{5.54}$$

where $R_{4-step}^{conv} = E_{3-step}^{conv}$, $R_{4-step}^{div} = R_{3-step}^{div}$,

$$R_{4-step}^{div-p} = \Delta t \int_{\Omega} p_{n+2/3} (\nabla \cdot \mathbf{u}_{n+1} - \nabla \cdot \mathbf{u}_{n+1/3}) d\mathbf{x}, \tag{5.55}$$

and

$$R_{4-step}^{press} = \frac{\Delta t}{2\rho^f} \int_{\Omega} \nabla p_{n+2/3} \cdot \nabla p_{n+2/3} d\mathbf{x}. \tag{5.56}$$

5.9 Summary

In this chapter, we decouple the implicit fully-coupled one-field FDM into several simple explicit steps using the operator splitting schemes. First, a 2-step splitting scheme is obtained by decoupling the convection and diffusion steps, such that the non-linear convection equation could be treated separately, leaving the diffusion equation to be a symmetric Stokes/saddle-point system. Second, a 3-step splitting is established by further decoupling the above diffusion step, which introduces a “Degenerate” Stokes equation. Finally, the “Degenerate” Stokes equation may be further split into a “Pressure Poisson” step and a velocity-update step. In this case,

the original problem is simplified step by step.

These explicit splitting schemes have been validated systematically by a selection of numerical tests. For the 4-step splitting scheme (projection method) the equal-order element is cheap and widely used in pure fluid problems [58]. However, we found that the equal-order element could not preserve energy for our FSI system, while the mixed element could preserve energy. We actually do not know the reason behind this, which needs further study.

A brief energy estimate for these splitting schemes are presented, which shows a similar property as the implicit scheme: the energy is essentially non-increasing with some additional energy terms that are proportional to Δt . As discussed in Section 3.5, the solution existence of the implicit scheme (Problem 3.3) may be proved based upon the energy estimate result in Section 3.4. Similarly the solution existence of the explicit splitting schemes may be proved based upon the energy estimate demonstrated in Section 5.8. However this will be investigated in greater detail in the future.

Chapter 6

Further investigations

In this chapter, we present some topics that follow directly from this work, and some topics that may be worth investigating in the future. In Section 6.1, we prove that the implicit Problem 3.2 and Problem 3.3 are well-posed based upon Assumptions 6.1 to 6.3. In Section 6.2 we introduce some initial results using a non-Newtonian fluid with the one-field FDM. In Section 6.3, contact problems and a contact model are presented. The formulation of the one-field FDM is introduced for a truss structure in Section 6.4. Finally the formulation in the case of a compressible solid is considered in Section 6.5.

6.1 Discussion of the well-posedness of one step of Problem 3.2 and Problem 3.3

In this section, we focus on the stationary problem corresponding to one step of the Problem 3.2 and consider its well-posedness and discretization in space (one step of the Problem 3.3) based on the following three assumptions.

Assumption 6.1. We assume a constant density and viscosity for both the fluid and solid, and further assume that the solid density is not less than the fluid density ($\rho^\delta \geq 0$) and the solid viscosity is the same as the fluid viscosity ($\nu^\delta = 0$).

Assumption 6.2. We neglect the convection term for convenience and assume that the boundary force is zero ($\bar{\mathbf{h}} = 0$). We also neglect term $\int_{\Omega_{n+1}^s} \mu^s J_{n+1}^{-1} \nabla \cdot \mathbf{v} dx$ in equation (3.9), which means $\mu^s J_{n+1}^{-1}$ has been absorbed into the solid pressure p^s . As noted in Remark 2.2, this is not a good idea when implementing on meshes without interface fitting. However we can only prove the well-posedness based on such an assumption, although we implement the proposed scheme with this non-linear term $\int_{\Omega_{n+1}^s} \mu^s J_{n+1}^{-1} \nabla \cdot \mathbf{v} dx$ in equation (3.9).

Assumption 6.3. We assume the map $\mathbf{x}(\cdot, t) : \Omega_{\mathbf{X}}^s \rightarrow \Omega_t^s$ is one-to-one, Lipschitz continuous, and invertible with Lipschitz inverse. By definition of Lipschitz continuous: $\forall t \in [0, T]$ and

$\mathbf{X}_1, \mathbf{X}_2 \in \Omega_{\mathbf{X}}^s$, $\exists k_0 > 0$ such that $\|\mathbf{x}(\mathbf{X}_1, t) - \mathbf{x}(\mathbf{X}_2, t)\| \leq k_0 \|\mathbf{X}_1 - \mathbf{X}_2\|$. By definition of invertible with Lipschitz inverse [18]: $\forall t \in [0, T]$ and $\mathbf{X}_1, \mathbf{X}_2 \in \Omega_{\mathbf{X}}^s$, $\exists k_1 > 0$ such that $\|\mathbf{x}(\mathbf{X}_1, t) - \mathbf{x}(\mathbf{X}_2, t)\| \geq k_1 \|\mathbf{X}_1 - \mathbf{X}_2\|$.

From the definition of Lipschitz continuous, we have: $\forall \mathbf{X}, \mathbf{h} \in \Omega_{\mathbf{X}}^s$,

$$\|\mathbf{x}(\mathbf{X} + \epsilon \mathbf{h}) - \mathbf{x}(\mathbf{X})\| \leq k_0 \epsilon \|\mathbf{h}\|, \quad (6.1)$$

or

$$\left\| \frac{\mathbf{x}(\mathbf{X} + \epsilon \mathbf{h}) - \mathbf{x}(\mathbf{X})}{\epsilon} \right\| \leq k_0 \|\mathbf{h}\|. \quad (6.2)$$

Let $\mathbf{h} = \mathbf{e}_i$ (the i^{th} component is 1 and all the other components are 0) and $\epsilon \rightarrow 0$, we know that every row of the deformation matrix \mathbf{F} is bounded, i.e.:

$$\|\mathbf{F}_i\| = \lim_{\epsilon \rightarrow 0} \left\| \frac{\mathbf{x}(\mathbf{X} + \epsilon \mathbf{e}_i) - \mathbf{x}(\mathbf{X})}{\epsilon} \right\| \leq k_0 \quad (i = 1, \dots, d). \quad (6.3)$$

Based on the Frobenius norm we use in this thesis, we have

$$\|\mathbf{F}\|^2 = \sum_{i=1}^d \|\mathbf{F}_i\|^2 \leq k_0^2 d. \quad (6.4)$$

Similarly, from the definition of Lipschitz inverse we know that every column of \mathbf{F}^{-1} is bounded, i.e.:

$$\left\| [\mathbf{F}^{-1}]_i \right\| \leq \frac{1}{k_1} \quad (i = 1, \dots, d), \quad (6.5)$$

and further

$$\|\mathbf{F}^{-1}\|^2 = \sum_{i=1}^d \left\| [\mathbf{F}^{-1}]_i \right\|^2 \leq \frac{d}{k_1^2}. \quad (6.6)$$

We summarize a corollary of Assumption 6.3 as follows.

Corollary 6.1. Both \mathbf{F} and \mathbf{F}^{-1} are bounded in $L^2(\Omega_{\mathbf{X}}^s)$ and $L^2(\Omega_t^s)$ respectively under Assumption 6.3.

Before analyzing the well-posedness, let us rewrite Problems 3.2 by introducing some bilinear and linear forms as follows. Define the following bilinear forms:

$$a^f(\mathbf{u}, \mathbf{v}) = \alpha \int_{\Omega} \mathbf{u} \cdot \mathbf{v} d\mathbf{x} + \frac{\nu^f}{2} \int_{\Omega} \mathbf{D}\mathbf{u} : \mathbf{D}\mathbf{v} d\mathbf{x}, \quad (6.7)$$

$$a^s(\mathbf{u}, \mathbf{v}) = \beta \int_{\Omega_{\mathbf{X}}^s} \mathbf{u} \cdot \mathbf{v} d\mathbf{X} + \gamma \int_{\Omega_{\mathbf{X}}^s} \nabla_{\mathbf{X}} \mathbf{u} : \nabla_{\mathbf{X}} \mathbf{v} d\mathbf{X}, \quad (6.8)$$

and

$$b(\mathbf{v}, q) = - \int_{\Omega} q \nabla \cdot \mathbf{v} d\mathbf{x}, \quad (6.9)$$

where $\alpha = \rho^f/\Delta t$, $\beta = \rho^\delta/\Delta t$ and $\gamma = \mu^s\Delta t$.

Remark 6.1. There would be a term $\frac{\nu^\delta}{2} \int_{\Omega_{n+1}^s} \mathbf{D}\mathbf{u} : \mathbf{D}\mathbf{v} d\mathbf{x}$ in the definition of $a^s(\mathbf{u}, \mathbf{v})$ in (6.8) if we do not assume $\nu^\delta = 0$, then $a^s(\mathbf{u}, \mathbf{v})$ cannot be regarded as bilinear because the domain Ω_{n+1}^s changes.

We also define the following linear forms:

$$\ell^f(\mathbf{v}) = \rho^f \int_{\Omega} \bar{\mathbf{g}} \cdot \mathbf{v} d\mathbf{x}, \quad (6.10)$$

and

$$\ell^s(\mathbf{v}) = \rho^\delta \int_{\Omega_{\mathbf{X}}^s} \bar{\mathbf{g}} \cdot \mathbf{v} d\mathbf{X} - \mu^s \int_{\Omega_{\mathbf{X}}^s} \mathbf{F}_n : \nabla_{\mathbf{X}} \mathbf{v} d\mathbf{X}, \quad (6.11)$$

where $\bar{\mathbf{g}} = \frac{1}{\Delta t} \mathbf{u}_n + \mathbf{g}$ in the above. Let

$$a(\mathbf{u}, \mathbf{v}) = a^f(\mathbf{u}, \mathbf{v}) + a^s(\mathbf{u}, \mathbf{v}), \quad (6.12)$$

and

$$\ell(\mathbf{v}) = \ell^f(\mathbf{v}) + \ell^s(\mathbf{v}), \quad (6.13)$$

then the weak form corresponding to one step of Problem 3.2 with $\mathbf{u} = \mathbf{u}_{n+1}$ and $p = p_{n+1}$, using the above notation and Assumptions 6.1 to 6.3, can be stated as:

Problem 6.1. Find $\mathbf{u} \in \mathbb{V}$, $p \in \mathbb{P}$, such that

$$\begin{cases} a(\mathbf{u}, \mathbf{v}) + b(\mathbf{v}, p) = \ell(\mathbf{v}) & \forall \mathbf{v} \in \mathbb{V} \\ b(\mathbf{u}, q) = 0 & \forall q \in \mathbb{P} \end{cases},$$

where $\mathbb{V} = H_0^1(\Omega)^d$ and $\mathbb{P} = L_0^2(\Omega)$.

For the rest of this section, let us use the following norms for vector functions and matrix functions respectively: $\|\mathbf{u}\|_{0,\omega}^2 = \sum_{i=1}^d \|u_i\|_{0,\omega}^2$ and $\|\mathbf{A}\|_{0,\omega}^2 = \sum_{i=1}^d \sum_{j=1}^d \|A_{ij}\|_{0,\omega}^2$, and denote $\|\mathbf{u}\|_{\mathbb{V}} = \|\mathbf{u}\|_{1,\Omega}$.

6.1.1 Well-posedness of Problem 6.1 (one step of Problem 3.2)

Following the standard Stokes problem, the well-posedness of Problem 6.1 relies on the following three facts: (1) $a(\mathbf{u}, \mathbf{v})$ and $b(\mathbf{v}, q)$ are well-defined bounded bilinear forms; (2) $\ell(\mathbf{v})$ is a well-defined bounded linear form, and; (3) $a(\mathbf{u}, \mathbf{v})$ is coercive. These are proved below.

Lemma 6.1. $a(\mathbf{u}, \mathbf{v})$ is bounded, i.e., there exists a positive real number C_a , such that $\forall \mathbf{u}, \mathbf{v} \in \mathbb{V}$,

$$|a(\mathbf{u}, \mathbf{v})| \leq C_a \|\mathbf{u}\|_{\mathbb{V}} \|\mathbf{v}\|_{\mathbb{V}}. \quad (6.14)$$

Proof. First

$$\begin{aligned} |a(\mathbf{u}, \mathbf{v})| &\leq \alpha \|\mathbf{u}\|_{0,\Omega} \|\mathbf{v}\|_{0,\Omega} + \frac{\nu^f}{2} \|\mathbf{D}\mathbf{u}\|_{0,\Omega} \|\mathbf{D}\mathbf{v}\|_{0,\Omega} \\ &+ \beta \|\mathbf{u}\|_{0,\Omega_{\mathbf{x}}^s} \|\mathbf{v}\|_{0,\Omega_{\mathbf{x}}^s} + \gamma \|\nabla_{\mathbf{x}} \mathbf{u}\|_{0,\Omega_{\mathbf{x}}^s} \|\nabla_{\mathbf{x}} \mathbf{v}\|_{0,\Omega_{\mathbf{x}}^s}. \end{aligned} \quad (6.15)$$

Noticing that

$$\|\nabla_{\mathbf{x}} \mathbf{u}\|_{0,\Omega_{\mathbf{x}}^s} \leq \|\mathbf{u}\|_{1,\Omega_{\mathbf{x}}^s} \leq \|\mathbf{u}\|_{1,\Omega}, \quad (6.16)$$

and

$$\|\mathbf{D}\mathbf{u}\|_{0,\Omega} \leq 2 \|\nabla \mathbf{u}\|_{0,\Omega} \leq 2 \|\mathbf{u}\|_{1,\Omega},$$

we can observe that (6.14) holds from (6.15), with $C_a = \alpha + \beta + 2\nu^f + \gamma$. \square

Lemma 6.2. $b(\mathbf{v}, q)$ is bounded, i.e., there exists a positive real number C_b , such that $\forall \mathbf{v} \in \mathbb{V}$ and $\forall q \in \mathbb{P}$

$$|b(\mathbf{v}, q)| \leq C_b \|\mathbf{v}\|_{\mathbb{V}} \|q\|_{\mathbb{P}}. \quad (6.17)$$

Proof. According to (6.9):

$$|b(\mathbf{v}, q)| \leq \|\nabla \mathbf{v}\|_{0,\Omega} \|q\|_{0,\Omega} \leq \|\mathbf{v}\|_{\mathbb{V}} \|q\|_{\mathbb{P}}. \quad (6.18)$$

\square

Lemma 6.3. $\ell(\mathbf{v})$ is bounded, i.e., there exists a positive real number C_ℓ , such that $\forall \mathbf{v} \in \mathbb{V}$,

$$|\ell(\mathbf{v})| \leq C_\ell \|\mathbf{v}\|_{\mathbb{V}}. \quad (6.19)$$

Proof.

$$\begin{aligned} |\ell(\mathbf{v})| &\leq \rho^f \|\bar{\mathbf{g}}\|_{0,\Omega} \|\mathbf{v}\|_{0,\Omega} + \rho^\delta \|\bar{\mathbf{g}}\|_{0,\Omega_{\mathbf{x}}^s} \|\mathbf{v}\|_{0,\Omega_{\mathbf{x}}^s} + \mu^s \|\mathbf{F}_n\|_{0,\Omega_{\mathbf{x}}^s} \|\nabla_{\mathbf{x}} \mathbf{v}\|_{0,\Omega_{\mathbf{x}}^s} \\ &\leq \rho^s \|\bar{\mathbf{g}}\|_{0,\Omega} \|\mathbf{v}\|_{0,\Omega} + \kappa \|\mathbf{F}_n\|_{0,\Omega_{\mathbf{x}}^s} \|\nabla_{\mathbf{x}} \mathbf{v}\|_{0,\Omega_{\mathbf{x}}^s}. \end{aligned}$$

We further get (6.19) using relation (6.16), with $C_\ell = \rho^s \|\bar{\mathbf{g}}\|_{0,\Omega} + \mu^s \|\mathbf{F}_n\|_{0,\Omega_{\mathbf{x}}^s}$. \square

Lemma 6.4. $a(\mathbf{u}, \mathbf{v})$ is coercive, i.e., there exists a positive real number c_a , such that $\forall \mathbf{u} \in \mathbb{V}$,

$$a(\mathbf{u}, \mathbf{u}) \geq c_a \|\mathbf{u}\|_{\mathbb{V}}^2. \quad (6.20)$$

Proof. According to the definition of $a(\mathbf{u}, \mathbf{v})$ and assumption $\beta = \rho^\delta / \Delta t \geq 0$:

$$a(\mathbf{u}, \mathbf{u}) = a^f(\mathbf{u}, \mathbf{u}) + a^s(\mathbf{u}, \mathbf{u}) \geq a^f(\mathbf{u}, \mathbf{u}).$$

Therefore, coercivity of the standard bilinear form $a^f(\mathbf{u}, \mathbf{v})$ from Stokes equation (see [44] or [24] for proof) guarantees the coercivity of $a(\mathbf{u}, \mathbf{v})$. \square

The above four lemmas imply the following inf-sup condition and further the well-posedness result [24, Lemma 12.2.12]:

Proposition 6.1 (Inf-Sup Condition). There exist $c_b > 0$ such that

$$\inf_{q \in \mathbb{P}} \sup_{\mathbf{v} \in \mathbb{V}} \frac{b(\mathbf{v}, q)}{\|\mathbf{v}\|_{\mathbb{V}} \|q\|_{\mathbb{P}}} \geq c_b. \quad (6.21)$$

Proof. The proof can be found in [24, Section 12.2]. \square

Theorem 1. Problem 6.1 has a unique solution $(\mathbf{u}, p) \in \mathbb{V} \times \mathbb{P}$.

Proof. The proof is the same as [24, Lemma 12.2.12]. \square

6.1.2 Well-posedness after discretization in space (one step of Problem 3.3)

The spatially discretized problem corresponding to Problem 6.1 is as follows, which is equivalent to Problem 3.3 simplified based on Assumptions 6.1 to 6.3.

Problem 6.2. Find $\mathbf{u}^h \in \mathbb{V}^h$, $p^h \in \mathbb{P}^h$, such that

$$\begin{cases} a^h(\mathbf{u}^h, \mathbf{v}^h) + b(\mathbf{v}^h, p^h) = \ell^h(\mathbf{v}^h) & \forall \mathbf{v}^h \in \mathbb{V}^h \\ b(\mathbf{u}^h, q^h) = 0 & \forall q^h \in \mathbb{P}^h \end{cases},$$

where $\mathbb{V}^h = V^h(\Omega^h)^d$, $\mathbb{P}^h = L^h(\Omega^h)$, a^h can be expressed as:

$$a^h(\mathbf{u}^h, \mathbf{v}^h) = a^f(\mathbf{u}^h, \mathbf{v}^h) + a^s(\mathbf{u}^{sh}, \mathbf{v}^{sh}), \quad (6.22)$$

and ℓ^h can be expressed as:

$$\ell^h(\mathbf{v}^h) = \ell^f(\mathbf{v}^h) + \ell^s(\mathbf{v}^{sh}). \quad (6.23)$$

where $\mathbf{u}^{sh} = P_{n+1}(\mathbf{u}^h)$ and $\mathbf{v}^{sh} = P_{n+1}(\mathbf{v}^h)$.

From the error estimate for interpolation [24, Chapter 4, Corollary 4.4.24], the approximation (3.15) can be bounded by:

$$\|P_{n+1}(\mathbf{u}^h(\mathbf{x})) - \mathbf{u}^h(\mathbf{x})\|_{1, \Omega_{n+1}^s} \leq C_h \|\nabla \mathbf{u}^h(\mathbf{x})\|_{0, \Omega_{n+1}^s}, \quad (6.24)$$

where C_h is a positive constant depending on the mesh Ω^{sh} . In order to prove Problem 6.2 is well-posed, we still need to prove the continuity of $a^h(\mathbf{u}^h, \mathbf{v}^h)$ and $\ell^h(\mathbf{v}^h)$, and the coercivity of $a^h(\mathbf{u}^h, \mathbf{v}^h)$. The main idea is to bound \mathbf{u}^{sh} and $\nabla_{\mathbf{X}} \mathbf{u}^{sh}$ in \mathbb{V} , which can be achieved by the above interpolation error estimate.

Lemma 6.5. *There exists a positive real number c_1 such that*

$$\|\mathbf{u}^{sh}(\mathbf{x})\|_{0,\Omega_{\mathbf{X}}^s} \leq c_1 \|\mathbf{u}^h(\mathbf{x})\|_{1,\Omega}. \quad (6.25)$$

Proof. From (6.24), we get

$$\begin{aligned} \|\mathbf{u}^{sh}(\mathbf{x})\|_{1,\Omega_{n+1}^s} &= \|P_{n+1}(\mathbf{u}^h(\mathbf{x}))\|_{1,\Omega_{n+1}^s} \\ &\leq \|\mathbf{u}^h(\mathbf{x})\|_{1,\Omega_{n+1}^s} + \|P_{n+1}(\mathbf{u}^h(\mathbf{x})) - \mathbf{u}^h(\mathbf{x})\|_{1,\Omega_{n+1}^s} \\ &\leq \|\mathbf{u}^h(\mathbf{x})\|_{1,\Omega_{n+1}^s} + C_h \|\nabla \mathbf{u}^h(\mathbf{x})\|_{0,\Omega_{n+1}^s} \\ &\leq (1 + C_h) \|\mathbf{u}^h(\mathbf{x})\|_{1,\Omega}. \end{aligned} \quad (6.26)$$

Using the Cauchy-Schwarz inequality, we have

$$\begin{aligned} \int_{\Omega_{\mathbf{X}}^s} \mathbf{u}^{sh} : \mathbf{u}^{sh} d\mathbf{X} &= \int_{\Omega_{n+1}^s} J^{-1} \mathbf{u}^{sh} : \mathbf{u}^{sh} d\mathbf{x} \\ &\leq \|J^{-1} \mathbf{u}^{sh}\|_{0,\Omega_{n+1}^s} \|\mathbf{u}^{sh}\|_{0,\Omega_{n+1}^s} \leq \|J^{-1}\|_{0,\Omega_{n+1}^s} \|\mathbf{u}^{sh}\|_{0,\Omega_{n+1}^s}^2, \end{aligned} \quad (6.27)$$

and further

$$\|\mathbf{u}^{sh}(\mathbf{x})\|_{0,\Omega_{\mathbf{X}}^s} \leq \|J^{-1}\|_{0,\Omega_{n+1}^s}^{1/2} \|\mathbf{u}^{sh}(\mathbf{x})\|_{0,\Omega_{n+1}^s}. \quad (6.28)$$

$\|J^{-1}\|_{0,\Omega_{n+1}^s}^{1/2} \leq C_I$ (C_I is a positive constant) because \mathbf{F}^{-1} is bounded in $L^2(\Omega_{n+1}^s)$ due to Corollary 6.1. Finally we have (6.25) with $c_1 = C_I(1 + C_h)$. \square

Lemma 6.6. *There exists a positive real number c_2 such that*

$$\|\nabla_{\mathbf{X}} \mathbf{u}^{sh}\|_{0,\Omega_{\mathbf{X}}^s} \leq c_2 \|\mathbf{u}^h\|_{1,\Omega}. \quad (6.29)$$

Proof. According to Cauchy-Schwarz inequality,

$$\begin{aligned} \int_{\Omega_{\mathbf{X}}^s} \nabla_{\mathbf{X}} \mathbf{u}^{sh} : \nabla_{\mathbf{X}} \mathbf{u}^{sh} d\mathbf{X} &= \int_{\Omega_{n+1}^s} J^{-1} (\nabla \mathbf{u}^{sh} \mathbf{F}) : (\nabla \mathbf{u}^{sh} \mathbf{F}) d\mathbf{x} \\ &\leq \|J^{-1} \nabla \mathbf{u}^{sh} \mathbf{F}\|_{0,\Omega_{n+1}^s} \|\nabla \mathbf{u}^{sh} \mathbf{F}\|_{0,\Omega_{n+1}^s} \leq \|J^{-1}\|_{0,\Omega_{n+1}^s} \|\nabla \mathbf{u}^{sh} \mathbf{F}\|_{0,\Omega_{n+1}^s}^2. \end{aligned} \quad (6.30)$$

Therefore:

$$\begin{aligned} \|\nabla_{\mathbf{X}} \mathbf{u}^{sh}\|_{0,\Omega_{\mathbf{X}}^s} &\leq \|J^{-1}\|_{0,\Omega_{n+1}^s}^{1/2} \|\mathbf{F}\|_{0,\Omega_{n+1}^s} \|\nabla \mathbf{u}^{sh}\|_{0,\Omega_{n+1}^s} \\ &\leq \|J^{-1}\|_{0,\Omega_{n+1}^s}^{1/2} \|J\|_{0,\Omega_{\mathbf{X}}^s}^{1/2} \|\mathbf{F}\|_{0,\Omega_{\mathbf{X}}^s} \|\nabla \mathbf{u}^{sh}\|_{0,\Omega_{n+1}^s} \\ &\leq C_I C_J C_F \|\nabla \mathbf{u}^{sh}\|_{0,\Omega_{n+1}^s} \leq C_{IJF} \|\mathbf{u}^{sh}\|_{1,\Omega_{n+1}^s}. \end{aligned} \quad (6.31)$$

In the above, $C_{IJF} = C_I C_J C_F$, $\|J\|_{0,\Omega_{\mathbf{X}}^s}^{1/2} \leq C_J$ (C_J is a positive constant) and $\|\mathbf{F}\|_{0,\Omega_{\mathbf{X}}^s} \leq C_F$

thanks to Corollary 6.1. Using (6.26), we finally have (6.29) with $c_2 = C_{IJF}(1 + C_h)$. The following inequality for a matrix norm is also used in the above proof.

$$\|\mathbf{AB}\|_{0,\Omega_{n+1}^s} \leq \|\mathbf{A}\|_{0,\Omega_{n+1}^s} \|\mathbf{B}\|_{0,\Omega_{n+1}^s}, \quad (6.32)$$

based upon definition (Frobenius norm): $\|\cdot\|_{0,\omega}^2 = \sum_{i=1}^d \sum_{j=1}^d \|\cdot_{ij}\|_{0,\omega}^2$. Let $\mathbf{A} = [a_{ij}] = [\mathbf{a}_i]$ and $\mathbf{B} = [b_{ij}] = [\mathbf{b}_j]$, where \mathbf{a}_i is the i^{th} row vector of \mathbf{A} and \mathbf{b}_j is the j^{th} column vector of \mathbf{B} , we briefly validate (6.32) as follows. Omit the subscript for convenience,

$$\begin{aligned} \|\mathbf{AB}\|^2 &= \sum_{i=1}^d \sum_{j=1}^d \sum_{k=1}^d (a_{ik} b_{kj})^2 = \sum_{i=1}^d \sum_{j=1}^d (\mathbf{a}_i \cdot \mathbf{b}_j)^2 \leq \sum_{i=1}^d \sum_{j=1}^d |\mathbf{a}_i|^2 |\mathbf{b}_j|^2 \\ &= \sum_{i=1}^d |\mathbf{a}_i|^2 \sum_{j=1}^d |\mathbf{b}_j|^2 = \left(\sum_{i=1}^d \sum_{j=1}^d a_{ij}^2 \right) \left(\sum_{i=1}^d \sum_{j=1}^d b_i^2 \right) = \|\mathbf{A}\|^2 \|\mathbf{B}\|^2. \end{aligned} \quad (6.33)$$

□

From the definition of $a^s(\mathbf{u}, \mathbf{v})$ (6.8) and $\ell^s(\mathbf{v})$ (6.11), using the above two lemmas, we have the following two corollaries.

Corollary 6.2. $a^s(\mathbf{u}^h, \mathbf{v}^h)$ is bounded in \mathbb{V}^h , i.e., there exists a positive real number C_s^h , such that $\forall \mathbf{u}^h, \mathbf{v}^h \in \mathbb{V}^h$,

$$|a^s(\mathbf{u}^h, \mathbf{v}^h)| \leq C_s^h \|\mathbf{u}^h\|_{\mathbb{V}} \|\mathbf{v}^h\|_{\mathbb{V}}. \quad (6.34)$$

Corollary 6.3. $\ell^s(\mathbf{v}^h)$ is bounded in \mathbb{V}^h , i.e., there exists a positive real number C_ℓ^h , such that $\forall \mathbf{v}^h \in \mathbb{V}^h$,

$$|\ell^s(\mathbf{v}^h)| \leq C_\ell^h \|\mathbf{v}^h\|_{\mathbb{V}}. \quad (6.35)$$

Lemma 6.7. $a^h(\mathbf{u}^h, \mathbf{v}^h)$ is coercive, i.e., there exists a positive real number c_a^h , such that $\forall \mathbf{u}^h \in \mathbb{V}^h$,

$$a^h(\mathbf{u}^h, \mathbf{u}^h) \geq c_a^h \|\mathbf{u}^h\|_{\mathbb{V}}^2. \quad (6.36)$$

Proof. This proof follows the same procedure as the proof for Lemma 6.4 by changing $a(\mathbf{u}, \mathbf{u})$ to $a^h(\mathbf{u}^h, \mathbf{u}^h)$. □

Lemma 6.8. $a^h(\mathbf{u}^h, \mathbf{v}^h)$ is bounded, i.e., there exists a positive real number C_a^h , such that $\forall \mathbf{u}^h, \mathbf{v}^h \in \mathbb{V}^h$,

$$|a^h(\mathbf{u}^h, \mathbf{v}^h)| \leq C_a^h \|\mathbf{u}^h\|_{\mathbb{V}} \|\mathbf{v}^h\|_{\mathbb{V}}. \quad (6.37)$$

Proof. By the Cauchy-Schwarz inequality, $a^f(\mathbf{u}^h, \mathbf{v}^h)$ is a bounded bilinear form. Using the definition (6.22), $a^h(\mathbf{u}^h, \mathbf{v}^h)$ is bounded due to (6.34). □

Lemma 6.9. $\ell^h(\mathbf{v}^h)$ is bounded, i.e., there exists a positive real number C_ℓ^h , such that $\forall \mathbf{v}^h \in \mathbb{V}^h$,

$$|\ell^h(\mathbf{v}^h)| \leq C_\ell^h \|\mathbf{v}^h\|_{\mathbb{V}}. \quad (6.38)$$

Proof. By the Cauchy-Schwarz inequality, $\ell^f(\mathbf{v}^h)$ is a bounded linear form. According to the definition (6.23), $\ell^h(\mathbf{v}^h)$ is bounded due to (6.35). \square

We choose the P_2/P_1 or $P_2/(P_1 + P_0)$ element which satisfies the following discrete inf-sup condition [16][24, Section 12.6]:

Proposition 6.2 (Discrete Inf-Sup Condition). There exist $c_b^h > 0$ such that

$$\inf_{q^h \in \mathbb{P}^h} \sup_{\mathbf{v}^h \in \mathbb{V}^h} \frac{b(\mathbf{v}^h, q^h)}{\|\mathbf{v}^h\|_{\mathbb{V}} \|q^h\|_{\mathbb{P}}} \geq c_b^h. \quad (6.39)$$

Using the above three lemmas (6.7 - 6.9) and the discrete inf-sup condition, we further have the following optimal error estimate result [24, Corollary 12.5.18].

Theorem 2. Let (\mathbf{u}, p) and (\mathbf{u}^h, p^h) be the solution pairs of Problem 6.1 and Problem 6.2 respectively, then there is a constant c depending on C_a^h , c_a^h and c_b^h such that

$$\|\mathbf{u} - \mathbf{u}^h\|_{\mathbb{V}} + \|p - p^h\|_{\mathbb{P}} \leq c \left(\inf_{\mathbf{v} \in \mathbb{V}^h} \|\mathbf{u} - \mathbf{v}\|_{\mathbb{V}} + \inf_{q \in \mathbb{P}^h} \|p - q\|_{\mathbb{P}} \right). \quad (6.40)$$

6.2 Application to a non-Newtonian fluid

In all of the examples studied up to this point we have considered only incompressible Newtonian fluids. Such a restriction is not necessary however, as we demonstrate in this section. We shall consider the Giesekus model for a viscoelastic fluid [35, 75], in which an additional viscoelastic stress \mathbf{s} is added to the Newtonian fluid model (2.8), i.e.:

$$\boldsymbol{\sigma} = \nu^f \mathbf{D}\mathbf{u} - p\mathbf{I} + \mathbf{s}, \quad (6.41)$$

where \mathbf{s} is given by:

$$\lambda \frac{\partial \mathbf{s}}{\partial t} + \lambda \mathbf{u} \cdot \nabla \mathbf{s} = \lambda [(\nabla^T \mathbf{u}) \mathbf{s} + \mathbf{s} (\nabla \mathbf{u})] + \nu^p (\nabla \mathbf{u} + \nabla^T \mathbf{u}) - \left(\mathbf{s} + \frac{\alpha^p \lambda}{\nu^p} \mathbf{s}^2 \right), \quad (6.42)$$

with λ being the relaxation time, ν^p being the polymer viscosity and α^p being the mobility parameter. Notice that the Giesekus model is reduced to the Oldroyd-B model when $\alpha^p = 0$ [75].

We shall use a splitting scheme to solve equation (6.42) for stress \mathbf{s} [65], which is similar to the 2-step splitting scheme introduced in Section 5.1. After computing the fluid velocity \mathbf{u}_{n+1} at time t_{n+1} , then \mathbf{s}_{n+1} is computed from \mathbf{u}_{n+1} and \mathbf{s}_n using the following two-step scheme.

– Step 1:

$$\frac{\mathbf{s}_{n+1/2} - \mathbf{s}_n}{\Delta t} + \mathbf{u}_{n+1} \cdot \nabla \mathbf{s}_{n+1/2} = 0, \quad (6.43)$$

– Step 2:

$$\begin{aligned} \lambda \frac{\mathbf{s}_{n+1} - \mathbf{s}_{n+1/2}}{\Delta t} &= \lambda \left[(\nabla^T \mathbf{u}_{n+1}) \mathbf{s}_{n+1} + \mathbf{s}_{n+1} (\nabla \mathbf{u}_{n+1}) \right] \\ &+ \nu^p (\nabla \mathbf{u}_{n+1} + \nabla^T \mathbf{u}_{n+1}) - \left(\mathbf{s}_{n+1} + \frac{\alpha^p \lambda}{\nu^p} \mathbf{s}_{n+1}^2 \right). \end{aligned} \quad (6.44)$$

In the second step we linearize \mathbf{s}_{n+1}^2 as $2\mathbf{s}_{n+1/2}\mathbf{s}_{n+1} - \mathbf{s}_{n+1/2}^2$, and use the Least-squares method to solve both steps (see Section 5.1.1 for an introduction of the Least-squares method).

6.2.1 Test13-2D (one particle): A single freely suspended particle in Oldroyd-B shear-flow

To illustrate this generalization we consider two examples. The first of these introduces a freely suspended particle in a square computational domain as shown in Figure 6.1 (which also illustrates the driving boundary conditions). The rigid particle is simulated using a large $\mu^s = 10^4$ in the neo-Hookean solid model, and the fluid is described by Stokes equation with $\nu^f = \nu^p = 0.5$, $\alpha^p = 0$ (Oldroyd-B) and different values of λ presented in Table 6.1. A background mesh and the corresponding particle mesh are shown in Figure 6.2. Two different particle sizes are tested in this example. The angular velocity as a function of time and Weissenberg number are plotted in Figure 6.3 and 6.4 respectively, which has good agreement with the results in [147].

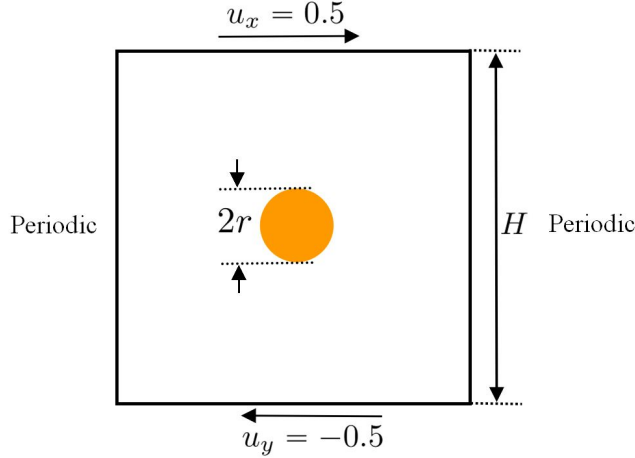


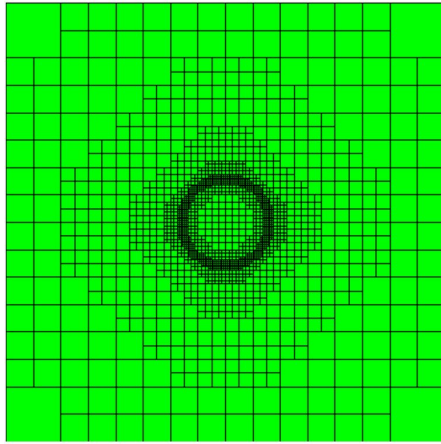
Figure 6.1: Computational domain for Test13-2D (one particle) in Section 6.2.1.

6.2.2 Test14-2D (two particles): Particle-particle interaction

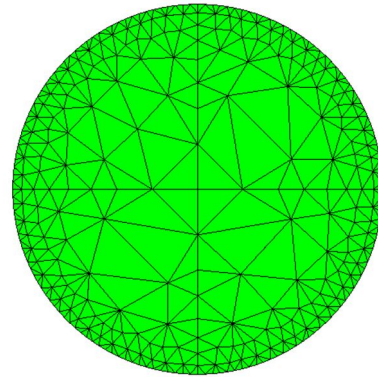
In this second test we consider two particles interacting with each other [147, 148]. The computational domain, boundary conditions and initial location of the particles are depicted in

λ	Steady state velocity for $r = 0.1$	Steady state velocity for $r = 0.05$
0.1	0.490	0.497
0.2	0.487	0.493
0.3	0.481	0.487
0.4	0.474	0.480
0.5	0.467	0.471
0.6	0.458	0.462
0.7	0.449	0.452
0.8	0.439	0.442

Table 6.1: Fluid properties and results of two different radii of the particle for Test13-2D (one particle) in Section 6.2.1. The Weissenberg number $Wi = \frac{\lambda \langle u \rangle}{H} = \frac{\lambda \cdot 1}{1} = \lambda$.



(a) Background mesh (9465 nodes, minimum mesh size: 0.004).



(b) Solid mesh (355 nodes, minimum mesh size: 0.004).

Figure 6.2: Meshes used for the simulation of Test13-2D (one particle) in Section 6.2.1.

Figure 6.5. Three different values for the initial distance of separation s are tested in order to demonstrate three different behaviours of the particles. The specific parameters are displayed in Table 6.2.

Fluid	Particle
$H = 1.0$	$r = 0.05$
$L = 4.0$	$\mu^s = 10^4$
$s = 0.07, 0.075$ or 0.08	$\lambda = 0.8$
$\nu^f = 0.5$	$\nu^p = 0.5$

Table 6.2: Fluid and particle properties and domain size for Test14-2D (two particles) in Section 6.2.2.

Two particles are initially located at the left and right side in the domain as shown in Figure 6.5. Snapshots of adaptive meshes with distribution of pressure are shown in Figure 6.6, and

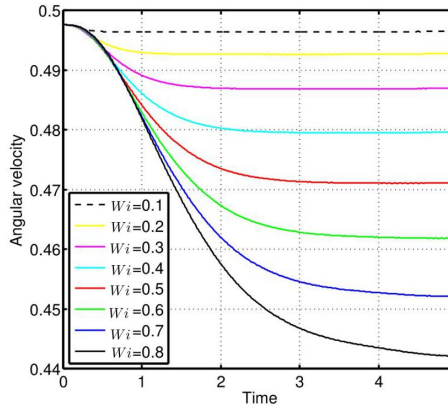


Figure 6.3: Angular velocity as a function of time for different Weissenberg numbers ($r = 0.05$). Test13-2D (one particle) in Section 6.2.1.

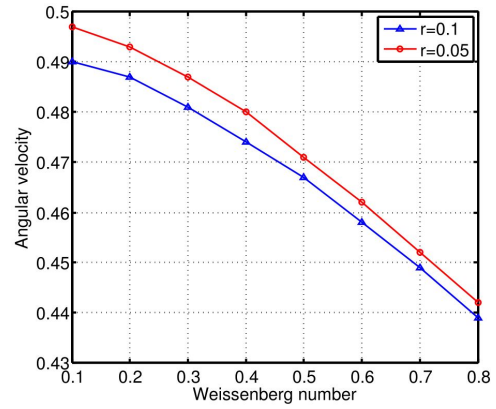


Figure 6.4: Angular velocity of a steady state as a function of Weissenberg number for two different particle sizes. Test13-2D (one particle) in Section 6.2.1.

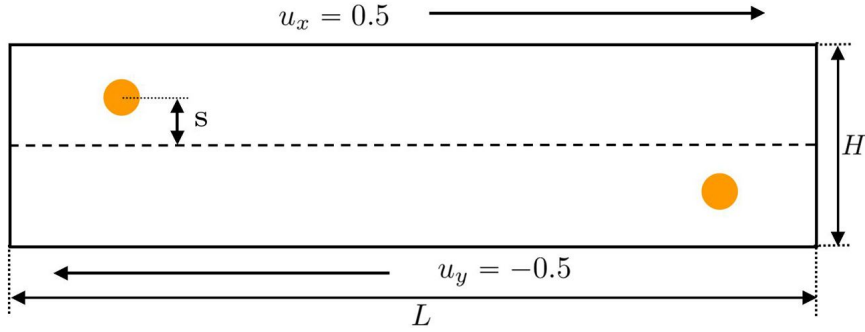


Figure 6.5: Computational domain for Test14-2D (two particles) in Section 6.2.2.

the meshes used by the two particles may be observed in Figure 6.7. With the three different values of initial separation of the two particles, three different behaviours are indeed observed. Trajectories of the two particles at their middle points are plotted in Figure 6.8. We successfully capture the “tumbling” behaviour which only occurs for non-Newtonian fluids.

6.3 Problems with contact

In this section we discuss how contact between solids may be treated within the framework of the one-field FDM. Before discussing a general contact model in Section 6.3.2, we first discuss the current situation in which there is no explicit contact algorithm.

6.3.1 Simulation without an explicit contact algorithm

It is possible to simulate many FSI problems without the explicit use of a contact algorithm [54]. Indeed, previous examples already considered in this thesis involve solid-solid interactions

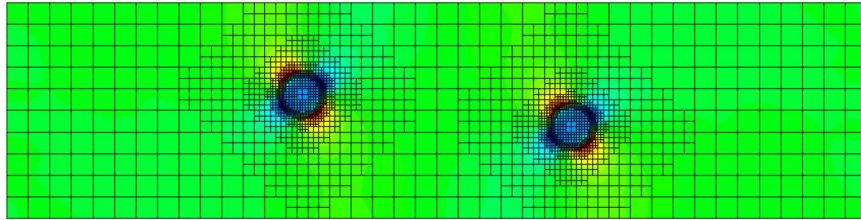
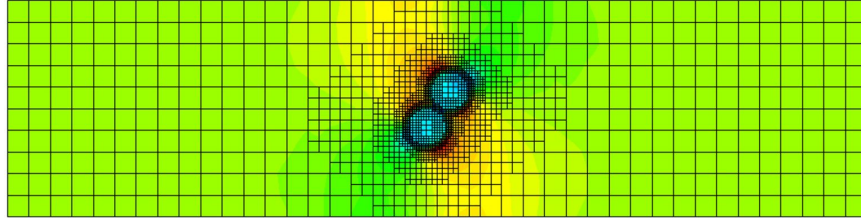
(a) Snapshots at $t = 5$.(b) Snapshots at $t = 48$.

Figure 6.6: Distribution of pressure on the adaptive background mesh in the case of $s = 0.075$ for Test14-2D (two particles) in Section 6.2.2.

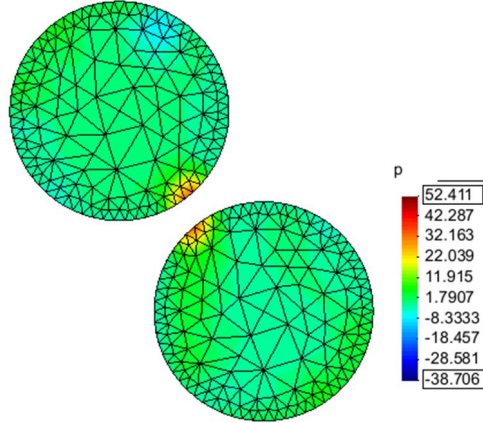


Figure 6.7: Distribution of pressure on the solid mesh in the case of $s = 0.075$ for Test14-2D (two particles) in Section 6.2.2.

even though no contact model has been incorporated. These include the second of the non-Newtonian problems in Section 6.2, as well as Test7-2D (cavity flow with a solid disc) and Test10-2D (multiple solids in a channel with gravity). Hence we take a close look at the performance of our algorithm in another example involving multiple solids. In this case we use a variant of the lid-driven cavity problem.

The background domain is the same as that in Section 4.5.4 (Figure 4.31) with the same boundary conditions, however there are six discs located in the cavity as shown in Figure 6.9. The fluid has a density of $\rho^f = 1$ and viscosity of $\nu^f = 0.01$. All the solids have the same density as the fluid, but have different μ^s as follows. Green discs (located at $(0.3, 0.5)$, $(0.7, 0.6)$)

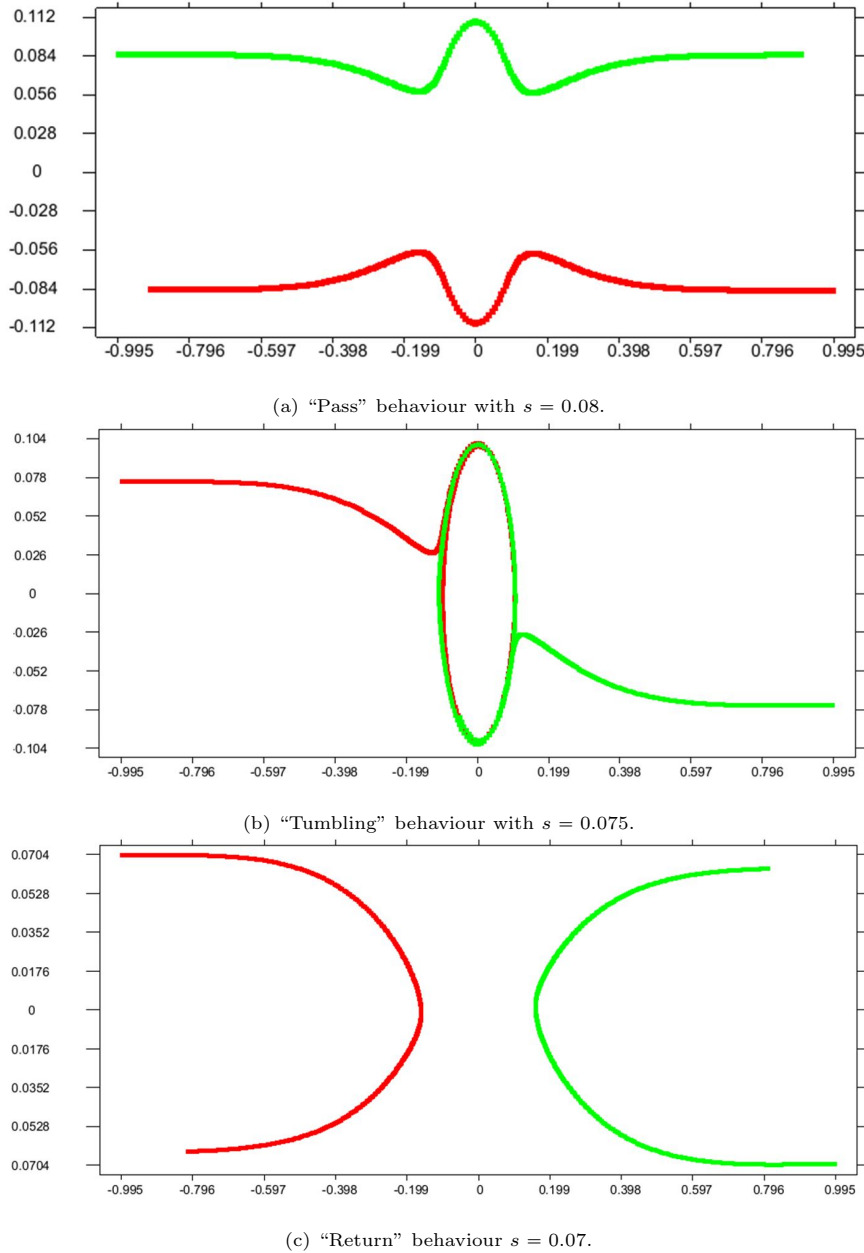


Figure 6.8: Trajectories of the two particles for the Test14-2D (two particles) in Section 6.2.2, using a radius 0.05 and a Weissenberg number of 0.8. Three different behaviours corresponding to three different initial separations.

and $(0.8, 0.2)$) have $\mu^s = 1$; the blue disc (located at $(0.5, 0.45)$) has $\mu^s = 5$; and the pink discs (located at $(0.4, 0.3)$ and $(0.7, 0.35)$) have $\mu^s = 10$. We use a time step of $\Delta t = 1.0 \times 10^{-3}$. The background mesh is same as that in Figure 4.32, and the solid meshes may be seen from Figure 6.10. We observe from Figure 6.10 (a) and (b) that a large pressure is built up when

two solid discs approach one another. This pressure has the effect of stopping the two discs colliding with each other, however the cost of this approach is that very small time steps are generally necessary.

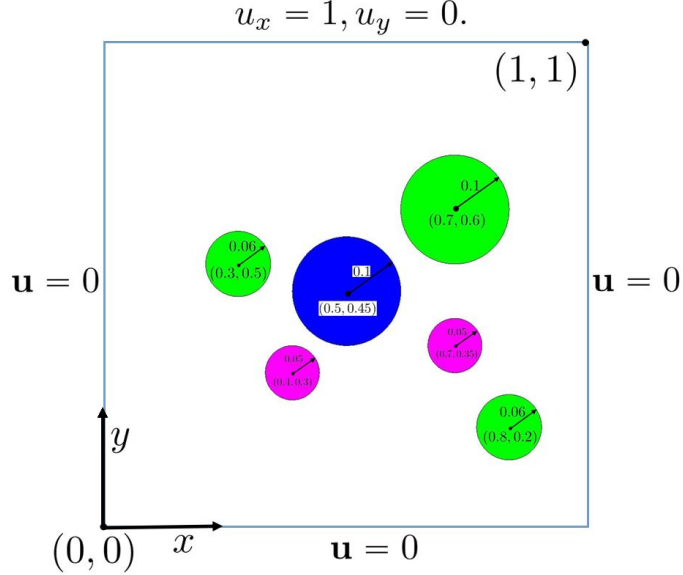


Figure 6.9: Multiple discs in a cavity flow ($[0,1] \times [0,1]$).

6.3.2 A general contact model

A potentially more robust approach to managing solid-solid interactions within our solver would be to incorporate an explicit contact model. When a solid contacts with a rigid surface (such as Γ_D) or contacts with another solid, the boundary Γ_t in Figure 2.1 may be decomposed into two parts: $\Gamma_t = \Gamma_{tc} \cup \Gamma_{t0}$, where Γ_{tc} denotes the contacted boundary and Γ_{t0} denotes the free/non-contacted boundary. Then the corresponding weak form (3.2) becomes:

$$\begin{aligned} & \int_{\Omega_t^f} \rho^f \frac{d\mathbf{u}}{dt} \cdot \mathbf{v} d\mathbf{x} + \frac{1}{2} \int_{\Omega_t^f} \boldsymbol{\sigma}^f : \mathbf{D}\mathbf{v} d\mathbf{x} + \int_{\Gamma_{t0}} \boldsymbol{\sigma}^f \mathbf{n}^s \cdot \mathbf{v} d\mathbf{x} \\ & + \int_{\Omega_t^s} \rho^s \frac{d\mathbf{u}}{dt} \cdot \mathbf{v} d\mathbf{x} + \frac{1}{2} \int_{\Omega_t^s} \boldsymbol{\sigma}^s : \mathbf{D}\mathbf{v} d\mathbf{x} - \int_{\Gamma_{t0}} \boldsymbol{\sigma}^s \mathbf{n}^s \cdot \mathbf{v} d\mathbf{x} - \int_{\Gamma_{tc}} \boldsymbol{\sigma}^s \mathbf{n}^s \cdot \mathbf{v} d\mathbf{x} \quad (6.45) \\ & = \int_{\Omega_t^f} \rho^f \mathbf{g} \cdot \mathbf{v} d\mathbf{x} + \int_{\Omega_t^s} \rho^s \mathbf{g} \cdot \mathbf{v} d\mathbf{x} + \int_{\Gamma_N} \bar{\mathbf{h}} \cdot \mathbf{v} d\Gamma. \end{aligned}$$

Remark 6.2. If Γ_t contacts with Γ_D , it makes no difference to the boundary condition on Γ_D . If Γ_t contacts with Γ_N , then $\boldsymbol{\sigma}^s \mathbf{n}^s = \bar{\mathbf{h}}$, and $\int_{\Gamma_N} \bar{\mathbf{h}} \cdot \mathbf{v} d\Gamma$ changes to $\int_{\Gamma_N - \Gamma_{tc}} \bar{\mathbf{h}} \cdot \mathbf{v} d\Gamma$, which is also equivalent to deleting the term $\int_{\Gamma_{tc}} \boldsymbol{\sigma}^s \mathbf{n}^s \cdot \mathbf{v} d\mathbf{x}$ in the above equation (6.45).

Generally $\int_{\Gamma_{tc}} \boldsymbol{\sigma}^s \mathbf{n}^s \cdot \mathbf{v} d\mathbf{x}$ cannot be known in advance, hence we replace $\boldsymbol{\sigma}^s \mathbf{n}^s$ by a Lagrange

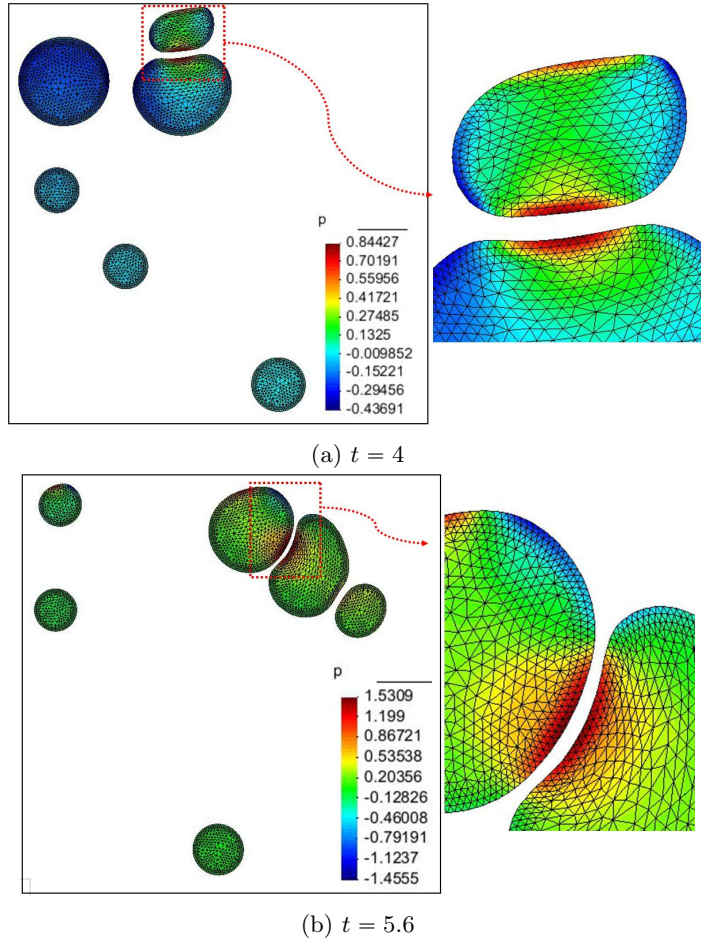


Figure 6.10: Distribution of pressure and velocity norm on the deformed solid for multiple discs in a cavity flow.

multiplier λ as an unknown, which may be determined by the contact condition. A specific contact condition depends on what kind of contact model is used. We shall not go into details of contact models here (see [132, 143, 154]). Instead, we simply assume a distance function $c(\mathbf{u})$ exists between the solid and the rigid surface (or two solids), and contact happens when $c(\mathbf{u}) \leq 0$. Consequently the contact problem may be expressed as follows (corresponding to Problem 3.1 with no contact) [22, 67].

Problem 6.3. Given \mathbf{u}_0 and Ω_0^s , for $t \in (0, T]$, find $\mathbf{u}(t) \in \{\mathbf{u}_D + H_0^1(\Omega)^d\}$, $p(t) \in L_0^2(\Omega)$, $\lambda \in H^{1/2}(\Gamma_{tc})^d$, Ω_t^s and Γ_{tc} , such that $\forall \delta \mathbf{u} \in H_0^1(\Omega)^d$, $\forall \delta p \in L^2(\Omega)$, $\forall \delta \lambda \in (H^{1/2}(\Gamma_{tc})^d)'$, the

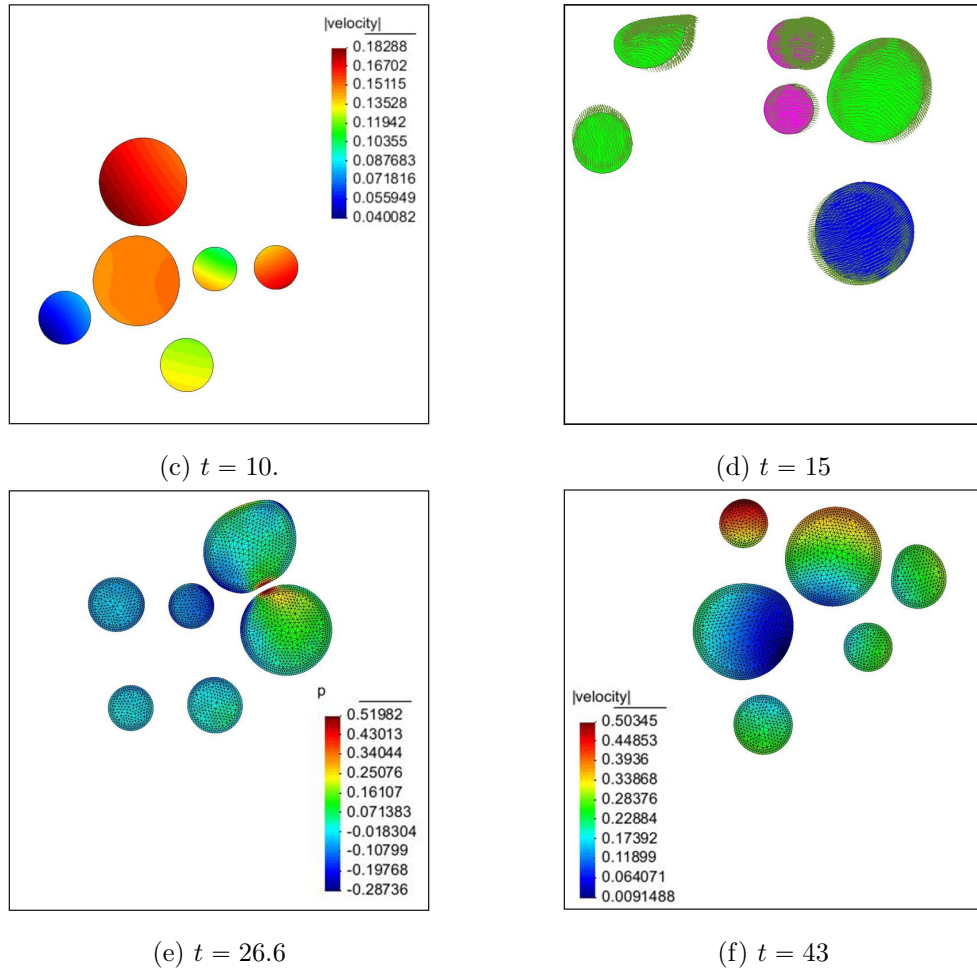


Figure 6.10 (continued).

following three equations hold:

$$\begin{aligned}
 & \int_{\Omega} \rho^f \frac{\partial \mathbf{u}}{\partial t} \cdot \delta \mathbf{u} d\mathbf{x} + \int_{\Omega} \rho^f (\mathbf{u} \cdot \nabla) \mathbf{u} \cdot \delta \mathbf{u} d\mathbf{x} + \frac{1}{2} \int_{\Omega} \nu^f D\mathbf{u} : D\delta \mathbf{u} d\mathbf{x} - \int_{\Omega} p \nabla \cdot \delta \mathbf{u} d\mathbf{x} \\
 & + \int_{\Omega_t^s} \rho^{\delta} \frac{\partial \mathbf{u}}{\partial t} \cdot \delta \mathbf{u} d\mathbf{X} + \frac{1}{2} \int_{\Omega_t^s} \nu^{\delta} D\mathbf{u} : D\delta \mathbf{u} d\mathbf{X} + \int_{\Omega_t^s} \mu^s \mathbf{F} : \nabla_{\mathbf{X}} \delta \mathbf{u} d\mathbf{X} - \int_{\Gamma_{tc}} \boldsymbol{\lambda} \cdot \delta \mathbf{u} d\Gamma \\
 & = \int_{\Omega_t^s} \mu^s J^{-1} \nabla \cdot \delta \mathbf{u} d\mathbf{x} + \int_{\Omega} \rho^f \mathbf{g} \cdot \delta \mathbf{u} d\mathbf{x} + \int_{\Omega_t^s} \rho^{\delta} \mathbf{g} \cdot \delta \mathbf{u} d\mathbf{X} + \int_{\Gamma_N} \bar{\mathbf{h}} \cdot \delta \mathbf{u} d\Gamma,
 \end{aligned} \tag{6.46}$$

with $\boldsymbol{\lambda} \geq 0$.

$$-\int_{\Omega} \delta p \nabla \cdot \mathbf{u} d\mathbf{x} = 0, \tag{6.47}$$

and

$$-\int_{\Gamma_{tc}} \delta \boldsymbol{\lambda} \cdot \mathbf{c}(\mathbf{u}) = 0. \quad (6.48)$$

In the above, $\{\mathbf{u}_D + H_0^1(\Omega)^d\}$ is the subspace of $H^1(\Omega)^d$ which satisfies the Dirichlet boundary condition (2.12).

We could use a splitting scheme to solve the above Problem 6.3. For example, as with the previous 3-step splitting scheme we obtain the following.

(1) Convection step:

$$\int_{\Omega} \frac{\mathbf{u}_{n+1/3} - \mathbf{u}_n}{\Delta t} \cdot \delta \mathbf{u} d\mathbf{x} + \int_{\Omega} (\mathbf{u}_{n+1/3} \cdot \nabla) \mathbf{u}_{n+1/3} \cdot \delta \mathbf{u} d\mathbf{x} = 0. \quad (6.49)$$

(2.1) “Degenerate” Stokes step:

$$\rho^f \int_{\Omega} \frac{\mathbf{u}_{n+2/3} - \mathbf{u}_{n+1/3}}{\Delta t} \cdot \delta \mathbf{u} d\mathbf{x} - \frac{1}{2} \int_{\Omega} p_{n+2/3} \nabla \cdot \delta \mathbf{u} d\mathbf{x} = 0, \quad (6.50)$$

and

$$-\int_{\Omega} \delta p \nabla \cdot \mathbf{u}_{n+2/3} d\mathbf{x} = 0. \quad (6.51)$$

(2.2) Lagrange multiplier step:

$$\rho^\delta \int_{\Omega_{\mathbf{X}}^s} \frac{\mathbf{u}_{n+2/3}^* - \mathbf{u}_{n+2/3}}{\Delta t} \cdot \delta \mathbf{u} d\mathbf{x} - \int_{\Gamma_{tc}} \boldsymbol{\lambda}_{n+1} \cdot \delta \mathbf{u} d\mathbf{x} = 0, \quad \boldsymbol{\lambda}_{n+1} \geq 0, \quad (6.52)$$

and

$$-\int_{\Gamma_{tc}} \delta \boldsymbol{\lambda} \cdot \mathbf{c}(\mathbf{u}_{n+2/3}^*) = 0. \quad (6.53)$$

(3) Diffusion step:

$$\begin{aligned} & \rho^f \int_{\Omega} \frac{\mathbf{u}_{n+1} - \mathbf{u}_{n+2/3}}{\Delta t} \cdot \delta \mathbf{u} d\mathbf{x} + \frac{\nu^f}{2} \int_{\Omega} \mathbf{D} \mathbf{u}_{n+1} : \mathbf{D} \delta \mathbf{u} d\mathbf{x} \\ & + \rho^\delta \int_{\Omega_{\mathbf{X}}^s} \frac{\mathbf{u}_{n+1} - \mathbf{u}_{n+2/3}^*}{\Delta t} \cdot \delta \mathbf{u} d\mathbf{x} + \mu^s \Delta t \int_{\Omega_{\mathbf{X}}^s} \nabla_{\mathbf{X}} \mathbf{u}_{n+1} : \nabla_{\mathbf{X}} \delta \mathbf{u} d\mathbf{X} \\ & = \mu^s \int_{\Omega_n^s} J_n^{-1} \nabla \cdot \delta \mathbf{u} d\mathbf{x} - \mu^s \int_{\Omega_{\mathbf{X}}^s} \mathbf{F}_n : \nabla_{\mathbf{X}} \delta \mathbf{u} d\mathbf{X} + \rho^f \int_{\Omega} \mathbf{g} \cdot \delta \mathbf{u} d\mathbf{x} \\ & + \rho^\delta \int_{\Omega_n^s} \mathbf{g} \cdot \delta \mathbf{u} d\mathbf{x} + \int_{\Gamma_N} \bar{\mathbf{h}} \cdot \delta \mathbf{u} d\Gamma + \frac{1}{2} \int_{\Omega} p_{n+2/3} \nabla \cdot \delta \mathbf{u} d\mathbf{x}. \end{aligned} \quad (6.54)$$

Although the above step (2.2) leads to a saddle point equation with constraint, the problem size is relatively small. We leave the implementation of the above scheme (in particular step (2.2)) for future work.

Remark 6.3. Notice that $\mathbf{u}_{n+2/3}^*$ is only defined in the solid domain, which is different from

$\mathbf{u}_{n+2/3}^s = P(\mathbf{u}_{n+2/3})$. The former has the information of the Lagrange multiplier/contact force, while the latter does not.

6.4 The case of a truss structure

Truss structures are composed of rod elements, which can only carry axial tension and compression. An example is shown in Figure 6.11, in which there are 11 rods and 7 connections/nodes. A rod element may be described locally by a 1D equation. Let ξ be the coordinate along the rod, then the equilibrium equation of the rod may be described as:

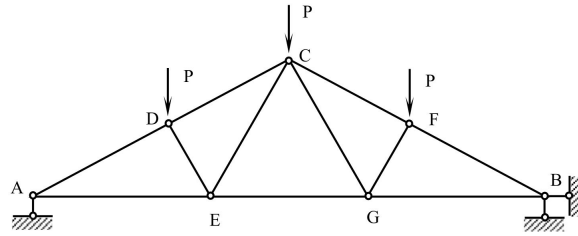


Figure 6.11: An example of truss structure.

$$\rho^s \frac{\partial u_\xi}{\partial t} = A \frac{\partial \sigma_\xi}{\partial \xi} + \rho^s g(\xi), \quad (6.55)$$

where A is the area of the cross section, ρ^s is the density, u_ξ and σ_ξ are the velocity and stress along the rod respectively, and $g(\xi)$ is a distributed force per unit mass along the rod. The weak form of (6.55), with a test function v , may be expressed as:

$$\rho^s \int_0^{l_i} \frac{\partial u_\xi}{\partial t} v d\xi + A \int_0^{l_i} \sigma_\xi \frac{\partial v}{\partial \xi} d\xi = \rho^s \int_0^{l_i} g(\xi) v d\xi + A (\sigma_\xi v)_0^{l_i}, \quad (6.56)$$

where l_i is the length of the i^{th} rod in the truss structure. Considering all the rods of the truss structure and using a linear elastic model

$$\sigma_\xi = E \frac{\partial d_\xi}{\partial \xi} \quad (6.57)$$

(d_ξ being the displacement), the weak form of the truss problem may be expressed as:

$$\rho^s \sum_{i=1}^{N_e} \int_0^{l_i} \frac{\partial u_\xi}{\partial t} v d\xi + AE \sum_{i=1}^{N_e} \int_0^{l_i} \frac{\partial d_\xi}{\partial \xi} \frac{\partial v}{\partial \xi} d\xi = \rho^s \sum_{i=1}^{N_e} \int_0^{l_i} g(\xi) v d\xi + \sum_{i=1}^{N_c} P_i v_i. \quad (6.58)$$

In the above, E is the elastic modulus, P_i is the concentrated force on the connections, N_e and N_c are the number of rod elements and connections in the truss structure respectively. Finally, the one-field formulation for a fluid-truss interaction system may be expressed as the following

problem.

Problem 6.4. Given \mathbf{u}_0 and Ω_0^s , find $\mathbf{u}(t) \in \{\mathbf{u}_D + H_0^1(\Omega)^d\}$, $p(t) \in L_0^2(\Omega)$ and Ω_t^s , such that $\forall \mathbf{v} \in H_0^1(\Omega)^d$, $\forall q \in L^2(\Omega)$, the following two equations hold:

$$\begin{aligned} & \int_{\Omega} \rho^f \frac{\partial \mathbf{u}}{\partial t} \cdot \mathbf{v} d\mathbf{x} + \int_{\Omega} \rho^f (\mathbf{u} \cdot \nabla) \mathbf{u} \cdot \mathbf{v} d\mathbf{x} + \frac{1}{2} \int_{\Omega} \nu^f \mathbf{D}\mathbf{u} : \mathbf{D}\mathbf{v} d\mathbf{x} - \int_{\Omega} p \nabla \cdot \mathbf{v} d\mathbf{x} \\ & \rho^{\delta} \sum_{i=1}^{N_e} \int_0^{l_i} \frac{\partial u_{\xi}}{\partial t} v d\xi + AE \sum_{i=1}^{N_e} \int_0^{l_i} \frac{\partial d_{\xi}}{\partial \xi} \frac{\partial v}{\partial \xi} d\xi \\ & = \int_{\Omega} \rho^f \mathbf{g} \cdot \mathbf{v} d\mathbf{x} + \int_{\Gamma_N} \bar{\mathbf{h}} \cdot \mathbf{v} d\Gamma + \rho^{\delta} \sum_{i=1}^{N_e} \int_0^{l_i} g(\xi) v d\xi + \sum_{i=1}^{N_c} P_i v_i, \end{aligned} \quad (6.59)$$

and

$$-\int_{\Omega} q \nabla \cdot \mathbf{u} d\mathbf{x} = 0. \quad (6.60)$$

In the above, \mathbf{u}_D is a suitable extension of the prescribed Dirichlet data $\bar{\mathbf{u}}$ on the boundary Γ_D , and $\{\mathbf{u}_D + H_0^1(\Omega)^d\}$ is the subspace of $H^1(\Omega)^d$ which satisfies the Dirichlet boundary condition (2.12).

Remark 6.4. After time discretization, the displacement d_{ξ} could be expressed in terms of velocity as with previous Section 3.2, although it is not necessary to go into details here again.

Remark 6.5. In order to implement the formulation (6.59) by the finite element method, we have to do a coordinate transformation. Taking the computation of term $AE \sum_{i=1}^{N_e} \int_0^{l_i} \frac{\partial d_{\xi}}{\partial \xi} \frac{\partial v}{\partial \xi} d\xi$ as an example: after expressing d_{ξ} in terms of u_{ξ} , we actually need to compute the integral $\int_0^{l_i} \frac{\partial u_{\xi}}{\partial \xi} \frac{\partial v}{\partial \xi} d\xi$, which gives the following term.

$$\begin{bmatrix} \int_0^{l_i} \frac{\partial \phi^1(\xi)}{\partial \xi} \frac{\partial \phi^1(\xi)}{\partial \xi} d\xi & \int_0^{l_i} \frac{\partial \phi^2(\xi)}{\partial \xi} \frac{\partial \phi^1(\xi)}{\partial \xi} d\xi \\ \int_0^{l_i} \frac{\partial \phi^1(\xi)}{\partial \xi} \frac{\partial \phi^2(\xi)}{\partial \xi} d\xi & \int_0^{l_i} \frac{\partial \phi^2(\xi)}{\partial \xi} \frac{\partial \phi^2(\xi)}{\partial \xi} d\xi \end{bmatrix} \begin{pmatrix} u_{\xi}^1 \\ u_{\xi}^2 \end{pmatrix},$$

where u_{ξ}^k and $\phi^k(\xi)$ are the velocity variable and its shape function defined on the k^{th} ($k = 1, 2$) node of element $[0, l_i]$ respectively. The above stiffness matrix is computed on a local coordinate ξ , which has to be transformed to the global coordinate system \mathbf{x} , so that it can be assembled to the final global matrix. See [94, 162] for more discussion about this coordinate transformation.

Remark 6.6. This approach may be extended to other structures such as a beam, which can also carry shear and bending forces. These forces are not only related to the node displacements of an element, but also related to the geometry of the element, such as the angle of rotation. Since we do not solve for the angles of rotation as variables, the shear and bending forces may be built into the right-hand side of equation (6.59) as a function of the angle of rotation. This may be a topic for future studies.

6.5 Extension to the case of a compressible solid

First, we argue that for the two-mesh methods it is not reasonable to use a compressible solid model if one solves $\nabla \cdot \mathbf{u} = 0$ in the whole domain Ω as shown in Figure 2.1, although there are papers which have done this [70, 156, 157]. The reason is as follows: no matter whether an interpolation [156, 157] or a Lagrange multiplier [70] is used, the ultimate purpose is to constrain the velocity on the solid mesh (say \mathbf{u}^s) to be the same as the velocity on the background mesh \mathbf{u} , i.e. $\mathbf{u} = \mathbf{u}^s$ in the fictitious domain (the domain on the background covered by the solid domain Ω_t^s). This is always a contradiction because $\nabla \cdot \mathbf{u} = 0$ while $\nabla \cdot \mathbf{u}^s \neq 0$ (compressible solid). Let us then consider whether it is possible to only solve $\nabla \cdot \mathbf{u} = 0$ in $\Omega - \Omega_t^s$.

We consider a compressible neo-Hookean solid model, as described by the constitutive equation (2.28). There two major differences compared with the incompressible case: (1) the incompressibility condition (2.7) only holds in the fluid domain $\Omega_t^f = \Omega - \Omega_t^s$; (2) there is no pressure defined in Ω_t^s , instead the last term in equation (2.28) ($J^{-1}\lambda^s \ln(J)$) will replace the pressure term. Based upon these two points and the weak formulation of the incompressible case (Problem 3.1), the weak formulation of the one-field FDM, using a compressible neo-Hookean solid, may be expressed as the following problem.

Problem 6.5. Given \mathbf{u}_0 and Ω_0^s , find $\mathbf{u}(t) \in \{\mathbf{u}_D + H_0^1(\Omega)^d\}$, $p(t) \in L_0^2(\Omega)$ and Ω_t^s , such that $\forall \mathbf{v} \in H_0^1(\Omega)^d$, $\forall q \in L^2(\Omega)$, the following two equations hold:

$$\begin{aligned} & \int_{\Omega} \rho^f \frac{\partial \mathbf{u}}{\partial t} \cdot \mathbf{v} d\mathbf{x} + \int_{\Omega} \rho^f (\mathbf{u} \cdot \nabla) \mathbf{u} \cdot \mathbf{v} d\mathbf{x} + \frac{1}{2} \int_{\Omega} \nu^f \mathbf{D}\mathbf{u} : \mathbf{D}\mathbf{v} d\mathbf{x} - \int_{\Omega} p \nabla \cdot \mathbf{v} d\mathbf{x} \\ & + \int_{\Omega_{\mathbf{X}}^s} \rho^s \frac{\partial \mathbf{u}}{\partial t} \cdot \mathbf{v} d\mathbf{X} + \frac{1}{2} \int_{\Omega_t^s} \nu^s \mathbf{D}\mathbf{u} : \mathbf{D}\mathbf{v} + \int_{\Omega_{\mathbf{X}}^s} \mu^s \mathbf{F} : \nabla_{\mathbf{X}} \mathbf{v} d\mathbf{X} \\ & = \int_{\Omega_t^s} \mu^s J^{-1} \nabla \cdot \mathbf{v} d\mathbf{x} \boxed{- \int_{\Omega_t^s} (p + J^{-1} \lambda^s \ln(J)) \nabla \cdot \mathbf{v} d\mathbf{x}} \\ & + \int_{\Omega} \rho^f \mathbf{g} \cdot \mathbf{v} d\mathbf{x} + \int_{\Omega_{\mathbf{X}}^s} \rho^s \mathbf{g} \cdot \mathbf{v} d\mathbf{X} + \int_{\Gamma_N} \bar{\mathbf{h}} \cdot \mathbf{v} d\Gamma, \end{aligned} \tag{6.61}$$

and

$$-\int_{\Omega} q \nabla \cdot \mathbf{u} d\mathbf{x} = \boxed{-\int_{\Omega_t^s} q \nabla \cdot \mathbf{u} d\mathbf{x}}. \tag{6.62}$$

In the above, \mathbf{u}_D is a suitable extension of the prescribed Dirichlet data $\bar{\mathbf{u}}$ on the boundary Γ_D , and $\{\mathbf{u}_D + H_0^1(\Omega)^d\}$ is the subspace of $H^1(\Omega)^d$ which satisfies the Dirichlet boundary condition (2.12).

Remark 6.7. There are two additional terms (boxed) in the above problem compared with Problem 3.1, both of which are zero in the incompressible case. The pressure in the solid domain Ω_t^s ($p|_{\Omega_t^s}$) may be interpreted as an extension of the fluid pressure from domain Ω_t^f . By comparing expression (2.28) and (2.29) we know pressure $p|_{\Omega_t^s}$ and the term $J^{-1}\lambda^s \ln(J)$ could

be canceled out with each other for the incompressible neo-Hookean solid, but however cannot in the compressible case.

The above formulation (6.61) and (6.62) looks plausible at first inspection, however the final linear system after discretization will be singular because the values of the matrix corresponding to the pressure variables in domain Ω_i^s will be zero. We therefore leave this for further investigation.

Chapter 7

Conclusions

Reviewing problems involving fluid-structure interactions (FSI), the crucial aspect is how to deal with the interface between the fluid and solid. There is little doubt that an interface-fitted mesh is always the best (at least in terms of accuracy), however creating an interface-fitted mesh is not cheap at all, especially in three dimensions. In addition, an interface-fitted mesh cannot guarantee a stable simulation automatically: design of the numerical scheme is highly significant. Therefore we used two meshes without interface fitting. Recently monolithic schemes have been regarded as the most robust approach in the area of fluid-structure interaction. Therefore, we adopted the monolithic idea and solve the fluid and solid equation in one system.

Let us recall our initial motivation (Section 1.3): we aim to design a general FEM scheme for FSI problems that can

- cheaply and accurately simulate large solid deformation,
- simulate FSI problems with a wide range of physical parameters.

The utilization of the two meshes is very convenient and efficient for large deformation, and the accuracy can be increased by local mesh refinement with hanging nodes (cheaper than full remeshing) near the interface, although the algorithm does not rely on this. The refinement can be carried out based on a general posteriori error estimate.

The proposed scheme is similar to the classical IFEM scheme, but we move all of the solid information to the left-hand side. What we achieve is that a range of FSI problems, from very soft solids to very hard solids, can be simulated in this scheme (whereas the classical IFEM methods are usually only effective for very soft solids). We have not adopted a name like “improved IFEM” or “modified IFEM”. One reason is that these terms have already been used in the literature for other methods. A further reason is that the formulation of the proposed scheme is very similar to the one used in the Fictitious Domain Methods (FDM).

In this thesis, the one-field FDM is introduced following a thorough review of the existing numerical approaches. Specific implementations of the proposed approach, including implicit

and explicit schemes, are presented with a systematic validation using multiple numerical examples. To close this thesis, we would like to summarize the achievements presented in previous chapters, and then point out some open problems that are worth investigating in the future.

7.1 Achievements of this thesis

In this section we briefly summarize the achievements that have been made in this thesis.

1. We thoroughly reviewed the finite element methods for FSI problems: introduced the details of formulations for these methods, discussed their advantages and disadvantages, and presented a complete categorization of the existing approaches.
2. We introduced a novel method for general FSI problems: presented the finite element weak formulation and discretization in time and space, analyzed the stability by energy estimate, and gave an initial proof of the well-posedness based upon some assumptions. This proposed method: extends the immersed finite element method (IFEM); can naturally handle the case of different densities (between fluid and solid) and permits a larger time step than the classical explicit IFEM (equivalent to an implicit IFEM but without requiring sub-iteration for convergence); simplifies the three (or four)-field fictitious domain method using distributed Lagrange multiplier (FDM/DLM); and only solve for one velocity field in the whole domain. In summary, the proposed one-field FDM combines the advantages of IFEM and FDM/DLM: efficiency of IFEM and robustness of FDM/DLM.
3. We implemented the proposed one-field FDM by a fully implicit scheme first, and then followed by three different types of explicit splitting schemes. We systematically tested these schemes, compared the three types of splitting schemes and discussed their pros and cons, by a selection of numerical examples including several benchmarks in the FSI literature.

7.2 Further work based on the proposed method

In this section we present some open problems that are worth studying in the future.

1. We do not know why the equal-order element for the 4-step splitting scheme does not preserve energy (or converge as $\Delta t \rightarrow 0$), while the mixed element does (see Section 5.6 and 5.9). In the future, we may start to investigate this problem by looking at the equal-order element for the implicit scheme with stabilization, then try to understand the equal-order element for the 4-step splitting scheme.
2. When implementing the one-field FDM based on the d -scheme and integrating in the current domain, the iterative solver struggles to converge. However, when implementing

the one-field FDM based on the F -scheme and integrating in the reference domain the same iterative solver works very well. We are not clear the reason behind this at the moment, but the matrix structure behind these two schemes is worth further study.

3. In Section 4.5, we found that the proposed scheme could be unstable when the solid viscosity is smaller than the fluid viscosity ($\nu^\delta < 0$). For an IFEM method in [157], the author ignored the fluid stress within the solid domain, which is equivalent to $\nu^\delta = 0$. For a FDM method in [18], the author only considered a constant viscosity through the whole domain Ω when analyzing the problem, although a general formulation was presented at the beginning. The same author in [17] directly assumes $\boldsymbol{\sigma} = \boldsymbol{\sigma}^s + \boldsymbol{\sigma}^f$ (equivalent to $\nu^s = \nu^f$ or $\nu^\delta = 0$) in Ω_t^s at the beginning of the paper. For a FDM method in [150], it was also found that the fluid stress integral in the solid domain was unimportant. An interesting question therefore is whether all two-mesh methods have a stability issue when $\nu^\delta < 0$ and $\Delta t \rightarrow 0$. We have not found the answer in the literature, and this is an interesting question about the general two-mesh FSI methodology for future study.
4. We mentioned, in Section 4.6 and Remark 5.5, that for the tests of a thin solid interacting with a fluid (Test8-2D: a leaflet and Test9-2D: a flag), the iterative linear solver (see Section 4.2) fails to converge when using the $P_2/(P_1 + P_0)$ element. It may be because too many unknowns P_0 have been added to the domain (we know the pressure is only discontinuous across the thin solid). However it is worth investigating the matrix structure to find the exact reason behind this.

Appendices

Appendix A

Implementation of the one-field FDM by updating solid stress

As discussed at the beginning of Chapter 5, the **F**-scheme (updating the deformation tensor \mathbf{F} as illustrated in formula (3.8) or (3.12)) does not converge (the mesh becomes distorted at some stage) for Test8-2D (leaflet). Alternatively we could also update the deviatoric part of the solid stress $\boldsymbol{\sigma}$ ($\boldsymbol{\sigma}$ -scheme) as discussed in this appendix, which converges for the above test. We have not thoroughly compared the **F**-scheme and $\boldsymbol{\sigma}$ -scheme in this thesis (this could form a future work), however from this test it can be seen that there is a numerical difference between these two schemes although mathematically they are the same. In order to obtain the $\boldsymbol{\sigma}$ -scheme, we first use (3.8) and replace term

$$\int_{\Omega_{\mathbf{X}}^s} \mu^s \mathbf{F}_n : \nabla_{\mathbf{X}} \mathbf{v} d\mathbf{X} + \Delta t \int_{\Omega_{\mathbf{X}}^s} \mu^s \nabla_{\mathbf{X}} \mathbf{u}_{n+1} : \nabla_{\mathbf{X}} \mathbf{v} d\mathbf{X} \quad (\text{A.1})$$

in equation (3.9) by

$$\int_{\Omega_{\mathbf{X}}^s} \mu^s \mathbf{F}_{n+1} : \nabla_{\mathbf{X}} \mathbf{v} d\mathbf{X} = \int_{\Omega_{n+1}^s} \mu^s J_{n+1}^{-1} \mathbf{F}_{n+1} \mathbf{F}_{n+1}^T : \nabla \mathbf{v} d\mathbf{x} = \int_{\Omega_{n+1}^s} J_{n+1}^{-1} \boldsymbol{\tau}_{n+1}^s : \nabla \mathbf{v} d\mathbf{x}. \quad (\text{A.2})$$

For an explicit scheme the above integral may be carried out in the known domain Ω_n^s , and the derivative may be taken with respect to the previous coordinate \mathbf{x}_n . That is to say integral (A.2) will be replaced by

$$\int_{\Omega_n^s} J_n^{-1} \boldsymbol{\tau}_{n+1}^s : \nabla_n \mathbf{v} d\mathbf{x}, \quad (\text{A.3})$$

where $\nabla_n(\cdot) = \frac{\partial(\cdot)}{\partial \mathbf{x}_n}$, and $\boldsymbol{\tau}_{n+1}^s$ may also be computed based on \mathbf{x}_n as follows:

$$\boldsymbol{\tau}_{n+1}^s = \mu^s (\nabla_{\mathbf{X}} \mathbf{x}_{n+1} \nabla_{\mathbf{X}}^T \mathbf{x}_{n+1} - \mathbf{I}). \quad (\text{A.4})$$

Using a chain rule, the last equation can also be expressed as:

$$\begin{aligned}\boldsymbol{\tau}_{n+1}^s &= \mu^s (\nabla_n \mathbf{x}_{n+1} \nabla_{\mathbf{x}} \mathbf{x}_n \nabla_{\mathbf{x}}^T \mathbf{x}_n \nabla_n^T \mathbf{x}_{n+1}) - \mu^s \mathbf{I} \\ &\quad + \mu^s (\nabla_n \mathbf{x}_{n+1} \nabla_n^T \mathbf{x}_{n+1}) - \mu^s (\nabla_n \mathbf{x}_{n+1} \nabla_n^T \mathbf{x}_{n+1})\end{aligned}\tag{A.5}$$

or

$$\begin{aligned}\boldsymbol{\tau}_{n+1}^s &= \mu^s (\nabla_n \mathbf{x}_{n+1} \nabla_n^T \mathbf{x}_{n+1} - \mathbf{I}) \\ &\quad + \mu^s \nabla_n \mathbf{x}_{n+1} (\nabla_{\mathbf{x}} \mathbf{x}_n \nabla_{\mathbf{x}}^T \mathbf{x}_n - \mathbf{I}) \nabla_n^T \mathbf{x}_{n+1},\end{aligned}\tag{A.6}$$

and then $\boldsymbol{\tau}_{n+1}^s$ can be expressed based upon the previous coordinate \mathbf{x}_n as follows:

$$\boldsymbol{\tau}_{n+1}^s = \mu^s (\nabla_n \mathbf{x}_{n+1} \nabla_n^T \mathbf{x}_{n+1} - \mathbf{I}) + \mu^s \nabla_n \mathbf{x}_{n+1} \boldsymbol{\tau}_n^s \nabla_n^T \mathbf{x}_{n+1}.\tag{A.7}$$

Using $\mathbf{x}_{n+1} - \mathbf{x}_n = \Delta t \mathbf{u}_{n+1}$ which is the displacement at the current step, the last equation can finally be expressed as:

$$\begin{aligned}\boldsymbol{\tau}_{n+1}^s &= \mu^s \Delta t (\nabla_n \mathbf{u}_{n+1} + \nabla_n^T \mathbf{u}_{n+1} + \Delta t \nabla_n \mathbf{u}_{n+1} \nabla_n^T \mathbf{u}_{n+1}) + \boldsymbol{\tau}_n^s \\ &\quad + \Delta t^2 \nabla_n \mathbf{u}_{n+1} \boldsymbol{\tau}_n^s \nabla_n^T \mathbf{u}_{n+1} + \Delta t \nabla_n \mathbf{u}_{n+1} \boldsymbol{\tau}_n^s + \Delta t \boldsymbol{\tau}_n^s \nabla_n^T \mathbf{u}_{n+1}.\end{aligned}\tag{A.8}$$

There are two nonlinear terms in the last equation, which may be linearized as follows:

$$\nabla_n \mathbf{u}_{n+1} \nabla_n^T \mathbf{u}_{n+1} = \nabla_n \mathbf{u}_{n+1} \nabla_n^T \mathbf{u}_n + \nabla_n \mathbf{u}_n \nabla_n^T \mathbf{u}_{n+1} - \nabla_n \mathbf{u}_n \nabla_n^T \mathbf{u}_n\tag{A.9}$$

and

$$\nabla_n \mathbf{u}_{n+1} \boldsymbol{\tau}_n^s \nabla_n^T \mathbf{u}_{n+1} = \nabla_n \mathbf{u}_{n+1} \boldsymbol{\tau}_n^s \nabla_n^T \mathbf{u}_n + \nabla_n \mathbf{u}_n \boldsymbol{\tau}_n^s \nabla_n^T \mathbf{u}_{n+1} - \nabla_n \mathbf{u}_n \boldsymbol{\tau}_n^s \nabla_n^T \mathbf{u}_n.\tag{A.10}$$

There should be no theoretical differences between updating the solid deformation \mathbf{F} and updating the solid deviatoric stress $\boldsymbol{\tau}^s$. However the former is an unsymmetric tensor and the latter is a symmetric tensor, and updating an unsymmetric tensor may be less accurate than updating a symmetric tensor [110]. This may be the reason why updating \mathbf{F} leads to a distorted solid mesh for Test8-2D (leaflet). A scheme updating the solid displacement is also introduced in [67, 110], and we discuss this scheme in the context of the proposed one-field FDM in Appendix F.

Appendix B

Assembling the global matrix and right-hand side vector

Using two space dimensions as an example in this appendix, we present the details of assembling the global mass matrix, stiffness matrix and the right-hand side vector in Section 4.2.

The matrix

$$\mathbf{M} = \rho^f \begin{bmatrix} \mathbf{M}_{11} & \\ & \mathbf{M}_{22} \end{bmatrix} \quad (\text{B.1})$$

is the velocity mass matrix of the fluid, where

$$[\mathbf{M}_{11}]_{km} = [\mathbf{M}_{22}]_{km} = \int_{\Omega^h} \varphi_k \varphi_m d\mathbf{x}, \quad (k, m = 1, 2, \dots, N^u + N_D^u). \quad (\text{B.2})$$

The matrix

$$\mathbf{M}^s = \rho^\delta \begin{bmatrix} \mathbf{M}_{11}^s & \\ & \mathbf{M}_{22}^s \end{bmatrix} \quad (\text{B.3})$$

is the velocity mass matrix of the solid, where

$$[\mathbf{M}_{11}^s]_{km} = [\mathbf{M}_{22}^s]_{km} = \int_{\Omega_X^{sh}} \varphi_k^s \varphi_m^s d\mathbf{X}, \quad (k, m = 1, 2, \dots, N^s). \quad (\text{B.4})$$

\mathbf{K} is the stiffness matrix of the fluid:

$$\mathbf{K} = \nu^f \begin{bmatrix} \mathbf{K}_{11} & \mathbf{K}_{12} \\ \mathbf{K}_{21} & \mathbf{K}_{22} \end{bmatrix}, \quad (\text{B.5})$$

where

$$[\mathbf{K}_{11}]_{km} = 2 \int_{\Omega^h} \left(\frac{\partial \varphi_k}{\partial x_1} \frac{\partial \varphi_m}{\partial x_1} \right) d\mathbf{x} + \int_{\Omega^h} \left(\frac{\partial \varphi_k}{\partial x_2} \frac{\partial \varphi_m}{\partial x_2} \right) d\mathbf{x}, \quad (\text{B.6})$$

$$[\mathbf{K}_{22}]_{km} = 2 \int_{\Omega^h} \left(\frac{\partial \varphi_k}{\partial x_2} \frac{\partial \varphi_m}{\partial x_2} \right) d\mathbf{x} + \int_{\Omega^h} \left(\frac{\partial \varphi_k}{\partial x_1} \frac{\partial \varphi_m}{\partial x_1} \right) d\mathbf{x}, \quad (\text{B.7})$$

$$[\mathbf{K}_{12}]_{km} = \int_{\Omega^h} \frac{\partial \varphi_k}{\partial x_1} \frac{\partial \varphi_m}{\partial x_2} d\mathbf{x}, \quad (\text{B.8})$$

$$[\mathbf{K}_{21}]_{km} = [\mathbf{K}_{12}]_{mk} = \int_{\Omega^h} \frac{\partial \varphi_k}{\partial x_2} \frac{\partial \varphi_m}{\partial x_1} d\mathbf{x}, \quad (\text{B.9})$$

and $k, m = 1, 2, \dots, N^u$.

\mathbf{K}^s is the stiffness matrix of the solid:

$$\mathbf{K}^s = \begin{bmatrix} \mathbf{K}_{11}^s & \mathbf{0} \\ \mathbf{0} & \mathbf{K}_{22}^s \end{bmatrix}, \quad (\text{B.10})$$

where

$$\begin{aligned} [\mathbf{K}_{11}^s]_{km} &= 2\nu^\delta \int_{\Omega^{sh}} \left(\frac{\partial \varphi_k^s}{\partial x_1} \frac{\partial \varphi_m^s}{\partial x_1} \right) d\mathbf{x} + \nu^\delta \int_{\Omega^{sh}} \left(\frac{\partial \varphi_k^s}{\partial x_2} \frac{\partial \varphi_m^s}{\partial x_2} \right) d\mathbf{x} \\ &+ \mu^s \Delta t \int_{\Omega_{\mathbf{X}}^{sh}} \left(\frac{\partial \varphi_k^s}{\partial x_1} \frac{\partial \varphi_m^s}{\partial x_1} + \frac{\partial \varphi_k^s}{\partial x_2} \frac{\partial \varphi_m^s}{\partial x_2} \right) d\mathbf{X}. \end{aligned}$$

It can be seen from the pattern of the above matrices that one can get \mathbf{K}_{22}^s by changing the subscript 1 to 2, and changing 2 to 1 in the formula of \mathbf{K}_{11}^s , and $k, m = 1, 2, \dots, N^s$.

The matrix \mathbf{B} has the following expression.

$$\mathbf{B} = - \begin{bmatrix} \mathbf{B}_1 \\ \mathbf{B}_2 \end{bmatrix}, \quad (\text{B.11})$$

where

$$[\mathbf{B}_1]_{mk} = \int_{\Omega^h} \phi_k \frac{\partial \varphi_m}{\partial x_1} d\mathbf{x}, \quad [\mathbf{B}_2]_{mk} = \int_{\Omega^h} \phi_k \frac{\partial \varphi_m}{\partial x_2} d\mathbf{x} \quad (\text{B.12})$$

($k = 1, 2, \dots, N^p$ and $m = 1, 2, \dots, N^u$). The vector

$$\mathbf{f} = \begin{pmatrix} \mathbf{f}_1 \\ \mathbf{f}_2 \end{pmatrix} \quad (\text{B.13})$$

is the fluid force vector, where

$$(\mathbf{f}_1)_m = \rho^f \int_{\Omega^h} \bar{g}_1 \varphi_m d\mathbf{x} + \int_{\Gamma^{N^h}} \bar{h}_1 \varphi_m d\Gamma \quad (\text{B.14})$$

and

$$(\mathbf{f}_2)_m = \rho^f \int_{\Omega^h} \bar{g}_2 \varphi_m d\mathbf{x} + \int_{\Gamma^{N^h}} \bar{h}_2 \varphi_m d\Gamma \quad (\text{B.15})$$

($m = 1, 2, \dots, N^u$), with

$$\bar{\mathbf{g}} = \mathbf{g} + \frac{\mathbf{u}_n^h}{\Delta t} - (\mathbf{u}_{n+1}^h \cdot \nabla) \mathbf{u}_{n+1}^h = \begin{pmatrix} \bar{g}_1 \\ \bar{g}_2 \end{pmatrix} \quad (\text{B.16})$$

in the above expression. The vector

$$\mathbf{f}^s = \begin{pmatrix} \mathbf{f}_1^s \\ \mathbf{f}_2^s \end{pmatrix} \quad (\text{B.17})$$

is the solid force vector, where

$$\begin{aligned} (\mathbf{f}_1^s)_m &= \rho^\delta \int_{\Omega_{\mathbf{X}}^{sh}} \tilde{g}_1 \varphi_m^s d\mathbf{X} + \mu^s \int_{\Omega_{n+1}^{sh}} J_{n+1}^{-1} \frac{\partial \varphi_m^s}{\partial x_1} \\ &\quad - \mu^s \int_{\Omega_{\mathbf{X}}^{sh}} [\mathbf{F}_n^{sh}]_{11} \frac{\partial \varphi_m^s}{\partial x_1} - \mu^s \int_{\Omega_{\mathbf{X}}^{sh}} [\mathbf{F}_n^{sh}]_{12} \frac{\partial \varphi_m^s}{\partial x_2} \end{aligned} \quad (\text{B.18})$$

and

$$\begin{aligned} (\mathbf{f}_2^s)_m &= \rho^\delta \int_{\Omega_{\mathbf{X}}^{sh}} \tilde{g}_2 \varphi_m^s d\mathbf{X} + \mu^s \int_{\Omega_{n+1}^{sh}} J_{n+1}^{-1} \frac{\partial \varphi_m^s}{\partial x_2} \\ &\quad - \mu^s \int_{\Omega_{\mathbf{X}}^{sh}} [\mathbf{F}_n^{sh}]_{21} \frac{\partial \varphi_m^s}{\partial x_1} - \mu^s \int_{\Omega_{\mathbf{X}}^{sh}} [\mathbf{F}_n^{sh}]_{22} \frac{\partial \varphi_m^s}{\partial x_2} \end{aligned} \quad (\text{B.19})$$

($m = 1, 2, \dots, N^s$), with

$$\tilde{\mathbf{g}} = \mathbf{g} + \frac{\mathbf{u}_n^{sh}}{\Delta t} = \begin{pmatrix} \tilde{g}_1 \\ \tilde{g}_2 \end{pmatrix} \quad (\text{B.20})$$

in the above expression.

Appendix C

A method of computing the interpolation matrix

In this appendix, we take the 2D linear quadrilateral element as an example to introduce the method of calculating the FEM interpolation matrix \mathbf{D} in (4.4) Section 4.2. The shape function of a linear quadrilateral element, as shown in Figure C.1 in the reference coordinate system (ξ, η) , may be expressed as follows.

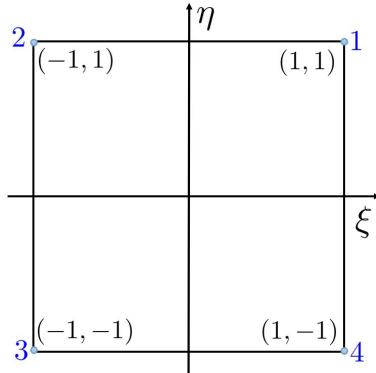


Figure C.1: Quadrilateral element in the reference coordinate system.

$$\phi_1(\xi, \eta) = \frac{1}{2} (1 - \xi)(1 - \eta), \quad (\text{C.1})$$

$$\phi_2(\xi, \eta) = \frac{1}{2} (1 + \xi)(1 - \eta), \quad (\text{C.2})$$

$$\phi_3(\xi, \eta) = \frac{1}{2} (1 + \xi)(1 + \eta), \quad (\text{C.3})$$

and

$$\phi_4(\xi, \eta) = \frac{1}{2}(1 - \xi)(1 + \eta). \quad (\text{C.4})$$

For a given point $P(x_0, y_0)$ in the original coordinate system (x, y) , one should first decide in which element the point is located. One method of checking whether $P(x_0, y_0)$ is located in an element $P_1(x_1, y_1)$, $P_2(x_2, y_2)$, $P_3(x_3, y_3)$ and $P_4(x_4, y_4)$ is successively checking the direction of the following four vectors:

$$\vec{a} = P_2P_1 \times P_2P, \quad \vec{b} = P_3P_2 \times P_3P, \quad \vec{c} = P_4P_3 \times P_4P \quad \text{and} \quad \vec{d} = P_1P_4 \times P_1P. \quad (\text{C.5})$$

If they point in the same direction, in other words, the following four scalars have the same sign.

$$s_1 = (x_1 - x_2)(y - y_2) - (x - x_2)(y_1 - y_2), \quad (\text{C.6})$$

$$s_2 = (x_2 - x_3)(y - y_3) - (x - x_3)(y_2 - y_3), \quad (\text{C.7})$$

$$s_3 = (x_3 - x_4)(y - y_4) - (x - x_4)(y_3 - y_4), \quad (\text{C.8})$$

$$s_4 = (x_4 - x_1)(y - y_1) - (x - x_1)(y_4 - y_1), \quad (\text{C.9})$$

then point P is in the element $P_1P_2P_3P_4$. According to the isoparametric transformation we have:

$$\begin{cases} x_0 = \sum_{i=1}^4 x_i \phi_i(\xi, \eta) \\ y_0 = \sum_{i=1}^4 y_i \phi_i(\xi, \eta) \end{cases}. \quad (\text{C.10})$$

Newton's method may be used to solve the above equations. Once ξ and η are computed, then the interpolation coefficients of point P are ϕ_1, ϕ_2, ϕ_3 and ϕ_4 , which may be used to form the interpolation matrix \mathbf{D} in (4.4).

Appendix D

An efficient approach for matrix multiplication

One needs to calculate $\mathbf{K} + \mathbf{D}^T \mathbf{K}^s \mathbf{D}$ in equation (4.2) in Section 4.2. An efficient way to do this is based on the element matrix, i.e., compute $\mathbf{D}_e^T \mathbf{K}_e^s \mathbf{D}_e$ and directly assemble to matrix \mathbf{K} , with \mathbf{K}_e^s being the local element matrix of \mathbf{K}^s and \mathbf{D}_e being the local interpolation matrix. For the sake of simplicity, suppose that the background mesh is formed of bilinear quadrilateral elements, and the solid mesh contains linear triangular elements (other types of elements follow the same principle), and let us also assume that there is only one variable defined at each node (for the case of more than one variable, the principle can still be applied). It should be mentioned that the three nodes of the triangular element may lie in different quadrilateral elements, such as is illustrated in Figure D.1.

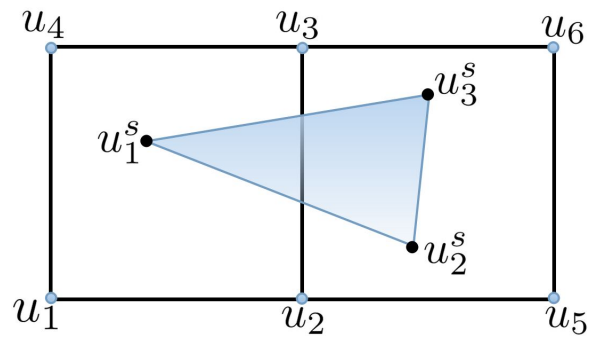


Figure D.1: An element of the solid mesh on the background meshes.

In the case as shown in Figure D.1,

$$\begin{pmatrix} u_1^s \\ u_2^s \\ u_3^s \end{pmatrix} = \mathbf{D}_e \begin{pmatrix} u_1 \\ u_2 \\ u_3 \\ u_4 \\ u_5 \\ u_6 \end{pmatrix}, \quad (\text{D.1})$$

where

$$\mathbf{D}_e = \begin{bmatrix} \phi_1 \\ \phi_2 \\ \phi_3 \end{bmatrix}, \quad \begin{cases} \phi_1 = (\phi_{11}, \phi_{12}, \phi_{13}, \phi_{14}, 0, 0) \\ \phi_2 = (0, \phi_{22}, \phi_{23}, 0, \phi_{25}, \phi_{26}) \\ \phi_3 = (0, \phi_{32}, \phi_{33}, 0, \phi_{35}, \phi_{36}) \end{cases}. \quad (\text{D.2})$$

In the above, ϕ_{ij} ($i = 1, 2, 3$; $j = 1, 2, \dots, 6$) is the interpolation coefficient (see Appendix C) of the i^{th} solid node with respect to the j^{th} background node. Let the non-zero coefficients be denoted by:

$$\begin{cases} \bar{\phi}_1 = (\phi_{11}, \phi_{12}, \phi_{13}, \phi_{14}) \\ \bar{\phi}_2 = (\phi_{22}, \phi_{23}, \phi_{25}, \phi_{26}) \\ \bar{\phi}_3 = (\phi_{32}, \phi_{33}, \phi_{35}, \phi_{36}) \end{cases}, \quad (\text{D.3})$$

then

$$\mathbf{D}_e^T \mathbf{K}_e^s \mathbf{D}_e = (\phi_1^T, \phi_2^T, \phi_3^T) \begin{bmatrix} k_{11} & k_{12} & k_{13} \\ k_{21} & k_{22} & k_{23} \\ k_{31} & k_{32} & k_{33} \end{bmatrix} \begin{pmatrix} \phi_1 \\ \phi_2 \\ \phi_3 \end{pmatrix}, \quad (\text{D.4})$$

or

$$\begin{aligned} \mathbf{D}_e^T \mathbf{K}_e^s \mathbf{D}_e &= k_{11} \phi_1^T \phi_1 + k_{12} \phi_1^T \phi_2 + k_{13} \phi_1^T \phi_3 \\ &\quad + k_{21} \phi_2^T \phi_1 + k_{22} \phi_2^T \phi_2 + k_{23} \phi_2^T \phi_3 \\ &\quad + k_{31} \phi_3^T \phi_1 + k_{32} \phi_3^T \phi_2 + k_{33} \phi_3^T \phi_3. \end{aligned} \quad (\text{D.5})$$

Assembling the matrix $\mathbf{D}_e^T \mathbf{K}_e^s \mathbf{D}_e$ into matrix \mathbf{K} is equivalent to assembling the nonzero elements of $k_{ij} \phi_i^T \phi_j$ ($i, j = 1, 2, 3$) to \mathbf{K} , which is also equivalent to assembling elements of $k_{ij} \bar{\phi}_i^T \bar{\phi}_j$ ($i, j = 1, 2, 3$) into \mathbf{K} .

Appendix E

A method to implement hanging nodes

An adaptive mesh with hanging nodes reduces the number of degrees of freedom compared to uniform refinement, hence decreases the cost of computation. However, the nature of hanging nodes has the potential to cause discontinuity which breaks the framework of the finite element method without special treatment to enforce continuity.

In order to treat the hanging nodes, one can construct a conforming shape function [56, 62] or generally constrain and cancel the degree of freedom at the hanging nodes [7, 56]. The former is very appealing, but it is difficult to extend to high-order shape functions [152]. In this thesis we will adopt the latter method and only use 2-level hanging nodes, which means that at most 2 hanging nodes are allowed in one element (this can be guaranteed by imposing safety layers to ensure that neighbouring element nodes differ by no more than one level of refinement). The implementation of arbitrary-level hanging nodes can be found in [104, 123, 152].

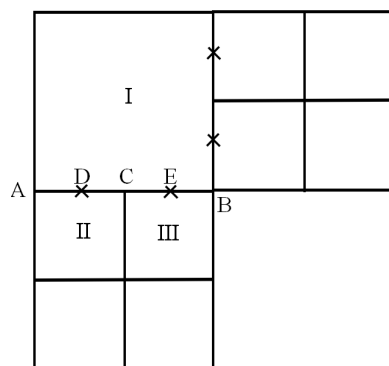


Figure A.1: Elements with hanging nodes.

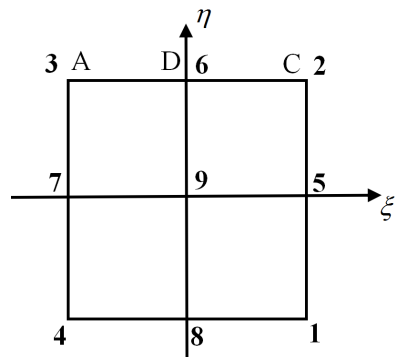


Figure A.2: Element II in Figure A.1 in the reference coordinate system.

For a quadrilateral element, when the velocity is interpolated by biquadratic shape functions and the pressure is interpolated by bilinear shape functions, the implementation of hanging nodes must be different for each, as shown in Figure A.1. For example, when velocity is interpolated, point D is a hanging node for element II, and point E is a hanging node for element III. When pressure is interpolated, point C is a hanging node for both the element II and III. Take element II for example, if we use the constraint method to cancel the hanging node degree of freedom, then

$$u_i^D = \frac{3}{8}u_i^A - \frac{1}{8}u_i^B + \frac{3}{4}u_i^C \quad i = (1, 2) \quad (\text{E.1})$$

and

$$p^C = \frac{1}{2}p^A + \frac{1}{2}p^B, \quad (\text{E.2})$$

where u_i and p are velocity components and pressure respectively defined at the corresponding nodes. The interpolation coefficients can be calculated by putting edge AB in a one dimensional finite element reference coordinate system.

Notice that when computing the element matrix II, point B is outside of the element, but the element matrix II still contributes to node B because of the hanging node D . So we can treat the two points B and D as a master-slave couple, which means letting them share the same equation number in the final global linear equation system. However one should modify the element matrix II according to (E.1) and (E.2) in the following way before assembling it to the global matrix.

Suppose the element II is enumerated in the reference coordinate system as shown in Figure A.2. Then, formulae (E.1) and (E.2) imply the following equations:

$$\begin{pmatrix} u_i^1 \\ u_i^2 \\ u_i^3 \\ u_i^4 \\ u_i^5 \\ u_i^6 \\ u_i^7 \\ u_i^8 \\ u_i^9 \end{pmatrix} = \mathbf{D}^v \begin{pmatrix} u_i^1 \\ u_i^2 \\ u_i^3 \\ u_i^4 \\ u_i^5 \\ u_i^B \\ u_i^7 \\ u_i^8 \\ u_i^9 \end{pmatrix}, \quad \mathbf{D}^v = \begin{bmatrix} 1 & & & & & & & & \\ & 1 & & & & & & & \\ & & 1 & & & & & & \\ & & & 1 & & & & & \\ & & & & 1 & & & & \\ \frac{3}{4} & \frac{3}{8} & & & & -\frac{1}{8} & & & \\ & & & & & & 1 & & \\ & & & & & & & 1 & \\ & & & & & & & & 1 \end{bmatrix}. \quad (\text{E.3})$$

$$\begin{pmatrix} p^1 \\ p^2 \\ p^3 \\ p^4 \end{pmatrix} = \mathbf{D}^p \begin{pmatrix} p^1 \\ p^B \\ p^3 \\ p^4 \end{pmatrix}, \quad \mathbf{D}^p = \begin{bmatrix} 1 & & & \\ & \frac{1}{2} & \frac{1}{2} & \\ & & 1 & \\ & & & 1 \end{bmatrix}. \quad (\text{E.4})$$

One should use matrices \mathbf{D}^v and \mathbf{D}^p to modify the element matrix II. Suppose \mathbf{K}_e is the stiffness matrix of element II without consideration of hanging nodes, and the unknowns are

arranged in the following column vector.

$$(u_1^1, u_1^2, \dots, u_1^9, v_1^1, v_1^2, \dots, v_1^9, p^1, p^2, \dots, p^4)^T. \quad (\text{E.5})$$

It is clear that $\mathbf{K}_e = [k_{ij}]$ is a $n \times n$ ($n=22$) matrix, and it could be modified by the following pseudocode, which distributes the contribution of hanging nodes to the corresponding nodes according to formula (E.1).

Algorithm 6: Modification of the element matrix related to velocity

$\mathbf{1}$ for j=1 to n $k_{i_1j} = k_{i_1j} + k_{i_0j} \cdot 3/8$ $k_{i_2j} = k_{i_2j} + k_{i_0j} \cdot 3/4$ end	for j=1 to n $k_{ji_1} = k_{ji_1} + k_{ji_0} \cdot 3/8$ $k_{ji_2} = k_{ji_2} + k_{ji_0} \cdot 3/4$ end	for j=1 to n $k_{i_0j} = -k_{i_0j}/8$ $k_{ji_0} = -k_{ji_0}/8$ end
---	---	---

Let $i_0 = 6$, $i_1 = 3$, and $i_2 = 2$ (based on (E.5)), then sequentially executing the above three pieces of code would modify the matrix \mathbf{K}_e corresponding to the first component of velocity. Similarly, letting $i_0 = 15$, $i_1 = 12$, and $i_2 = 11$ (based on (E.5)), executing the above code would modify the matrix \mathbf{K}_e corresponding to the second component of velocity. In order to modify the matrix corresponding to pressure, one can execute the following code which is based on formula (E.2).

Algorithm 7: Modification of the element matrix related to pressure

$\mathbf{1}$ for j=1 to n $k_{i_1j} = k_{i_1j} + k_{i_2j}/2$ end	for j=1 to n $k_{ji_1} = k_{ji_1} + k_{ji_2}/2$ end	for j=1 to n $k_{i_2j} = -k_{i_2j}/2; k_{ji_2} = -k_{ji_2}/2$ end
---	---	---

Selecting $i_1 = 21$ and $i_2 = 20$ yields the required modification. Executing all the above pieces of code is equivalent to performing the following matrix multiplication.

$$\begin{bmatrix} \mathbf{D}^v & & \\ & \mathbf{D}^v & \\ & & \mathbf{D}^p \end{bmatrix}^T \mathbf{K}_e \begin{bmatrix} \mathbf{D}^v & & \\ & \mathbf{D}^v & \\ & & \mathbf{D}^p \end{bmatrix}. \quad (\text{E.6})$$

The modification of the mass matrix is similar but easier if a lumped mass is adopted, though it is unnecessary to present details here. Once the element matrix is modified, it can then be assembled directly to the global matrix to implement the constraint of the hanging node (because the hanging node shares the same equation number with its related node in the neighbouring element).

Appendix F

F-scheme and d-scheme

The terms **F**-scheme and **d**-scheme are introduced by Professor Olivier Pironneau. We have not found the paper in which he adopted these terms, however the meanings are clear from [67, 110]. This is actually related to the implementation of his method, and we ought to be able to use the schemes similarly here in our method. From equation (3.6) we can see that there is a term ($\int_{\Omega_{\mathbf{X}}^s} \mu^s \mathbf{F} : \nabla_{\mathbf{X}} \mathbf{v} d\mathbf{X}$) integrated in the reference domain $\Omega_{\mathbf{X}}^s$, and \mathbf{F} could be updated at the end of every time step (see equation (3.8)). This is called the **F**-scheme. Alternatively, we can also transform this term to be integrated in the current domain Ω_t^s :

$$\int_{\Omega_{\mathbf{X}}^s} \mu^s \mathbf{F} : \nabla_{\mathbf{X}} \mathbf{v} d\mathbf{X} = \int_{\Omega_t^s} \mu^s J^{-1} \mathbf{F} \mathbf{F}^T : \nabla \mathbf{v} d\mathbf{x} = \int_{\Omega_t^s} \boldsymbol{\tau}^s : \nabla \mathbf{v} d\mathbf{x}, \quad (\text{F.1})$$

and express

$$\boldsymbol{\tau}^s = \mu^s J^{-1} \mathbf{B} = \mu^s J^{-1} \mathbf{F} \mathbf{F}^T, \quad (\text{F.2})$$

with respect to the displacement **d**, which is then called the **d**-scheme.

Let us only consider a 2D case, readers may refer to [34] for the 3D case. According to the Cayley-Hamilton theorem, \mathbf{B} satisfies its characteristic equation, i.e.,

$$\mathbf{B}^2 - \text{tr}_{\mathbf{B}} \mathbf{B} + J^2 \mathbf{I} = 0, \quad (\text{F.3})$$

from which we immediately have:

$$\mathbf{B} = \text{tr}_{\mathbf{B}} \mathbf{I} - J^2 \mathbf{B}^{-1}. \quad (\text{F.4})$$

From the definition of \mathbf{F} , we get

$$\mathbf{F} = \nabla_{\mathbf{X}} \mathbf{x} = \nabla_{\mathbf{X}} (\mathbf{X} + \mathbf{d}) = \mathbf{I} + \mathbf{F} \nabla \mathbf{d}, \quad (\text{F.5})$$

which further gives:

$$\mathbf{F}^{-1} = \mathbf{I} - \nabla \mathbf{d}. \quad (\text{F.6})$$

Substituting (F.4) and (F.6) into (F.2), we finally express $\boldsymbol{\tau}^s$ by displacement as follows:

$$\boldsymbol{\tau}^s = -\mu^s J (\mathbf{I} - \nabla \mathbf{d})^T (\mathbf{I} - \nabla \mathbf{d}) + \mu^s J^{-1} \operatorname{tr}_{\mathbf{B}} \mathbf{I}, \quad (\text{F.7})$$

which can be written as

$$\boldsymbol{\tau}^s = \mu^s J (\mathbf{D} \mathbf{d} - \nabla^T \mathbf{d} \nabla \mathbf{d}) + \bar{p} \mathbf{I}, \quad (\text{F.8})$$

where $\bar{p} = \mu^s J^{-1} \operatorname{tr}_{\mathbf{B}} - \mu^s J$ is introduced as an additional unknown.

Remark F.1. The difference between the **F**-scheme and **d**-scheme can merit a further study. We have implemented the **d**-scheme for Test1-2D (activated disc) and Test4-2D (rotating disc) using the 2-step splitting scheme, and found that the iterative linear solver (see Section 4.2) could not converge. However the same iterative solver works very well for the **F**-scheme. The direct solver gives the same results for both the **F**-scheme and **d**-scheme. Therefore the matrix structure behind these two schemes is worth further study.

Bibliography

- [1] M. Aletti, J.-F. Gerbeau, and D. Lombardi. A simplified fluid–structure model for arterial flow. Application to retinal hemodynamics. *Computer Methods in Applied Mechanics and Engineering*, 306:77–94, 2016.
- [2] M. Ambati, T. Gerasimov, and L. De Lorenzis. A review on phase-field models of brittle fracture and a new fast hybrid formulation. *Computational Mechanics*, 55(2):383–405, 2015.
- [3] D. N. Arnold, F. Brezzi, B. Cockburn, and L. D. Marini. Unified analysis of discontinuous Galerkin methods for elliptic problems. *SIAM Journal on Numerical Analysis*, 39(5):1749–1779, 2002.
- [4] F. Auricchio, D. Boffi, L. Gastaldi, A. Lefieux, and A. Reali. A study on unfitted 1d finite element methods. *Computers & Mathematics with Applications*, 68(12):2080–2102, 2014.
- [5] F. P. Baaijens. A fictitious domain/mortar element method for fluid-structure interaction. *International Journal for Numerical Methods in Fluids*, 35(7):743–761, 2001.
- [6] W. Bai and R. E. Taylor. Fully nonlinear simulation of wave interaction with fixed and floating flared structures. *Ocean Engineering*, 36(3):223–236, 2009.
- [7] W. Bangerth and O. Kayser-Herold. Data structures and requirements for hp finite element software. *ACM Transactions on Mathematical Software*, 36(1):1–31, 2009.
- [8] K.-J. Bathe, H. Zhang, and S. Ji. Finite element analysis of fluid flows fully coupled with structural interactions. *Computers & Structures*, 72(1-3):1–16, 1999.
- [9] Y. Bazilevs, V. M. Calo, Y. Zhang, and T. J. Hughes. Isogeometric fluid–structure interaction analysis with applications to arterial blood flow. *Computational Mechanics*, 38(4-5):310–322, 2006.
- [10] Y. Bazilevs, M.-C. Hsu, I. Akkerman, S. Wright, K. Takizawa, B. Henicke, T. Spielman, and T. Tezduyar. 3d simulation of wind turbine rotors at full scale. Part I: Geometry modeling and aerodynamics. *International Journal for Numerical Methods in Fluids*, 65(1-3):207–235, 2011.

- [11] Y. Bazilevs, M.-C. Hsu, J. Kiendl, R. Wüchner, and K.-U. Bletzinger. 3d simulation of wind turbine rotors at full scale. Part II: Fluid–structure interaction modeling with composite blades. *International Journal for Numerical Methods in Fluids*, 65(1-3):236–253, 2011.
- [12] Y. Bazilevs, M.-C. Hsu, Y. Zhang, W. Wang, T. Kvamsdal, S. Hentschel, and J. G. Isaksen. Computational vascular fluid–structure interaction: methodology and application to cerebral aneurysms. *Biomechanics and Modeling in Mechanobiology*, 9(4):481–498, 2010.
- [13] Y. Bazilevs, M.-C. Hsu, Y. Zhang, W. Wang, X. Liang, T. Kvamsdal, R. Brekken, and J. Isaksen. A fully-coupled fluid-structure interaction simulation of cerebral aneurysms. *Computational Mechanics*, 46(1):3–16, 2010.
- [14] Y. Bazilevs, K. Takizawa, and T. E. Tezduyar. *Computational fluid-structure interaction: methods and applications*. John Wiley & Sons, 2013.
- [15] P. B. Bochev and M. D. Gunzburger. *Least-squares finite element methods*, volume 166. Springer Science & Business Media, 2009.
- [16] D. Boffi, N. Cavallini, F. Gardini, and L. Gastaldi. Local mass conservation of Stokes finite elements. *Journal of Scientific Computing*, 52(2):383–400, 2011.
- [17] D. Boffi, N. Cavallini, and L. Gastaldi. The finite element immersed boundary method with distributed Lagrange multiplier. *SIAM Journal on Numerical Analysis*, 53(6):2584–2604, 2015.
- [18] D. Boffi and L. Gastaldi. A fictitious domain approach with Lagrange multiplier for fluid-structure interactions. *Numerische Mathematik*, 135(3):711–732, 2016.
- [19] P. Bollada, P. Jimack, and A. Mullis. Bracket formalism applied to phase field models of alloy solidification. *Computational Materials Science*, 126:426–437, 2017.
- [20] J. Bols, J. Degroote, B. Trachet, B. Verhegge, P. Segers, and J. Vierendeels. A computational method to assess the in vivo stresses and unloaded configuration of patient-specific blood vessels. *Journal of Computational and Applied Mathematics*, 246:10–17, 2013.
- [21] R. Boman and J.-P. Ponthot. Finite element simulation of lubricated contact in rolling using the arbitrary Lagrangian–Eulerian formulation. *Computer Methods in Applied Mechanics and Engineering*, 193(39):4323–4353, 2004.
- [22] S. Boyd and L. Vandenberghe. Convex optimization problems. In *Convex Optimization*, pages 127–214. Cambridge University Press.
- [23] F. Boyer, C. Lapuerta, S. Minjeaud, B. Piar, and M. Quintard. Cahn–Hilliard/Navier–Stokes model for the simulation of three-phase flows. *Transport in Porous Media*, 82(3):463–483, 2010.

- [24] S. Brenner and R. Scott. *The mathematical theory of finite element methods*, volume 15. Springer Science & Business Media, 2007.
- [25] H.-J. Bungartz, M. Mehl, and M. Schäfer. *Fluid Structure Interaction II: Modelling, Simulation, Optimization*, volume 73. Springer Science & Business Media, 2010.
- [26] A. Calderer, X. Guo, L. Shen, and F. Sotiropoulos. Coupled fluid-structure interaction simulation of floating offshore wind turbines and waves: a large eddy simulation approach. *Journal of Physics: Conference Series*, 524:012091, 2014.
- [27] M. Calvache and A. Pulido-Bosch. Effects of geology and human activity on the dynamics of salt-water intrusion in three coastal aquifers in southern Spain. *Environmental Geology*, 30(3):215–223, 1997.
- [28] P. Causin, J.-F. Gerbeau, C. Guivier, and P. Métier. An embedded surface method for valve simulation. application to stenotic aortic valve estimation. In *ESAIM: Proceedings*, volume 14, pages 48–62. EDP sciences, 2005.
- [29] P. Causin, J.-F. Gerbeau, and F. Nobile. Added-mass effect in the design of partitioned algorithms for fluid–structure problems. *Computer Methods in Applied Mechanics and Engineering*, 194(42):4506–4527, 2005.
- [30] V. Chabannes, G. Pena, and C. Prud’homme. High-order fluid–structure interaction in 2d and 3d application to blood flow in arteries. *Journal of Computational and Applied Mathematics*, 246:1–9, 2013.
- [31] K.-W. Cheng and T.-P. Fries. XFEM with hanging nodes for two-phase incompressible flow. *Computer Methods in Applied Mechanics and Engineering*, 245:290–312, 2012.
- [32] R. Cheng, Y. G. Lai, and K. B. Chandran. Three-dimensional fluid-structure interaction simulation of bileaflet mechanical heart valve flow dynamics. *Annals of Biomedical Engineering*, 32(11):1471–1483, 2004.
- [33] Y. Chi, R. Löhner, and L. Haidong. An unstructured-grid based volume-of-fluid method for extreme wave and freely-floating structure interactions. *Journal of Hydrodynamics, Ser. B*, 18(3):415–422, 2006.
- [34] C.-Y. Chiang, O. Pironneau, T. Sheu, and M. Thiriet. Numerical study of a 3d Eulerian monolithic formulation for incompressible fluid-structures systems. *Fluids*, 2(2):34, 2017.
- [35] Y. J. Choi, M. A. Hulsen, and H. E. Meijer. An extended finite element method for the simulation of particulate viscoelastic flows. *Journal of Non-Newtonian Fluid Mechanics*, 165(11):607–624, 2010.

- [36] G. Conte and A. Serrani. Modelling and simulation of underwater vehicles. In *Computer-Aided Control System Design, 1996. Proceedings of the 1996 IEEE International Symposium on*, pages 62–67. IEEE, 1996.
- [37] P. Crosetto, P. Reymond, S. Deparis, D. Kontaxakis, N. Stergiopoulos, and A. Quarteroni. Fluid–structure interaction simulation of aortic blood flow. *Computers & Fluids*, 43(1):46–57, 2011.
- [38] L. Davidson, D. Cokljat, J. Fröhlich, M. A. Leschziner, C. Mellen, and W. Rodi. *LESFOIL: Large Eddy Simulation of Flow Around a High Lift Airfoil: Results of the Project LESFOIL Supported by the European Union 1998–2001*, volume 83. Springer Science & Business Media, 2012.
- [39] R. De Sutter, R. Verhoeven, and A. Krein. Simulation of sediment transport during flood events: laboratory work and field experiments. *Hydrological Sciences Journal*, 46(4):599–610, 2001.
- [40] J. Degroote, K.-J. Bathe, and J. Vierendeels. Performance of a new partitioned procedure versus a monolithic procedure in fluid–structure interaction. *Computers & Structures*, 87(11-12):793–801, 2009.
- [41] J. Degroote, P. Bruggeman, R. Haelterman, and J. Vierendeels. Stability of a coupling technique for partitioned solvers in FSI applications. *Computers & Structures*, 86(23):2224–2234, 2008.
- [42] T. Dunne. An Eulerian approach to fluid–structure interaction and goal-oriented mesh adaptation. *International Journal for Numerical Methods in Fluids*, 51(9-10):1017–1039, 2006.
- [43] T. Dunne and R. Rannacher. Adaptive finite element approximation of fluid-structure interaction based on an Eulerian variational formulation. In *Lecture Notes in Computational Science and Engineering*, pages 110–145. Springer Science Business Media, 2006.
- [44] G. Duvaut and J. L. Lions. *Inequalities in Mechanics and Physics*. Springer Berlin Heidelberg, 1976.
- [45] A. C. Elias. *Fluid-Structure Interaction Simulation of Complex Floating Structures and Waves*. PhD thesis, University of Minnesota, 2015.
- [46] H. Elman, D. Silvester, and A. Wathen. *Finite Elements and Fast Iterative Solvers*. Oxford University Press, 2014.
- [47] G. C. Everstine and F. M. Henderson. Coupled finite element/boundary element approach for fluid–structure interaction. *The Journal of the Acoustical Society of America*, 87(5):1938–1947, 1990.

- [48] E. Fadlun, R. Verzicco, P. Orlandi, and J. Mohd-Yusof. Combined immersed-boundary finite-difference methods for three-dimensional complex flow simulations. *Journal of Computational Physics*, 161(1):35–60, 2000.
- [49] Z.-G. Feng and E. E. Michaelides. The immersed boundary-Lattice Boltzmann method for solving fluid-particles interaction problems. *Journal of Computational Physics*, 195(2):602–628, 2004.
- [50] M. Á. Fernández and M. Moubachir. A Newton method using exact Jacobians for solving fluid-structure coupling. *Computers & Structures*, 83(2):127–142, 2005.
- [51] T. Feseker. Numerical studies on saltwater intrusion in a coastal aquifer in northwestern Germany. *Hydrogeology Journal*, 15(2):267–279, 2007.
- [52] W. Finnegan and J. Goggins. Numerical simulation of linear water waves and wave-structure interaction. *Ocean Engineering*, 43:23–31, 2012.
- [53] C. Förster, W. A. Wall, and E. Ramm. Artificial added mass instabilities in sequential staggered coupling of nonlinear structures and incompressible viscous flows. *Computer Methods in Applied Mechanics and Engineering*, 196(7):1278–1293, 2007.
- [54] S. Frei. *Eulerian finite element methods for interface problems and fluid-structure interactions*. PhD thesis, Universitt Heidelberg, 2016.
- [55] S. Frei and T. Richter. A locally modified parametric finite element method for interface problems. *SIAM Journal on Numerical Analysis*, 52(5):2315–2334, 2014.
- [56] T.-P. Fries, A. Byfut, A. Alizada, K. W. Cheng, and A. Schöder. Hanging nodes and XFEM. *International Journal for Numerical Methods in Engineering*, 86(4-5):404–430, 2010.
- [57] A. Gerstenberger and W. A. Wall. An extended finite element method/Lagrange multiplier based approach for fluid-structure interaction. *Computer Methods in Applied Mechanics and Engineering*, 197(19-20):1699–1714, 2008.
- [58] R. Glowinski. Finite element methods for incompressible viscous flow. In *Handbook of Numerical Analysis*, pages 3–1176. Elsevier, 2003.
- [59] R. Glowinski, T. Pan, T. Hesla, D. Joseph, and J. Périaux. A fictitious domain approach to the direct numerical simulation of incompressible viscous flow past moving rigid bodies: Application to particulate flow. *Journal of Computational Physics*, 169(2):363–426, 2001.
- [60] R. Glowinski, T.-W. Pan, T. Hesla, and D. Joseph. A distributed Lagrange multiplier/fictitious domain method for particulate flows. *International Journal of Multiphase Flow*, 25(5):755–794, 1999.

- [61] P. M. Gresho, R. L. Lee, and R. L. Sani. Advection-dominated flows, with emphasis on the consequences of mass lumping. In *International Symposium on Finite Element Methods in Flow Problems*, pages 745–756, 1976.
- [62] A. K. Gupta. A finite element for transition from a fine to a coarse grid. *International Journal for Numerical Methods in Engineering*, 12(1):35–45, 1978.
- [63] C. Habchi, S. Russeil, D. Bougeard, J.-L. Harion, T. Lemenand, A. Ghanem, D. Della Valle, and H. Peerhossaini. Partitioned solver for strongly coupled fluid–structure interaction. *Computers & Fluids*, 71:306–319, 2013.
- [64] J. Hao, Z. Li, and S. R. Lubkin. An augmented immersed interface method for moving structures with mass. *Discrete and Continuous Dynamical Systems. Series B*, 17(4):1175, 2012.
- [65] J. Hao and T.-W. Pan. Simulation for high Weissenberg number: viscoelastic flow by a finite element method. *Applied Mathematics Letters*, 20(9):988–993, 2007.
- [66] J. Hao, T.-W. Pan, R. Glowinski, and D. D. Joseph. A fictitious domain/distributed Lagrange multiplier method for the particulate flow of Oldroyd-B fluids: A positive definiteness preserving approach. *Journal of Non-Newtonian Fluid Mechanics*, 156(1-2):95–111, 2009.
- [67] F. Hecht and O. Pironneau. An energy stable monolithic Eulerian fluid-structure finite element method. *International Journal for Numerical Methods in Fluids*, 2017.
- [68] M. Heil. An efficient solver for the fully coupled solution of large-displacement fluid–structure interaction problems. *Computer Methods in Applied Mechanics and Engineering*, 193(1-2):1–23, 2004.
- [69] M. Heil, A. L. Hazel, and J. Boyle. Solvers for large-displacement fluid–structure interaction problems: segregated versus monolithic approaches. *Computational Mechanics*, 43(1):91–101, 2008.
- [70] C. Hesch, A. Gil, A. A. Carreño, J. Bonet, and P. Betsch. A mortar approach for fluid–structure interaction problems: Immersed strategies for deformable and rigid bodies. *Computer Methods in Applied Mechanics and Engineering*, 278:853–882, 2014.
- [71] T. Hibiya. Generation mechanism of internal waves by a vertically sheared tidal flow over a sill. *Journal of Geophysical Research: Oceans*, 95(C2):1757–1764, 1990.
- [72] G. Hou, J. Wang, and A. Layton. Numerical methods for fluid-structure interactiona review. *Communications in Computational Physics*, 12(2):337–377, 2012.

- [73] J. Hron and S. Turek. A monolithic fem/multigrid solver for an ALE formulation of fluid-structure interaction with applications in biomechanics. *Fluid-structure interaction*, pages 146–170, 2006.
- [74] B. Hübner, E. Walhorn, and D. Dinkler. A monolithic approach to fluid-structure interaction using space-time finite elements. *Computer Methods in Applied Mechanics and Engineering*, 193(23):2087–2104, 2004.
- [75] M. A. Hulsen, R. Fattal, and R. Kupferman. Flow of viscoelastic fluids past a cylinder at high Weissenberg number: stabilized simulations using matrix logarithms. *Journal of Non-Newtonian Fluid Mechanics*, 127(1):27–39, 2005.
- [76] S. Idelsohn, E. Onate, and F. Del Pin. A Lagrangian meshless finite element method applied to fluid-structure interaction problems. *Computers & Structures*, 81(8-11):655–671, 2003.
- [77] S. R. Idelsohn, J. Martí, A. Limache, and E. Oñate. Unified Lagrangian formulation for elastic solids and incompressible fluids: application to fluid-structure interaction problems via the PFEM. *Computer Methods in Applied Mechanics and Engineering*, 197(19-20):1762–1776, 2008.
- [78] A. Ivankovic, A. Karac, E. Dendrinos, and K. Parker. Towards early diagnosis of atherosclerosis: the finite volume method for fluid-structure interaction. *Biorheology*, 39(3, 4):401–407, 2002.
- [79] C. Kadapa, W. Dettmer, and D. Perić. A fictitious domain/distributed Lagrange multiplier based fluid-structure interaction scheme with hierarchical b-spline grids. *Computer Methods in Applied Mechanics and Engineering*, 301:1–27, 2016.
- [80] V. Kalro and T. E. Tezduyar. A parallel 3d computational method for fluid-structure interactions in parachute systems. *Computer Methods in Applied Mechanics and Engineering*, 190(3):321–332, 2000.
- [81] J. Kim, D. Kim, and H. Choi. An immersed-boundary finite-volume method for simulations of flow in complex geometries. *Journal of Computational Physics*, 171(1):132–150, 2001.
- [82] M. Krafczyk, J. Tölke, E. Rank, and M. Schulz. Two-dimensional simulation of fluid-structure interaction using Lattice-Boltzmann methods. *Computers & Structures*, 79(22-25):2031–2037, 2001.
- [83] U. Kttler and W. A. Wall. Fixed-point fluid-structure interaction solvers with dynamic relaxation. *Computational Mechanics*, 43(1):61–72, 2008.

- [84] U. Küttler and W. A. Wall. Fixed-point fluid–structure interaction solvers with dynamic relaxation. *Computational Mechanics*, 43(1):61–72, 2008.
- [85] P. Larroude and T. Oudart. SPH model to simulate movement of grass meadow of posidonia under waves. *Coastal Engineering Proceedings*, 1(33):56, 2012.
- [86] H. Laval and L. Quartapelle. A fractional-step Taylor–Galerkin method for unsteady incompressible flows. *International Journal for Numerical Methods in Fluids*, 11(5):501–513, 1990.
- [87] P. Le Tallec and J. Mouro. Fluid structure interaction with large structural displacements. *Computer Methods in Applied Mechanics and Engineering*, 190(24):3039–3067, 2001.
- [88] C.-W. Lee, Y.-B. Kim, G.-H. Lee, M.-Y. Choe, M.-K. Lee, and K.-Y. Koo. Dynamic simulation of a fish cage system subjected to currents and waves. *Ocean Engineering*, 35(14):1521–1532, 2008.
- [89] T.-R. Lee, Y.-S. Chang, J.-B. Choi, D. W. Kim, W. K. Liu, and Y.-J. Kim. Immersed finite element method for rigid body motions in the incompressible Navier–Stokes flow. *Computer Methods in Applied Mechanics and Engineering*, 197(25–28):2305–2316, 2008.
- [90] A. Legay, J. Chessa, and T. Belytschko. An Eulerian–Lagrangian method for fluid–structure interaction based on level sets. *Computer Methods in Applied Mechanics and Engineering*, 195(17):2070–2087, 2006.
- [91] Y. Li, A. Castro, T. Sinokrot, W. Prescott, and P. Carrica. Coupled multi-body dynamics and CFD for wind turbine simulation including explicit wind turbulence. *Renewable Energy*, 76:338–361, 2015.
- [92] Z. Li. An augmented cartesian grid method for Stokes–Darcy fluid–structure interactions. *International Journal for Numerical Methods in Engineering*, 106(7):556–575, 2016.
- [93] Z. Li and C. Kleinstreuer. Blood flow and structure interactions in a stented abdominal aortic aneurysm model. *Medical Engineering & Physics*, 27(5):369–382, 2005.
- [94] G. Liang and Y. Zhou. *Finite Element Language and its Application (in Chinese)*. Science Press, 2013.
- [95] G.-R. Liu and Y.-T. Gu. *An Introduction to Meshfree Methods and Their Programming*. Springer-Verlag, 2005.
- [96] W. K. Liu, D. W. Kim, and S. Tang. Mathematical foundations of the immersed finite element method. *Computational Mechanics*, 39(3):211–222, 2007.
- [97] J. R. Magnus and H. Neudecker. Matrix differential calculus with applications in statistics and econometrics. *Wiley Series in Probability and Mathematical Statistics*, 1988.

- [98] H. G. Matthies and J. Steindorf. Partitioned strong coupling algorithms for fluid–structure interaction. *Computers & Structures*, 81(8):805–812, 2003.
- [99] D. Mitrovic and D. Zubrinic. *Fundamentals of applied functional analysis*, volume 91. CRC Press, 1997.
- [100] P. Moireau, N. Xiao, M. Astorino, C. A. Figueira, D. Chapelle, C. Taylor, and J.-F. Gerbeau. External tissue support and fluid–structure simulation in blood flows. *Biomechanics and Modeling in Mechanobiology*, 11(1-2):1–18, 2012.
- [101] D. P. Mok and W. Wall. Partitioned analysis schemes for the transient interaction of incompressible flows and nonlinear flexible structures. *Trends in Computational Structural Mechanics, Barcelona*, 2001.
- [102] R. L. Muddle, M. Mihajlović, and M. Heil. An efficient preconditioner for monolithically-coupled large-displacement fluid–structure interaction problems with pseudo-solid mesh updates. *Journal of Computational Physics*, 231(21):7315–7334, 2012.
- [103] H. Noguchi and G. Gompper. Shape transitions of fluid vesicles and red blood cells in capillary flows. *Proceedings of the National Academy of Sciences of the United States of America*, 102(40):14159–14164, 2005.
- [104] E. Ooi, H. Man, S. Natarajan, and C. Song. Adaptation of quadtree meshes in the scaled boundary finite element method for crack propagation modelling. *Engineering Fracture Mechanics*, 144:101–117, 2015.
- [105] D. Owen, C. Leonardi, and Y. Feng. An efficient framework for fluid–structure interaction using the Lattice Boltzmann method and immersed moving boundaries. *International Journal for Numerical Methods in Engineering*, 87(1-5):66–95, 2011.
- [106] N. Patankar, P. Singh, D. Joseph, R. Glowinski, and T.-W. Pan. A new formulation of the distributed Lagrange multiplier/fictitious domain method for particulate flows. *International Journal of Multiphase Flow*, 26(9):1509–1524, 2000.
- [107] C. S. Peskin. The immersed boundary method. *Acta Numerica*, 11:479–517, 2002.
- [108] O. Pironneau. *Finite element methods for fluids*. Wiley Chichester, 1989.
- [109] O. Pironneau. An energy preserving monolithic Eulerian fluid-structure numerical scheme. *arXiv:1607.08083v1 [cs.CE]* 27 Jul 2016, 2016.
- [110] O. Pironneau. Numerical study of a monolithic fluid–structure formulation. In *Variational Analysis and Aerospace Engineering*, pages 401–420. Springer International Publishing, 2016.

- [111] C. Pozrikidis. Numerical simulation of the flow-induced deformation of red blood cells. *Annals of Biomedical Engineering*, 31(10):1194–1205, 2003.
- [112] T. T. J. Prestero. *Verification of a six-degree of freedom simulation model for the REMUS autonomous underwater vehicle*. PhD thesis, Massachusetts Institute of Technology, 2001.
- [113] T. Rabczuk, R. Gracie, J.-H. Song, and T. Belytschko. Immersed particle method for fluid–structure interaction. *International Journal for Numerical Methods in Engineering*, 81(1):48–71, 2010.
- [114] L. B. Rall. *Nonlinear functional analysis and applications: proceedings of an advanced seminar conducted by the Mathematics Research Center, the University of Wisconsin, Madison, October 12-14, 1970*. Number 26. Elsevier, 2014.
- [115] R. Rannacher and T. Richter. An adaptive finite element method for fluid–structure interaction problems based on a fully Eulerian formulation. In *Fluid Structure Interaction II*, pages 159–191. Springer Berlin Heidelberg, 2010.
- [116] T. Richter. A fully Eulerian formulation for fluid–structure-interaction problems. *Journal of Computational Physics*, 233:227–240, 2013.
- [117] T. Richter and T. Wick. Finite elements for fluid–structure interaction in ALE and fully Eulerian coordinates. *Computer Methods in Applied Mechanics and Engineering*, 199(41–44):2633–2642, 2010.
- [118] A. Robinson-Mosher, C. Schroeder, and R. Fedkiw. A symmetric positive definite formulation for monolithic fluid structure interaction. *Journal of Computational Physics*, 230(4):1547–1566, 2011.
- [119] H. Sauerland and T.-P. Fries. The stable XFEM for two-phase flows. *Computers & Fluids*, 87:41–49, 2013.
- [120] T. W. Secomb, B. Styp-Rekowska, and A. R. Pries. Two-dimensional simulation of red blood cell deformation and lateral migration in microvessels. *Annals of Biomedical Engineering*, 35(5):755–765, 2007.
- [121] X. Shi and S. P. Lim. A LBM–DLM/FD method for 3d fluid–structure interactions. *Journal of Computational Physics*, 226(2):2028–2043, 2007.
- [122] A. Slone, K. Pericleous, C. Bailey, and M. Cross. Dynamic fluid–structure interaction using finite volume unstructured mesh procedures. *Computers & Structures*, 80(5-6):371–390, 2002.
- [123] P. Šolín, J. Červený, and I. Doležel. Arbitrary-level hanging nodes and automatic adaptivity in the hp-FEM. *Mathematics and Computers in Simulation*, 77(1):117–132, 2008.

- [124] Y. Sudhakar, J. M. De Almeida, and W. A. Wall. An accurate, robust, and easy-to-implement method for integration over arbitrary polyhedra: application to embedded interface methods. *Journal of Computational Physics*, 273:393–415, 2014.
- [125] M. Suzuki, A. Ido, Y. Sakuma, and H. Kajiyama. Full-scale measurement and numerical simulation of flow around high-speed train in tunnel. *Journal of Mechanical Systems for Transportation and Logistics*, 1(3):281–292, 2008.
- [126] M. Suzuki, T. Maeda, and N. Arai. Numerical simulation of flow around a train. In *Computation of three-dimensional complex flows*, pages 311–317. Springer, 1996.
- [127] V. Symeonidis, G. E. Karniadakis, and B. Caswell. Schmidt number effects in dissipative particle dynamics simulation of polymers. *The Journal of Chemical Physics*, 125(18):184902, 2006.
- [128] T. E. Tezduyar and S. Sathe. Modelling of fluid–structure interactions with the space–time finite elements: solution techniques. *International Journal for Numerical Methods in Fluids*, 54(6–8):855–900, 2007.
- [129] F.-B. Tian, H. Luo, L. Zhu, J. C. Liao, and X.-Y. Lu. An efficient immersed boundary–Lattice Boltzmann method for the hydrodynamic interaction of elastic filaments. *Journal of computational physics*, 230(19):7266–7283, 2011.
- [130] Q. Tian, Y. Zhang, L. Chen, and J. J. Yang. Simulation of planar flexible multibody systems with clearance and lubricated revolute joints. *Nonlinear Dynamics*, 60(4):489–511, 2010.
- [131] K.-I. Tsubota, S. Wada, and T. Yamaguchi. Particle method for computer simulation of red blood cell motion in blood flow. *Computer Methods and Programs in Biomedicine*, 83(2):139–146, 2006.
- [132] M. Tur, F. Fuenmayor, and P. Wriggers. A mortar-based frictional contact formulation for large deformations using Lagrange multipliers. *Computer Methods in Applied Mechanics and Engineering*, 198(37–40):2860–2873, 2009.
- [133] W. A. Wall. *Fluid-struktur-interaktion mit stabilisierten finiten elementen*. PhD thesis, Universität Stuttgart, 1999.
- [134] W. A. Wall, A. Gerstenberger, P. Gamnitzer, C. Forster, and E. Ramm. Large deformation fluid-structure interaction-advances in ALE methods and new fixed grid approaches. *Lecture Notes in Computational Science and Engineering*, 53:195, 2006.
- [135] W. A. Wall, D. P. Mok, and E. Ramm. Partitioned analysis approach of the transient coupled response of viscous fluids and flexible structures. In *Solids, Structures and Coupled Problems in Engineering, Proceedings of the European Conference on Computational Mechanics ECCM*, volume 99, 1999.

- [136] X. Wang, C. Wang, and L. T. Zhang. Semi-implicit formulation of the immersed finite element method. *Computational Mechanics*, 49(4):421–430, 2011.
- [137] X. Wang and L. T. Zhang. Interpolation functions in the immersed boundary and finite element methods. *Computational Mechanics*, 45(4):321–334, 2009.
- [138] X. Wang and L. T. Zhang. Modified immersed finite element method for fully-coupled fluid–structure interactions. *Computer Methods in Applied Mechanics and Engineering*, 267:150–169, 2013.
- [139] Y. Wang, P. K. Jimack, and M. A. Walkley. A one-field monolithic fictitious domain method for fluid–structure interactions. *Computer Methods in Applied Mechanics and Engineering*, 317:1146–1168, 2017.
- [140] F. Wessels and K. Hutter. Interaction of internal waves with a topographic sill in a two-layered fluid. *Journal of Physical Oceanography*, 26(1):5–20, 1996.
- [141] T. Wick. Adaptive finite elements for monolithic fluid-structure interaction on a prolonged domain: Applied to a heart valve simulation. *archiv.ub.uni-heidelberg.de:11822*, 2011.
- [142] T. Wick. Coupling of fully Eulerian and arbitrary Lagrangian–Eulerian methods for fluid–structure interaction computations. *Computational Mechanics*, 52(5):1113–1124, 2013.
- [143] P. Wriggers and T. A. Laursen. *Computational contact mechanics*, volume 2. Springer, 2006.
- [144] G. Wu and Z. Hu. Simulation of nonlinear interactions between waves and floating bodies through a finite-element-based numerical tank. In *Proceedings of the Royal Society of London A: Mathematical, Physical and Engineering Sciences*, volume 460, pages 2797–2817. The Royal Society, 2004.
- [145] K. Wu, D. Yang, and N. Wright. A coupled SPH-DEM model for fluid-structure interaction problems with free-surface flow and structural failure. *Computers & Structures*, 177:141–161, 2016.
- [146] S. Yiantisios. On the distributed Lagrange multiplier/fictitious domain method for rigid-particle-laden flows: a proposition for an alternative formulation of the Lagrange multipliers. *International Journal for Numerical Methods in Fluids*, 70(8):1027–1047, 2011.
- [147] S. Yoon. *An adaptive finite element method for particle suspension in viscoelastic fluid*. PhD thesis, University of Leeds, 2010.
- [148] S. Yoon, M. Walkley, and O. Harlen. Two particle interactions in a confined viscoelastic fluid under shear. *Journal of Non-Newtonian Fluid Mechanics*, 185–186:39–48, 2012.

- [149] A. R. York, D. Sulusky, and H. L. Schreyer. Fluid–membrane interaction based on the material point method. *International Journal for Numerical Methods in Engineering*, 48(6):901–924, 2000.
- [150] Z. Yu. A DLM/FD method for fluid/flexible-body interactions. *Journal of Computational Physics*, 207(1):1–27, 2005.
- [151] Z.-S. Yu and X.-M. Shao. A three-dimensional fictitious domain method for the simulation of fluid-structure interactions. *Journal of Hydrodynamics, Ser. B*, 22(5):178–183, 2010.
- [152] N. Zander, T. Bog, S. Kollmannsberger, D. Schillinger, and E. Rank. Multi-level hp-adaptivity: high-order mesh adaptivity without the difficulties of constraining hanging nodes. *Computational Mechanics*, 55(3):499–517, 2015.
- [153] E. A. Zedler and R. L. Street. Large-eddy simulation of sediment transport: currents over ripples. *Journal of Hydraulic Engineering*, 127(6):444–452, 2001.
- [154] D.-W. Zhang and H. Ou. Relationship between friction parameters in a Coulomb–Tresca friction model for bulk metal forming. *Tribology International*, 95:13–18, 2016.
- [155] J. Zhang, P. C. Johnson, and A. S. Popel. Red blood cell aggregation and dissociation in shear flows simulated by Lattice Boltzmann method. *Journal of Biomechanics*, 41(1):47–55, 2008.
- [156] L. Zhang and M. Gay. Immersed finite element method for fluid-structure interactions. *Journal of Fluids and Structures*, 23(6):839–857, 2007.
- [157] L. Zhang, A. Gerstenberger, X. Wang, and W. K. Liu. Immersed finite element method. *Computer Methods in Applied Mechanics and Engineering*, 193(21):2051–2067, 2004.
- [158] L. T. Zhang and M. Gay. Imposing rigidity constraints on immersed objects in unsteady fluid flows. *Computational Mechanics*, 42(3):357–370, 2008.
- [159] N. Zhang and Z. C. Zheng. An improved direct-forcing immersed-boundary method for finite difference applications. *Journal of Computational Physics*, 221(1):250–268, 2007.
- [160] Z.-Q. Zhang, G. R. Liu, and B. C. Khoo. Immersed smoothed finite element method for two dimensional fluid-structure interaction problems. *International Journal for Numerical Methods in Engineering*, 90(10):1292–1320, 2012.
- [161] H. Zhao, J. B. Freund, and R. D. Moser. A fixed-mesh method for incompressible flow–structure systems with finite solid deformations. *Journal of Computational Physics*, 227(6):3114–3140, 2008.
- [162] O. C. Zienkiewicz and R. L. Taylor. *The finite element method for solid and structural mechanics*. Elsevier, 2005.

- [163] O. C. Zienkiewicz, R. L. Taylor, and P. Nithiarasu. *The Finite Element Method for Fluid Dynamics*. Elsevier, 2005.